STUDIES OF WIRE-MATRIX INTERACTION IN SOME TUNGSTEN WIRE REINFORCED STAINLESS STEELS

A thesis submitted in partial fulfilment
of the requirements for the Degree
of
DOCTOR OF PHILOSOPHY IN MECHANICAL ENGINEERING
in the
UNIVERSITY OF CANTERBURY
by

PAWAN KUMAR

University of Canterbury

2013

Preface

This thesis is submitted as a partial requirement for the degree of Doctor of Philosophy in Mechanical Engineering in the University of Canterbury. The research described herein was conducted under the supervision of Professor Milo V. Kral and Dr. Catherine Bishop in the Mechanical Engineering Department, University of Canterbury, between December 2008 and November 2013. A part of the work has been presented in the following publication:

P. Kumar, M.V. Kral, "Interface Evolution in Tungsten Wire Reinforced Stainless Steel Composites", in: TMS 2011 Proceedings, Volume 2, Materials Fabrication, Properties, Characterization and Modelling, Minerals, Metals & Materials Society (TMS), 2011, pp. 874-883.

Acknowledgements

I take this opportunity to acknowledge the support and encouragement of many people who have contributed towards various stages of this thesis.

My sincere thanks to my research supervisors Prof. Milo V. Kral and Dr. Catherine Bishop for their invaluable guidance and intellectual input in this work. It was a great honour for me to work with them.

I gratefully acknowledge the University of Canterbury Doctoral scholarship program and the New Zealand Foundation for Research, Science and Technology (FRST) Pre-Seed Accelerator Fund (PSAF) for supporting this research.

Technical staff of Mechanical Engineering department provided their unconditional support in the experimental aspects of this research, and I thank Scott Amies, Ken Brown, David Read, Paul Southward, Julian Murphy, and Eric Cox for this. I also acknowledge the help rendered by Mike Flaws and Kevin Stobbs in mechanical testing, metallography, and microscopy.

My special thanks to past and present colleagues and friends: Amy, Ben G., Ben R., Dan, Karl, and Mandeep for providing friendly environment and helping me out in various ways. My sincere appreciation to Karl for the support and stimulating discussion on microscopy related issues.

Finally, a big thank to my family and friends for their support and understanding throughout the period of my studies.

Table of Contents

List of Tables

List of Figures

Abbreviations and Symbols

$\bar{\bar{\widetilde{D}}}_{eff}$	Average effective interdiffusion coefficient
$\widetilde{D}_{11}^{3}\ and\ \widetilde{D}_{21}^{3}$	main-interdiffusion coefficients in a three component system
$\widetilde{D}_{12}^{3}\ and\ \widetilde{D}_{22}^{3}$	cross-interdiffusion coefficients in a three component system
$\widetilde{D}_{ij}^{n}$	interdiffusion coefficient of component *i* with respect to the concentration gradient of component *j* in an *n* component system
$\widetilde{D}_{int}^{i}$	integrated interdiffusion coefficient
$\tilde{V}_A$	partial molar volume of component A
A_N	Avogadro's number
$\widetilde{D}$	interdiffusion coefficient
$N_i^+\ and\ N_i^-$	mole fraction of component i at extreme right and left ends of an infinite diffusion couple
N_i^*	mole fraction of *i* at the point of diffusion flux measurement
Y_i^*	relative concentration variable
316L, HP	designations of two austenitic stainless steels
AKS grade	tungsten wire doped with aluminium, potassium and silicon
ANOVA	analysis of variance
BCC	body centred cubic
BSE	backscattered electron
cps	counts per second
CTE	coefficient of linear thermal expansion
D_A	intrinsic diffusion coefficient of component A
EBSD	electron backscattered diffraction
EBSP	electron backscattered pattern
EDS	energy dispersive spectroscopy
EPMA	electron probe microanalysis
FCC	face centred cubic
FEG	field emission gun

HIP	hot isostatic pressing
J_i	diffusion flux of specie i
k or K	growth constant
k_0, D_0	pre-exponential factor for growth, diffusion
keV	kiloelectron volt
N_A , N_B	mole fraction of components *A, B.*
ppm	parts per million
Q_G, Q_D	activation energy for growth, diffusion
R	ideal gas constant
R^2	coefficient of determination
R_{in} *and* R_{out}	input and output count rates
SE	secondary electron
SEM	scanning electron microscopy
T	temperature
t	time
v	interface velocity
V_A, V_B	molar volume of the pure components *A, B*
V_{cell}	volume of a unit cell
V^k	velocity of the markers in a diffusion couple
V_m	molar volume of an alloy containing ideal solution
vol.%	volume percent
W/316L	tungsten wire reinforced 316L stainless steel
W/Fe-Ni-Cr	tungsten wire reinforced Fe-Ni-Cr alloys
W/HP	tungsten wire reinforced HP alloy
wt.%	weight percent
x	reaction layer thickness
ZAF	atomic number (Z), X-ray absorption (A) and X-ray fluorescence (F)
θ	specimen tilt angle

λ	Boltzmann variable
$erf\,\frac{x}{2\sqrt{Dt}}$	Gaussian error function
∇C_i	concentration gradient of species i

μ,M_7N_6	intermetallic phase which contains Cr, Fe, Ni and W
Co	Cobalt
Cr	Chromium
Fe	Iron
$M_{23}C_6$	Cr-rich carbide that may also contain Fe, Ni and W
Mn	Manganese
Mo	Molybdenum
Nb	Niobium
NbC	Niobium carbide
Ni	Nickel
Si	Silicon
Ta	Tantalum
ThO_2	Thorium dioxide, also called as thoria
Ti	Titanium
W	Tungsten
η	$M_{12}C$ carbide which contains Cr, Fe, Ni and W

Abstract

There is potential for improving creep properties of stainless steels by reinforcing them with tungsten (W) wires. Past studies have shown that a detrimental factor that impairs the mechanical properties of tungsten wire reinforced superalloy composites is the formation of brittle intermetallic phases due to the interaction between W wire and constituents of the alloy matrices. Formation and growth of the intermetallic phases strongly depends on the matrix chemistry and for the retention of creep strength, matrix compositions that do not form intermetallic phases with tungsten are desirable for fabricating W wire reinforced composites for high temperature applications.

This research investigated the formation and growth of reaction phases in W wire reinforced 316L (W/316L) stainless steel and HP alloy steel (W/HP) that were fabricated by casting method. Additionally, the effect of composition on the evolution and kinetics of reaction phases was studied in some W wire reinforced experimental alloys based on Fe-Ni-Cr only (W/Fe-Ni-Cr). The fabricated composites were diffusion annealed in the temperature range 1000-1200°C for 25-500 hours. Microstructure and chemistry of the reaction phases in the as-cast and diffusion annealed composites were studied using scanning electron microscopy, energy dispersive spectroscopy and electron backscattered diffraction techniques. Growth kinetics of the reaction layers and average effective interdiffusion coefficients in the layers were determined for the composites.

Results showed that an intermetallic phase isostructural with μ-phase formed in the as-cast W/316L and W/Fe-Ni-Cr composites with 1 and 2 Fe:Ni matrix ratios. In W/HP a phase $M_{12}C$ with crystal structure similar to η-carbide was formed. These phases developed and formed brittle reaction layers around the W wires during diffusion annealing. A parabolic relationship between the μ-phase and η-carbide growth and diffusion annealing time indicated that the growth of reaction layers was diffusion controlled. In the W/Fe-Ni-Cr composites, formation of intermetallic phases did not occur in the matrices with 0.5Fe:Ni ratio, instead some isolated tungsten particles were observed in the matrix adjacent to the wires after diffusion annealing. In W/Fe-Ni-Cr composites with 1 and 2 Fe:Ni matrix ratio, the growth of μ-phase reaction layers during annealing was observed to be dependent on the

matrix composition. It was found that with an increase in the Ni content in the matrix, growth of μ-phase reaction layer decreased.

The study presented in this thesis gives first-hand information on phase formation and growth kinetics of the reaction layers in W/316L and W/HP composites. It revealed that the interaction of W with 316L and HP alloy matrices leads to formation of cracked intermetallic and carbide reaction layers which are not desirable in the composites designed for high temperature applications. It has also been shown in this study that in W/Fe-Ni-Cr composites, intermetallic phase formation can be suppressed by increasing Ni content in the matrix. In the composite with high Ni contents in the matrix (0.5Fe:Ni ratio) intermetallic phases do not form even after diffusion annealing at 1200°C. This intermetallic free W/Fe-Ni-Cr composite can further be studied for its creep strength.

Chapter 1. Introduction

Austenitic stainless steels are an important class of materials that are extensively used in the chemical and process industry. Many operations in these industries involve high temperature and pressure, which eventually results in service failure of the equipment due to creep. Additionally, increasing demand for improving process efficiency has necessitated the development of materials with better creep strength that can maintain their structural integrity at high temperature. During the last few decades, a better understanding of alloying effects, advances in melting technology and development of controlled thermo-mechanical processing have led to creep resistant stainless steel grades, like HP 25/35 and HP micro alloy steels. However, the property optimization in these alloys has achieved its peak and no significant further enhancement is foreseen in these monolithic alloys. Superalloys, another class of high temperature materials, have superior creep and oxidation resistance, but their high cost and requirements of special fabrication techniques have limited their use to critical applications only. Though refractory metals exhibit good creep strength, they have poor oxidation resistance and cannot be used in high temperature applications without any oxidation protection.

One novel alternative method to improve creep strength of engineering materials is by fabricating them in the form of a composite with suitable reinforcement. The ideal composite for high temperature applications requires a ductile and oxidation resistant matrix and a reinforcement that can retain its tensile properties at elevated temperature. Stainless steels and tungsten wires possess suitable properties of matrix and reinforcement and composite formed by these constituents can possess better creep strength.

There have been a few studies done in past on the reinforcement of superalloys with W wires [1-7]. Significant improvement in the short time creep strength was observed in the reinforced superalloys. These studies also reported formation of intermetallic phases as a result of wire-matrix interaction during the fabrication of the composites. These phases further developed as brittle reaction layers at high temperature (1000-1200°C). Intermetallic phase formation and growth is considered detrimental to the creep strength of the composites,

as the brittle intermetallic layers weaken the bond between the reinforcement and the alloy matrix.

Past studies on W reinforced high temperature alloys are limited to some selected superalloy compositions. The scope of these studies was to quickly see the effect of reinforcement on the mechanical properties of superalloys in order to access their feasibility in commercial applications (mainly as turbine blades in aero engines). Therefore, past work did not study in detail the microstructural evolution and growth kinetics of the reaction phases in W wire reinforced superalloy matrices.

This thesis extends the concept of W wire reinforcement to some commercial stainless steel grades that are widely used in the petrochemical and chemical and process industries. These steels typically operate in the temperature range 500-950°C and any improvement in their creep strength due to the reinforcement can increase their service temperature, which could be economically beneficial.

1.1 Research Objectives

The initial goal of this thesis was to investigate the formation and growth of reaction phases in two W wire reinforced stainless steel alloy matrices. Commercial stainless steels grades 316L and HP alloy were used as matrices for the reinforcement. At the beginning of this research, the following objectives were set:

- fabrication of W wire reinforced stainless steel (W/316L) and HP alloy (W/HP) composites by casting method
- microstructure and chemical characterization of the reaction products in the composites
- assessment of the growth kinetics of the reaction layers
- calculation of interdiffusion coefficients in the reaction layers

The results from the first series of experiments suggested that growth kinetics of the reaction layer in the W/HP was slow compared to W/316L. This quantitative information was useful to rank the alloys based on the growth constants of the reaction layers, but the experiments

were not sufficient to delineate the reason behind the sluggish growth of reaction layer in W/HP composite. Under identical fabrication and diffusion annealing conditions, the growth of reaction layers should be a strong function of chemical composition of the matrix. 316L and HP alloy steel have multi-elemental composition and in a broader sense, the sluggish growth of reaction layer in HP alloy matrix was thought to be related to low iron (Fe) and high nickel (Ni) content in the matrix compared to 316L. Therefore, based on first series of experiments it was hypothesised that the reaction layer growth in HP alloy matrix was slow due to its low Fe:Ni ratio.

A second series of experiments was therefore planned to study the effect of Fe:Ni ratios on the phase evolution and their growth in W wire reinforced Fe-Ni-Cr alloys. For this purpose, the following objectives were set:

- design and cast experimental alloy compositions based on Fe-Ni-Cr only with varying Fe:Ni ratios
- reinforce the experimental Fe-Ni-Cr alloys with W wires by casting method
- study the microstructure evolution and growth kinetics of reaction phases in the fabricated W/Fe-Ni-Cr composites
- establish a relationship between the growth kinetics of reaction layers and Fe:Ni ratio of the composite matrix

The outcome of the second series of experiments indicated that the formation of reaction layers and their growth in W reinforced Fe-Ni-Cr alloys is indeed a function of Fe and Ni contents in these alloys. It has been established through these experiments that in the matrices with 15-21wt%Cr and 0.5 Fe:Ni ratio, the formation of brittle μ-phase reaction layer is completely supressed. Higher Fe:Ni ratios (1 and 2) in the composites did favour formation of intermetallic phases, but their growth was slow in the matrices with lower Fe:Ni ratio. This validated the hypothesis that increased Ni content at the expense of Fe in composite matrix reduces reaction layer growth.

1.2 Thesis Preview

This thesis consists of nine chapters and can be broadly classified into four sections. Section I comprises the introduction and literature review (Chapter 1-3). Section II covers fabrication and reaction layer growth studies in W/316L and W/HP composites (Chapters 4-6). Section III covers preparation of the experimental alloys based on Fe-Ni-Cr, their reinforcement with W wires and growth kinetics studies of reaction layers in the reinforced alloys (Chapters 7-8). Section IV is on conclusions and future work emanating from this research (Chapters 9). The contents of each chapter are described below:

Chapter 1 (present chapter) discusses the introductory aspects of this research and rationale behind taking up this study. The objectives of this research are highlighted.

Chapter 2 gives an overview of the development of W wire reinforced high temperature matrices for creep strength. Results on the mechanical properties, reaction phase characterization and important findings are reported.

In Chapter 3 a description of the continuum approach adopted to study diffusion in this thesis is presented. The methods used for interdiffusion coefficient measurement are discussed with an emphasis on multi-component systems. Finally, data on the past studies of diffusion and growth kinetics studies on W wire reinforced alloys is summarized.

Chapter 4 covers the experimental procedures followed in this research. A description of materials used to fabricate the composites and their composition is provided. Details of the casting method used to fabricate the composites are discussed. The procedures followed for sample preparation and diffusion annealing for the intended investigations are explained. The procedures of different characterization techniques followed to characterize the samples are also detailed.

Chapter 5 and 6 provide details of the microstructure and chemical characterization of the as-cast and diffusion annealed W/316L and W/HP composites, respectively. The results on growth kinetics and diffusivity in the reaction layers of the composites are presented in terms of growth constants, activation energy for growth, average

effective interdiffusion coefficients and activation energy for diffusion in the reaction layers.

Chapter 7 describes the composition design and casting of five Fe-Ni-Cr based experimental alloys with different Fe:Ni ratios. The results on chemical analysis of the cast alloys are reported.

Chapter 8 gives details on the microstructure and reaction layer growth studies on W/Fe-Cr-Ni composites. The fabricated composites were subjected to similar kinds of studies done on W/316L and W/HP composites. The results of these studies are presented and discussed in this chapter.

Chapter 9 lists the conclusions drawn from this research. Future outlook originating from the current research is also highlighted.

In addition to nine chapters, this thesis contains two appendices. Appendix A provides details on the working principles of energy dispersive spectroscopy (EDS) and electron backscattered diffraction (EBSD) techniques that were extensively used in this research. The important factors that affect the analysis while using these techniques are also discussed. Appendix B gives detail about the F-test which was used to select the reliable data for the determination of average effective interdiffusion coefficients in the reaction layers of the composites.

Chapter 2. Development of Tungsten Wire Reinforced Composites for Creep Strength

Tungsten wire reinforced high temperature composites have been researched for the last five decades. The impetus for this initial work was to develop more creep resistant materials for aerospace and space applications and therefore, the majority of past studies were carried out utilizing superalloys as the matrix materials for the reinforcement. Because of this fact the literature on the reinforcement of stainless steels with W wires is scarce. This chapter highlights the past developments on W wire reinforcement of high temperature alloy matrices.

2.1 Selection of Tungsten wires as Reinforcing Phase

Initial studies on high temperature composite development were started by assessing ceramic fibers/whiskers as potential candidates for the high temperature alloy reinforcement. Ceramics, in the form of fibers/whiskers possess good specific strength and modulus, but they are brittle and have poor thermal shock resistance. Additionally, they are difficult to handle because of their small diameter and inherent brittleness. Initial experiments on the reinforcement of superalloys with ceramic fibers resulted in the degradation of the reinforcements by dissolution/reaction and fragmentation in the matrices. Silicon carbide and carbon fibers reacted and dissolved in superalloys at fabrication temperatures above 900°C [5]. The initial assessments of ceramic based reinforcements in superalloys showed their unsuitability for high temperature composites [4].

Although the specific strength of refractory metal wires is inferior to ceramic fibers, their ductility and strength retention ability at elevated temperature give them an edge over ceramic reinforcements. In earlier studies, superalloy matrices were reinforced with cold drawn wires of W, tantalum (Ta), molybdenum (Mo), and niobium (Nb) to identify the best reinforcing material. It was found that during composite fabrication, Mo and Nb wires dissolved in superalloy matrices due to the formation of low temperature eutectics [1, 5, 8]. Ta is expensive and being similar, does not offer properties better than W. Studies indicated that W wires have better strength retention and stability above 1000°C in various superalloy

matrices and were therefore chosen as the best reinforcing candidate for high temperature alloys.

2.2 Composite Fabrication Methods

Generally, metal matrix composites can be fabricated by solid state as well as liquid state methods. Past studies employed both of these methods to reinforce the alloy matrices with W wires. It must be emphasised here that both of these methods have their inherent advantages and disadvantages. The liquid state method is appealing because of low cost involved and fewer restrictions on casting shapes, but it may cause more damage to reinforcing wires due to the high temperature involved (~1500°C) during composite fabrication. Since solidification of the alloys proceeds immediately and completes quickly, the time during which the reinforcing phase remains in contact with liquid alloy is relatively shorter for liquid state fabrication (typically 10 seconds to 1 minute) [5]. But there are opportunities for better control on process parameters in this method. The contact time and therefore wire/matrix reactions can be minimized by using a better mold design for fast heat extraction during solidification and utilizing a controlled superheat temperature.

Solid state fabrication methods make use of metal powders which are pressed along with the reinforcing phase and then sintered. The sintering is done at relatively low temperature (~1200°C), but a long contact time (10 min to several hours) is generally required to produce a sound composite [5]. The use of the lower temperature may slow down wire/matrix reaction, but this advantage is offset by longer time required for optimum sintering. Therefore, both these methods have room for optimization and a common factor is that a consideration of process parameters is always needed to minimize wire degradation during composite fabrication.

Table 2.1 summarizes the fabrication methods used in past studies for the reinforcement of various alloy matrices with W wires. Different variants of solid state methods used to fabricate the composites include powder consolidation by compaction, slip casting followed by sintering, hot isostatic pressing (HIP), diffusion bonding, spray forming, electroplating and extrusion. In liquid state methods, melt infiltration was used to fabricate the composites. It can be noted from Table that the majority of past studies employed Ni-base alloys as matrix materials and a few cobalt (Co) and iron (Fe) base alloys. Various grades of W wires with diameters ranging from 75-1250 µm were used as reinforcement. Rectangular and cylindrical

samples with 20-50% volume fraction of tungsten wires in various matrices were produced for testing purpose.

Table 2.1: Summary of tungsten wire reinforced composites fabricated by different fabrication methods.

Fabrication Method	Precursors		Sample size	Reference
	Matrix	Reinforcement		
Liquid state fabrication				
Melt infiltration	Ni-base alloys[1]	W wires (250 µm) 40-50 Vol.%	1.5 cm φ x 12 cm L	[9]
	Ni-base alloys[2]	W, W-5%Re wires (1000-1250µm) 20-50 Vol.%	5 cm φ x 25 cm L	[8]
	Ni-base alloys[3]	W wire (100 µm) 30 Vol.%	0.6 cm φ x 3.5 cm L	[10]
	Co-base alloy[4] and variants	W-2%ThO_2 (75 µm) 42 Vol.%	Standard tensile test samples	[11]

[1] NIMONIC 75 0.1C- 5Fe-20Cr-1Mo-1Si (bal. Ni)
EPD 16 6Al-6Cr-11W-2Mo-1.5Nb
SM322 1C-0.75Ti-21.5Cr-9W-4.5Ta-2.25Zr
NIMOCAST 258 0.2C-3.7Ti-4.8Al-10Cr-20Co
NIMONIC 115 0.15C-4Ti-5Al-15Cr-15Co-3.5Mo

[2] NIMOCAST 713C 12Cr-6Al-4.5Mo-2Nb (bal. Ni)

[3] CMSX3 4Co, 8Cr, 5.7Al, 0.7Ti, 5.7Ta, 9W, 0.1Hf (bal. Ni)

[4] Mar M322 1C-21.5Cr--9W-0.75Ti-4.5Ta-1.5Zr (bal. Co)

Fabrication Method	Precursors		Sample size	Reference
	Matrix	Reinforcement		
Solid state fabrication				
Slip casting, sintering and hot isostatic pressing	Ni-base alloy[5]	W, W-1%ThO_2, W-2%ThO_2, W-5%Rh-1%ThO_2 , (250-500μm) 20-70 Vol.%	--	[2]
Vacuum hot rolling	Ni-base alloys[6]	W wire (200μm) 25 Vol.%	--	[12]
Thermal spray	Fe-base alloy wires[7]	W wire (200 μm)	38 cm x 122 cm	[13]
Hot isostatic pressing and swaging	304 stainless steel	W-2%ThO_2 (300 μm) 20 Vol.%	--	[14]
Electroplating	Ni metal	W wires (100-300μm) Up to 50 Vol.%	Standard tensile test samples	[15]

[5] 2Al-15Cr-2Ti-25W (bal. Ni)

[6] VZh98 25Cr-15W-0.7Ti (bal. Ni)

[7] FECRALLOY 4.5Al-15Cr-0.5Y (bal. Fe)

2.3 Mechanical Properties Assessment

Past studies on W wire reinforced alloys were primarily aimed at fabricating small test coupons and assessing their structural stability by evaluating their mechanical properties-mainly creep rupture and thermal fatigue. The important findings on these studies are summarised below.

- Reinforced alloys exhibited better rupture strength compared to their unreinforced counterparts. Dean [9] studied creep rupture strength of some W wire reinforced Ni-base superalloys fabricated by liquid metal casting method and found substantial improvement in rupture strength at temperatures greater than 900°C. Petrasek et al. [2] also reported a two-fold increase in 100 hours stress rupture strength in Ni-base superalloy composites. Similarly, improvement in rupture strength was reported in Co-base reinforced alloys by Ahmad et al. [11]. Brentell et al. [16] observed substantial improvement in rupture strength in Fe-base composites (W/FeArCrAlY) at 1050°C.

- Creep studies require elevated temperature exposure of composites for a prolonged time and during this time period, considerable reaction between wires and matrix takes place. Therefore, creep strength of W wire reinforced composites strongly depends on the composition of matrix materials. Past studies showed an overall increase in the creep strength of Fe-base composites, while in Ni-base matrices a decrease in creep strength was observed after long term exposure to high temperature [2, 17].

- Thermal cycling of the composites based on Fe and Ni-base matrices resulted in distortion and/or cracking of matrices and intermetallic phases [8, 9, 18, 19] with exception in W/KOVAR (Fe-29Ni-17Co) composite that did not show adverse response to thermal cycling [16, 20].

2.4 Reactions Phases in Tungsten Wire Reinforced Alloys

W wires and a superalloy matrix altogether constitute a thermodynamically unstable system. When exposed to high temperature, the reaction between W wires and the matrices leads to the microstructural alteration and formation of new phases in the reaction zone. Previous

studies have reported stability issues of W wires in superalloy matrices. Three main outcomes of the wires/matrix interaction were identified. These were (1) W wire dissolution in matrices during fabrication, (2) recrystallization of the wires and (3) development and growth of intermetallic phases in the reaction zones of the composites. All these factors led to deterioration of creep properties of the reinforced alloys when they were exposed to high temperature (>1000°C).

Because of the fact that in very few cases composites were fabricated via liquid state fabrication method, there is limited literature available on wire dissolution during liquid metal fabrication of reinforced alloys. The available data on W/Ni superalloy composites indicates that little interaction occurs between W and Ni during fabrication, but there is no quantitative information available [8, 9]. In the composites fabricated by a powder metallurgy method, formation of intermetallic phases and recrystallization of wires were dominant. Mirotvorskii at el. [21-23] investigated in detail the interaction of W wires with various binary alloys based on Fe, Ni, Co, Ti and Cr. The alloys were prepared by pressing the alloy mixtures with W wires at room temperature. The compacts based on Fe, Ni and Co were then annealed in vacuum at 1200-1400°C for one hour. The wire/matrix interaction was investigated by metallographic analysis of the composite samples.

Mirotvorskii et al. showed that recrystallization of W wires was dominant in Ni-base matrices and it started at a temperature as low as 1200°C. At 1300°C, the wires recrystallized completely. Other studies have shown that the recrystallization temperature of W in Ni matrix further decreases (~1100°C) depending on the dilution of the matrix with other elements which are less active towards W [24]. Fewer cases of wire recrystallization were observed in the Fe and Co-base matrices in the temperature range 1200-1300°C. At 1400°C, the wires recrystallized irrespective of the composition of matrix materials. Higher recrystallization temperatures (about 1450°C) of W wires were reported in Fe-base matrices such as stainless steels with low Ni contents [25, 26]. It can be inferred from these studies that recrystallization temperature of W wires is greatly reduced in Ni-base alloy matrices.

Formation of intermetallics in the reaction zone occurred in all the studied superalloys, stainless steels and some binary alloy matrices reinforced with W wires. The intermetallics and other phases formed in the reaction zone were identified in very few cases. In most of the studies, the phases were identified based on the chemical analysis results generated by Energy Dispersive Spectroscopy (EDS) and by arranging the composition to fit the

stoichiometric formula of the expected phase from the binary phase diagram. The data indicate that the majority of intermetallic layers formed in the reaction zones of the W wire reinforced superalloy composites were isostructural with the μ-phase, which is a M_7N_6 (M: Fe, Ni, Co and N: W, Cr) type phase with rhombohedral crystal structure.

Warren et al. [26] did phase identification in the reaction zones of W/304SS[8] and W/KOVAR[9] alloy composites by X-ray diffraction and found that the phases present in the reaction zone of these systems were isomorphous with μ-phase. Caulfield et al. [27, 28] also reported the isomorphous nature of reaction zone phases with μ in W/INCOLOY 903[10] composite system. In another study [29] referenced in [26] , M_6C (M: Co, Cr, Ni, W) carbide phase was detected in the reaction zone of W/MAR-M200[11] alloy composite. While no details of identification techniques used are available, it can be inferred that in the matrices with higher carbon contents, the occurrence of carbide phases in the reaction zone is more likely.

Problems associated with wire stability were addressed to a certain extent by (i) applying a diffusion barrier coating on the W wires [29, 31] and (ii) modifying matrix alloy's chemistry [1, 28, 32]. Application of diffusion barrier coatings is promising but difficulties were experienced in forming a reproducible and successful barrier coating on refractory metal wires [33]. Modification of matrix chemistry may lead to the evolution of undesirable precipitates during service that may degrade useful properties of matrix materials [34]. To minimize reinforcement damage during fabrication, the only method which seems promising is control of processing parameters during composite fabrication. Fabrication by liquid metal casting can offer greater flexibility than powder metallurgy in this regard.

2.5 Probable Phases in W/316L and W/HP Composites

In order to identify unknown phases in any alloy, it is a pre-requisite to have first-hand information of the phases that could form in the alloys during solidification and subsequent heat treatment. For the alloys containing two or three components, the information about the likely phases can be extracted from the binary or ternary equilibrium phase diagrams. The

[8] Fe-18Cr-10Ni-1.5Mn (wt.%)

[9] Fe-29.5Ni-17 Co (wt.%)

[10] Fe-32Ni-15Co-1.2Al-1.9 Ti & Nb each (at.%)

[11] 59Ni - 0.15C -9.0Cr -12.5W -10Co -5Al -2Ti -1Cu -0.05Zr (wt.%) [30]

wire reinforced alloys under investigation in the current study are fabricated utilizing grades 316L and HP 25Cr/35Ni stainless steels, and this can lead to the formation of phases in the reaction zones with as many as four elements[12] (Cr, Fe, Ni, and W). The minor (Mo, Mn, Si in 316L and Mn, Nb, Si in W/HP) and trace (mainly carbon) elements present in the stainless steels further add complexity. Therefore, the information about the unknown phases in multi-component alloys can not be obtained from the phase diagrams alone. The information about the likely phases in such cases can be obtained by searching the published database and finding the matching phases those contain approximate composition of the elements (identified using EDS) present in the phase/alloy under investigation. If there is no published data available on probable phases, calculations based on computational thermodynamic databases such as Thermo-Calc, Pandant or FactSage can be used to generate the information about the likely phases in multicomponent alloys.

For the current study, a list of possible phases was generated from the compiled data [35] extracted from various studies. The list is presented in the Table 2.2. Most of the steels contain carbon and its relatively high concentration (~0.45 wt.%) in HP alloy steel can result in the formation of carbides. Therefore, while looking for the probable phases W/316L and W/HP alloy composites, the phases containing carbon were also taken into consideration and are included in the table.

[12] This does not rule out the possibility of the formation of binary and ternary phases that can still be predicted from the phase diagrams for different combination of elements in the alloy

Table 2.2: List of probable phases used to identify the unknown phases in the current study.

Phase	**Pearson's symbol**	**Cell Parameters**		**Space group**	**Reference**
		a, b, c (Å)	**α, β, γ (°)**		
Fe_2W (λ)	*hP*12	4.74, 7.726	90, 120	$P6_3/mmc$ (194)	[36]
Fe_7W_6(μ)	*hR*39	4.76, 25.85	90, 120	*R*-3*m* h (166)	[37]
$(Ni,Fe,W)_{12}C$ (η)	*cF*104	10.96	90	*Fd*-3*m*O2 (227)	[38]
$C_2Cr_2W_2$	*hP*4	2.94, 4.66	90, 120	$P6_3/mmc$ (194)	[39]
C_6Cr_{23}	*cF*116	10.66	90	*Fm*-3*m* (225)	[40]
C_2Cr_3	*oP*20	5.53, 2.83, 11.47	90	Pnma(62)	[41]
CFe_6W_6 (κ)	*cF*104	10.93	90	*Fd*-3*m* (227)	[42]
Ni_4W	*tI*10	5.73, 3.55	90	$I4/m$ (87)	[43]
NbC	*cF*8	4.4647	90	*Fm*-3*m* (225)	[44]
$Cr_{0.31}Mo_{0.07}Mn_{0.02}Fe_{0.52}Ni_{0.08}$ (σ)	*tP*30	8.839, 4.597	90	$P4_2/mnm$ (136)	[45]

2.6 Summary

Tungsten wire reinforced high temperature composites have demonstrated superior short term creep rupture properties over their monolithic counterparts, but their performance degrades with long term exposure at high temperature. This is due to the growth of brittle intermetallic phases mainly μ and/or carbides in the reaction zones of the W wire reinforced superalloys and stainless steel matrices. There are number of probable intermetallic and carbide phases that could form in W/316L and W/HP composites. Since the formation and growth of these phases strongly depends upon matrix composition, nature of phases and the exposure temperature, practical applications of W wire reinforced composites require in-depth studies of wire/matrix interaction in terms of evolution and growth kinetics of the reaction phases.

Chapter 3. Diffusion and Reaction Layer Growth in Alloys

Diffusion is the most fundamental and elementary process in materials that involves transport of atoms or molecules under the influence of a chemical potential gradient. Important metallurgical processes like heat treatment, phase transformations in metals and alloys are directly related to diffusion. Structural materials when used at elevated temperature can undergo diffusion and subsequent microstructural modifications in the vicinity of fiber/matrix interface. This often results in the formation and growth of new phases that may degrade their performance. Therefore, in order to design materials with better high temperature properties, an understanding of diffusion phenomena in materials is essential.

There are two approaches that are generally adopted to study diffusion in materials: the continuum and the atomistic approach. The continuum approach stems from the laws of conservation of matter and the diffusing species in this approach are considered as continuous media. By its very nature, this macroscopic theory makes no reference to the discrete atomic events which give rise to macroscopically observable diffusion. This approach is based on Fick's laws and provides a suitable formalism to quickly quantify the diffusion of moving species in materials. The diffusion data generated using the continuum approach can directly be applied to optimize the performance of materials. In the atomistic approach, the movement and/or jumping of the diffusing species is taken into consideration to gain insight into diffusion phenomena.

Current research makes use of a continuum approach to investigate diffusion phenomena. A detailed description of the approach along with various methods used to quantify diffusion is provided in the following sections of this chapter. A model describing the growth of precipitates as a result of reaction diffusion is discussed. Finally, a summary of the results on growth kinetics in of the reaction layers in W wire reinforced alloys compiled from past studies is presented.

3.1 Fick's Laws of Diffusion

3.1.1 First Law

Fick's first law of diffusion relates diffusion flux (J_i) of the species i to the concentration gradient (∇C_i) as per Equation:

$$J_i = -D\nabla \mathrm{C}_i \qquad 3.1$$

where *D* is the diffusion constant. Depending upon the frame of reference chosen to calculate *D*, J_i and C_i can take different units. For planar diffusion in one dimension, Fick's first law can be written as:

$$J_i = -D\frac{\partial C_i}{\partial x} \qquad 3.2$$

3.1.2 Second Law

Fick's second law of diffusion gives the relationship between the concentration gradient of the species *i* and the rate of change of its concentration $\left(\frac{\partial C_i}{\partial t}\right)$ caused by its diffusion at a given point in the system

$$\frac{\partial C_i}{\partial t} = \nabla \cdot (D\nabla C_i) \qquad 3.3$$

For planar diffusion along the *x* direction the equation reduces to:

$$\frac{\partial C_i}{\partial t} = \frac{\partial}{\partial x}\left[D\left(\frac{\partial C_i}{\partial x}\right)\right] \qquad 3.4$$

When *D* is independent of position, Equation 3.4 takes the form:

$$\frac{\partial C_i}{\partial t} = D\left(\frac{\partial^2 C_i}{\partial x^2}\right) \qquad 3.5$$

In most practical situations, diffusion in materials occurs under non-steady state conditions. The flux and the concentration gradient at a particular point in the diffusion zone change with time, resulting in net accumulation or depletion of diffusing species.

3.2 Diffusion Measurement in Binary Alloys

3.2.1 Constant Diffusivity

Depending on the variation of *D* with composition, there are two methods to determine diffusion coefficients in alloys. If *D* is constant (or varies very slightly with composition) and diffusion distance is small compared to the length of the diffusion couple in the direction of diffusion, Equation 3.5 can be solved analytically and the solution can be expressed in terms

of error functions by specifying boundary conditions [46]. Considering a binary diffusion couple formed by welding two alloys A and B having composition C_i^+ and C_i^- at the extreme ends at the start of the diffusion process, the initial and boundary conditions for such a diffusion couple are:

$$C_i(x < x_0, t = 0) = C_i^- \text{ and } C_i(x > x_0, t = 0) = C_i^+ \text{ and} \qquad 3.6$$

$$C_i(x = -\infty, t > 0) = C_i^- \text{ and } C_i(x = +\infty, t > 0) = C_i^+ \qquad 3.7$$

The solution to Fick's second law can be written as:

$$C_i(x,t) = \frac{(C_i^- - C_i^+)}{2} + \frac{(C_i^+ - C_i^-)}{2}\, erf\frac{x}{2\sqrt{Dt}} \qquad 3.8$$

where C_i the composition at a distance x from the interface, the expression $erf\frac{x}{2\sqrt{Dt}}$ represents the Gaussian error function which is defined by the equation:

$$erf\ (y) = \frac{2}{\sqrt{\pi}}\int_0^y \exp(-Z^2)\, dZ \qquad 3.9$$

The values of the Gaussian error function are given in mathematical tables for various arguments. By using the value of the error function from the tables [47] , the diffusion coefficient can be calculated using the Equation 3.8.

3.2.2 Variable Diffusivity

In a situation where diffusivity is not constant but rather varies with composition, the error function analysis given above can not be used to determine the diffusion coefficient. We see from Fick's second law of diffusion that Equation 3.5 is a non-linear partial differential equation and its analytical solution for any arbitrary concentration dependence of $\widetilde{D}(C)$ is not possible. Under such circumstances, it is possible to extract diffusivity from the concentration distance profiles by numerical integration. There are two methods to determine $\widetilde{D}(C)$ from the concentration profiles - classical Boltzmann-Matano method [48] and a related approach developed by Sauer and Freise [49]. Both these methods make use of the Boltzmann transformation.

3.2.2.1 Boltzmann Transformation

This is a mathematical transformation suggested by Boltzmann and is used to transform a non-linear partial differential equation to a non-linear ordinary differential equation if $\widetilde{D}$ is a function of concentration alone. Boltzmann [50] showed that when $\widetilde{D}$ is a function of concentration only, for certain boundary conditions, concentration may be expressed in terms of a single variable of space and time. Fick's second law can therefore be reduced to an ordinary differential equation by introducing the variable. Boltzmann introduced a variable (λ) which is a combination of space *(x)* and time *(t)*, respectively and is written as:

$$\lambda = \frac{x}{\sqrt{t}} \tag{3.10}$$

Since λ is a function of concentration only, using the definition of λ and differentiating by the chain rule, we can write:

$$\frac{\partial C}{\partial t} = \frac{dC}{d\lambda}\frac{\partial \lambda}{\partial t} = -\frac{1}{2}\frac{x}{t^{3/2}}\frac{dC}{d\lambda} \tag{3.11}$$

and

$$\frac{\partial C}{\partial x} = \frac{dC}{d\lambda}\frac{\partial \lambda}{\partial x} = \frac{1}{t^{1/2}}\frac{dC}{d\lambda} \tag{3.12}$$

Inserting Equations 3.11 and 3.12 in Fick's second law (Equation 3.4):

$$-\frac{1}{2}\frac{x}{t^{3/2}}\frac{dC}{d\lambda} = \frac{\partial}{\partial x}\left(\frac{\widetilde{D}}{\sqrt{t}}\frac{dC}{d\lambda}\right) = \frac{1}{t}\frac{d}{d\lambda}\left(\widetilde{D}\frac{dC}{d\lambda}\right) \tag{3.13}$$

Using definition of the λ from the Equation 3.10, the Equation 3.13 can be written as:

$$-\frac{\lambda}{2}\frac{dC}{d\lambda} = \frac{d}{d\lambda}\left(\widetilde{D}\,\frac{dC}{d\lambda}\right) \tag{3.14}$$

This transformation of Fick's second law into an ordinary differential equation is known as Boltzmann transformation and was first used by Matano to extract interdiffusion coefficients from the concentration profiles acquired from the diffusion zone of a binary diffusion couple.

3.2.2.2 Boltzmann-Matano Method

Matano proposed a method to calculate concentration dependent diffusion in binary diffusion couples [48]. For the derivation of the method we consider an infinite diffusion couple with terminal compositions of C_i^- and C_i^+. The initial conditions are:

$$C_i = C_i^- \ for\ (x < 0\ at\ t = 0)$$
$$C_i = C_i^+ for\ (x > 0\ at\ t = 0) \qquad 3.15$$

Since at *t=0*, the concentration is not a function of distance, the initial and boundary conditions for the partial differential equation can be expressed in terms of Boltzmann variable as:

$$C_i = C_i^-\ at\ \lambda = -\infty$$
$$C_i = C_i^+ at\ \lambda = +\infty \qquad 3.16$$

Equation 3.14 can be integrating between initial composition C_i^- and C_i^*, where C_i^* is any concentration between C_i^- and C_i^+ ($C_i^- < C_i^* < C_i^+$)

$$-\frac{1}{2}\int_{C_i^-}^{C_i^*} \lambda dC_i = \left[\widetilde{D}\frac{dC_i}{d\lambda}\right]_{C_i^-}^{C_i^*} \qquad 3.17$$

The data on C_i^* is always at some fixed time, so substituting for λ and using $\frac{dC_i}{dx}$=0 at C_i^- gives:

$$-\frac{1}{2}\int_{C_i^-}^{C_i^*} x dC_i = \widetilde{D}t\left[\frac{dC_i}{dx}\right]_{C_i^-}^{C_i^*} = \widetilde{D}t\left(\frac{dC_i}{dx}\right)_{C_i^*} \qquad 3.18$$

From the additional fact that $\frac{dC_i}{dx}$ = 0 at C_i^+, we have the condition:

$$\int_{C_i^-}^{C_i^+} x dC_i = 0 \qquad 3.19$$

Equation 3.19 defines the Matano plane at which *x=0* and with this definition of *x*, $\widetilde{D}(C_i^*)$ can be determined from the equation:

$$\widetilde{D}\,(C_i^*) = -\frac{1}{2t}\left(\frac{dx}{dC_i}\right)_{C_i^*} \int_{C_i^-}^{C_i^*} x dC_i \qquad 3.20$$

where $\widetilde{D}$ is the interdiffusion coefficient at the composition of interest (C_i^*), $\left(\frac{dx}{dc_i}\right)$ is the inverse of the slope of the penetration curve at C_i^*, and $\int_{C_i^-}^{C_i^*} x dC_i$ is the area under the concentration profile curve up to the Matano plane. The Matano plane is a plane where the net flux of the diffusing species crossing it from either side of the diffusion couple is zero.

The position of the Matano plane is determined from the concentration distance profiles of diffusion couples generated by the EDS or EPMA (Electron Probe Microanalysis) methods. This is usually done by evaluating the area under the curve by numerical integration. A schematic of the various terms involved in Boltzmann-Matano method for binary diffusion couple is shown in Figure 3.1.

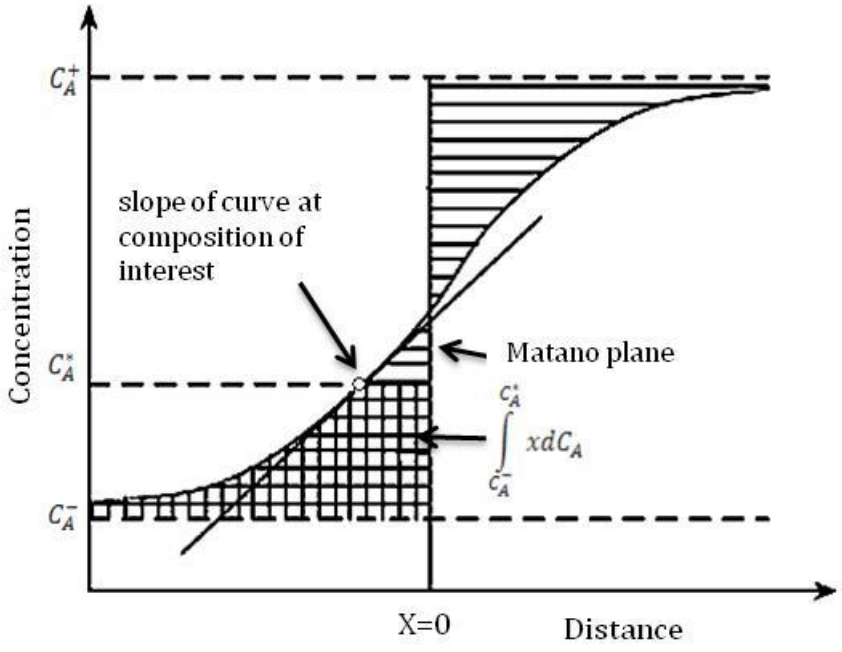

Figure 3.1: Schematic of a concentration distance profile showing the terms used in the Boltzmann-Matano method to determine interdiffusion coefficient in binary alloys.

The Boltzmann-Matano method is applicable in the case of infinite diffusion couples where the concentration change does not reach the ends of the diffusion couples and where the diffusion couple does not experience a change in total molar volume after the diffusion annealing. The interdiffusion coefficient determined by this method can further be used to

study the intrinsic diffusivity of species in binary diffusion couples by tagging the initial interface of the diffusion couple with some inert markers (such as particles of ThO_2, fine wires of W or Mo). By measuring the velocity of the markers (v^k) and using $\widetilde{D}$, the intrinsic diffusivities can be calculated from Darken's equations:

$$\widetilde{D} = N_A D_B + N_B D_A \qquad 3.21$$

$$v^k = (D_A - D_B)\frac{\partial N_A}{\partial x} \qquad 3.22$$

where D_A and D_B are the intrinsic diffusion coefficients of components *A* and *B* in the binary alloy. N_A and N_B are the mole fractions of *A* and *B* in the alloy. The solution of these simultaneous equations will give values of D_A and D_B in the diffusion couples composed of binary alloys.

The method proposed by Boltzmann-Matano is not suitable for the diffusion couples in which a considerable change in total molar volume in the diffusion zone occurs upon reaction/mixing during diffusion. This is because of the fact that due to a change in overall dimension of the diffusion couple, the determination of the exact location of the Matano plane is rather vague because it depends upon the reference end of the diffusion couple used for the determination of the plane. Depending upon whether it is determined from the left or right hand side of the diffusion couple, there will be two different values of the Matano plane. In such cases, the method given by Sauer-Freise is used which is described below.

3.2.2.3 Sauer-Freise Method

Alloys containing ideal solutions obey Vegard's law and no change in molar volume takes place on diffusion in these alloys. The molar volume of a binary alloy A-B in the ideal case is given as

$$V_m = V_A N_A + V_B N_B \qquad 3.23$$

where V_A and V_B are the molar volumes of the pure components *A* and *B*. N_A and N_B are the mole fraction of components *A* and *B*.

Alloys with non-ideal solutions do not obey Vegard's law and total molar volume of the alloy changes on diffusion. Depending upon the positive or negative deviation from the ideal

behaviour, the diffusion couple will swell or shrink due to change in molar volume upon diffusion. The partial molar volume of the components *A* and *B* in such case can be written as

$$\tilde{V}_A = V_m - N_B \left(\frac{\partial V_m}{\partial N_A}\right) \qquad 3.24$$

and

$$\tilde{V}_B = V_m + (1 - N_B) \left(\frac{\partial V_m}{\partial N_B}\right) \qquad 3.25$$

These partial molar volumes are related to the total molar volume of the alloy by Equation $\tilde{V}_m = \tilde{V}_A N_A + \tilde{V}_B N_B$ and can be obtained graphically from the intersections of the relevant tangent with the ordinate as shown in the Figure 3.2.

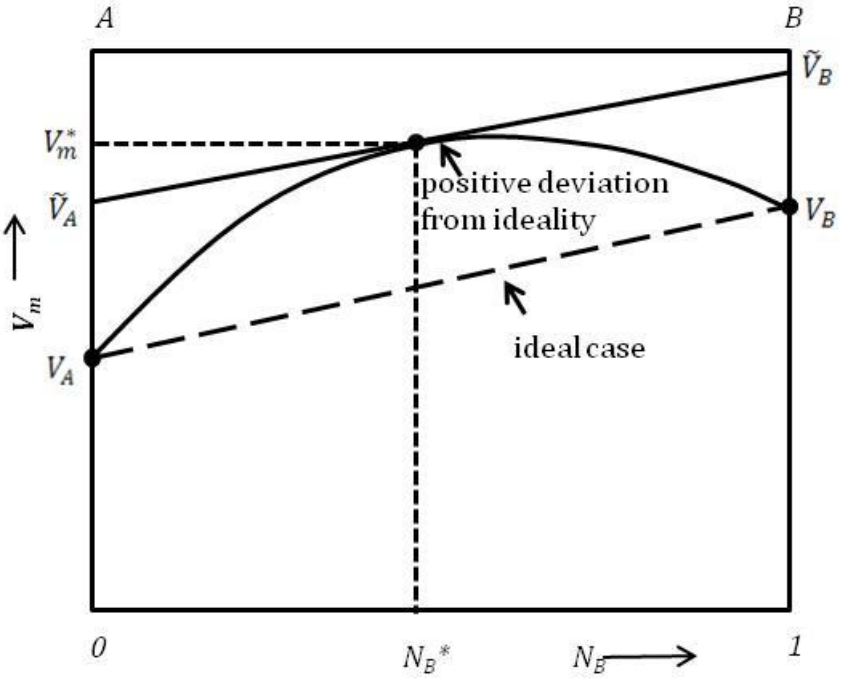

Figure 3.2: Schematic plot showing Vegard's Law and a non-ideal case where a deviation from the law occurs.

The Sauer-Freise method [49] is a modification of the Boltzmann-Matano method which eliminates the need to identify Matano Plane. This method also takes into account any change in the total molar volume of the system that occurs due to diffusion. Sauer and Freise introduced an auxiliary variable Y_i^* based on the ratio of mole fraction of component i in a diffusion couple

$$Y_i^* = \frac{N_i^* - N_i^-}{N_i^+ - N_i^-} \qquad 3.26$$

Where N_i^+ and N_i^- are the mole fraction of component *i* at the extreme right and left ends of the diffusion couple. N_i^* is the mole fraction of *i* at the point of interest. Using the variable, equation for interdiffusion coefficient can be written as:

$$\widetilde{D}(Y^*) = \frac{V_m}{2t}\left(\frac{\partial x}{\partial Y}\right)_{N_i^*}\left[(1-Y^*)\int_{N_i^-}^{N_i^*}\frac{Y}{V_m}dx + Y^*\int_{N_i^*}^{N_i^+}\frac{1-Y}{V_m}dx\right] \qquad 3.27$$

Molar volume V_m in the above equation can be calculated from the knowledge of the lattice parameter as a function of composition. Equation 3.27 can be derived in the similar fashion as explained in Section 3.3.2 for the determination of interdiffusion flux from the concentration profiles. Measurement of the interdiffusion flux with the Sauer-Freise method requires construction of three graphs as described below:

- graph of the normalised composition (*Y*) as a function of diffusion distance (*x*),
- graph of $\frac{Y}{V_m}$ versus *x* and
- graph of $\frac{1-Y}{V_m}$ versus *x*

Using these three graphs and performing numerical analysis, interdiffusion coefficient can be determined at any point (composition) of interest in the diffusion zone of a binary diffusion couple.

3.3 Diffusion Measurement in Multicomponent Alloys

The diffusion process becomes complex in the alloy systems with greater than two components. A description of interdiffusion in such systems requires an understanding of the interactions between all components. The complexity arises because all the elements interact with each other during diffusion annealing and the diffusion of one element is not only due to its own concentration gradient, but also due to the concentration gradients of other elements

present in the diffusion zone. The different approaches developed to determine diffusion under such circumstances are discussed below.

3.3.1 From Multiple Diffusion Couples

Following Fick's law of diffusion, the interdiffusion flux $\tilde{J}_i$ of component *i* in a multicomponent system can be represented by the following equation [51, 52]:

$$\tilde{J}_i = -\sum_{j=1}^{n-1} \widetilde{D}_{ij}^{n} \frac{\partial C_j}{dx} \quad (i = 1, 2, 3 \ldots . (n-1)) \qquad 3.28$$

where $\left(\frac{\partial C_j}{\partial x}\right)$ is the concentration gradient of component *j*, *n* is the total number of components in the system and *x* is position . $\widetilde{D}_{ij}^{n}$ represents the interdiffusion coefficient of component *i* with respect to the concentration gradient of component *j* in an *n* component system.

According to Equation 3.28, there will be *(n-1)* flux equations and $(n-1)^2$ interdiffusion coefficients in an *n* component system. Therefore, for example in a ternary system, one needs to solve two flux equations to extract four interdiffusion coefficients. These flux equations for a ternary system can be written as:

$$\tilde{J}_1 = -\widetilde{D}_{11}^{3} \frac{\partial C_1}{\partial x} + \widetilde{D}_{12}^{3} \frac{\partial C_2}{\partial x} \qquad 3.29$$

$$\tilde{J}_2 = -\widetilde{D}_{21}^{3} \frac{\partial C_1}{\partial x} + \widetilde{D}_{22}^{3} \frac{\partial C_2}{\partial x} \qquad 3.30$$

where $\widetilde{D}_{11}^{3}$ and $\widetilde{D}_{22}^{3}$ are the main-interdiffusion coefficients and $\widetilde{D}_{12}^{3}$ and $\widetilde{D}_{21}^{3}$ are called as the cross-interdiffusion coefficients.

The experimental determination of these interdiffusion coefficients can be achieved by employing either the Boltzmann-Matano or the Sauer-Freise method. For a ternary alloy the analyses require setting up two independent diffusion couples having a common composition in their respective diffusion zones. Hence, for the composition that corresponds to the intersection of diffusion paths, the interdiffusion coefficients can be calculated by solving the Equations 3.29 and 3.30.

Determination of diffusion parameters in quaternary and higher order systems are more complex and seldom done employing the methods discussed above. In such cases average

interdiffusion coefficients can be determined from single diffusion couples, a method for which is described below in detail.

3.3.2 From Single Diffusion Couple

3.3.2.1 Main- and Cross-Interdiffusion Coefficients

There is an alternative method which can be used to determine the average interdiffusion coefficients in multicomponent systems from a single diffusion couple [53]. According to this method, interdiffusion fluxes of all the components in a multicomponent system can be determined directly from their concentration distance profiles measured on a single diffusion couple. From the concentration profiles, interdiffusion flux at any position *x* can be expressed by the relation [54]:

$$\tilde{J}_i(x^*) = \frac{1}{2t} \int_{C_i^+ or\ C_i^-}^{C_i(x^*)} (x - x_0)\, dC_i \quad (i = 1, 2, 3 \ldots . n) \qquad 3.31$$

Where *t* is the diffusion time, C_i^+ and C_i^- are the terminal compositions and x_0 is the location of the Matano plane. In the above equation, total molar volume change in the diffusion zone is considered negligible and calculation of diffusion coefficients by the above method requires determination of Matano plane.

Dayananda et al. [55] further showed that by expressing the concentration in terms of a relative concentration variable Y_i, the need for determination of the Matano plane can be eliminated. This relative concentration variable is defined as:

$$\mathrm{Y_i^*} = \frac{C_i^* - C_i^-}{C_i^+ - C_i^-} \qquad 3.32$$

where C_i is the concentration of component i in moles.m^{-3} at any section of the diffusion zone. Figure 3.3 shows a schematic of relative concentration variable as a function of diffusion distance *x*.

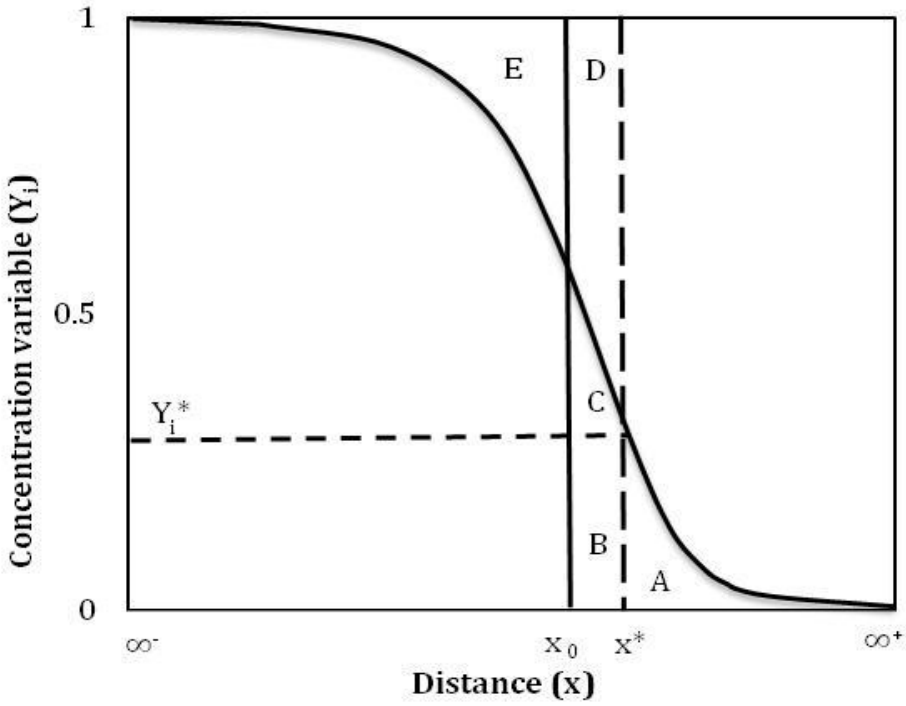

Figure 3.3: Schematic plot of the relative concentration variable (Y_i) versus distance (x) for the diffusing component *i* in a diffusion couple.

In Figure 3.3, the position of the Matano plane is x_0 , which can be determined by the mass balance in terms of area under the curve as:

$$E = A + B + C \qquad 3.33$$

for a given section *x**, it follows from Figure 3.3:

$$E + D = A + B + C + D$$

or

$$(E + D) - A = (B + C + D)$$

From Figure 3.3 we can write:

$$\int_{\infty^-}^{x*} (1 - Y_i)dx - \int_{x*}^{\infty^+} Y_i \, dx = (x^* - x_0) \qquad 3.34$$

In terms of Y_i and $\Delta C_i = C_i^- - C_i^+$, Equation 3.31 can be written as:

$$\tilde{J}_i(x^*) = \frac{\Delta C_i}{2t}\int_0^{Y_i^*}(x - x_0)dY_i \qquad 3.35$$

and integrating by parts:

$$= \frac{\Delta C_i}{2t}\left[(x^* - x_0)Y_i^* + \int_{x^*}^{\infty^+} Y_i dx\right] \qquad 3.36$$

On substituting Equation 3.34 into the Equation 3.36, the expression for flux at any position can be written as:

$$\tilde{J}_i(x^*) = \frac{\Delta C_i}{2t}\left[Y_i^*\int_{\infty^-}^{x^*}(1 - Y_i)dx + (1 - Y_i^*)\int_{x^*}^{\infty^+} Y_i dx\right] \qquad 3.37$$

Equation 3.37 allows the calculation of interdiffusion flux without the need for determining the Matano plane position. For the cases where a change in molar volume with diffusion cannot be ignored, Equation 3.37 can be modified to [56]:

$$\tilde{J}_i^M(x^*) = \frac{\Delta C_i}{2t}\left[Y_i^*\int_{\infty^-}^{x^*}\frac{(1 - Y_i)}{V_m}dx + (1 - Y_i^*)\int_{x^*}^{\infty^+}\frac{Y_i}{V_m}dx\right] \qquad 3.38$$

where $\tilde{J}_i^M$ is the interdiffusion flux of species *i* based on molar fixed frame of reference.

In order to determine the main- and cross-interdiffusion coefficients, the interdiffusion flux determined from either of Equation 3.31 or 3.38 can be integrated over a selected region of interest. On the basis of Equation 3.31 for a ternary system, integration between the position x_1 and x_2 yields [53]:

$$\int_{x_1}^{x_2}\tilde{J}_i\,dx = -\int_{C_1(x_1)}^{C_1(x_2)}\widetilde{D}_{i1}^3\,dC_1 - \int_{C_2(x_1)}^{C_2(x_2)}\widetilde{D}_{i2}^3\,dC_2$$
$$= \overline{\widetilde{D}}_{i1}^3[C_1(x_1) - C_1(x_2)] + \overline{\widetilde{D}}_{i2}^3[C_2(x_1) - C_2(x_2)] \qquad 3.39$$

where $\overline{\widetilde{D}}_{i1}^3$ and $\overline{\widetilde{D}}_{i2}^3$ are the average values of the main- and cross-interdiffusion coefficients over the composition range along the diffusion path between $C_i(x_1)$ and $C_i(x_2)$. These average interdiffusion coefficients can be defined as:

$$\overline{\overline{D}}_{ij}^{3} = \frac{\int_{C_j(x_1)}^{C_j(x_2)} \overline{\overline{D}}_{ij}^{3} dC_j}{\int_{C_j(x_1)}^{C_j(x_2)} dC_j} \text{ for i, j = 1,2,3…….n} \qquad 3.40$$

The values of $\overline{\overline{D}}_{ij}^{3}$ defined in Equation 3.40 are characteristics of the diffusion path; therefore, they can be treated as constant over the selected range of composition. On the basis of $\overline{\overline{D}}_{i1}^{3}$ and $\overline{\overline{D}}_{i2}^{3}$ taken as constants, Onsager's flux equation (Equation 3.28) can be modified to:

$$\tilde{J}_{\mathrm{i}} = -\overline{\overline{D}}_{i1}^{3} \frac{\partial C_1}{\partial x} + \overline{\overline{D}}_{i2}^{3} \frac{\partial C_2}{\partial x} \qquad 3.41$$

Multiplying both sides of Equation 3.41 by (x-x_0) and integrating between x_1 and x_2 in the diffusion zone, we get:

$$\int_{x_1}^{x_2} \tilde{J}_i \, (x - x_0) dx = -\overline{\overline{D}}_{i1}^{3} \int_{C_1(x_1)}^{C_1(x_2)} (x - x_0) dC_1 - \overline{\overline{D}}_{i1}^{3} \int_{C_2(x_1)}^{C_2(x_2)} (x - x_0) dC_2 \qquad 3.42$$

$$\int_{x_1}^{x_2} \tilde{J}_i \, (x - x_0) dx = 2t \left\{ \overline{\overline{D}}_{i1}^{3} \left[\tilde{J}_1 \, (x_1) - \tilde{J}_1 (x_2) \right] + \overline{\overline{D}}_{i2}^{3} \left[\, \tilde{J}_2 (x_1) - \tilde{J}_2 (x_2) \right] \right\} \qquad 3.43$$

Equations 3.39 and 3.43 provide flux equations involving four interdiffusion coefficients (two main and two cross). By solving these equations over the selected composition ranges in the diffusion zones, the main and cross-interdiffusion coefficients can be calculated.

3.3.2.2 Integrated and Effective Interdiffusion Coefficients

Interdiffusion coefficient determination in multicomponent alloys employing multiple diffusion couples with intersecting diffusion paths yields main- and cross-interdiffusion coefficients, the number of which depends upon the number of components present in the diffusion couple. For more than three components, preparation of multiple diffusion couples with common composition in the diffusion zone is quite difficult. The large number of main- and cross-interdiffusion coefficients does not give a clear picture of diffusion phenomena in the multicomponent alloy systems. Alternatively, using a single diffusion couple we can calculate effective interdiffusion coefficients for each element in multicomponent alloys.

These effective interdiffusion coefficients give a better idea of the interdiffusion behaviour of individual components under investigation. Under such conditions, the Onsager equation can be reduced to

$$\tilde{J}_i = -\tilde{D}^i_{eff}\frac{\partial C_i}{\partial x} \qquad 3.44$$

For the calculation of $\tilde{D}^i_{eff}$, Equation 3.44 requires determination of the concentration gradient on the concentration profile curve obtained from the diffusion zone under investigation. Some intermediate phases such as intermetallics are characterized by a narrow composition range. The concentration gradient over which these phases exist can be very small and it is practically difficult and inaccurate to measure such a small gradient on the concentration profiles. In such cases, Wagner [57] suggested the determination of integrated diffusion coefficient $\tilde{D}^i_{int}$ instead of interdiffusion coefficient, which is essentially the $\tilde{D}^i_{eff}$ integrated over the composition range of the phase of interest. The $\tilde{D}^i_{int}$ can be related to $\tilde{D}^i_{eff}$ by

$$\tilde{D}^i_{int} = \int_{N_i^1}^{N_i^2} \tilde{D}^i_{eff}\, dN_i = \bar{\tilde{D}}_{eff}\Delta N_i \qquad 3.45$$

where $\bar{\tilde{D}}_{eff}$ is the average effective interdiffusion coefficient. N_i^1 and N_i^2 represent minimum and maximum composition of specie i (in mole fraction) in the phase of interest. Using the relation $C_i = \frac{N_i}{V_m}$ and Equations 3.44 and 3.45, the $\tilde{D}^i_{int}$ in terms of the flux of diffusing species can be written as [58]:

$$\tilde{D}^i_{int} = -V_m \int_{x_1}^{x_2} \tilde{J}_i\, dx \qquad 3.46$$

Where V_m is the molar volume of the phase of interest and x_1 and x_2 are the positions corresponding to the composition range ΔN. Once $\tilde{D}^i_{int}$ is determined, the $\bar{\tilde{D}}_{eff}$ can be calculated from Equation 3.45. For a multicomponent alloy system, there will be a unique $\bar{\tilde{D}}_{eff}$ for each element present in the interdiffusion zone, and using the above procedure, these can be measured from a single diffusion couple.

3.4 Diffusion-Controlled Growth of Reaction Phase in Multiphase Systems

Growth of precipitates/reaction layers in the solid state annealing experiments is controlled by thermally activated movement of atoms to the interface and is said to be diffusion controlled.

In most practical cases, diffusion occurs in the presence of more than one phase. Diffusion in multiphase system can be understood by considering a diffusion couple made up of two pure metals A and B which are not completely miscible in each other [59]. In such a diffusion couple an intermediate phase (β) forms in addition to solid solutions of A (α) and B (γ). Figure 3.4 shows a hypothetical phase diagram and concentration distance profile developed during diffusion annealing of the diffusion couple.

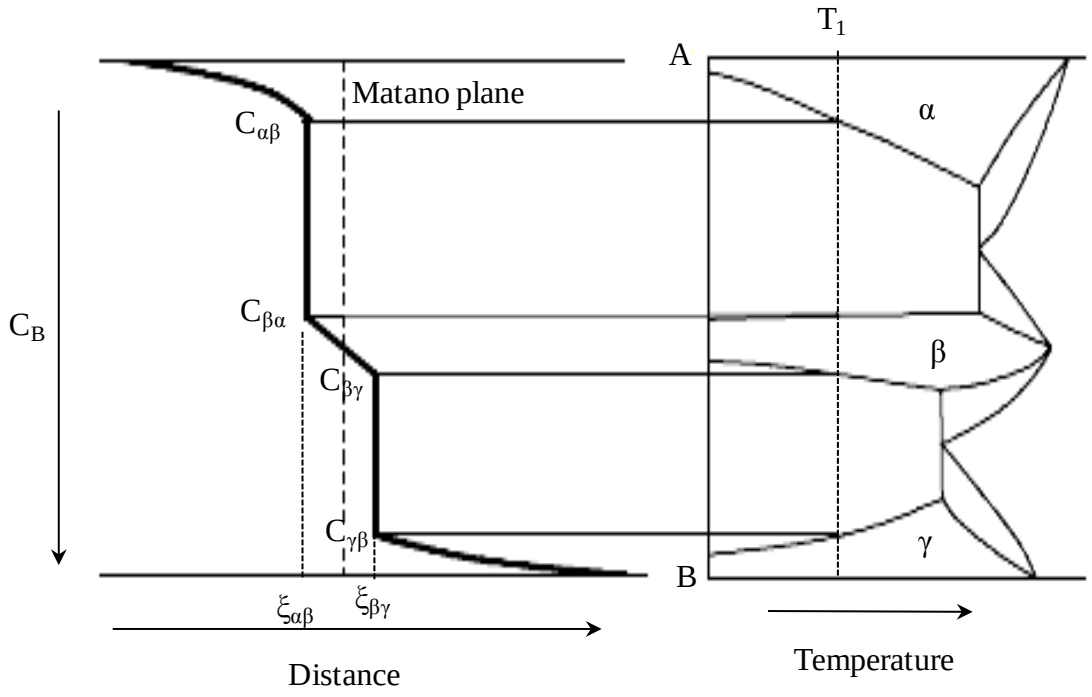

Figure 3.4 Hypothetical phase diagram of a binary system and concentration profile developed during diffusion annealing at temperature T_1

Assuming that the concentrations are in local equilibrium at α/β and β/γ interfaces, an expression for the rate at which the interfaces move can be obtained. If we consider flux of material from left to right, the rate of movement of the interface at $\xi_{\alpha\beta}$ will be:

$$[C_{\alpha\beta} - C_{\beta\alpha}]\frac{d\xi_{\alpha\beta}}{dt} = J_{\alpha\beta} - J_{\beta\alpha} \qquad 3.47$$

This means that the flux from α phase at the interface must supply the surplus quantity $[C_{\alpha\beta} - C_{\beta\alpha}]d\xi_{\alpha\beta}$ per unit time in order to advance α phase into β phase region. Applying Fick's first law of diffusion (Equation 3.2), Equation 3.47 can be written as:

$$\frac{\partial \xi_{\alpha\beta}}{\partial t} = \frac{1}{C_{\alpha\beta} - C_{\beta\alpha}}\left[\left(-D\frac{\partial C}{\partial x}\right)_{\alpha\beta} - \left(-D\frac{\partial C}{\partial x}\right)_{\beta\alpha}\right] \qquad 3.48$$

By expressing concentration as a function of a single parameter λ=x/√t (refer to Section 3.2.2.1), we can write

$$\frac{\partial C}{\partial x} = \frac{1}{\sqrt{t}}\frac{dC}{d\lambda} \qquad 3.49$$

Since concentration remains constant at the interface, λ and hence $\frac{dC}{d\lambda}$ will also be constant at the interface. Therefore, Equation 3.48 can be re-written as

$$\frac{d\xi_{\alpha\beta}}{dt} = \left[\frac{(DA)_{\beta\alpha} - (DA)_{\alpha\beta}}{C_{\alpha\beta} - C_{\beta\alpha}}\right]\frac{1}{\sqrt{t}} \qquad 3.50$$

Where

$$A_{ij} = \left(\frac{dC}{d\lambda}\right)_{ij} = \sqrt{t}\left(\frac{\partial C}{\partial x}\right)_{ij} \qquad 3.51$$

Integrating Equation 3.50:

$$\xi_{\alpha\beta} = 2\left[\frac{(DA)_{\beta\alpha} - (DA)_{\alpha\beta}}{C_{\alpha\beta} - C_{\beta\alpha}}\right]\sqrt{t} \qquad 3.52$$

Similarly for $\xi_{\beta\gamma}$ interface

$$\xi_{\beta\gamma} = 2\left[\frac{(DA)_{\gamma\beta} - (DA)_{\beta\gamma}}{C_{\beta\gamma} - C_{\gamma\beta}}\right]\sqrt{t} \qquad 3.53$$

From Equations 3.52 and 3.53, width of the intermediate layer as a function of time is given by:

$$x_\beta = \xi_{\beta\gamma} - \xi_{\alpha\beta} \qquad 3.54$$

or

$$x_\beta = 2\sqrt{t}\left\{\left[\frac{(DA)_{\gamma\beta} - (DA)_{\beta\gamma}}{C_{\beta\gamma} - C_{\gamma\beta}}\right] - \left[\frac{(DA)_{\beta\alpha} - (DA)_{\alpha\beta}}{C_{\alpha\beta} - C_{\beta\alpha}}\right]\right\} \qquad 3.55$$

or

$$x_\beta = k_\beta\sqrt{t} \qquad 3.56$$

This gives a parabolic relation with a temperature dependent rate constant (k_β) which involves a complex sum of diffusion coefficients in the adjacent phases as well as in the β phase also.

A special case of above described model was presented by Zener [60, 61] for one dimensional growth of precipitates in an alloy matrix. The model is applicable to binary systems which have limited solubility in primary phases and no intermediate phase is formed during diffusion annealing. It is shown that under diffusion controlled growth, there exists a parabolic relationship between interface movement and time. This relationship can be derived by considering growth of a planar precipitate β in a matrix α as shown in Figure 3.5(a). Initially the concentration of the solute is higher in the precipitates than in the bulk of matrix and at the α/β interface the matrix composition is depleted in solute *B* (Figure 3.5(b)). By assuming that the time for the solute atoms to cross the interface is smaller than their diffusion up to the precipitate, the concentration of the solute at α/β will be in equilibrium (C_e).

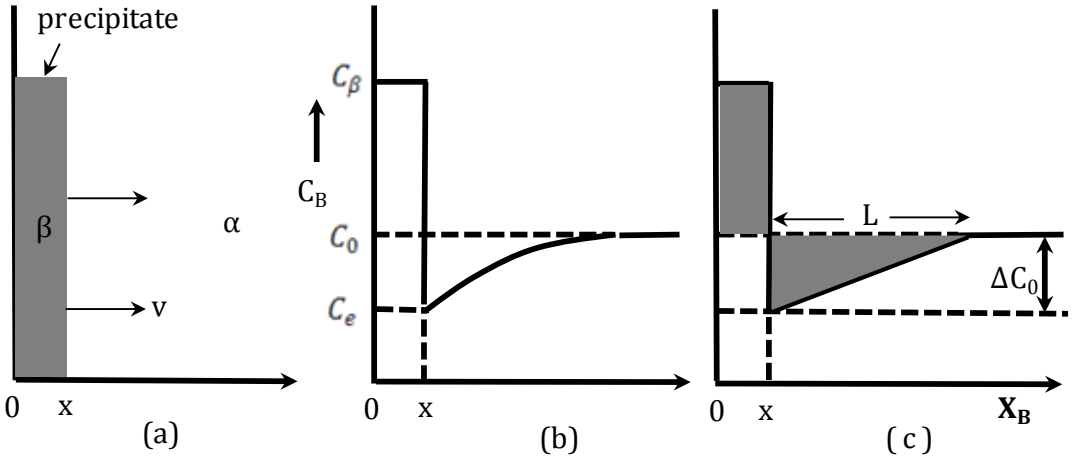

Figure 3.5: (a) Schematic showing diffusion controlled growth of a planar precipitate (b) composition variation with distance (c) approximation for the composition profile.

For the growth of the precipitate by a distance *dx* in time *dt*, the number of moles of *B* to be consumed at the interface per unit area is:

$$(C_\beta - C_e)dx \qquad 3.57$$

According to Fick's first law, this number should be equal to:

$$-Jdt = D\left(\frac{dC}{dx}\right)dt \qquad 3.58$$

where J is flux of B and D is the diffusion coefficient. Equating Equations 3.57 and 3.58, and solving for interface velocity:

$$v = \frac{dx}{dt} = \frac{D}{(C_\beta - C_e)}\frac{dC}{dx} \qquad 3.59$$

The solution to the above equation can be obtained by assuming that the concentration profile in the matrix is linear as shown in Figure 3.5(c). Noting that conservation of the solute is required in the two shaded regions shown in the diagram, we can write:

$$(C_\beta - C_0)x = \frac{L\Delta C_0}{2} \qquad 3.60$$

where $\Delta C_0 = C_0 - C_e$, and x is the thickness of the precipitate. The growth rate therefore becomes:

$$v = \frac{D(\Delta C_0^2)}{2(C_\beta - C_e)(C_\beta - C_0)x} \qquad 3.61$$

By assuming constant molar volume (V_m), the concentration in the above equation can be replaced by mole fraction ($X=CV_m$). Further assuming that $(C_\beta - C_e) \cong (C_\beta - C_0)$, and integrating Equation 3.61 gives:

$$x = \frac{\Delta X_0}{(X_\beta - X_e)}\sqrt{(Dt)} \qquad 3.62$$

and

$$v = \frac{\Delta X_0}{2(X_\beta - X_e)}\sqrt{\frac{D}{t}} \qquad 3.63$$

where $\Delta X = X_0 - X_e$ is the supersaturation prior to precipitation.

Equations 3.62 and 3.63 indicate that for one dimensional growth, the interface position varies as $\sqrt{Dt}$ and its velocity as $\sqrt{D/t}$. The equations are valid for all the cases where the diffusion distance ahead of precipitate/matrix interface increases as the particles grow. The equations also suggest that for a given time, precipitate growth is proportional to supersaturation of the matrix. Dependence of v on $1/\sqrt{t}$ means that with increasing time, the rate of precipitate growth must decrease. This decrease is due to the fact that as the precipitate grows, it continues to draw solute atoms from the matrix resulting in a decrease in concentration gradient next to the growing precipitate in the matrix.

The growth constant described in Equation 3.56 can be calculated from thickness measurements of the reaction layer as a function of time at the given temperature. The constant also follows similar temperature dependent Arrhenius relationship given for diffusion coefficient as:

$$D = D_0\, exp^{\left(-\frac{Q_D}{RT}\right)} \qquad 3.64$$

where D_0 is the pre-exponential factor, Q_D is the activation energy for diffusion (J mole^{-1}), R is the ideal gas constant (8.314 J mole^{-1} K^{-1}) and T is the diffusion annealing temperature (Kelvin).

By plotting log of growth constant or diffusion coefficients against reciprocal of absolute temperature, activation energy for growth (Q_G) and diffusion (Q_D) can be determined from the slope of Arrhenius plot.

For the determination of growth constant and therefore Q_G, two different equations have been used in past studies (Table 3.1). These are:

$$x = \sqrt{Kt} \qquad 3.65$$

$$x = k\sqrt{t} \qquad 3.66$$

where x is the thickness of the reaction layer developed in time t during diffusion annealing and K or k is the growth constant.

Since Equation 3.65 is equivalent to $x = \sqrt{Dt}$ used to approximate the penetration depth of diffusion species, the relation between two different growth constants can be written as $k^2 = K = D$. Accordingly, Q_G calculated from k values using Equation 3.66 will be half of Q_D. But according to Equation 3.56, growth constant in case of multiphase diffusion has complex meaning. It depends on diffusivities in the bordering layers as well as on the diffusivity of the growing phase, on the concentration gradients on both sides of the interfaces and on the solubility limits of the phases. Therefore the activation energy deduced from the growth constant also has complex meaning and may not be correlated with activation energy for diffusion.

3.5 Growth of Reaction Layers in W Wire Reinforced Alloys

Table 3.1 summarises the literature on the diffusion and growth kinetics parameters for the reaction layers in W wire reinforced composites. Diffusion coefficients were determined by Boltzmann-Matano and moving boundary methods. Growth kinetics of the reaction layers were determined by fitting the data to the parabolic growth law. Due to the limited data available and the fact that vastly different alloy compositions were used for reinforcement, no conclusive trend about the intermetallic growth and diffusion can be predicted from past studies. Roughly we can say that measured diffusion coefficients in the temperature range 1100-1200°C lie between 10^{-11}-10^{-13} cm^2sec^{-1} in all the cases. In the case of INCOLOY 903, the activation energy for diffusion increases by approximately 10% when the INCOLOY 903 matrix was modified by adding 10wt.% tungsten. Two studies on 304 and 316 stainless steel matrices were limited to calculation of growth constants only. The data in the latter case is limited in the sense that the k value was calculated at 1093°C only. The information is insufficient to determine Q_G over a range of temperature for comparison with W/316L in the present investigation.

Table 3.1: Summary of the diffusion and growth kinetics studies in tungsten wires reinforced high temperature alloys.

Composition (wt.%)	Diffusion & Growth Characteristics					Ref.
	Temperature °C	Equation	coefficient (cm^2sec^{-1})		Q (kJ $mole^{-1}$)	
W/NIMOCAST 713C 12Cr-6Al-4.5Mo-2Nb (bal. Ni)	1100	$x^2=4Dt+C$	D=1.66E-13		-	[8]
W/65Ni-20Cr-15W W/60Ni-20Cr-20W	1200 1200	$x^2=Kt$	K=1.87 E-11 0.0071 E-11		-- --	[62]
W/80Ni-20Cr	1100	$x^2=Kt$ BM method	$\widetilde{D}_{35W}$= 4.0 E-11 $\widetilde{D}_{5W}$= 2.9 E-11	K=0.53 E-12	Q_G=444±25	[63]
W/304 SS 0.08C-18Cr-8Ni-2Mn-1Si (bal. Fe)	1000-1200	$x=k\sqrt{t}$	$k=13\ [\exp(-239.5/RT)]t^{1/2}$		Q_G=239.5±20	[64]
W/INCOLOY 903 38Ni-15Co-3.1Nb (bal. Fe)	1100 1200	Moving boundary method	$\widetilde{D}_{IM\ layer}$ = 11 E-12 47 E-12		Q_D =268	[27]
W/INCOLOY 903 (modified with ~10%W)	1100 1200		$\widetilde{D}_{IM\ layer}$ = 14 E-12 80 E-12		$Q_{D=}$ 291	
W/316SS	1093	$x^2=Kt$	k=4.9E-12			[65]

3.6 Summary

Methods of diffusion coefficient measurement in binary and multicomponent alloys were reviewed in this chapter. A model for the diffusion-controlled solid state growth of precipitates which is also applicable for the growth of reaction layers was discussed and the results on the diffusion and growth kinetics of some studied tungsten wire reinforced composites were compiled.

Determination of interdiffusion parameters in multicomponent alloys is rather difficult. Depending on the molar volume change during diffusion annealing, either the Boltzmann-Matano or the Sauer-Freise methods can be successfully employed to extract diffusion coefficients in the diffusion couples composed of ternary alloys. The methods can also be used to study interdiffusion in higher order systems; but the fabrication of multiple diffusion couples with intersecting diffusion paths is difficult. Also, the number of main- and cross-interdiffusion coefficients determined using these methods increase with increasing components of the alloy system. Therefore the above mentioned methods are less practical for understanding diffusion in multicomponent systems. In such cases, calculation of average effective interdiffusion coefficients will be more useful to compare the diffusion behaviour of individual components in the multicomponent systems and can be done utilizing a single diffusion couple.

Past studies utilized different equations to determine the growth kinetics of the reaction layers in the composites. Based on parabolic growth, these studies suggest that growth of layers in the composites is diffusion controlled. There is no previous quantitative data available on the growth kinetic and interdiffusion in the composites investigated in this thesis. Therefore, the data generated in this thesis will serve as an important source of information for future studies on similar composite systems.

Chapter 4. Composite Fabrication and Characterization Procedures

In this chapter a description of materials used to make the composites, fabrication procedure and the techniques employed to characterize the composites are presented. The composites were fabricated by a casting method and were diffusion annealed at different temperatures for different time intervals. Specimens from as-cast and diffusion annealed composites were characterized by Scanning Electron Microscopy (SEM), Energy Dispersive Spectroscopy (EDS) and Electron Backscattered Diffraction (EBSD) techniques. All the procedural steps from composites fabrication to characterization and data acquisition are explained in this chapter.

4.1 Materials

4.1.1 Matrix Alloys

Two commercial stainless steel grades, 316L stainless steel (316L) and HP-35Ni-25Cr alloy steel (HP) were used as matrix materials in the present study. Typical chemical composition of both the matrix alloys determined by EDS is given in Table 4.1.

Table 4.1: Chemical composition of 316L and HP stainless steels used in the present study. The composition was determined by EDS. Error is standard deviation over five measurements.

Alloy	**Composition (wt. %)**					
	Cr	Fe	Ni	Mn	Si	others
316L	17.6 ±0.2	68.0 ±0.3	9.9 ±0.2	1.9 ±0.1	0.5 ±0.1	Mo-2± 0.2
HP-35Ni-25Cr	25.0 ±0.1	34.6 ±0.1	34.6 ±0.2	0.5 ±0.1	1.7 ±0.1	Nb-1.1 ±0.1

316L stainless steel is a Fe-Ni-Cr based alloy with a fully austenitic microstructure at room temperature. It has very low carbon content <0.03 wt.% C, which is necessary to prevent its

sensitization at elevated temperature. Addition of 2-3 wt.% Mo in 316L improves its corrosion resistance and provides increased strength at elevated temperature. Typical uses of 316L include exhaust manifolds, furnace parts, heat exchangers, chemical equipment, digesters, tanks, evaporators, paper and textile processing equipment and parts exposed to marine atmospheres and tubing.

HP alloy steel is also a Fe-Ni-Cr based austenitic stainless having 25 wt.%Cr and a Fe:Ni ratio close to 1. In contrast to 316L, the carbon content in this steel is quite high ~ 0.45 wt.%. Because of these compositional attributes this steel exhibits much higher creep-rupture strength, carburization and oxidation resistance than 316L. Consequently, it is used at higher service temperatures. Typical uses of HP alloy steel are in ammonia, methanol and hydrogen reforming operations (furnace parts, tube supports and hangers), ethylene pyrolysis (coils and fittings), steam super-heaters and tube sheets.

4.1.2 Reinforcement

Commercial purity W wires (AKS grade), procured from Midwest Tungsten Service-USA were used for reinforcing the stainless steel matrices. The diameter of the wires was 381µm (from supplier's report), and they were received in as-drawn and cleaned condition. The chemical composition of the W wires used in this study is reported in Table 4.2.

Table 4.2: Chemical composition of tungsten wire (from the supplier's test report).

W	Al	P	Si	impurities
99.95 wt.% (min.)	35 ppm (max.)	100 ppm (max.)	40 ppm (max.)	30-50 ppm C, Cr, Cu, Fe, Zn, Mo, Na Ni, O

As seen in the Table 4.2, AKS grade W has deliberate but very small addition of Al, P and Si in it. W is doped with aluminium potassium silicate that causes formation of potassium bubbles at the grain boundaries of W. The potassium bubbles promote highly interlocked grain formation on recrystallization [66]. This interlocking of grains extends creep life of the wires by inhibiting grain boundary sliding and diffusional creep. Figure 4.1 shows secondary electron (SE) images of the longitudinal and transverse cross-sections of the as-drawn W wires.

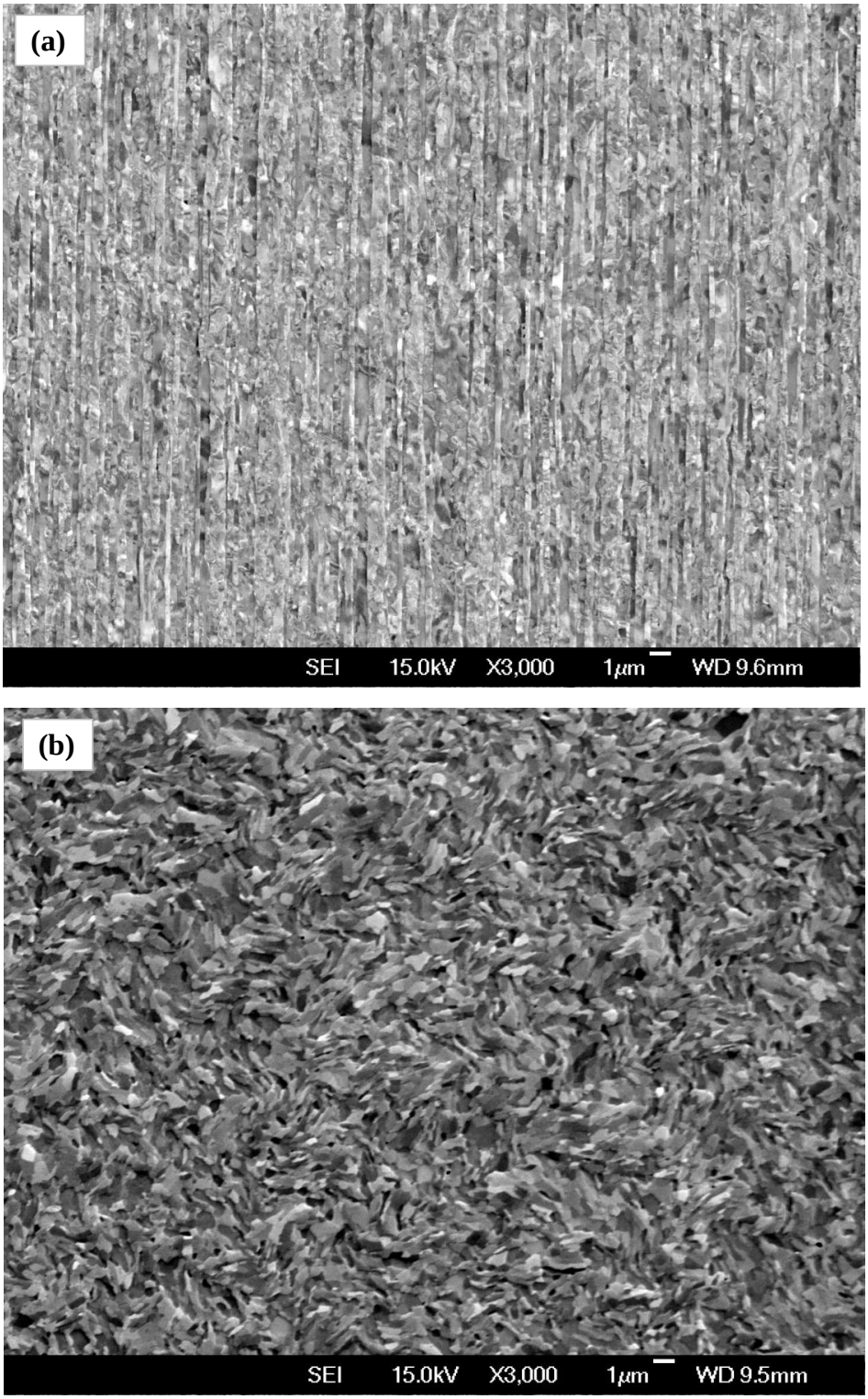

Figure 4.1: Typical microstructure of the tungsten wires used in present study. (a) longitudinal cross- section and (b) transverse cross-section.

The microstructure of the longitudinal cross-section of the wire shows a fibrous appearance indicating heavily deformed grains along the drawing direction.

4.2 Composite Fabrication

The reinforced alloys (composites) under investigation in this study were fabricated by a casting method. A rectangular split mold (160mm x 160mm x 62mm) made of 304 grade stainless steel was used (Figure 4.2). The mold had a cavity of size 110mm x 110mm x 12mm. A thin layer of a refractory coating (Boron Nitride Releasecoat-Blue®) was applied inside the mold cavity before affixing the wires in the mold. Short lengths of W wires (~125mm) were cut, straightened, and arranged longitudinally in the mold. No wire was placed in the path of the liquid metal flow into the mold in order to ensure a smooth and turbulence-free flow of molten alloy during casting. Closing and fastening of both the halves of the split mold facilitated the locking of W wires to their respective positions inside the mold. The entire mold setup was preheated to 110°C to eliminate moisture before pouring the liquid alloy.

For composite fabrication, small pieces of the respective alloys were melted in a high purity alumina crucible (Size: ID 90mm x H 140mm, procured from Certec-New Zealand) inside a bench top resistance furnace that has the capability of attaining 1700°C temperature (heating zone Size: 150mm x 150mm x180mm,. make: Ceramic Engineering-Sydney, Australia). About 1.2 kg of alloy was melted for making each composite casting. After melting, the molten metal was held for 30 minutes at the desired temperature and then poured into the stainless steel mold. A 50°C superheat temperature was used for pouring. The melting points of the alloys are 1370-1400°C and ~1350°C, respectively for 316L and HP alloy [67].

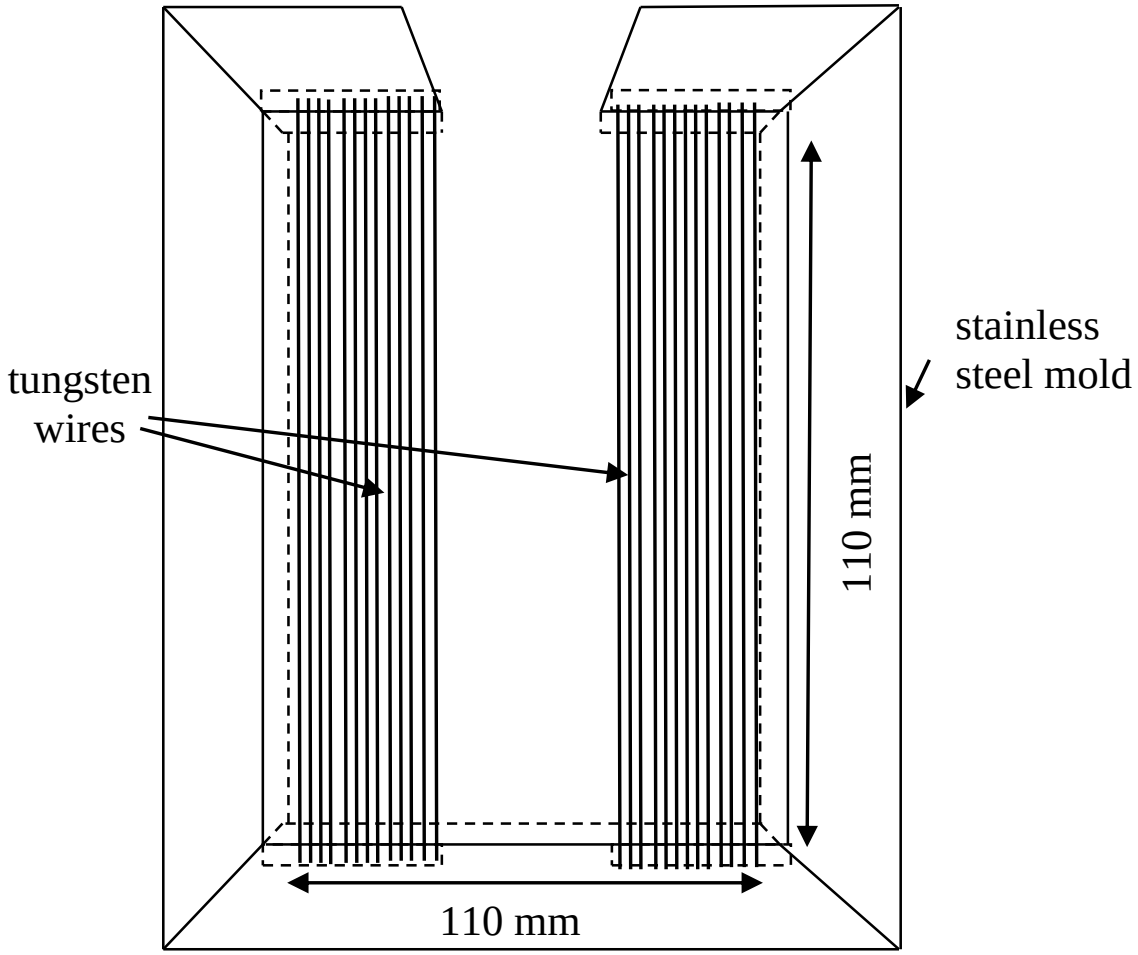

Figure 4.2: Schematic diagram of stainless steel split mold used to cast the composites. The tungsten wire arrangement is shown inside the mold.

Once the mold was cooled down to room temperature, the cast plate was removed from the mold. Five composite plates were cast using each alloy. The cast plates were then subjected to X-ray radiography in order to assess the condition of W wires inside the castings. A typical photograph of a cast plate and its X-ray radiograph are shown in the Figure 4.3. The radiograph shows no apparent damage to the W wires inside the composite plate. There are a few voids in the casting (visible as white spots), but they do not pose a problem for the microstructural studies.

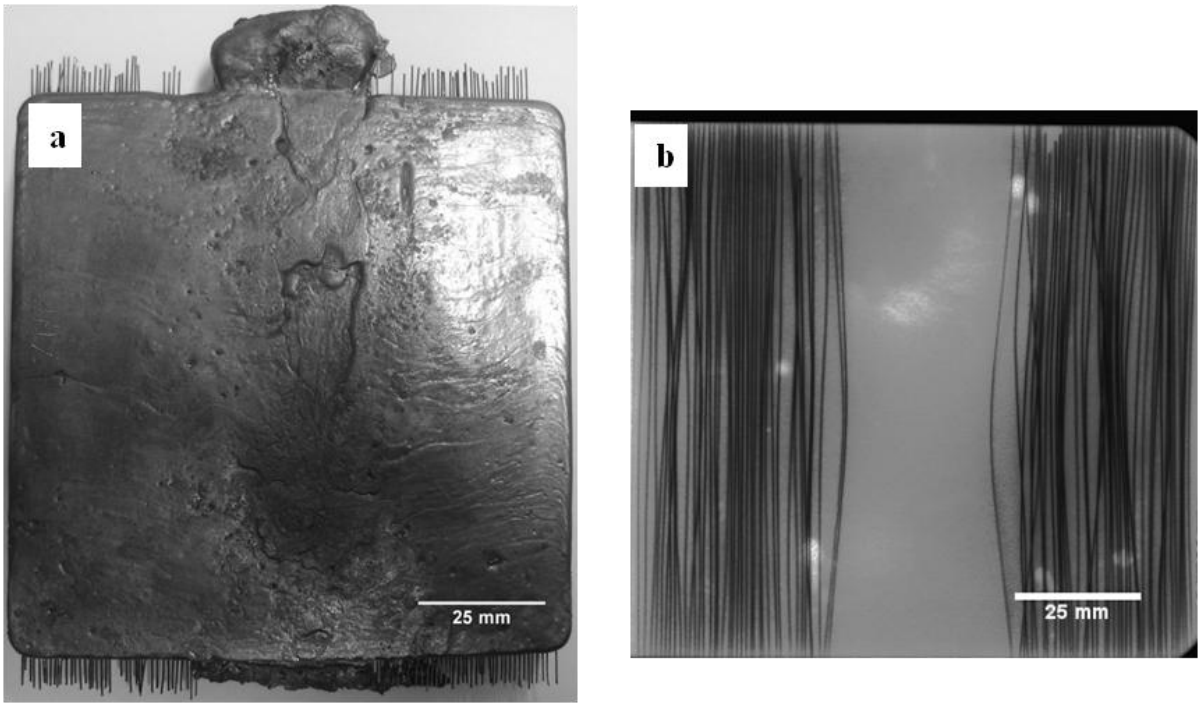

Figure 4.3: (a) A typical as-cast tungsten reinforced stainless steel composite plate (b) X-ray radiograph of the same plate showing the condition of wires inside the composite. The white dots seen on the radiograph are voids present in the cast plates.

4.3 Diffusion Annealing

Samples from the fabricated composite plates (W/316L and W/HP) were used to study the reaction products, growth kinetics of reaction layers and their interdiffusion characteristics. In order to perform these investigations rectangular samples of size 20mm x 10mm x 10mm were sectioned from the cast plates. The samples were annealed in a resistance furnace at four different temperatures 900°C, 1000°C, 1100°C and 1200°C. Due to the poor oxidation resistance of 316L above 850°C, the samples were encapsulated in evacuated quartz tubes prior to annealing (Figure 4.4). For the diffusion study, each set of five samples was annealed as above and the samples were removed after 25, 50, 100, 200 and 500 hours and quenched in water.

Figure 4.4: W/316L samples encapsulated in quartz tubes for diffusion annealing at 900-1200°C.

4.4 Specimen Preparation

Specimens of size 10mm x 10mm x10mm were sectioned from the cast composite plates using an abrasive wheel cutter (Buehler Abrasimet).While cutting the samples, it was ensured that the reinforced wire axis is perpendicular to the cut surface. Similarly, specimens approximately from the middle of the diffusion annealed composites were sectioned using the abrasive cutter. A diagram of the sampling scheme of the diffusion annealed specimens is shown in Figure 4.5. For the ease of handling and edge retention, all the sectioned samples were mounted in a conductive mounting compound (Buehler Probemet®) using a hot mounting press.

The mounted cast and diffusion annealed specimens were firstly wet ground successively on silicon carbide emery papers (Buehler Carbimet®) of sizes 180, 200, 400, 600 grits using water as a lubricant. This operation removed bulk surface defects, scratches and made the sample's surface flat enough for fine polishing. Secondly, the specimens were subjected to

fine polishing using 9, 3 and 1µm size diamond particles suspended in water (Buehler MetaDi® Supreme). Thoroughly washed fine polished samples were further subjected to final polishing using 0.06 and 0.02 µm (Buehler MasterMet®) colloidal silica suspensions

.

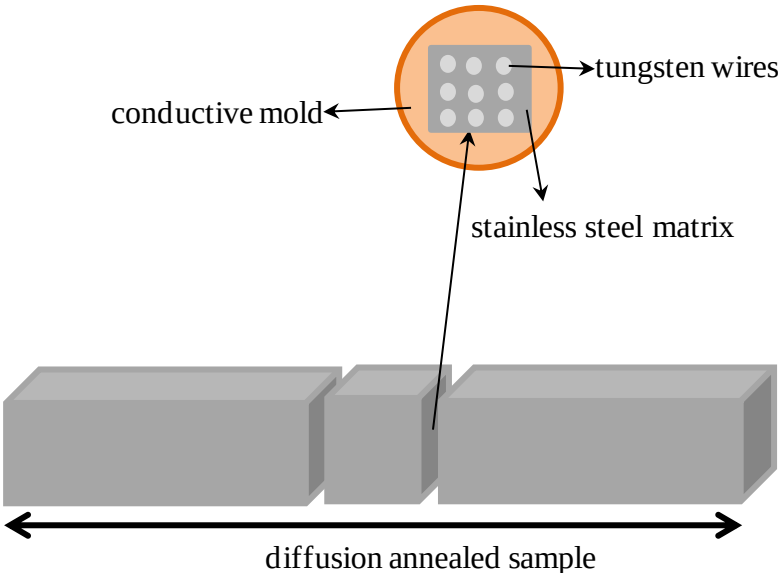

Figure 4.5: Sampling scheme for the characterization of diffusion annealed composites. Small specimens were sectioned approximately from the middle of the diffusion annealed samples and the surface view perpendicular to the wire length was mounted for examination.

4.5 Characterization

Polished specimens from the as-cast and diffusion annealed plates were investigated for microstructure and chemistry. Additionally, thickness measurements on the reaction layers in diffusion annealed specimens were performed to establish the growth kinetics of the layers. The composition profiles acquired across the reaction layers were utilized to determine the average effective interdiffusion coefficients in the layers. The procedures are described below.

4.5.1 Microscopy and Measurements

The microstructure of the specimens was analysed with a JEOL 7000F scanning electron microscope equipped with a field emission gun (FEG-SEM). Wherever required, images were acquired in both secondary electron (SE) and backscattered electron (BSE) imaging

modes. All the images were acquired at 20keV accelerating voltage and a working distance approximately 10 mm between microscope objective and the sample.

The thickness of the reaction layers was measured on the acquired micrographs using a length measuring tool incorporated in the EDS software. The values reported in this thesis are average thickness of 20 measurements on multiple micrographs.

For measuring the diameter of the tungsten wires inside the composite matrices, image analysis software "image J" [68] was utilised. By segmenting the SEM image, the area of the wire was measured and its diameter was calculated. A total 10 wires in different micrographs representing each composite were analysed to calculate average wire diameter.

4.5.2 Chemical Analysis

An EDS detector (JEOL EX-2300 BU) attached to the FEG-SEM was used to perform chemical analyses on the polished samples of the composites. The ZAF (atomic number (Z), X-ray absorption (A) and X-ray fluorescence (F)) standardless method was used for the quantification of various elements in this research.

4.5.2.1 Composition Profiles Acquisition

Composition profiles were used to calculate diffusion coefficients in the reaction layers. For their acquisition, line scan analyses were performed on the polished samples covering the entire width of the reaction layer and parts of W wire and the matrix of the composites. The electron beam was scanned across a line and a spectrum was acquired at equidistant points with separation 1 to 2 µm in each sample.

For obtaining localized chemical information from a particular feature/region on the image, point and area analysis modes were used to collect the X-ray spectra. These spectra were then analysed quantitatively to obtain chemical composition of the elements present.

4.5.2.2 X-ray Mapping

X-ray mapping on the composite samples was done to learn about the distribution of various elements in the reaction zones of the composites. The X-ray map acquisition reported in this thesis was done at 20keV accelerating voltage, 0.59nA probe current, and 10mm focal length. The beam current was adjusted to obtain numbers of counts per second (cps) in the range 5000-30,000 and the dead time was maintained between 25-35%. The X-ray maps were

acquired for 100 frames for each sample. The following steps were followed to collect X-ray maps with the help of EDS:

- An image of the area of the interest on the specimen was acquired in the EDS software. X-ray spectrum from the entire area in the image was then collected to survey the presence of chemical elements in the area.

- Once the probable elements present in the samples were identified, X-ray maps of the identified elements were collected from the entire image of the sample under investigation to visualize the elemental distribution.

4.5.3 Phase Identification

An EDS assisted EBSD methodology was used to identify the unknown phases in the reinforced alloy composites. A JEOL JSM-6100 SEM with an Oxford EDS detector (with Moran Scientific QXAS QUOLL software) and EBSD detector (HKL Technology Nordlys II) attachments were used for this purpose. All the images and the backscattered electron diffraction patterns (EBSP) were collected at 20keV accelerating voltage and 30 mm working distance.

For the identification of crystal structures, crystallographic data [35] of all the likely phases was input in the EBSD software (HKL CHANNEL 5 Flamenco) to create the match units needed in the indexing procedure. A match unit is a list of diffracted planes in a particular crystal structure. The following steps were used in phase identification:

- Using the imaging mode in the EBSD software, the unknown phase was located, imaged and the image was frozen.

- Switching to chemical analysis, the composition of the elements in the unknown phase was established with EDS. Based on this compositional information, a phase database of the phases that contain the elements in approximate proportion identified by EDS analysis was selected in the EBSD software.

- With the help of the frozen image, the electron beam was positioned on the unknown phase. The EBSP was acquired from the phase and the bands on the pattern were detected.

- The EBSP was indexed and compared with the stored selected phase data in order to obtain acceptable solutions. The identification was considered successful when the simulated pattern from the selected database matched the EBSP from the unknown phase with mean angle of deviation 0.5°.

Since this study mainly makes use of EDS and EBSD techniques to characterize the composites. Important features of these techniques and major factors affecting the analysis using these techniques are discussed in Appendix A [69-74].

4.6 Summary

Starting materials and the procedures followed to fabricate and characterize the composites were described in this chapter. Plates of W/316L and W/HP alloys composite were fabricated by a casting method. The samples from the composites were diffusion annealed in temperature 1000-1200°C for 25-500 hours. SEM, EDS and EBSD techniques were used to characterize the composites, the results of which are presented in chapters 5 and 6.

Chapter 5. Reaction Layer Formation and Growth in Tungsten Wire Reinforced 316L Stainless Steel

This chapter presents the studies on reaction layer formation and growth in W/316L composites. Phase diagrams and past studies of some W wire reinforced Fe based alloy matrices suggest that different intermetallic phases can evolve in the fabricated composites due to the interaction between W wire and matrix constituents. Depending on their growth kinetics, the intermetallic phases can be harmful for the creep properties of the composite. In order to study growth behaviour of the reaction phases, the fabricated composites were annealed in the temperature range 1000-1200°C. The results of these studies are discussed in terms of microstructure evolution, phase identification on the reaction layers, growth constants of the layers and average effective interdiffusion coefficients of different elements in the layers. A key finding of these studies is that interaction of W with 316L stainless steel results in the formation of a brittle intermetallic layer that is consistent with μ-phase.

5.1 Experimental Procedures

The detailed procedures followed for the composite fabrication, diffusion annealing, sample preparation and characterization of the W/316L composites are described in the Sections 4.2 to 4.5 of this thesis. A brief overview is given below.

The W/316L composite plates were fabricated by introducing molten 316L alloy into a permanent mold with W wires pre-arranged in it. The specimens were sectioned from the plates and sealed in evacuated quartz tubes for diffusion annealing. As-cast and diffusion annealed composite specimens were investigated for microstructural evolution, chemistry and crystal structure of the evolved phases by SEM-EDS and EBSD techniques. Thickness measurements on the reaction layers were performed and used to determine the growth kinetics of the layers. Composition profiles acquired across the reaction layers in the annealed specimens were used to calculate the average effective interdiffusion coefficients of various elements in the layers.

5.2 Results

5.2.1 Microstructure and Chemistry

5.2.1.1 As-cast Composites

Figure 5.1(a) shows microstructure of the as-cast W/316L composite representing transverse cross-sections of a W wire in 316L matrix. A magnified view (Figure 5.1(b)) shows the microstructural features of the composite, in particular a 2 μm thick reaction layer around the wire periphery. The layer has multiple cracks on it that indicate its brittle nature. Additionally, there is a region adjacent to layer/matrix interface which appears to have an altered matrix composition and is about 10 μm thick. The grains in the W wire have experienced the effect of temperature during the casting process i.e. recrystallization- that has transformed their morphology from fibrous (Figure 4.1) to equiaxed.

Distribution of major alloying elements around the reaction zone was mapped using EDS and the collected X-ray maps of Cr, Fe, Ni, and W are shown in Figure 5.2. The BSE image (Figure 5.2(a)) show composition contrast based on the atomic number (Z) of different elements and this contrast can be related to the specific elements in the X-ray colour maps. As seen from W map (Figure 5.2(f)), the reaction layer around the wire contains significant amount of W. Some regions in the matrix are enriched with Cr (Figure 5.2(d)), but the same regions are depleted in Fe and Ni (Figure 5.2(c) and (e)). The X-ray maps of Ni in the Figure 5.2(e) shows false contrast in the W wires as there appears to be substantial presence of Ni in the wire. The X-ray spectrum collected on the W wire close to the wire/reaction layer interface ruled out any presence of Ni in it. This false contrast likely to arises due to dependence of X-ray continuum on atomic number[13].

[13] X-ray maps from a sample are collected by defining an energy window across a peak for a specific element. The measured X-ray count contains two contributions- characteristics X-rays of the peak and continuum X-rays from the sample background. Since continuum X-rays vary linearly with average atomic number of the electron excited region, during multiphase sample beam scanning, measured intensity of the window for an element may change as the beam scans different phases even if the element is entirely absent in that region. This results in false contrast which is entirely due to the response of X-ray continuum to the concentration changes during beam scanning [69].

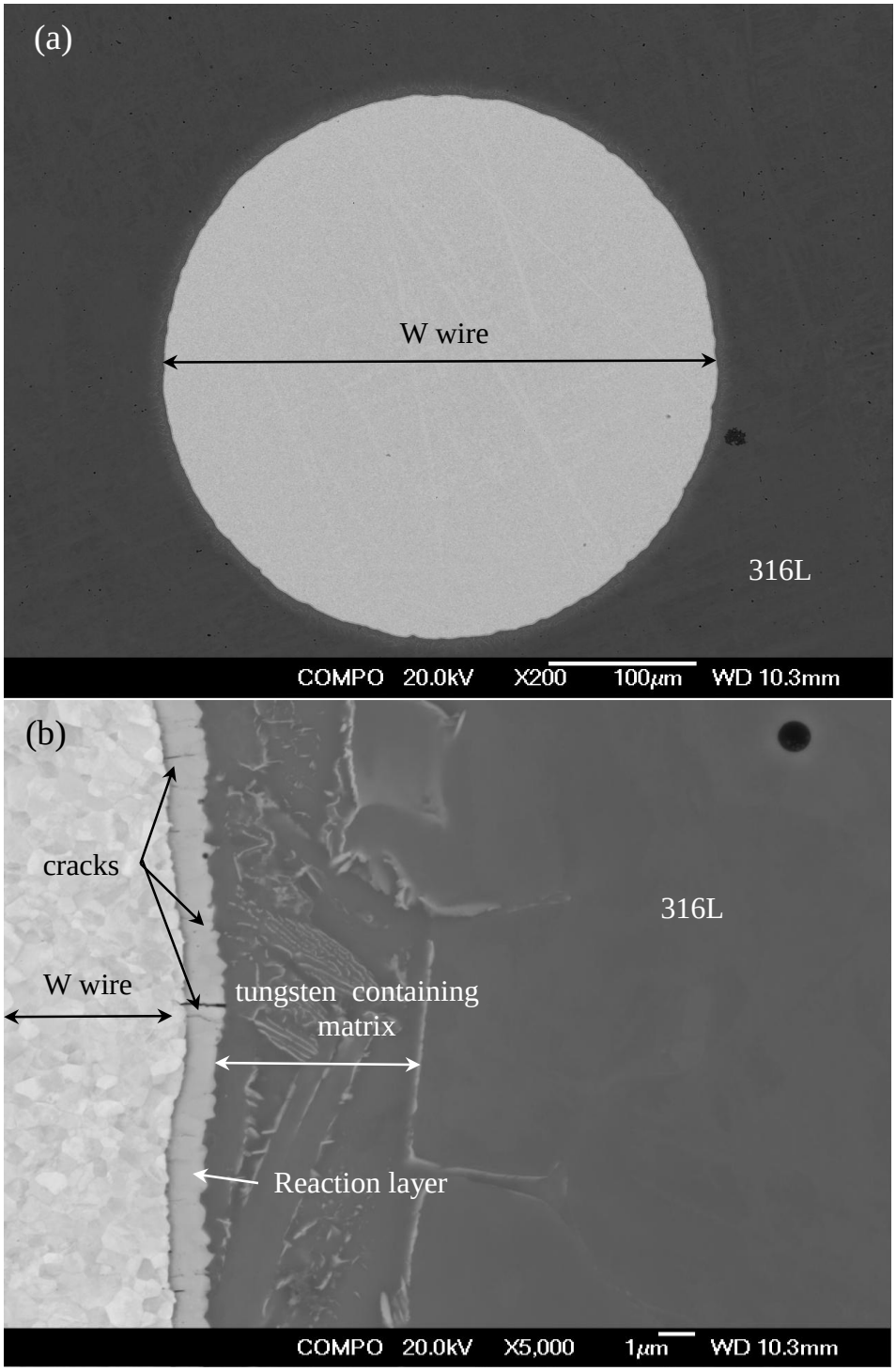

Figure 5.1: (a) General appearance of tungsten wire in 316L matrix in the as-cast composite. (b) Microstructure of the reaction zone showing presence of a reaction layer and matrix region around the wire with altered microstructure.

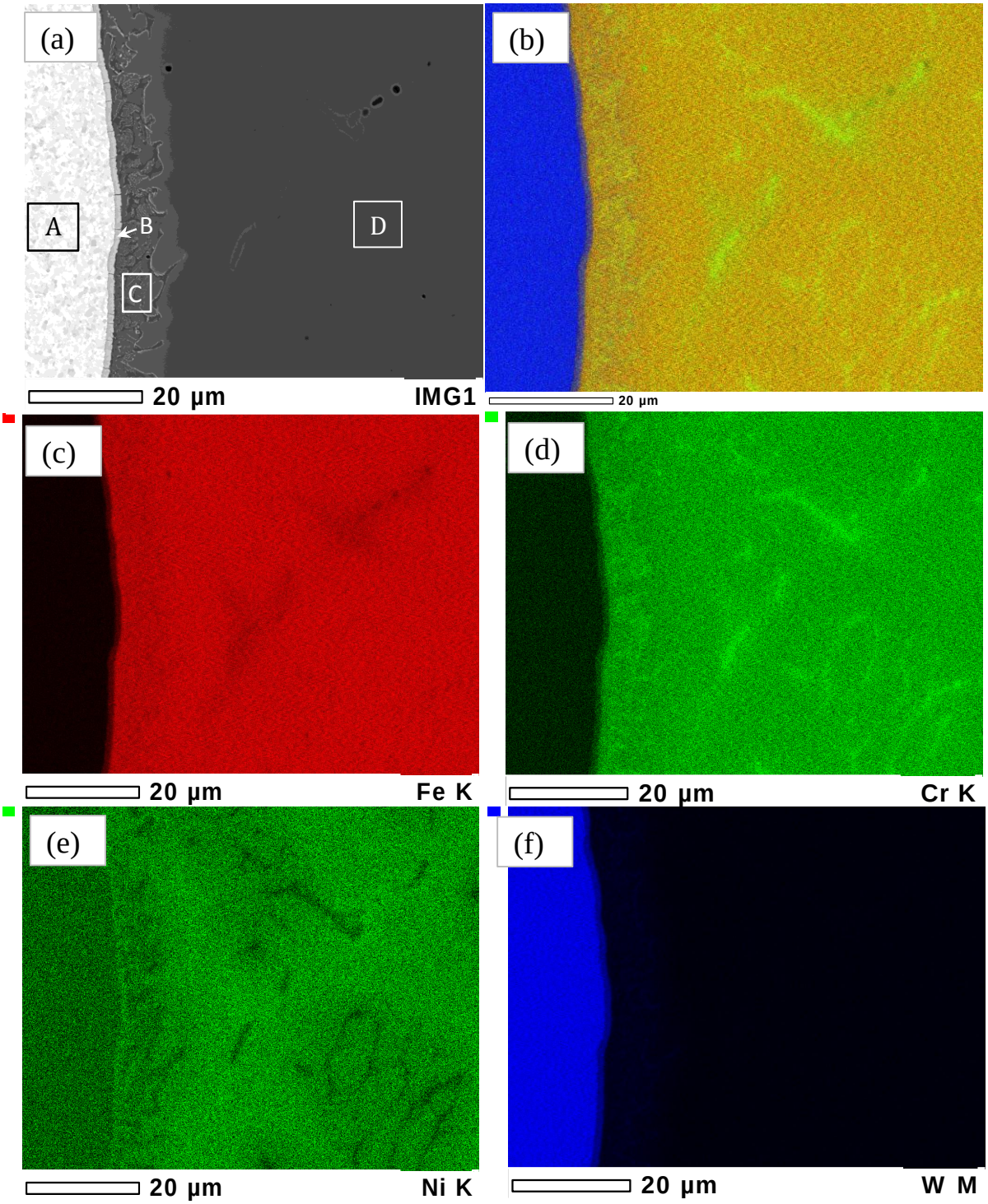

Figure 5.2: Scanning electron micrograph and the X-ray maps showing elemental distribution in the as-cast W/316L composite: (a) BSE image, (b) composite image formed by superimposing X-ray maps of Fe (red), Cr (green), and W (blue). (c), (d), (e), and (f) are the coloured X-ray maps of Fe, Cr, Ni, and W, respectively.

Chemical composition of regions A, B, C and D (shown in Figure 5.2(a)) was determined by EDS. Typical EDS spectra from these regions are shown in Figure 5.3. The spectrum from the W wire (location A) consists of all the peaks originated from L and M shells of W only and no peak corresponding to other elements is present in this spectrum. In the spectra from the locations B, C and D, the major X-ray peaks correspond to K_α and K_β lines of Fe, Ni and Cr. Additionally, there are weak Mo L_α peaks present in the spectra collected from these locations. The results of quantitative analysis of these spectra from reaction layer (location B), W containing matrix (location C) and matrix region away from the reaction zone (location D) are shown in Table 5.1.

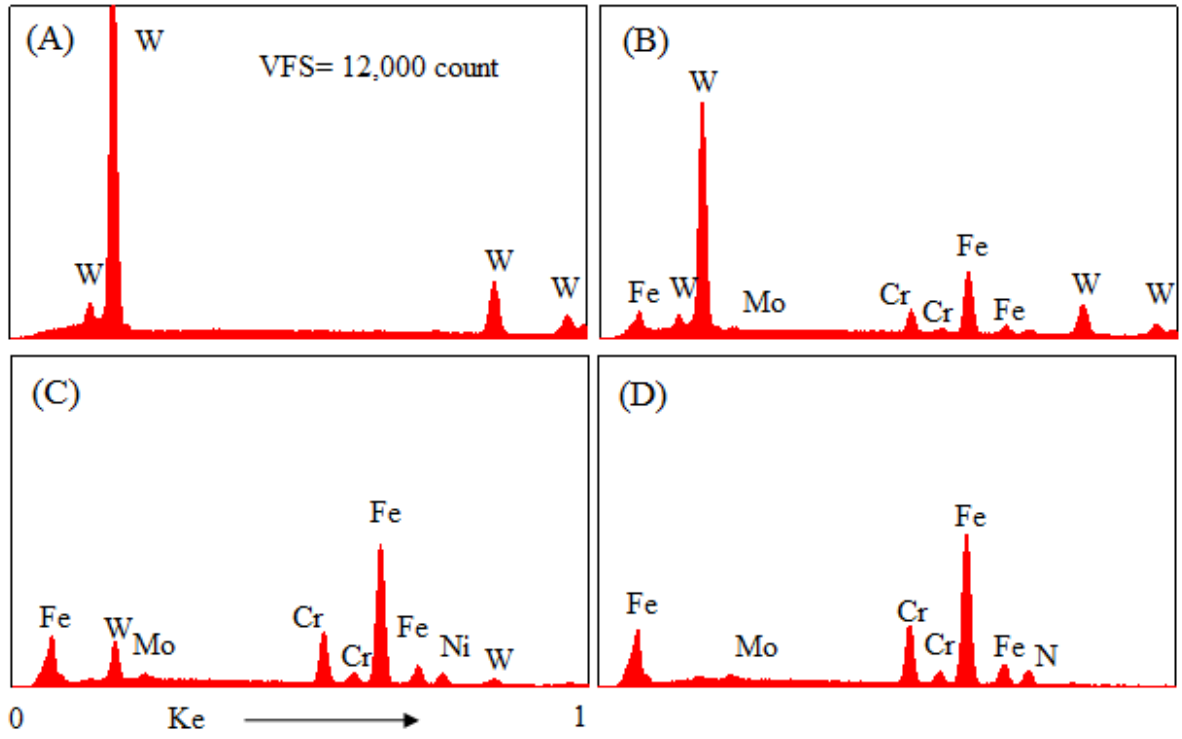

Figure 5.3: X-ray spectra collected from the regions A (tungsten wire close to the reaction layer), B (reaction layer), C (altered matrix adjacent to reaction layer/matrix interface) and D (matrix away from reaction zone) in Figure 5.2(a).

Table 5.1: Chemical composition in various regions (Figure 5.2 (a)) of as-cast W/316L composite. Error is standard deviation of five measurements. The deviations below 0.05 are not reported.

Region	Composition (wt.%)					
	Cr	Mn	Fe	Ni	Mo	W
B	6.7 ±0.4	0.3 ±0.0	28.4 ±1.5	2.5 ±0.3	1.5 ±0.3	60.8 ±2.2
C	14.2 ±0.2	1.0 ±0.1	62.4 ±0.2	8.1 ±0	1.5 ±0.3	12.9 ±0.4
D	16.8 ±0.7	1.4 ±0.2	70.3 ±1.0	9.9 ±1.3	1.4 ±0.4	0.6 ±0.4

For the identification of crystal structure of the reaction layer, EBSP were collected from the layer and analysed as per the procedure described in section 4.5. A typical pattern and its indexing is shown in Figure 5.4. Out of the phases listed in Table 2.2, the acquired EBSP matched well with μ-phase with a mean angular deviation equal to 0.52[14]. This phase has a rhombohedral close-packed structure with 39 atoms/unit cell and space group 166. Its lattice parameters are in the range- a=4.76-4.79Å, c=25.57-25.59Å.

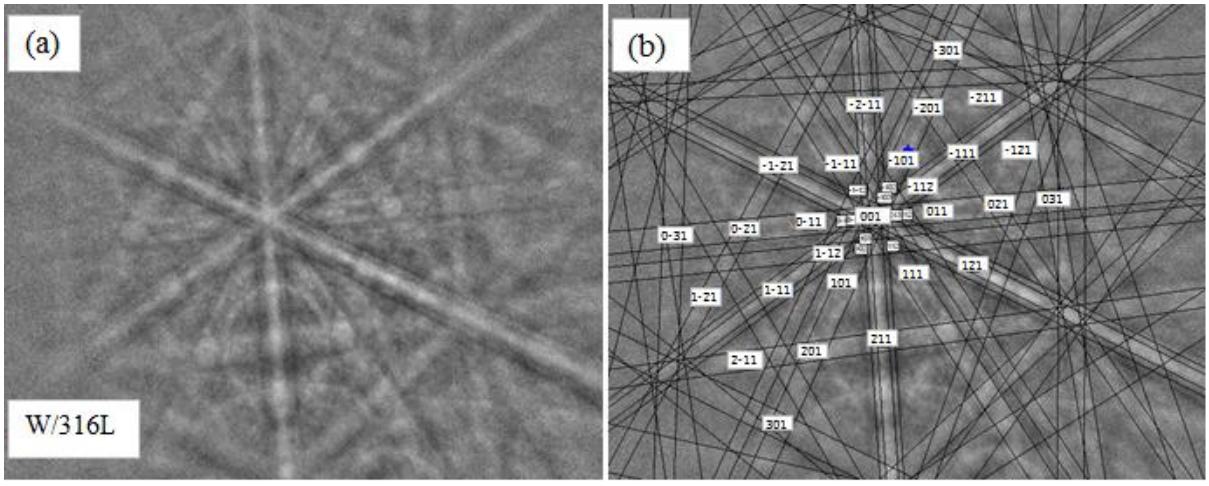

Figure 5.4: (a) Typical EBSP collected from the reaction layer of the composite (b) Indexing shows that the pattern is consistent with μ-phase. The mean angular deviation between the experimental and simulated pattern is 0.52°.

[14] In EBSD phase identification, Mean Angular Deviation (MAD) is the goodness of fit of the solution that specifies average angular misfit between acquired and simulated pattern. It is represented in degree and smaller number signifies better matching. A number less than 1° is acceptable for most systems.

According to the Fe-W phase diagram [75], the stoichiometric formula for μ-phase is Fe_7W_6 but it exists over a range of composition which, for W, ranges from 42.1-44.5 at. %.

On the basis of reaction layer composition given in Table 5.1, the atomic ratio in the layer is 12.3Cr:0.6Mn:49.2Fe:4.2Ni:1.5Mo:32.1W. Using this and considering crystal structure similarities between Cr, Mo, W (BCC) and Fe, Ni, Mn (FCC), the formula for μ-phase can be written as $(Fe, Ni, Mn)_{54}$ $(Cr, Mo, W)_{46}$, which is very close to the stoichiometric formula Fe_7W_6. Therefore, it seems probable that the reaction layer in the composite is isomorphous with μ-phase with generalized formula M_7N_6, where M stands for Fe, Ni, Mn and N for Cr, Mo and W.

5.2.1.2 Diffusion Annealed Composites

Samples from the fabricated W/316L composites were diffusion annealed at temperatures 900-1200°C for time ranging from 25-500 hours. The microstructure of the composites after 500 hours annealing at 900°C is shown in Figure 5.5. There is relatively slow growth of the intermetallic layer at this temperature as it has grown to approximately 4 μm thickness (initial thickness was ~2μm) after annealing for 500 hours. However, W-rich precipitates have formed near the intermetallic layer in the matrix region, which had supersaturated with W during the casting process.

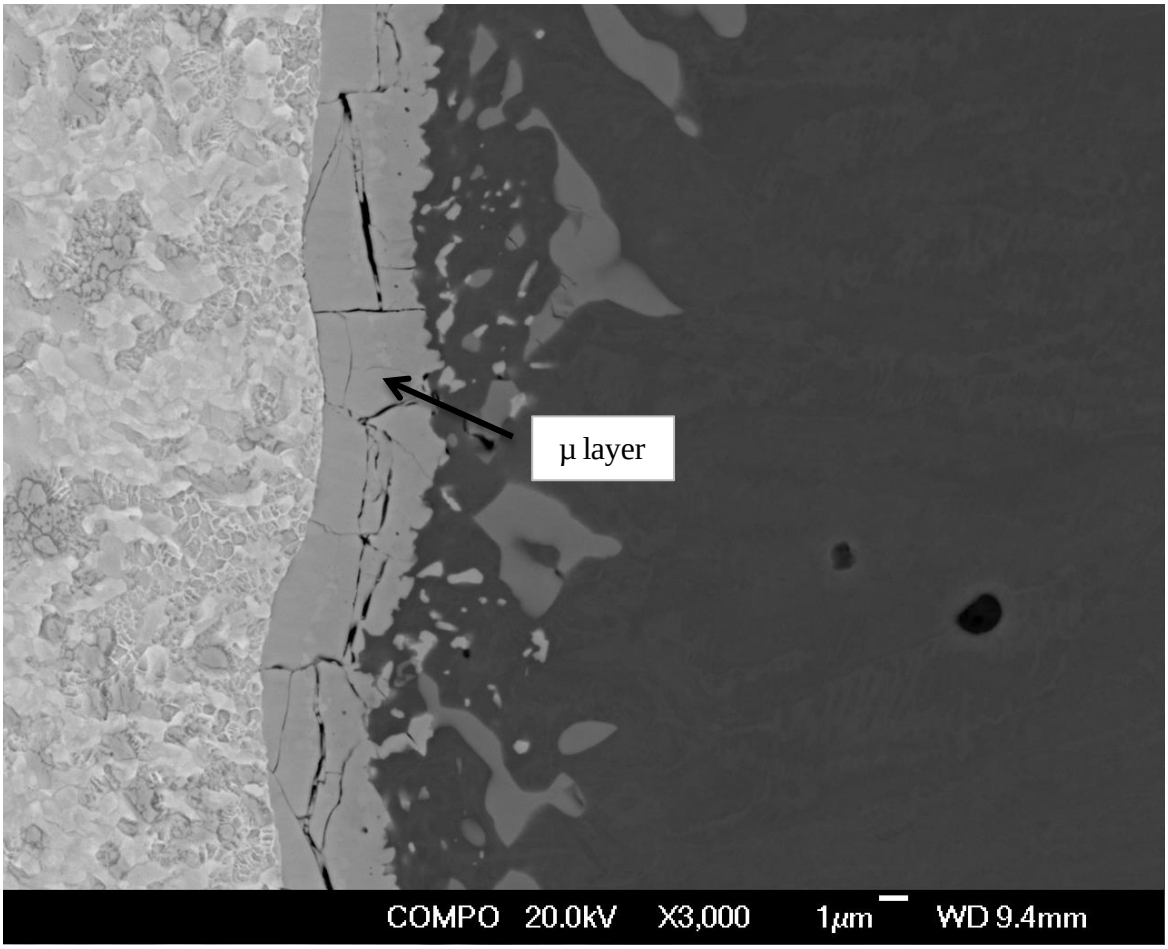

Figure 5.5: Microstructure of the W/316L composites after 500 hours diffusion annealing at 900°C.

Diffusion annealing of the composites at higher temperatures (1000-1200°C) caused substantial changes in the microstructures of the reaction zones (Figure 5.6). The developed intermetallic layers consumed all the precipitates that were seen at shorter diffusion annealing times. The intermetallic layers contain substantial cracking. The voids that appear at the layer/matrix interface in the composites are likely to be due to Kirkendall effect. With the increase in annealing temperature, these voids coalesced and caused debonding between W wire and stainless steel matrix (Figure 5.6(c) and (f)).

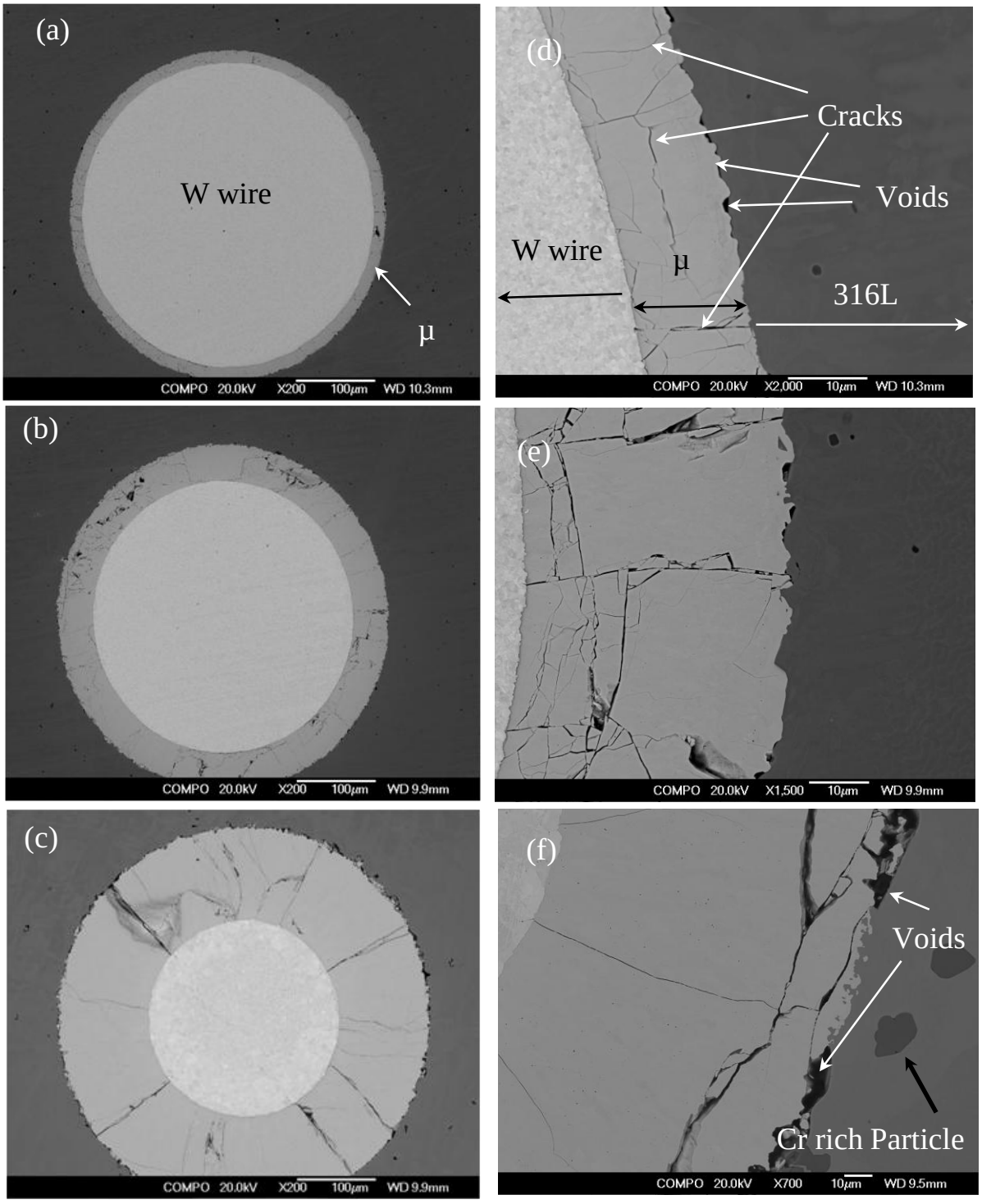

Figure 5.6: Microstructure of diffusion annealed W/316L composite samples: (a, b, c) full wire view inside the matrix after 500 hours annealing at 1000, 1100 and 1200°C, respectively. (d, e, f) corresponding magnified images around the reaction layers.

The X-ray maps of Cr, Fe, Ni and W in the composites annealed for 500 hours at 1000, 1100 and 1200°C are shown in Figures 5.7 to 5.9. The reaction layers consist of one phase only as there is no observable Z contrast on the layers at all the temperatures.

Chemical composition of the reaction layers in annealed composites was determined by EDS and is plotted in Figure 5.10. All the layers have quite similar W contents of 64-66wt.%. Comparison of the layers' composition show that in the diffusion annealed composites the layers have more W and less Fe than in the as-cast composites. The crystal structure identification by EBSD on these layers confirmed that they are isostructural with μ-phase. A typical EBSP from the reaction layer and the indexed pattern are shown in Figure 5.11.

Few Cr-rich particles (shown by arrows in Figure 5.9 (a)) appear near the reaction layer/matrix interface in the composite at 1200°C. These particles were subjected to EDS analysis and a typical spectrum is shown in Figure 5.12. The spectrum shows Al, Cr, O and V peaks. The presence of O indicates that these particles are likely to be Cr based oxides. Crystal structure of these particles could not be identified using EBSD. This was because of a complex oxide phase whose crystal structure information was not present in the software database.

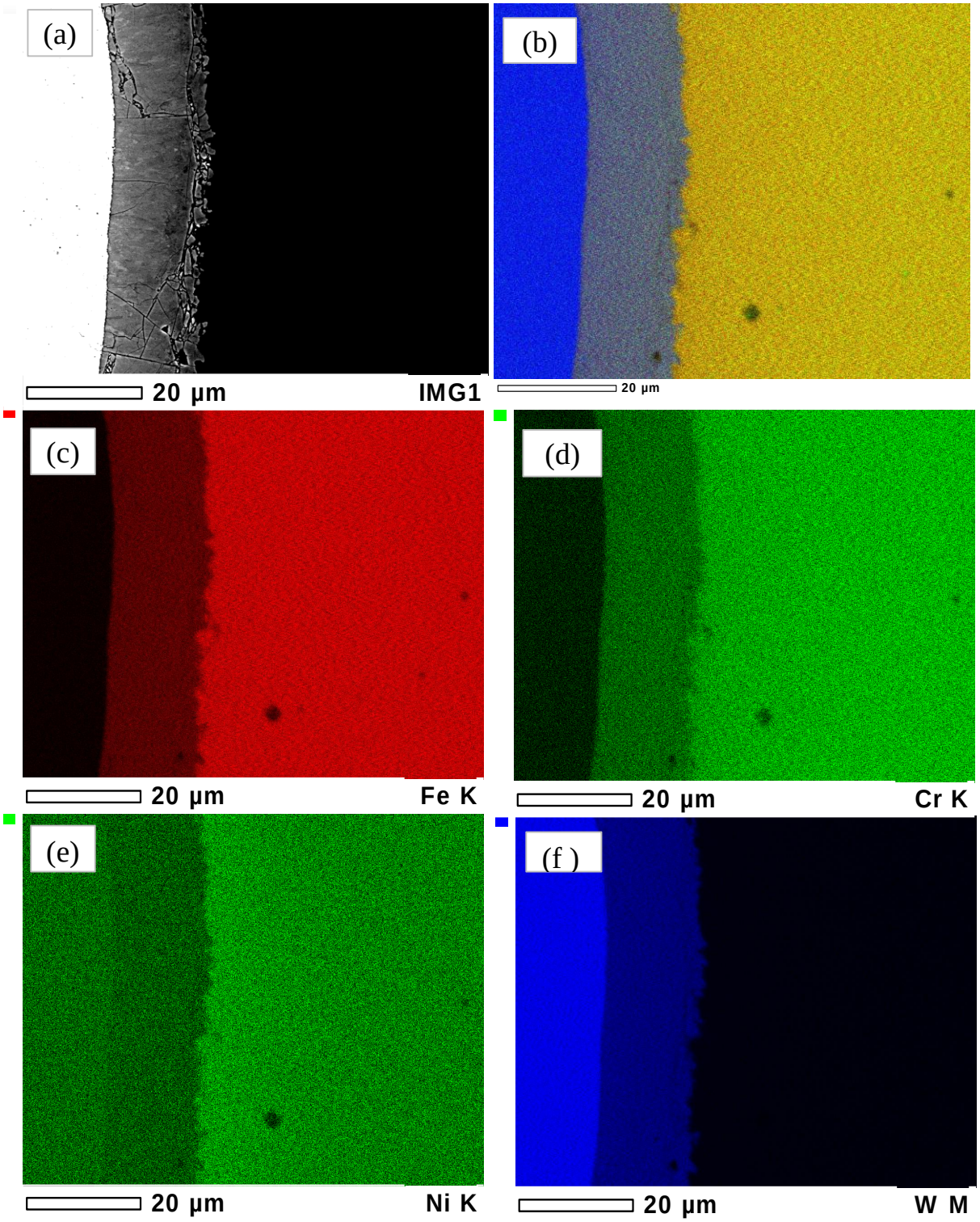

Figure 5.7: (a) BSE image, and (b) colour composite image of 1000°C/500hours annealed W/316L sample. (c), (d), (e) and (f) are the X-ray maps of Fe, Cr, Ni and W.

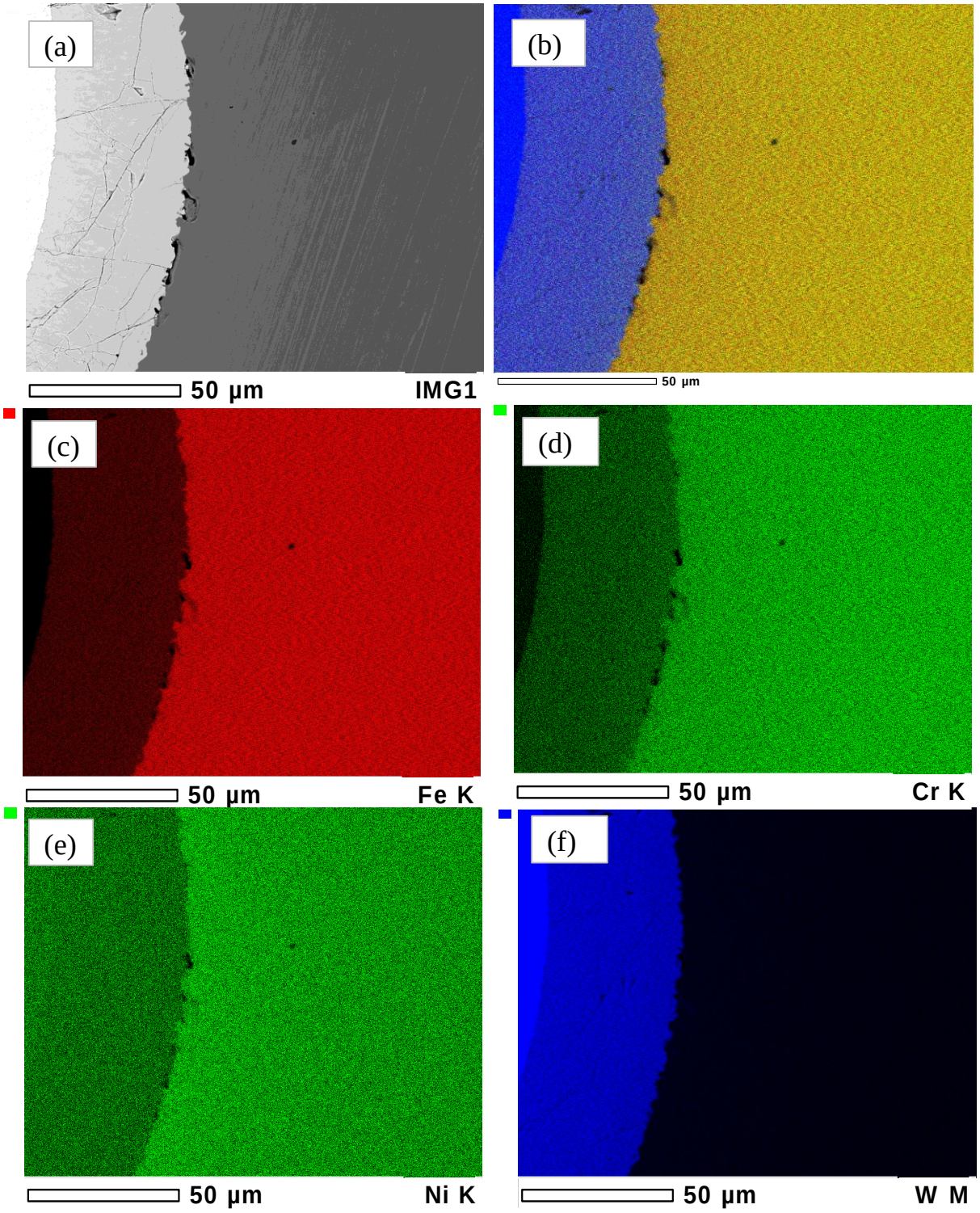

Figure 5.8: (a) BSE image, and (b) colour composite image of 1100°C/500hours annealed W/316L sample. (c), (d), (e) and (f) are the X-ray maps of Fe, Cr, Ni and W.

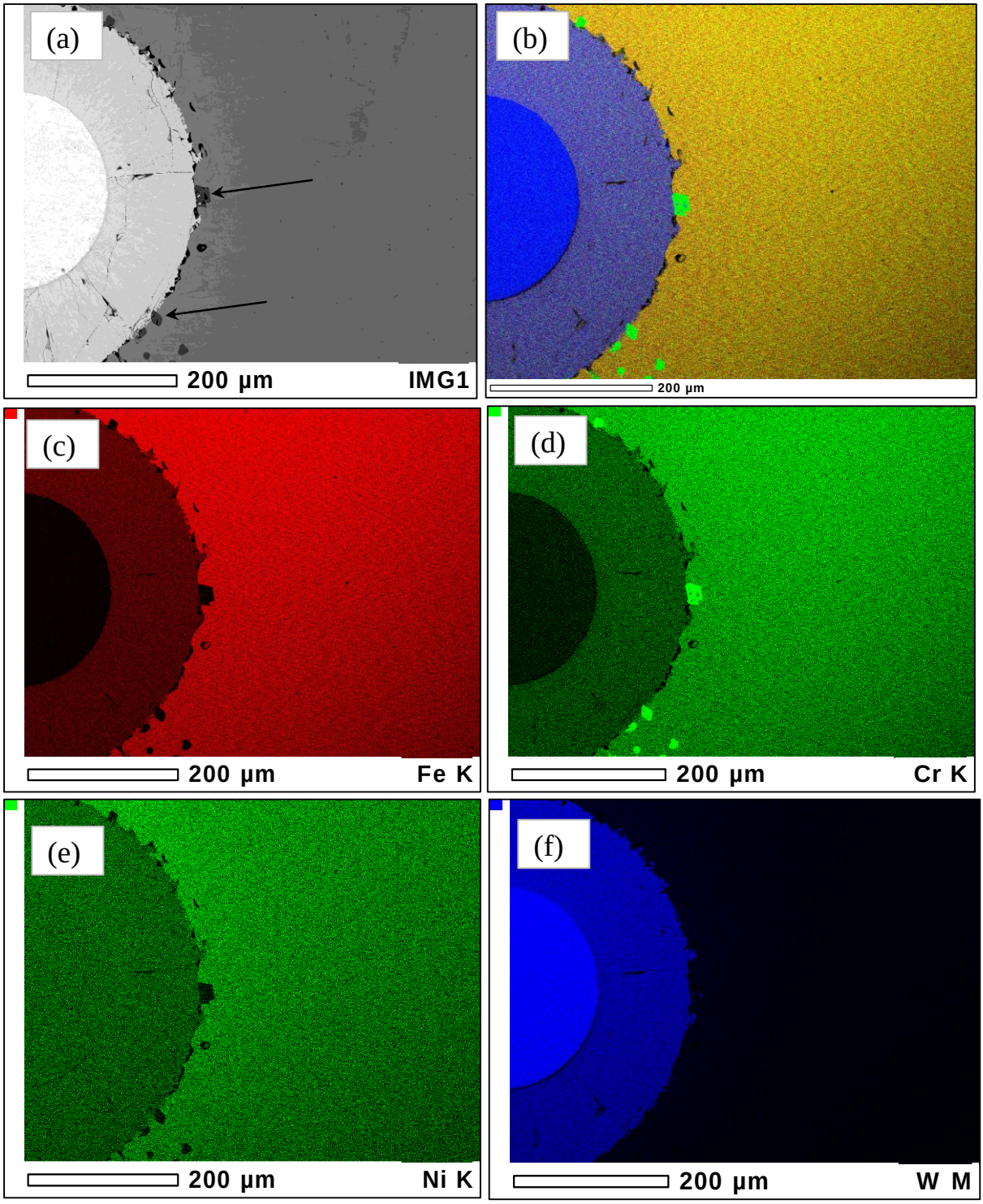

Figure 5.9: (a) BSE image and (b) colour composite image for 1200°C/500hours annealed W/316L sample. (c), (d), (e) and (f) are the X-ray maps of Fe, Cr, Ni and W.

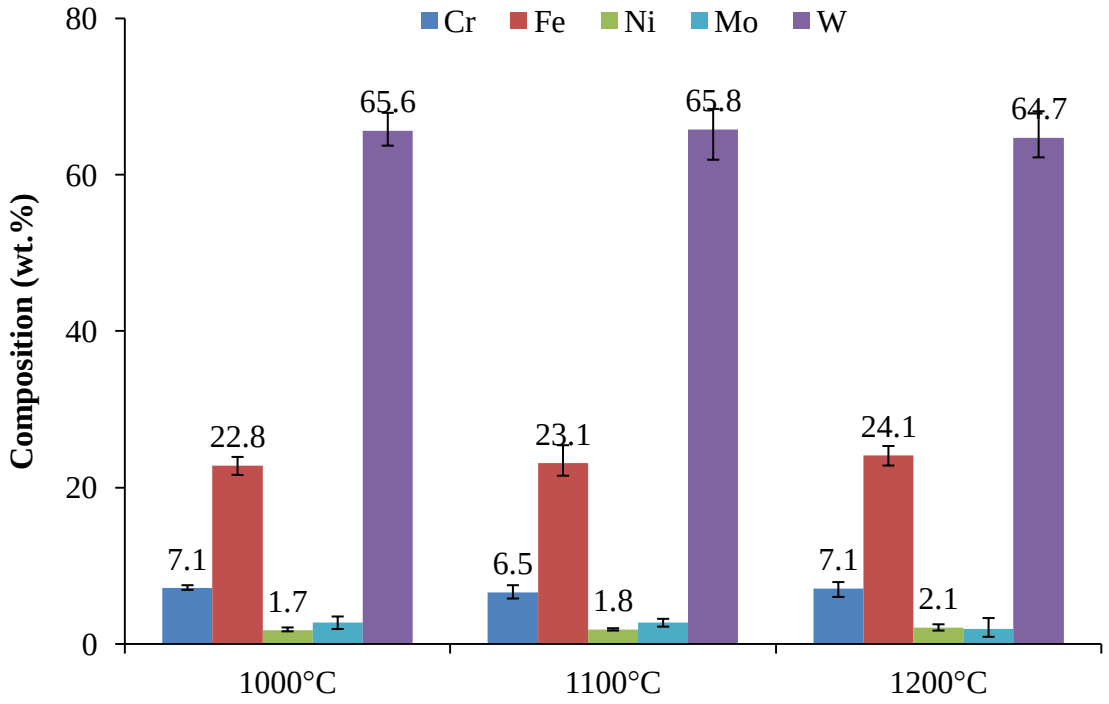

Figure 5.10: Chemical composition of the reaction layers in the composites annealed for 500 hours at different temperatures. Error bars represent composition range (maximum and minimum) for 10 measurements.

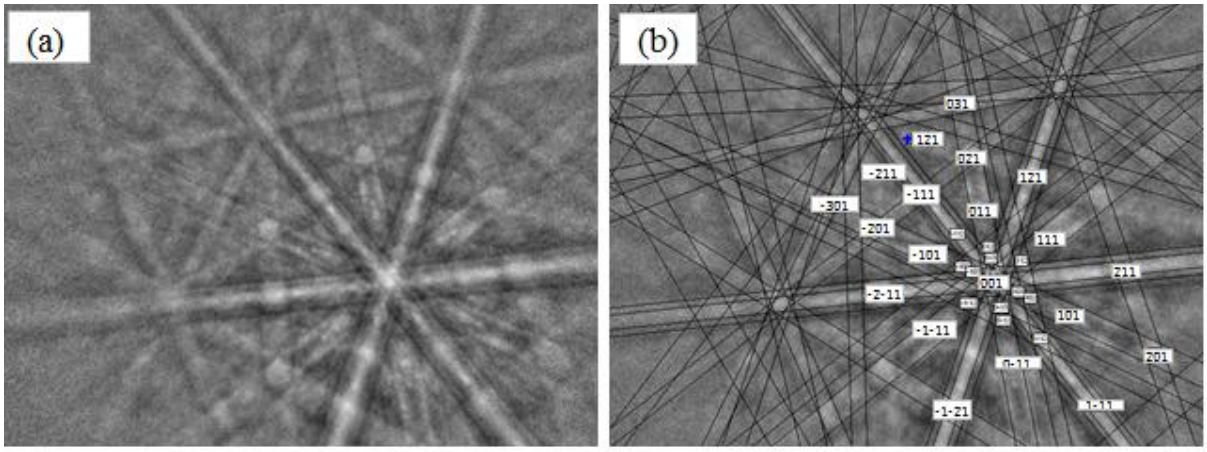

Figure 5.11: (a) Acquired electron backscattered pattern from the reaction layer and (b) simulated pattern of μ-phase superimposed on the collected pattern. The mean angular deviation between the acquired and simulated patter is 0.46.

	Composition (wt.%)			
O	Al	V	Cr	Mn
	1.5±0.7	1.6±0.2	48.1±3	27.6±2.4

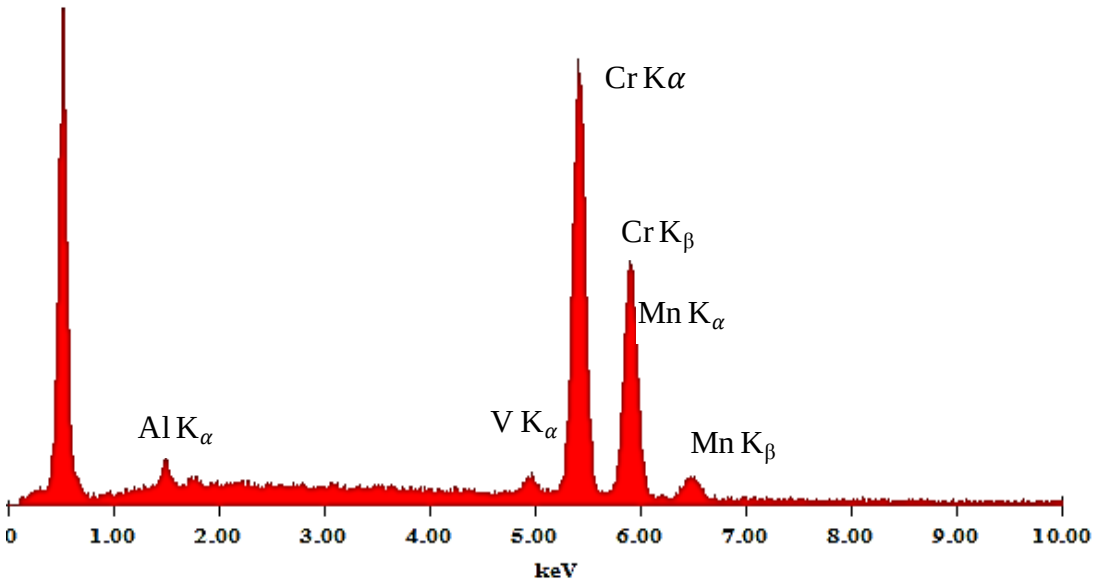

Figure 5.12: EDS spectrum obtained from Cr-rich phase in 1200°C/500hours diffusion annealed composite. Composition of various elements in the phase is given in the inset table.

5.2.1.3 Microstructure of μ-phase Reaction Layer

The microstructure of the reaction layer in 1200°C/500hours annealed composite is shown in Figure 5.13. The layer consists of fine grains with a complex morphology. There are twinned grains within the layer that formed during the diffusion annealing treatment. The BSE images show grains with orientation contrast (shown by black arrows in Figure 5.13(b)) in the intermetallic layer. Another noticeable characteristic in the microstructure of the intermetallic layer is the presence of small (< 1 μm) spherical voids (represented by white arrows in Figure 5.13(b)). These voids are randomly distributed within the reaction layers.

The exact cause of the twin formation in the intermetallic layer is not clear. These twins in the present case may be due to the large mismatch in coefficient of thermal expansion of W and 316L stainless steel. The mismatch might have induced strain and consequently, mechanical twins in the growing reaction layer. Some other studies have also reported this kind of twinned morphology in binary Fe_7W_6, Co_7Mo_6 and Co_7W_6 versions of the μ-phase [76-78]

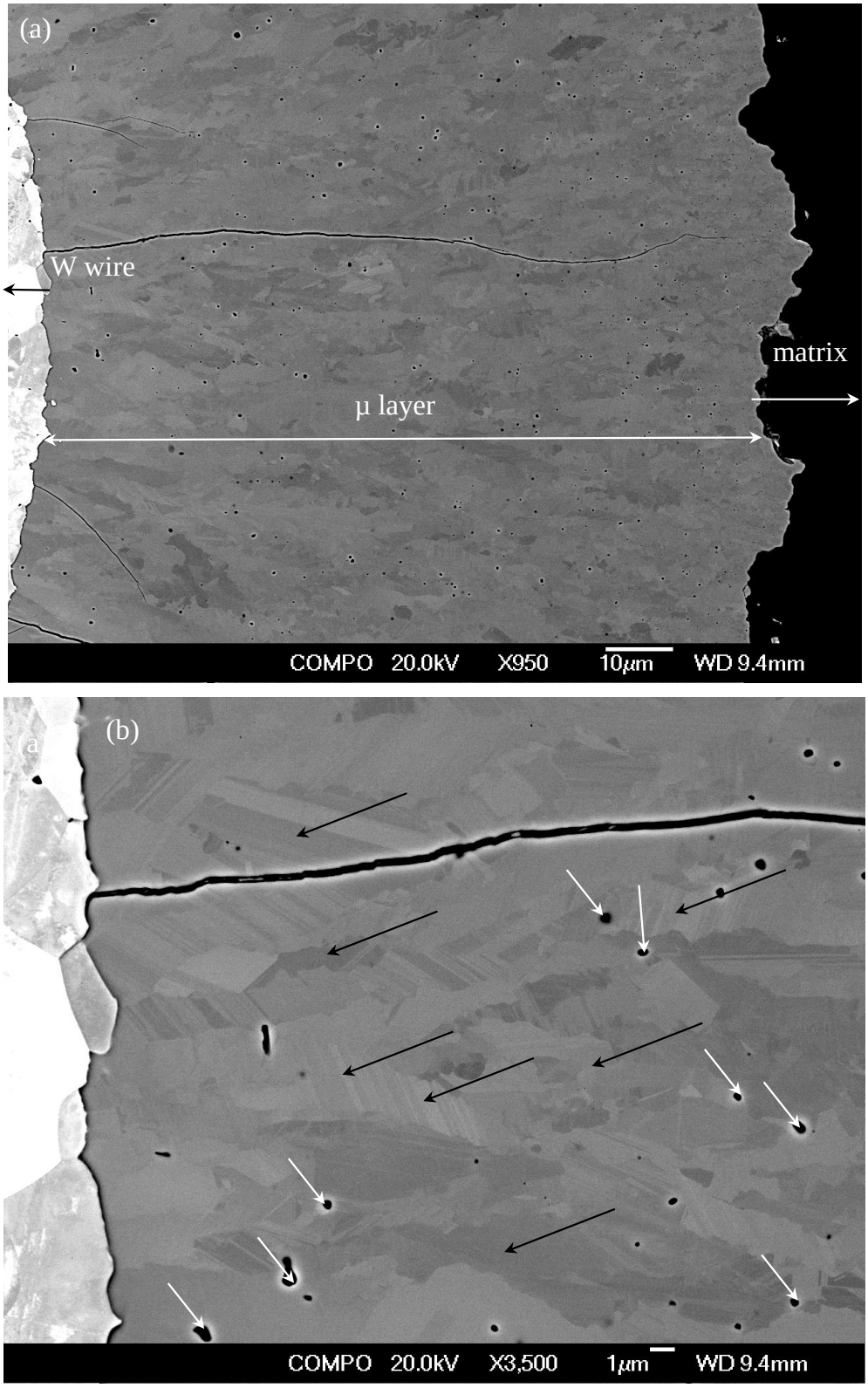

Figure 5.13: BSE images of reaction layer microstructure developed in W/316L during 1200°C/500hours annealing. (a) low magnification image and (b) high magnification image showing twins with orientation contrast (black arrows) and randomly distributed voids (white arrows) in the microstructure.

5.2.2 Growth Kinetics of the Intermetallic Layer

As discussed in Section 3.4, in solid state diffusional transformations the growth of the reaction layers is often parabolic and is described by the relation:

$$x = k\sqrt{t} \qquad 5.1$$

where x is the thickness of the reaction layer (µm) developed in annealing time t (hours) and k is the growth constant (µm/√h).

As per Equation 5.1, a plot of x and $\sqrt{t}$ is shown in Figure 5.14. The resulting linear fits with R^2 values greater than 0.97 in all the cases, suggest that the growth of the intermetallic layer is indeed diffusion controlled in the composite. The growth constants k that characterize the kinetics of the reaction layers at different annealing temperatures were extracted as the slope of the lines from the plots (Figure 5.14). The values of k are given in Table 5.2.

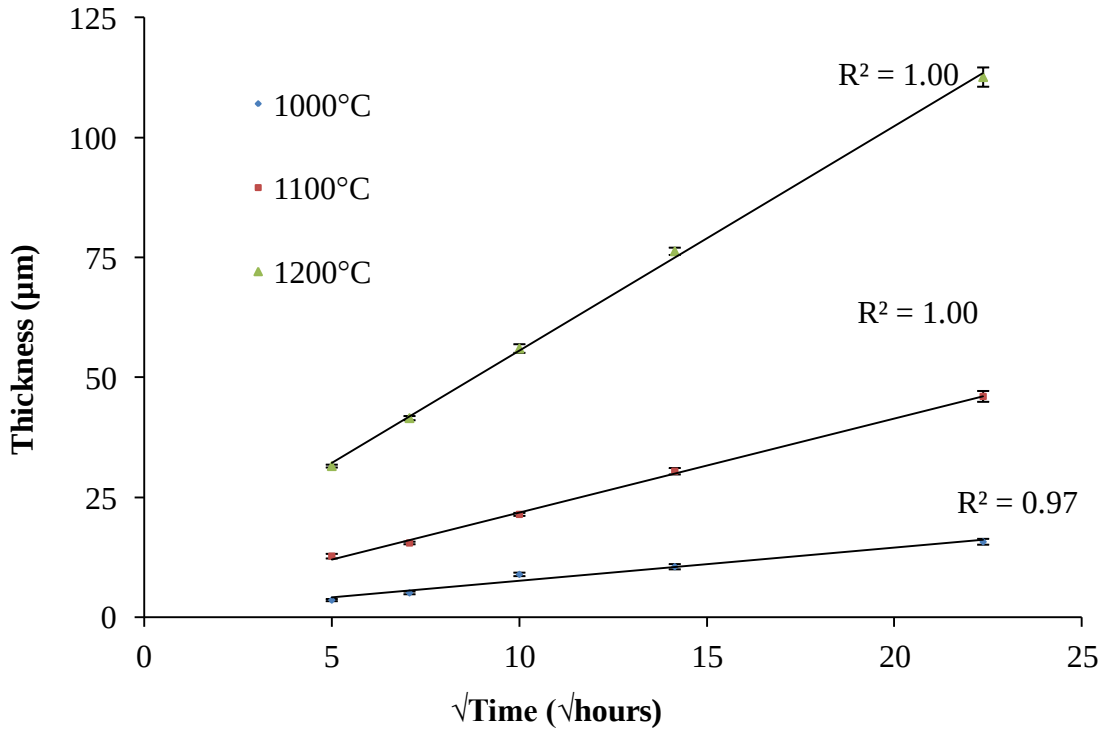

Figure 5.14: Reaction layer kinetics as a function of square root of time at different diffusion annealing temperatures in W/316L composite. The slope of each line is the growth constant at that temperature. Error bars are the standard deviation calculated on 10 measurements on the reaction layers.

Table 5.2: Growth constants of μ-phase intermetallic layers at different temperatures.

Temperature (°C)	k (μm√h)
1000	0.69 ±0.07
1100	1.96 ±0.05
1200	4.68 ±0.07

The activation energy for growth (Q_G) and pre-exponential factor (k_0) in Equation 3.51 were calculated from the temperature dependence of the growth constants. A plot of *lnk* and *1/T* is shown in Figure 5.15. From the plot, the calculated Q_G and k_0 values for μ-phase reaction layer growth are 149 ±1kJmole^{-1}and 9.31E+05 μm√h, respectively.

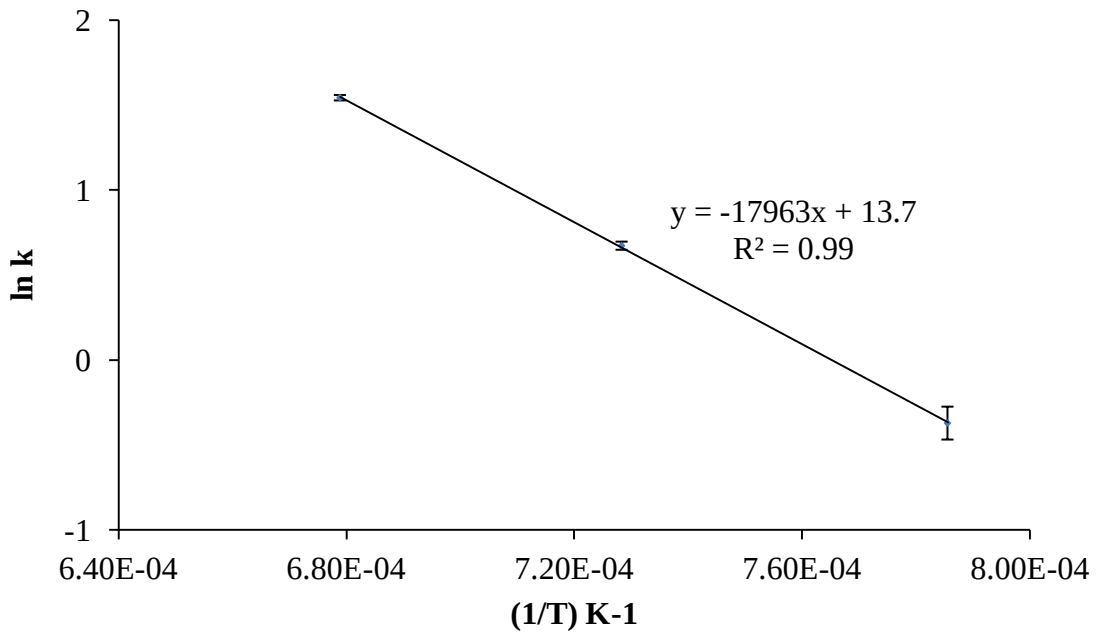

Figure 5.15: Arrhenius plot for μ-phase reaction layer growth constants in W/316L composite.

5.2.3 Interdiffusion Behaviour

5.2.3.1 Composition Profiles

Typical composition profiles acquired across the intermetallic layers in the annealed composite are shown in Figures 5.16-5.18. Depending on the abrupt changes in composition three distinct regions can be identified in these profiles: matrix, reaction layer and W wire. Generally a positive composition gradient of W and a negative gradient of Fe (towards W wire) across μ-phase intermetallic layers are observed in all the composition profiles. Cr profile shows negative composition gradient on the layers at all the temperatures. Positive W gradient suggests its diffusion from the wire to the matrix. Similarly Cr and Fe diffuse from matrix to the wire. The Ni composition in the intermetallic layers seems to be constant at all the annealing temperatures. This indicates its limited solubility in μ-phase. In the composition profiles, localised variation in elemental composition of the reaction layers was observed. However, only single intermetallic phase μ was identified on the entire reaction layers in the diffusion annealed composites.

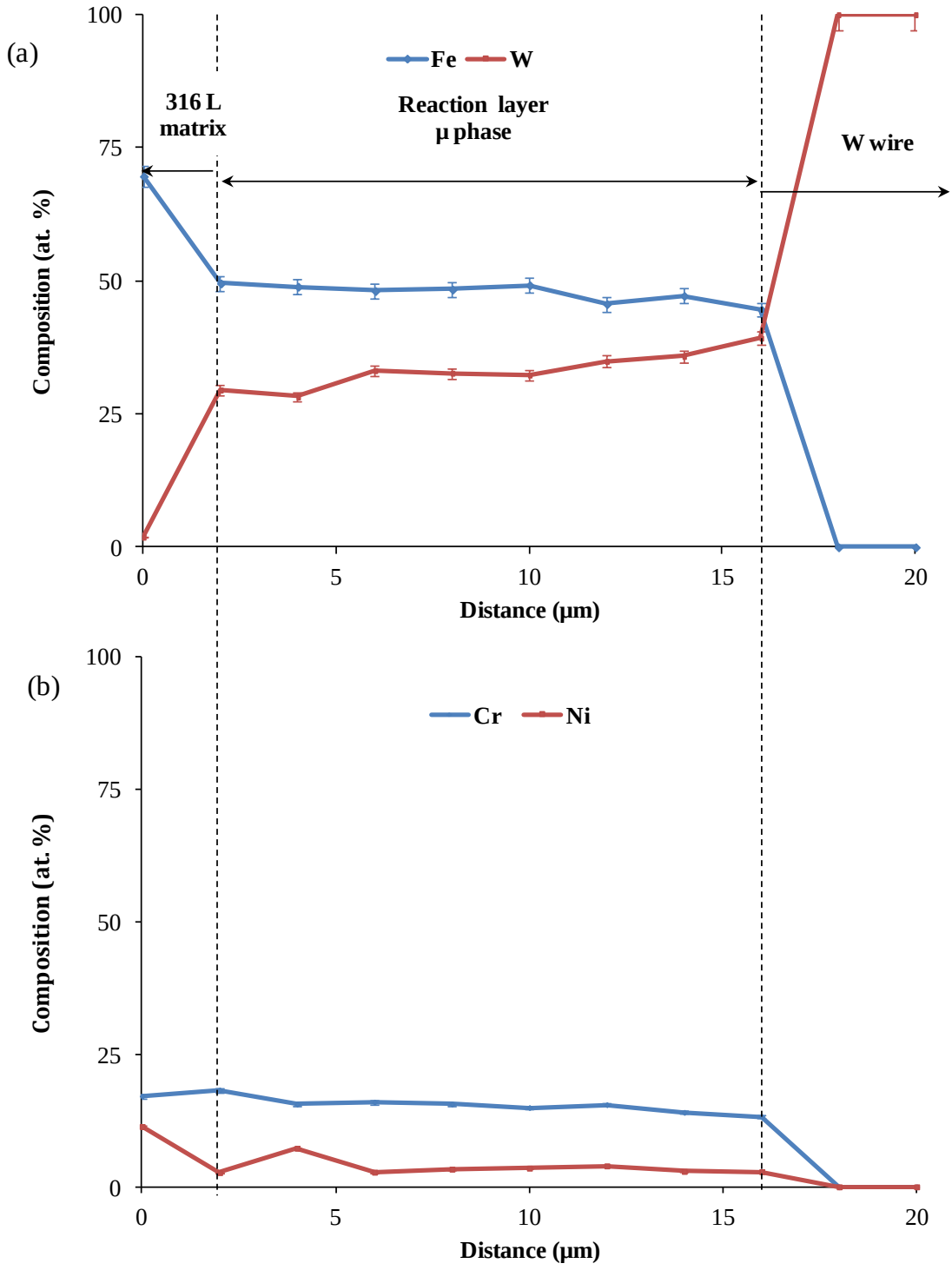

Figure 5.16: Composition profiles of (a) Fe, W and (b) Cr, Ni in W/316L composite diffusion annealed at 1000°C/500hours. Error bars represent ±2% relative error[15].

[15] In all the composition profiles in this thesis, error bars represent ±2% relative error which is typical error in EDS measurements.

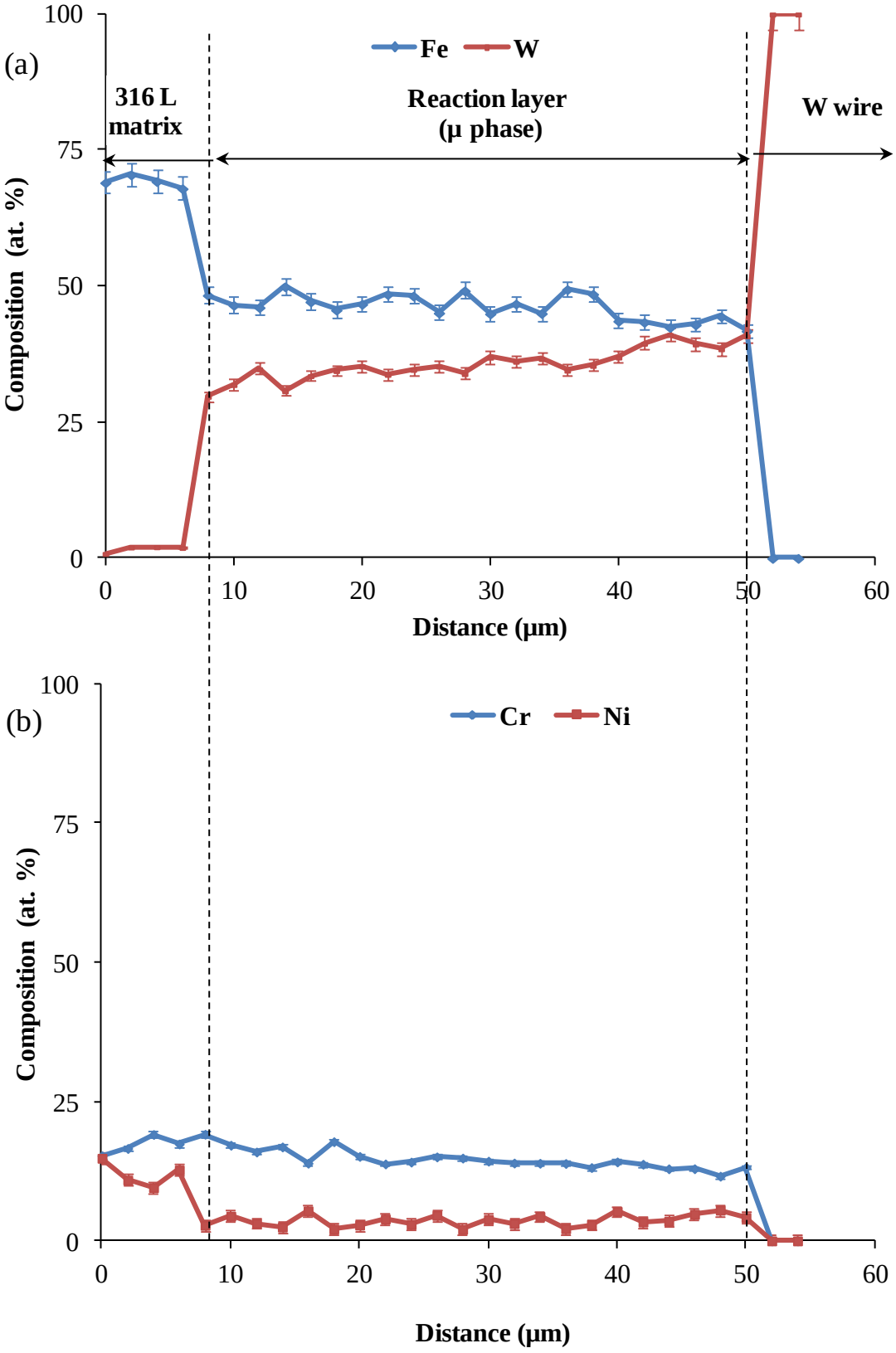

Figure 5.17: Composition profiles of (a) Fe, W and (b) Cr, Ni in W/316L composite diffusion annealed at 1100°C/500hours.

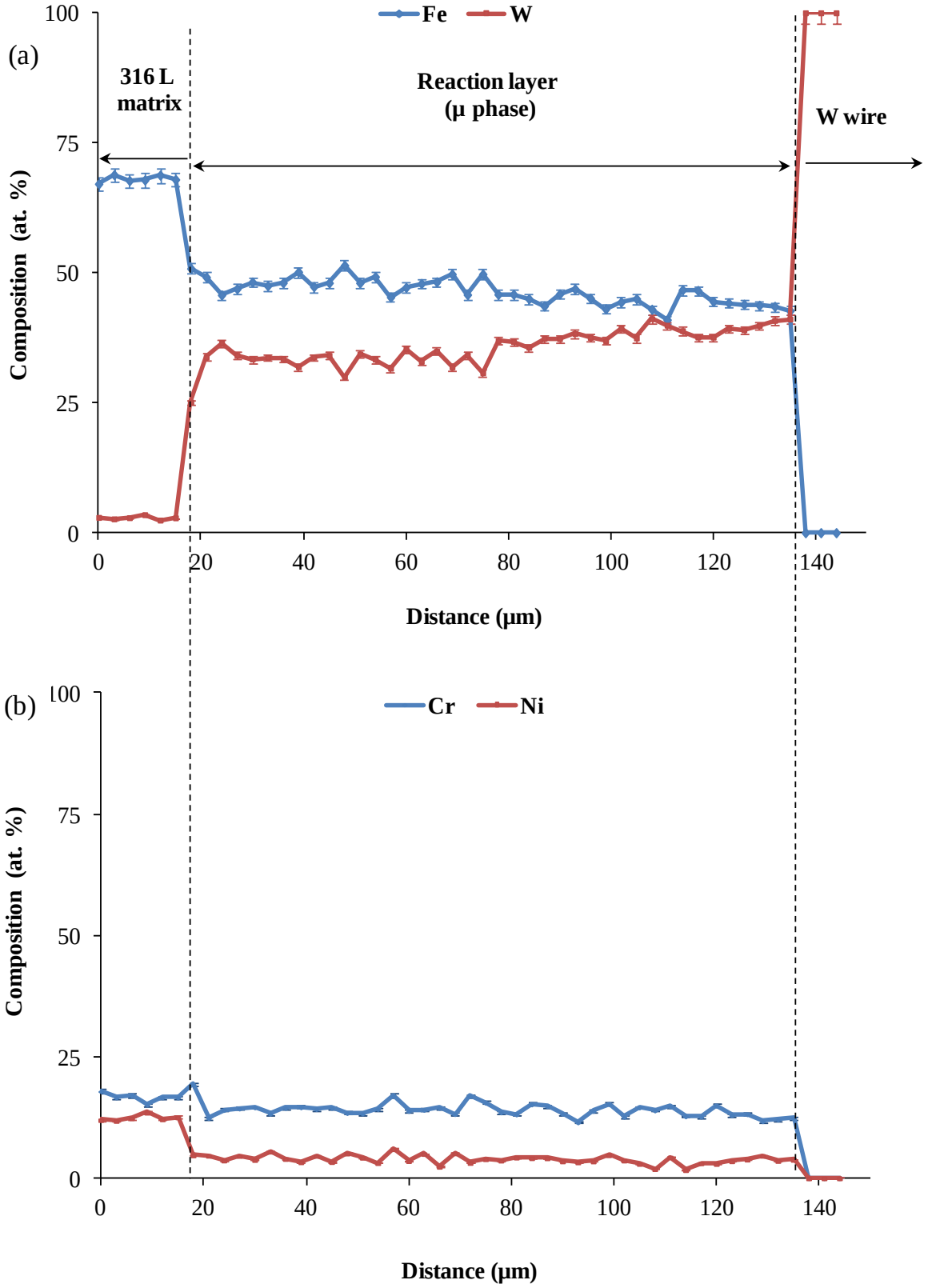

Figure 5.18: Composition profiles of (a) Fe, W and (b) Cr, Ni in in W/316L composite annealed at 1200°C/500hours.

5.2.3.2 Diffusion Coefficients

For the determination of average effective interdiffusion coefficients in μ-phase reaction layers of the composite, the composition profiles were fitted to a line. An example of the fitting for 1200°C/500hours annealed W/316L is given in Figure 5.19 below. The goodness of fit (R^2) values obtained for these plots are 0.16, 0.54, 0.15 and 0.64, respectively for Cr, Fe, Ni and W.

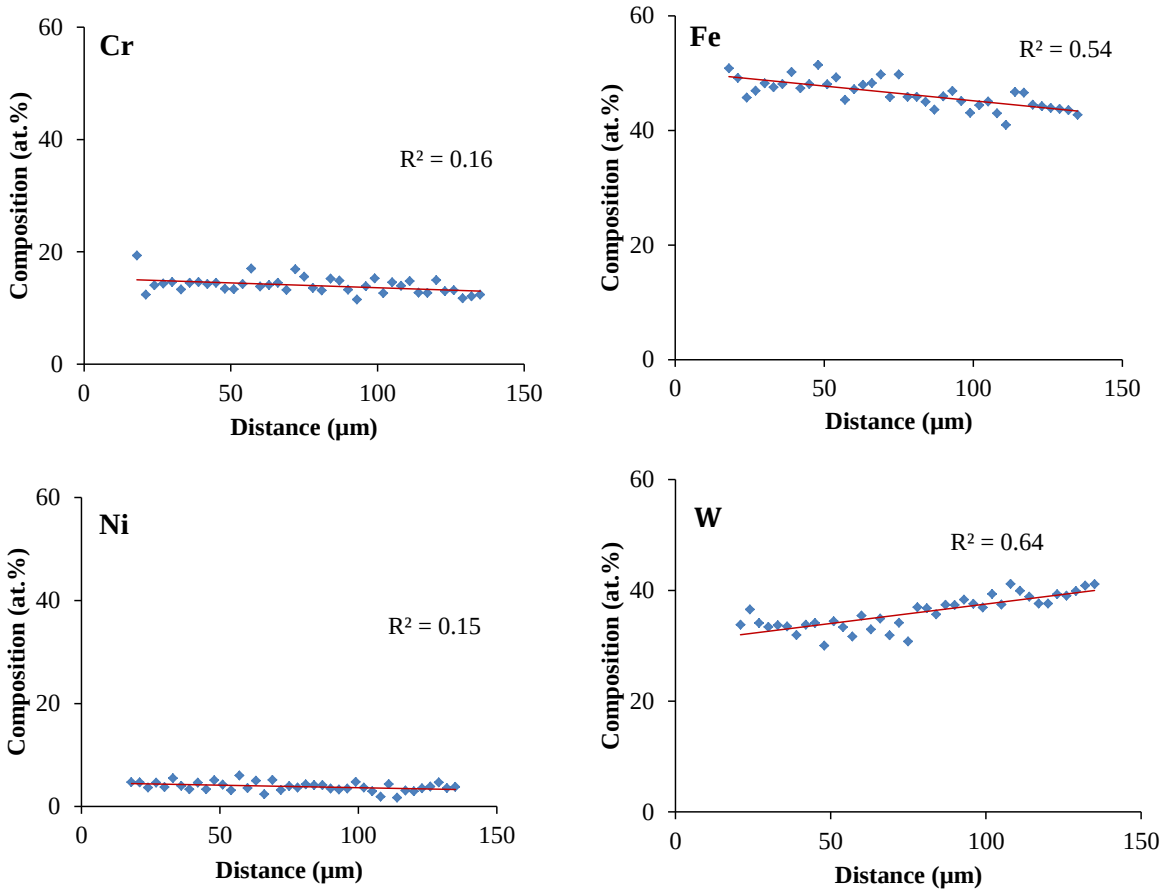

Figure 5.19: Linear fitting of the composition profiles in the μ-phase intermetallic layer of 1200°C/500hours diffusion annealed composite.

R^2 is an indication of association between the independent and dependent variables and it greatly depends upon the scatter of data points and population of data set. It measures the variation of the observed values around the mean that is explained by the fitted regression model. There is no threshold value for R^2 to tell us what low value is significant in order to prove a linear relation between the dependent and independent variables. Therefore, another statistical test, Analysis of Variance Fischer (ANOVA F), which is a better predictor of the linear relationship between the data points, was used in current study to select the linear

composition profiles for diffusion calculation. The detailed description of the test is given in Appendix B. Based on the test, the profiles that did not show a linear trend between the data points were excluded from further analysis.

The data points on the selected composition profiles were converted to concentration (C_i) using molar volume (V_m) of the respective components of the composites by:

$$C_i = \frac{N_i}{V_m} \qquad 5.2$$

where N_i is the composition of the element i in mole fraction.

The V_m of the reaction layer phase was calculated from the available crystal data [35] using the relation, $V_m = \frac{V_{cell}}{n} \times A_N$, where V_{cell} is the volume of cell containing n number of atoms and A_N is Avogadro's number. The calculated V_m for W, μ, and γFe (for matrix region) are 9.78, 7.84 and 8.00 cm^3 $mole^{-1}$, respectively. Due to the unavailability of data on composition dependence of V_m, it was assumed constant for each phase.

Following this, $\widetilde{\overline{D}}^{i}_{\text{eff }(\mu)}$ in the intermetallic layers of the composite were calculated for Cr, Fe, Ni and W using the method described in Section 3.3.2. Calculated values of $\widetilde{\overline{D}}^{i}_{\text{eff }(\mu)}$ show little dependence on the composition within the reaction layers of the composites. Therefore, average values of $\widetilde{\overline{D}}^{i}_{\text{eff }(\mu)}$are shown in Table 5.3. In most of the cases, these values are average of $\widetilde{\overline{D}}^{i}_{\text{eff }(\mu)}$calculated on two composition profiles for each diffusion condition. The values for Ni at 1000 and 1100°C were not calculated because all the corresponding composition profiles were rejected in ANOVA F-Test.

Table 5.3: $\overline{\widetilde{D}}^{i}_{eff\,(\mu)}$ of various elements in the reaction layers of W/316L composite.

Temperature (°C)	$\overline{\widetilde{D}}^{i}_{eff\,(\mu)}$ (m^2/s)			
	Cr	Fe	Ni	W
1000	1.61E-17	2.05E-16	--	1.29E-16
1100	3.98E-16	1.33E-15	--	1.01E-15
1200	4.25E-15	1.84E-14	8.42E-15	1.19E-14

We can see that in the intermetallic layer, $\overline{\widetilde{D}}^{Fe}_{eff\,(\mu)}$ and $\overline{\widetilde{D}}^{W}_{eff\,(\mu)}$ have same order of magnitude at all the diffusion annealing temperatures. $\overline{\widetilde{D}}^{Cr}_{eff\,(\mu)}$ and $\overline{\widetilde{D}}^{Ni}_{eff\,(\mu)}$ are one order of magnitude lower than Fe and W at 1200°C. Cr is the slowest diffusing element in W/316L reaction layers in 1000-1200°C.

The temperature dependence of $\overline{\widetilde{D}}^{i}_{eff\,(\mu)}$ was investigated by plotting ln $\overline{\widetilde{D}}^{i}_{eff\,(\mu)}$ versus *1/T*. These plots for Cr, Fe and W are shown in Figure 5.20. Fitted straight lines in these plots are consistent with the Arrhenius relation (Equation 3.64) for diffusion.

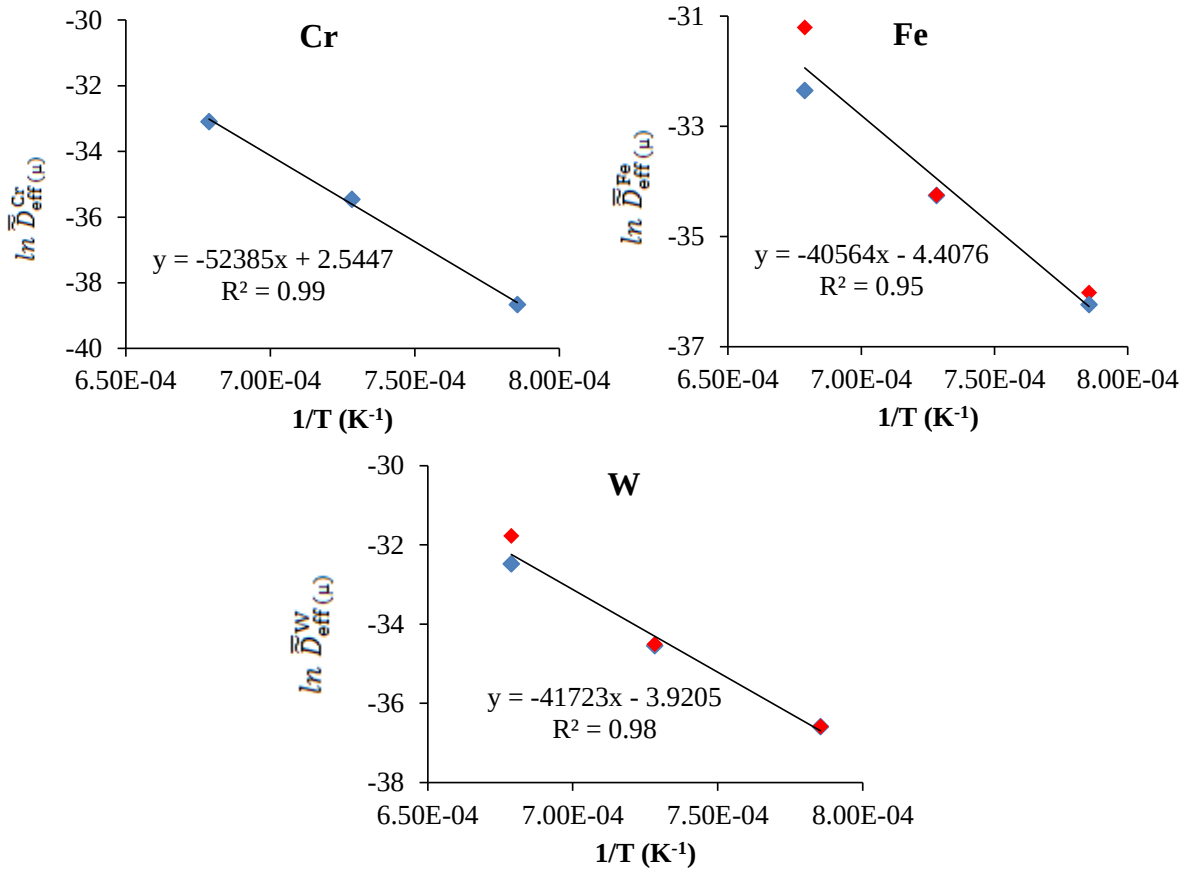

Figure 5.20: ln $\overline{\overline{D}}^{i}_{eff\,(\mu)}$ versus 1/T plots for Cr, Fe, and W in µ-phase reaction layers of W/316L composite annealed in the temperature range 1000-1200°C. Two datasets are plotted (blue and red markers) and fitted to a straight line.

The activation energies (Q_D) of diffusion and pre-exponential factors (D_0) for different elements in the intermetallic layers were calculated from the Arrhenius plots and are listed in Table 5.4.

Table 5.4: Activation energies for diffusion (Q_D) and pre-exponential factor (D_0) of various elements in the µ-phase reaction layers of W/316L composites.

Element	Q_D^i (kJ mole^{-1})	D_0(m^2/s)
Cr	436	1.3E+01
Fe	337	1.2E-02
W	347	2.0E-02

5.3 Discussion

A key result of this study is that an intermetallic layer isostructural with μ-phase evolved in the fabricated composite. 316L stainless steel solidifies with fully austenitic structure which is stable down to room temperature. Interaction of W with the steel alters the phase equillibria and leads to formation of new phases. As listed in Table 2.2, there are several phases that could form due to the interaction of W with stainless steel matrices. In order to fully understand the phase formation and transformation in W/316L, isothermal sections of Fe-Ni-Cr-W phase diagrams at different temperatures are needed which are not available in literature. Also, the phase relationships in the available Fe-Ni-W and Fe-W phase diagrams are not well established and contradictory information about the existence and stability of various phases is reported in literature.

A binary Fe-W phase diagram [75] given in Figure 5.21 shows the existence of three phases between W and Fe: Fe_2W (λ), Fe_7W_6 (μ) and FeW. According to the diagram, μ-phase forms via peritectic reaction, L+W→μ at 1637°C. It also appears from the phase diagram that μ-phase is not stable at room temperature and exists only above 1190°C. Thus, under equilibrium conditions, the only binary Fe-W phases that can exist at room temperature should be Fe_2W and FeW. But, some recent phase diagrams have illustrated the stability of μ-phase at room temperature [79, 80]

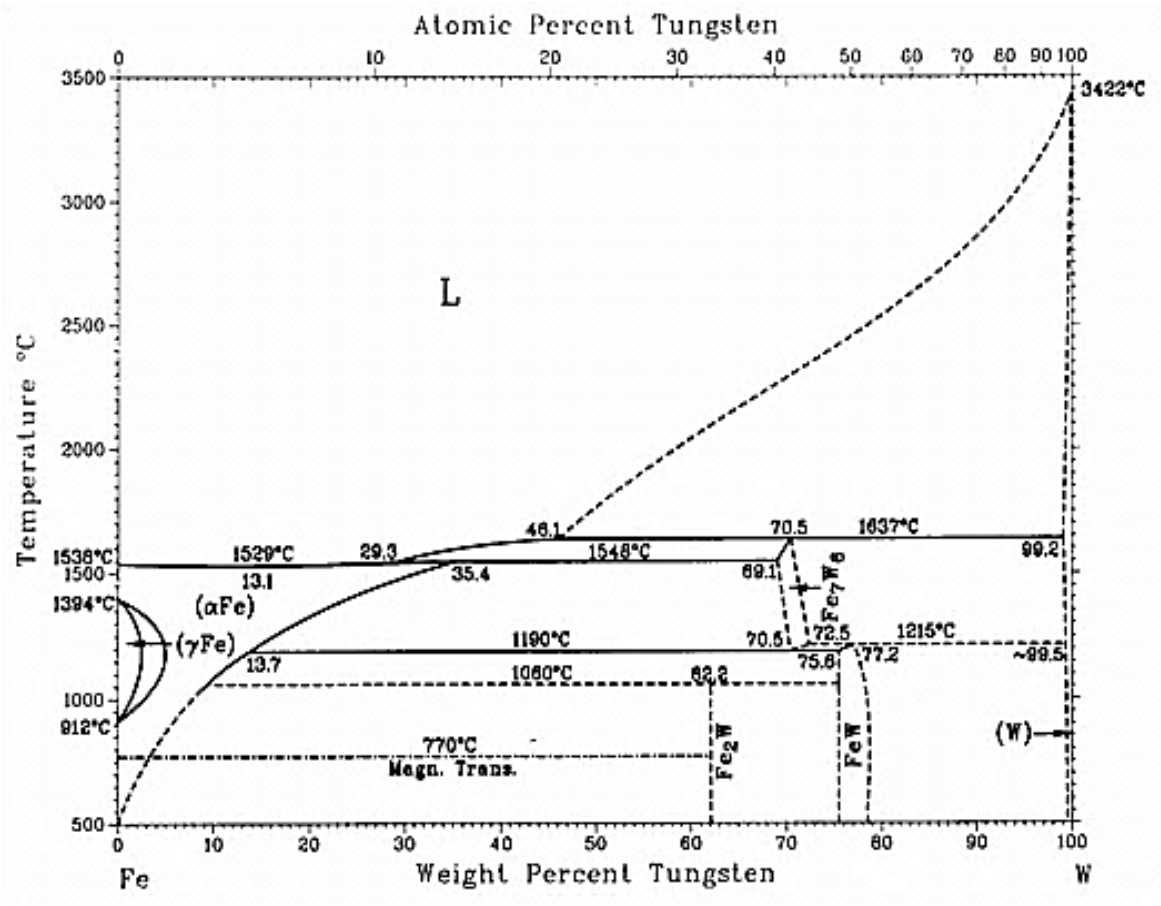

Figure 5.21: Fe-W phase diagram showing presence of three phases in the system [75].

Cr and Ni are the other major alloying elements present in 316L steel that could effect the phase equillibria between Fe and W shown in Figure 5.21. An Fe-Ni-W isothermal section at 1000°C shows [81] the equilibrium phases that co-exist with γ (austenite) are α, μ and W (Figure 5.22). A red line representing the approximate Fe:Ni ratio in the 316L alloy lies across the γ and γ+μ phase fields. This means that formation of μ-phase is probable during diffusion annealing in the temperature around 1000°C.

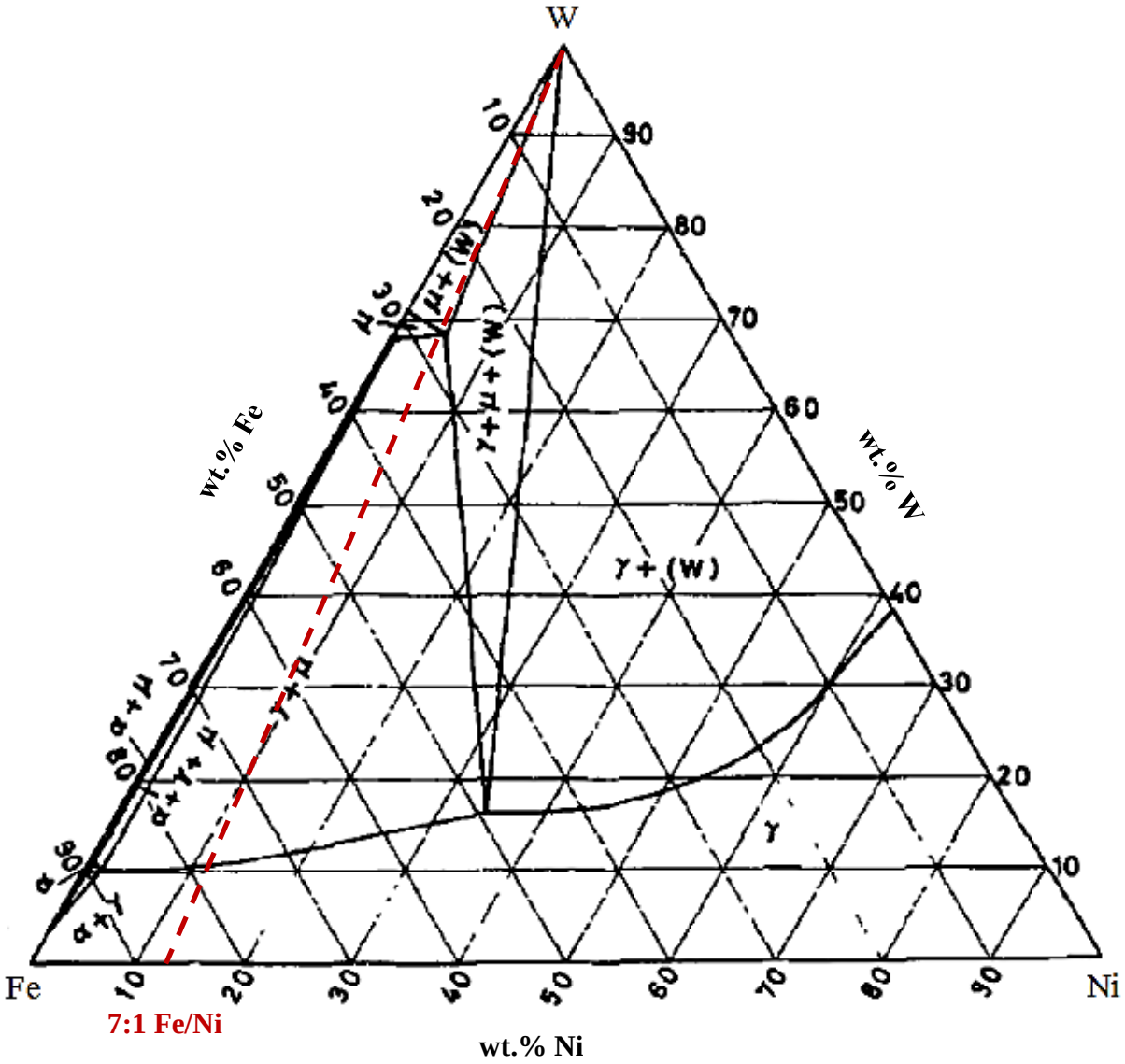

Figure 5.22: Isothermal section of Fe-Ni-W ternary diagram at 1000°C [81]. The dotted red line represents the approximate Fe:Ni ratio in 316L stainless steel.

Because of crystal structure similarities, Cr is expected to substitute for W in the μ-phase reaction layers of the W/316L composite. Although Cr is a ferrite stabilizer, addition of Ni in 316L results in fully austenitic structure at room temperature. Therefore, the effect of Cr on Fe-Ni-W phase equillibria can be thought of pushing the boundary between γ and other phases toward Fe-Ni side of the isothermal sections of Fe-Ni-W phase diagram.

Past studies on some W wire reinforced high temperature composites, such as W/304SS, W/KOVAR and W/INCOLOY 903, have reported the formation of only μ-phase in the

reaction layers of these composites [26, 65], although there is remarkable contrast in the composition of these matrix alloys. This suggests that the μ-phase can be stable at room temperature and can have complex multi-elemental composition.

The reaction layers formed in W/316L contain a large number of cracks and an increase in the number of cracks was observed at higher annealing temperature. Such type of cracked layers have also been reported in some past studies on W/superalloy matrices [27]. Authors usually related the cracks to large thermal expansion mismatch between reinforcement and matrix phase of the composites. Actually, a combination of three factors can contribute to the crack formation in W wire reinforced 316L composites. These are (i) volume change during phase transformations, (ii) differential thermal expansion of the phases of the composites during heating and cooling and (iii) the lack of ductility in the reaction layers due to presence of intermetallic phase.

The stress state in the reaction layer can be assessed by determining the ratio of volume of the reaction layer formed to the volume of the matrix constituents consumed to form the layer. This ratio known as Pilling-Bedworth ratio is generally used to determine the nature of stresses in oxide layers formed due to oxidation of metals, but has also been used to determine the nature of stresses in the formation of intermetallic coatings [82]. The molar volumes (V_m) of W wire and the developed μ-phase reaction layer are 9.78 and 7.84 $cm^3 \cdot mole^{-1}$, respectively. The calculated value of $\frac{V_m^{\mu}}{V_m^{W}}$ is 0.8. Since the ratio is <1, tensile stresses will set up in the reaction layer. The thermal expansion coefficient of austenitic stainless steels is approximately four times greater than that of W (19.5×10^{-6} $°C^{-1}$ from 20-1000°C for 316 stainless steel and 4.5 - 5.7 $\times 10^{-6}$ $°C^{-1}$ from 20-1200˚C for W) [66, 83]. During cooling after fabrication and diffusion annealing, a large magnitude of thermal strain results due to the thermal expansion mismatch. Since $\alpha_{matrix} > \alpha_{reinforcement}$, the matrix would tend to contract more than the reinforcement upon cooling. This will set up compressive stresses in reinforcement and tensile stresses in the matrix. These stresses acting on the brittle reaction layers can cause multiple cracking on them. At higher diffusion annealing temperature, a thicker layer will be experiencing the thermal stresses, giving rise to increased number of cracks on the layer.

Formation of voids observed at the reaction layer/matrix interface at high temperatures may take place either by matrix contamination or differences in the diffusivities of the diffusing

species (Kirkendall effect). Similar kind of voids have also been reported in W/316 composites fabricated by powder metallurgy method [65]. Authors attributed the void formation to insufficient binder burn off during sintering of the composite. Due to the different fabrication method employed, the composites in the present case were free from such type of contamination. Therefore, the voids most likely formed due to Kirkendall effect. The formation of voids in the matrix region implies that movement of Cr, Fe and Ni to the layer/matrix interface was faster than the movement of W to the matrix. In a previous study, the values of Q_D for the bulk diffusion of Cr^{51}, Fe^{59}, Ni^{57} tracers in Fe-15Cr-20Ni alloys have been reported [84] as 309, 308, 300 kJ $mole^{-1}$, respectively (in temperature range 960-1400°C). In the present study, calculated value of Q_D for W diffusion in the reaction layer is 347 kJ $mole^{-1}$, which is higher than Q_D of matrix elements in γ. This is consistent with the concept that the diffusion of matrix elements to the layer/matrix interface was faster compared to the W diffusion through the reaction layer to the layer/matrix interface, thus resulting in the formation of voids in the matrix adjacent to reaction layer/matrix interface.

It has been discussed in section 3.4 that when using Equation 3.66, the calculated Q_G should be half of that $2Q_D$. The value $2Q_G$ = 298 kJ $mole^{-1}$ obtained in present study is lower than the Q_D vales for Cr, Fe and Ni (Table 5.4). The reason for this discrepancy is that the growth of reaction layer does not only depend on the diffusivity of elements in the layer. Two other factors that strongly affect the growth kinetics of reaction layers are composition gradient on either side of the interfaces of the growing layer and its solubility limit with the phases it is growing from. Therefore, the activation energy derived from growth constants will have a complex meaning and its value will not always be half of Q_D in the growing layer [85]. Q_G is useful empirically and can be used to compare growth kinetic of the phases [59].

The ultimate aim of reinforcing stainless steels with W wires is to develop a composite with improved creep strength compared to its unreinforced counterparts. This study has demonstrated that a brittle reaction layer grows in W/316L composite during the course of diffusion annealing. Also, the growth of this intermetallic layer is accompanied by a decrease in the volume fraction of the W wire (and corresponding increase in volume fraction of brittle interphase in the composite) which would be the main creep strengthening phase in the composites. Both these interrelated factors - brittle intermetallic layer growth and corresponding decrease in the W wire volume fraction would make the W/316L composite unsuitable for creep resistant applications in the studied temperature range. The purpose of

choosing high diffusion annealing temperatures in this study was to have accelerated growth kinetics, but 316L stainless steel is never used in service at these high temperatures. The steel resists oxidation up to 800°C, but its service temperature is limited to 650°C only. Above 650°C, its falling strength limits its use [86]. Annealing experiments have shown that μ-phase reaction layer growth at 900°C was very sluggish in W/316L composite. The growth could be negligible at lower temperatures (<900°C) suggesting that there is room for increasing current service temperature of 316 stainless steel by reinforcing it with W. But, the initial layer thickness formed during composite fabrication and precipitates formation at the intended service temperature can still degrade composite properties. Therefore, in order to envisage commercial applicability of W/316L, creep testing of the composites is required to study the effect of initial reaction layer thickness on the properties of W/316L composites.

5.4 Summary

The microstructure evolution in the diffusion zone of as-cast and diffusion annealed W/316L composites was investigated. The growth kinetics and average effective interdiffusion coefficients were determined in the temperature range 1000-1200°C. Following are the key results of this study.

- A brittle intermetallic layer consistent with μ-phase (M_7N_6) evolved in the as-cast W/316L composites.

- The reaction layer developed in thickness during the diffusion annealing. A parabolic relationship between layer growth and diffusion annealing time was observed which suggests that the reaction layer growth was diffusion controlled. The growth constants of the layers are 0.69, 1.96 and 4.68 μm/√h at 1000, 1100 and 1200°C temperatures. The activation energy associated with the layer growth is 149 ±1kJ mole^{-1} in the studied temperature range.

- The calculated values of $\overline{\widetilde{D}}^{Fe}_{eff\,(\mu)}$ and $\overline{\widetilde{D}}^{W}_{eff\,(\mu)}$ in the intermetallic layer are 2.05E-16, 1.33E-15, 1.84E-14 and 1.29E-16, 1.01E-15, 1.19E-14 m^2/s at 1000, 1100 and 1200°C. The values of $\overline{\widetilde{D}}^{Cr}_{eff\,(\mu)}$ are 1.61E-17, 3.98E-16 and 4.25E-15 at respective temperatures. The activation energies for diffusion are 436, 337 and 347 kJ mole^{-1}, respectively for Cr, Fe and W in the studied temperature range.

- μ-phase reaction layers developed in the annealed composites have multiple cracks which formed due to the stresses generated by molar volume change during layers formation and different thermal expansion coefficients of W and 316L. Also Kirkendall voids formation at the reaction layer/matrix interface resulted in de-cohesion between reaction layer and matrix. These undesirable features make the composites unsuitable for use above 900°C. Since this temperature is well above the service temperature of 316L steel, a small improvement in the service temperature of the steel may be possible by W reinforcement but, further tests are required to validate this point.

Chapter 6. Reaction Phase Formation and Growth in Tungsten Wire Reinforced HP Alloy

This chapter reports the studies on W wire reinforcement of HP alloy, which has a significantly different composition than 316L steel. It has 25% Cr content and a Fe:Ni ratio close to 1. Additionally, it has high carbon content (0.45wt.%C) that favours formation of Cr and Nb based carbides in the alloy. These carbides impart creep resistance to the alloy. Since W also has strong affinity for carbon, its interaction with HP alloy can lead to the formation of mixed carbides in the microstructure of the composite. The studies show that η carbide phase forms in the diffusion zone of as-cast composites. The phase develops into a well-defined reaction layer around the W wire when the composite is diffusion annealed at 1000-1200ºC for 500 hours. The results discussed in this chapter comprise microstructure characterization of the composite, growth kinetics of η-phase layer and average effective interdiffusion coefficients in the η-phase layers in the temperature range 1000-1200°C.

6.1 Experimental Procedures

The detailed procedures followed for the composite fabrication, diffusion annealing, sample preparation and characterization of the W/HP composites are described in the Sections 4.2 to 4.5 of this thesis.

6.2 Results

6.2.1 Microstructure and Chemistry

6.2.1.1 As-cast Composites

The SEM micrographs in Figure 6.1 illustrate the as-cast microstructure of W/HP alloy composite. There is formation of a phase around the W wire periphery. A magnified view of the microstructure is presented in Figure 6.1(b).There are two phases (A and B in the image) in the reaction zone of the composite. Phase A that has evolved around the wire periphery is arranged in a Chinese script morphology that consists of needles and some blocky particles. Phase B appears to be present at the grain boundaries of the matrix. Figure 6.1(c) shows evidence of molten metal penetration inside W wire, which preferentially occurred along the grain boundaries of W. The penetration likely led to the detachment and dissolution of W

grains in the molten alloy. Following this, the solidification of W supersaturated liquid occurred which caused the precipitation of the phases in the reaction zone of the composite.

In order to analyse elemental distribution in the reaction zone of the composite, an EDS spectrum around the reaction zone was acquired. Qualitative analysis of the spectrum confirmed the presence of four major elements-Fe, Cr, Ni and W in the composites. Based on this information, X-ray maps of Fe, Cr, Ni and W were collected from the area of interest. Figure 6.2 shows X-ray maps of the corresponding elements along with BSE and colour composite image produced by primary colour overlay of Cr, Fe and W maps.

We can see in the composite image (Figure 6.2(b)) that there is mixing of colours in the interdiffusion zone and the matrix while the W wire is represented only by its primary colour (blue) in the composite, indicating that there is no penetration of matrix elements into the undissolved W wire. The phase evolved as Chinese script (location A in Figure 6.2(a)) around the wire is rich in W. X-ray maps from the grain boundary phase in the matrix (location B in Figure 6.2(a)) suggest that the phase is rich in Cr , but depleted in Fe, Ni and W. The chemical composition of these W-rich, Cr-rich phases (location A and B in Figure 6.2(a)) and the composite matrix (location C in Figure 6.2(a)) was determined by EDS and is shown in Figure 6.3.

There is another minor phase present at the matrix grain boundaries (shown by arrows in Figure 6.2(b). According to X-ray maps, this phase is depleted in Cr, Fe and Ni. Qualitative analysis of the EDS spectrum from this phase revealed that the phase is rich in Nb. Therefore, the phase is likely to be NbC, which is commonly observed in Nb modified HP alloys.

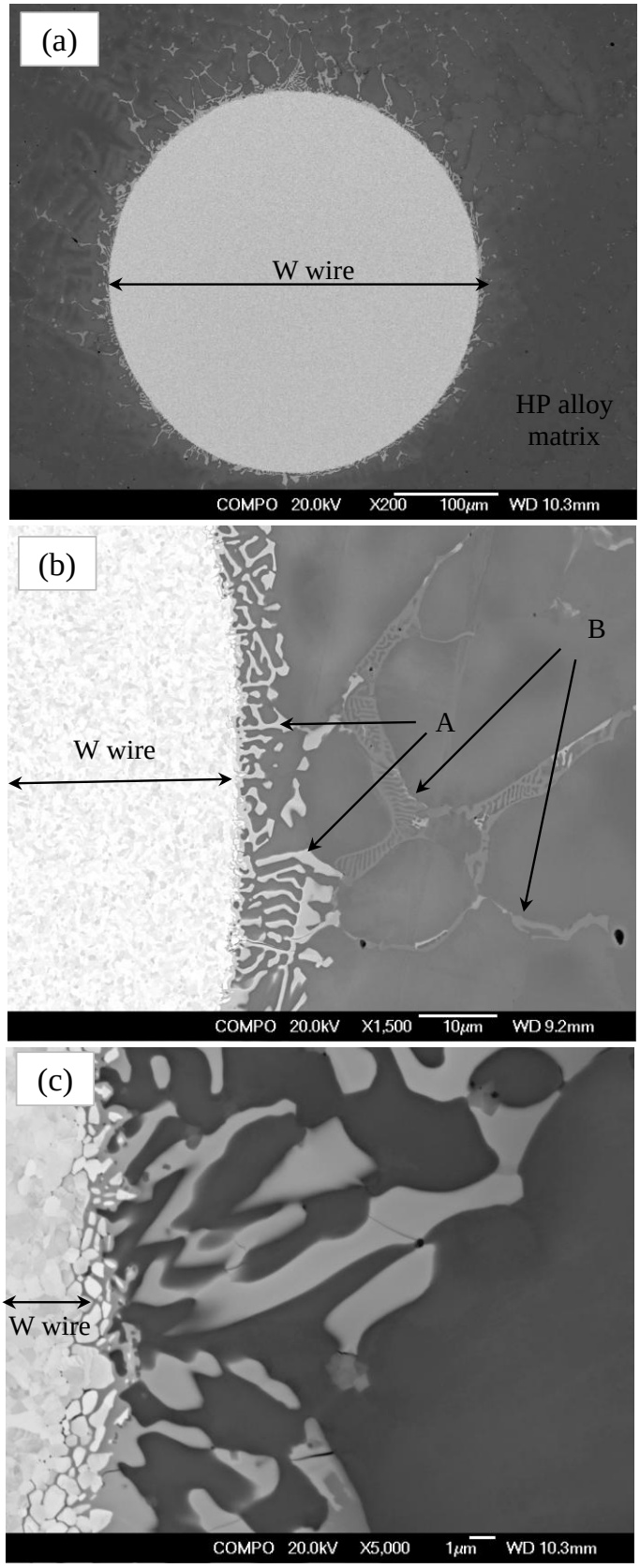

Figure 6.1: General appearance of W wire in as-cast W/HP composite. (a) Full wire view in the matrix, (b) magnified view around the wire/matrix interface showing various phases and (c) further magnified view around the reaction zone.

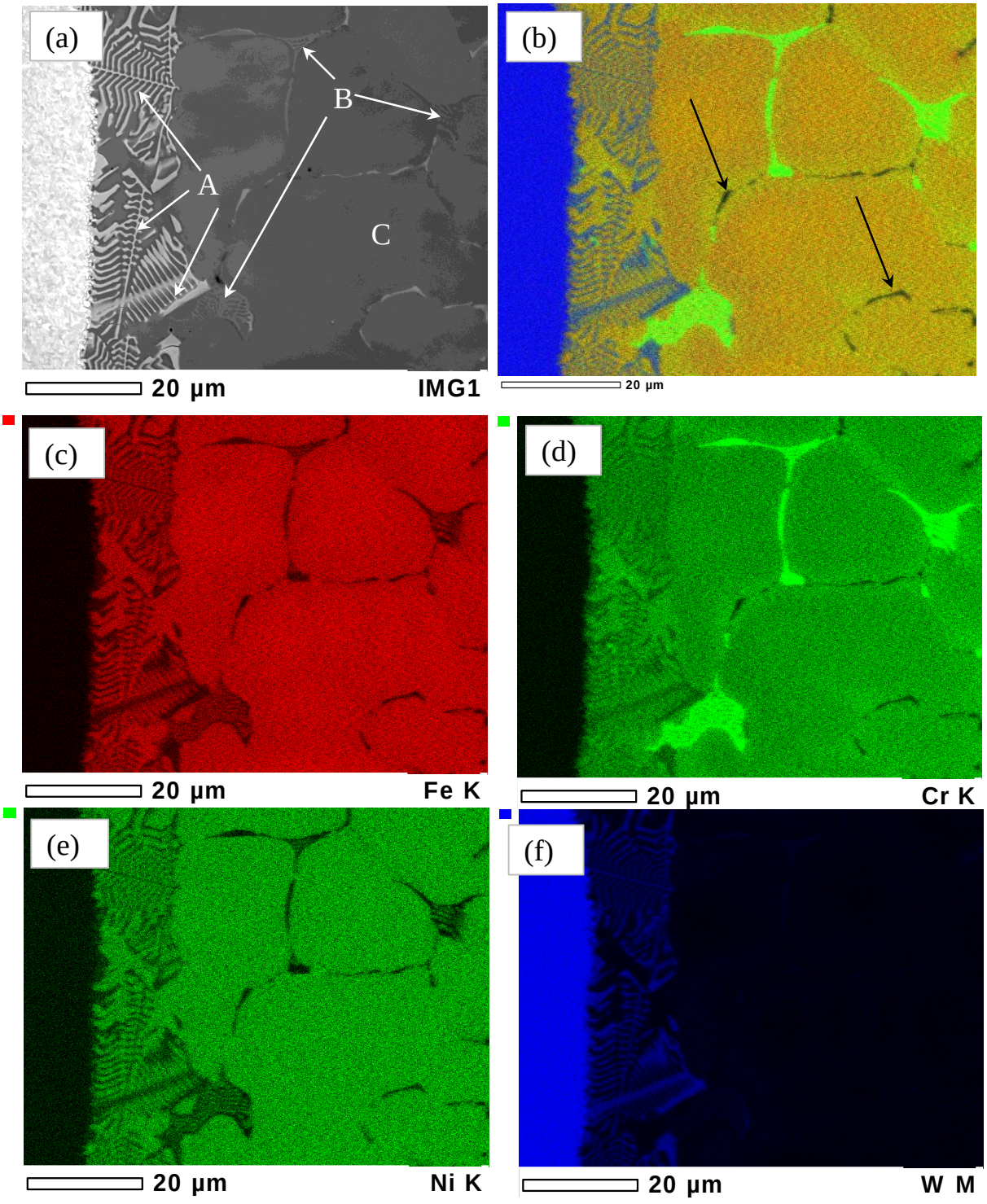

Figure 6.2: A scanning electron image and X-ray maps showing distribution of major elements in as-cast W/HP composite: (a) BSE image, (b) composite image formed by superimposing Fe (red), Cr (green) and W (blue) X-ray maps. (c), (d), (e), and (f) are the coloured X-ray maps of Fe, Cr, Ni and W.

The matrix composition (region C, Figure 6.2(a)) is close to the standard alloy (see Table 4.1) except it contains 5% W. The Cr-rich phase at matrix grain boundaries (region B) contains about 54% Cr. It is depleted in Fe and Ni compared to matrix, but has 17% W dissolved in it. The phase evolved around the W wire (region A) contains about 55%W and 17%Cr. Fe and Ni contents in this phase are 15 and 11%, respectively.

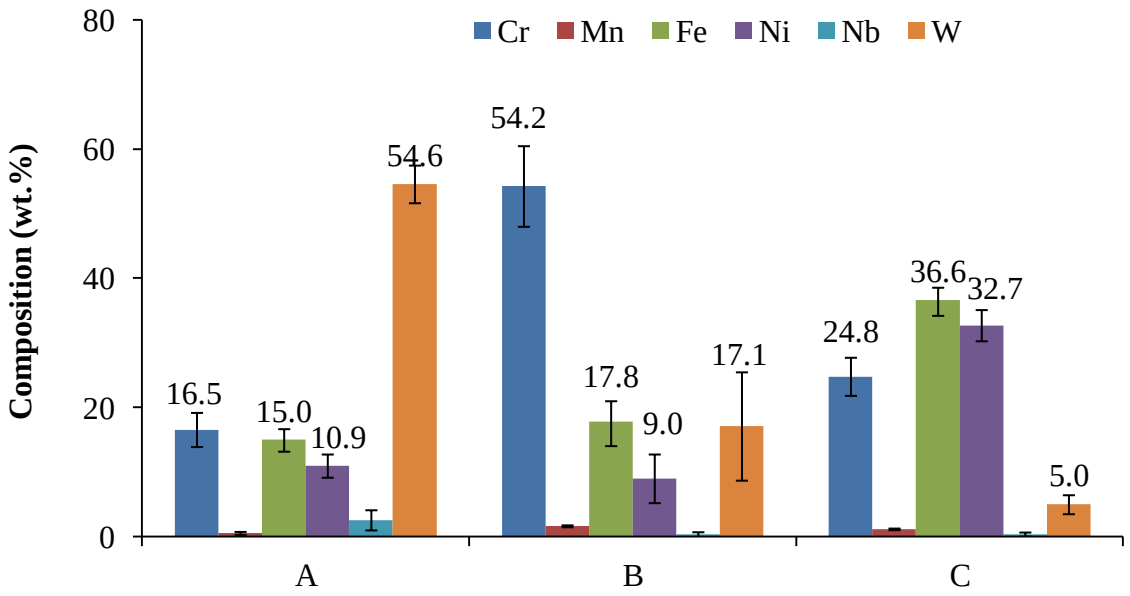

Figure 6.3: Average chemical composition of various phases observed in as-cast W/HP composite. The ordinate in the plot represents the locations (shown in Figure 6.2) where the composition was determined. Error is the maximum and minimum composition.

The crystal structure of the phases observed at locations A and B was identified by EBSD. The phase formed around the wire closely matched with the simulated pattern of η-phase (cubic with lattice parameter 10.6Å and space group 227) with a mean angular deviation equal to 0.53. The stoichiometry of this phase is represented by the formulas $(Ni,Fe,W)_{12}C$ [38] where M stands for Fe, Ni, and W. Since Cr can substitute for W in the lattice, the formula for this phase in the present case can be written as $[Ni, Fe, (Cr, W)]_{12}C$. The experimental and indexed patterns of the η-phase in W/HP composite are given in Figure 6.4.

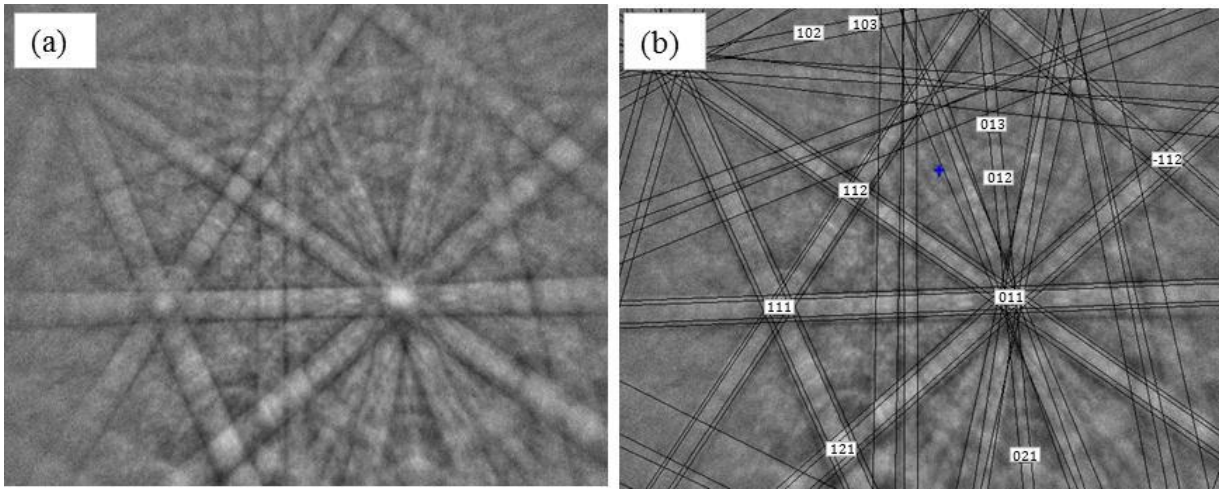

Figure 6.4: (a) Electron backscattered pattern collected from location A in Figure 6.2(a), (b) its matching with simulated pattern of η-phase. The mean angular deviation between the collected and simulated pattern is 0.53.

The Cr-rich grain boundary phase (location B in Figure 6.2(a)) in the composite was identified as $M_{23}C_6$ by EBSD analysis, where M represents Cr, Fe, Ni and W. This phase has a cubic structure with lattice parameter 10.67Å and space group 225. The experimental and simulated patterns for this phase are shown in Figure 6.5.

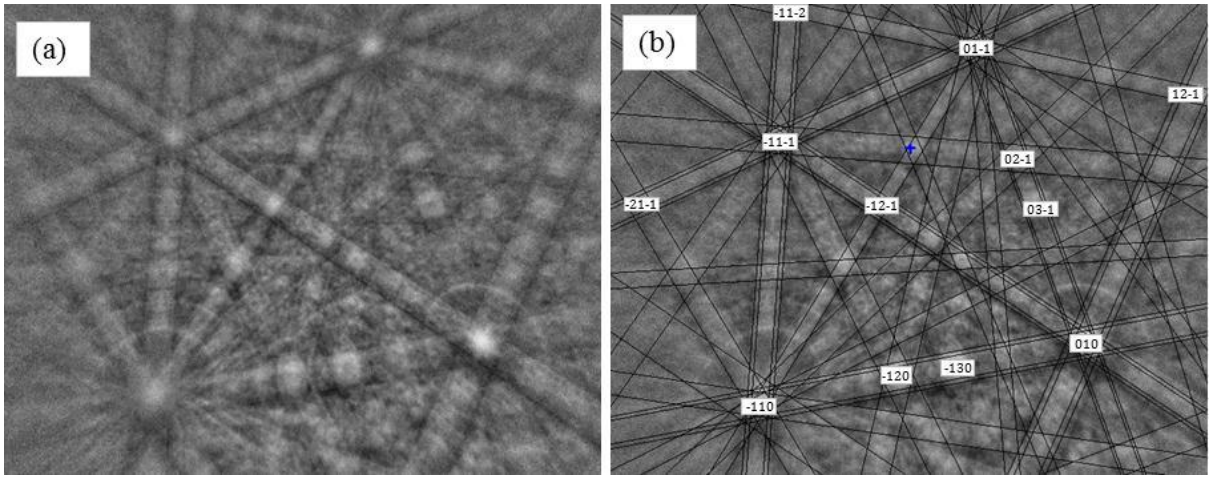

Figure 6.5: (a) Experimental and (b) indexed electron backscattered pattern from Cr-rich phase in the W/HP annealed composite. The mean angular deviation is 0.31.

6.2.1.2 Diffusion Annealed Composites

Samples from the fabricated W/HP composite were subjected to diffusion annealing at temperatures 900-1200°C for times ranging from 25-500 hours. In 900°C/500hours annealed composite, a morphological transition in the η-phase takes place (Figure 6.6). The Chinese script morphology seen in as-cast composites is replaced by blocky particles. Consequently, a thin reaction layer starts to evolve around the W wire. Also, there is precipitation of fine particles in the diffusion zone in the matrix under these diffusion annealed conditions.

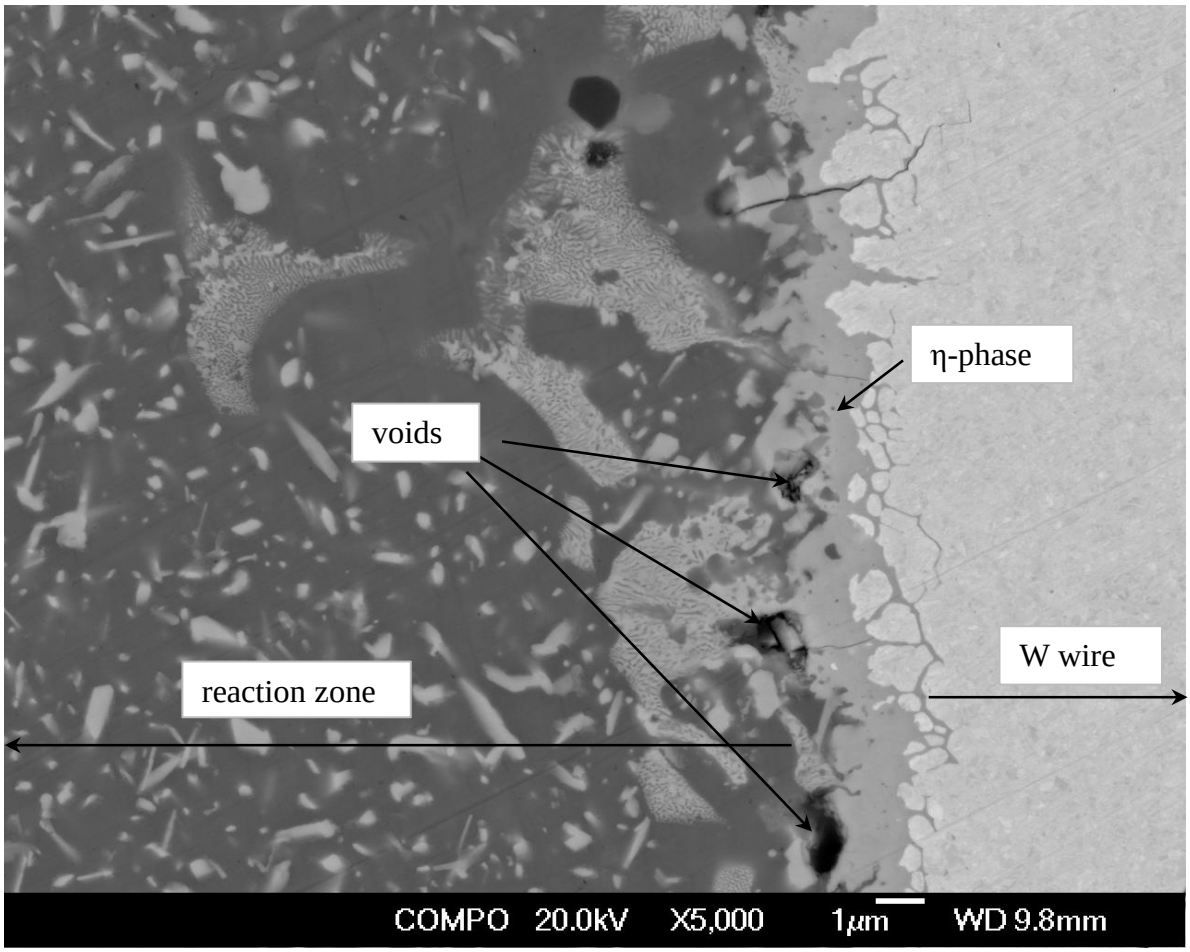

Figure 6.6: Microstructure of W/HP composite after diffusion annealing for 500 hours at 900°C.

The microstructural features of the composite diffusion annealed in the temperature range 1000-1200°C for 500 hours are shown in Figure 6.7. A complete transition in the morphology of the reaction phase has occurred during annealing and it gradually transformed to a distinct layer surrounding the W wires. The layer thickness increased with the annealing temperature and after 1200°C/500hours, the layer thickness was about 85μm. The appearance of the cracks on the reaction layer suggests its brittle nature. The particles observed in the reaction zone of the composite coalesce into bigger particles as a function of annealing temperature and ultimately become part of the continuous η-phase reaction layer around the W wire at 1200°C.

The X-ray maps of Cr, Fe, Ni, and W collected from diffusion annealed composites are shown in Figures 6.8 to 6.10. The colour composite image illustrates the distribution of these elements in the reaction zones of the composites. In the 1000°C/500hours annealed sample two types of precipitates, light and dark coloured, can be seen in the BSE image (D and E in Figure 6.8(a)). The corresponding colour composite image indicates that the precipitates with light contrast mainly consist of W and the precipitates with dark contrast are rich in Cr. The W-rich precipitates are present inside the grains and at grain boundaries, but the Cr-rich precipitates appear only in the grain boundary area. Chemical analyses by EDS showed that light precipitates contain approximately 19Cr, 14Fe, 13Ni, 4Nb and 51W (wt.%). The composition of the dark precipitates is 55Cr, 11Fe, 1Mn, 5Ni and 22W (wt.%). As the annealing proceeds at high temperature (Figure 6.9 and 6.10), these precipitates grow and finally, W-rich precipitates disappear by merging into Cr-rich precipitates. The Cr-rich phase forms a continuous layer (G in Figure 6.10(b)) around the η-phase reaction layer (F in Figure 6.10(b)) at 1200°C.

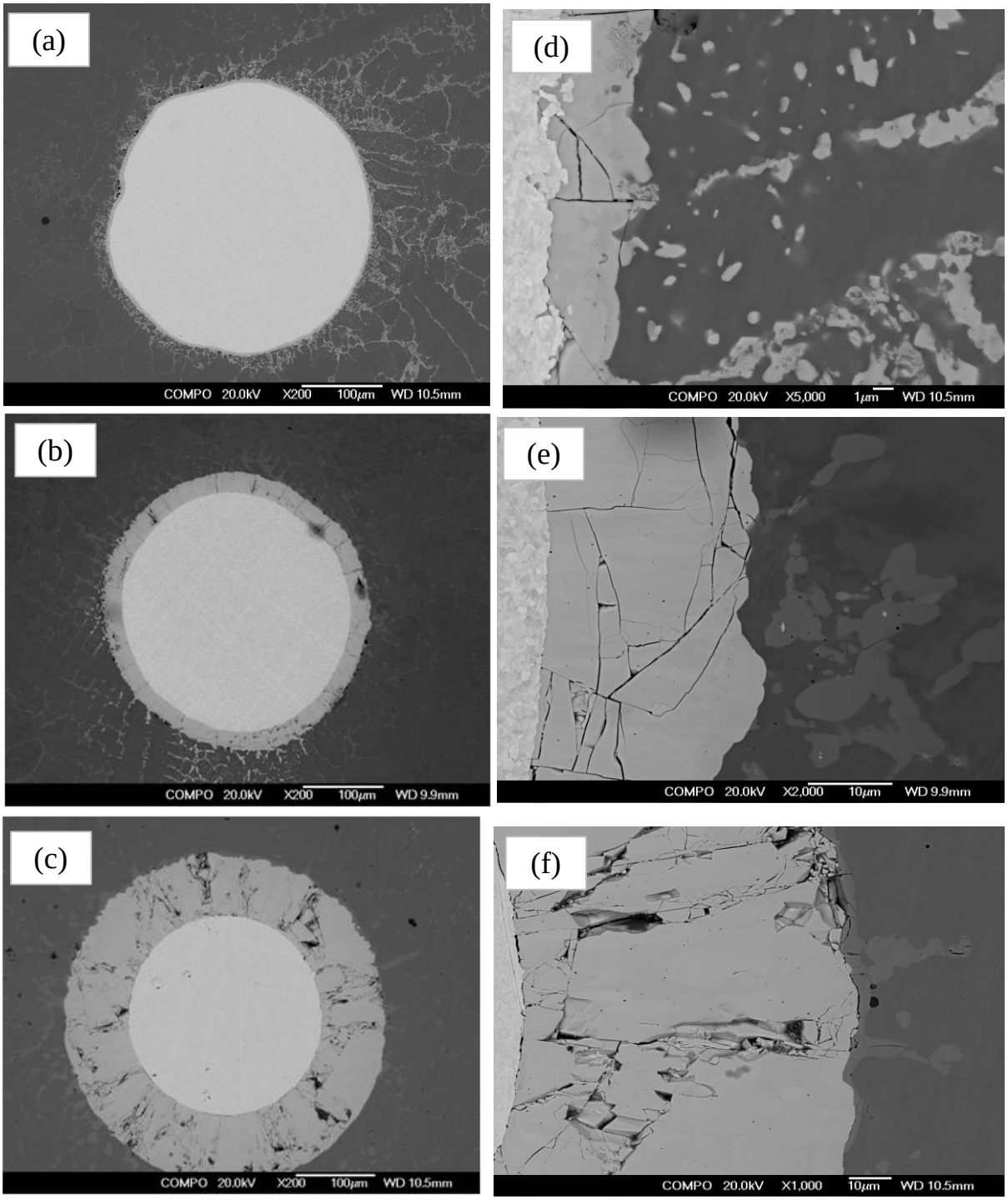

Figure 6.7: Microstructure of W/HP alloy composite diffusion annealed for 500 hours at (a) 1000°C, (b) 1100°C and (c) 1200°C. (e), (f) and (g) are the magnified views of the microstructure at the corresponding temperatures.

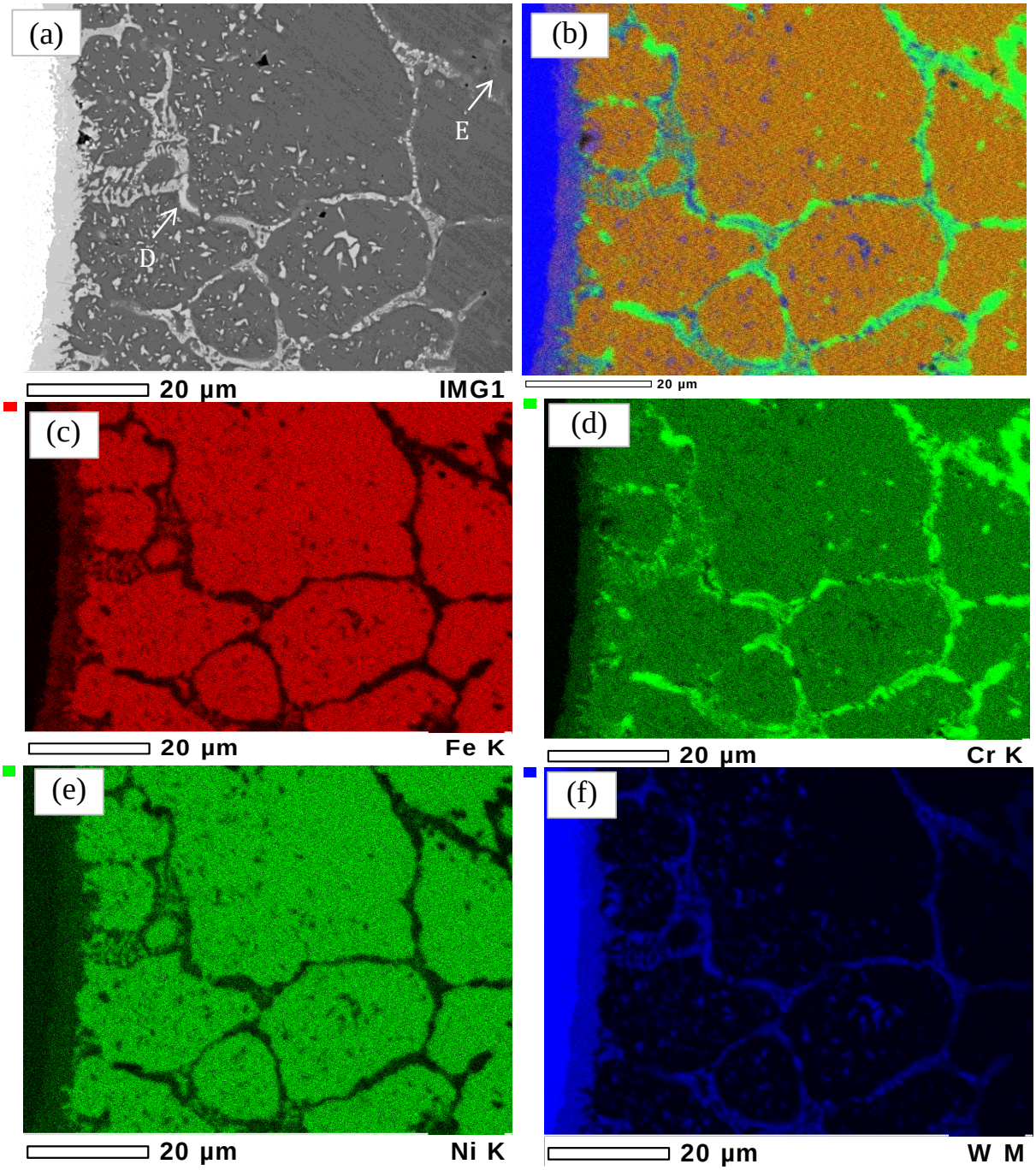

Figure 6.8: (a) BSE image and (c, d, e, f) X-ray maps of Fe, Cr, Ni and W in W/HP composite after 1000°C/500hours annealing. (b) is the colour composite image formed by combining X-ray maps of Cr, Fe and W.

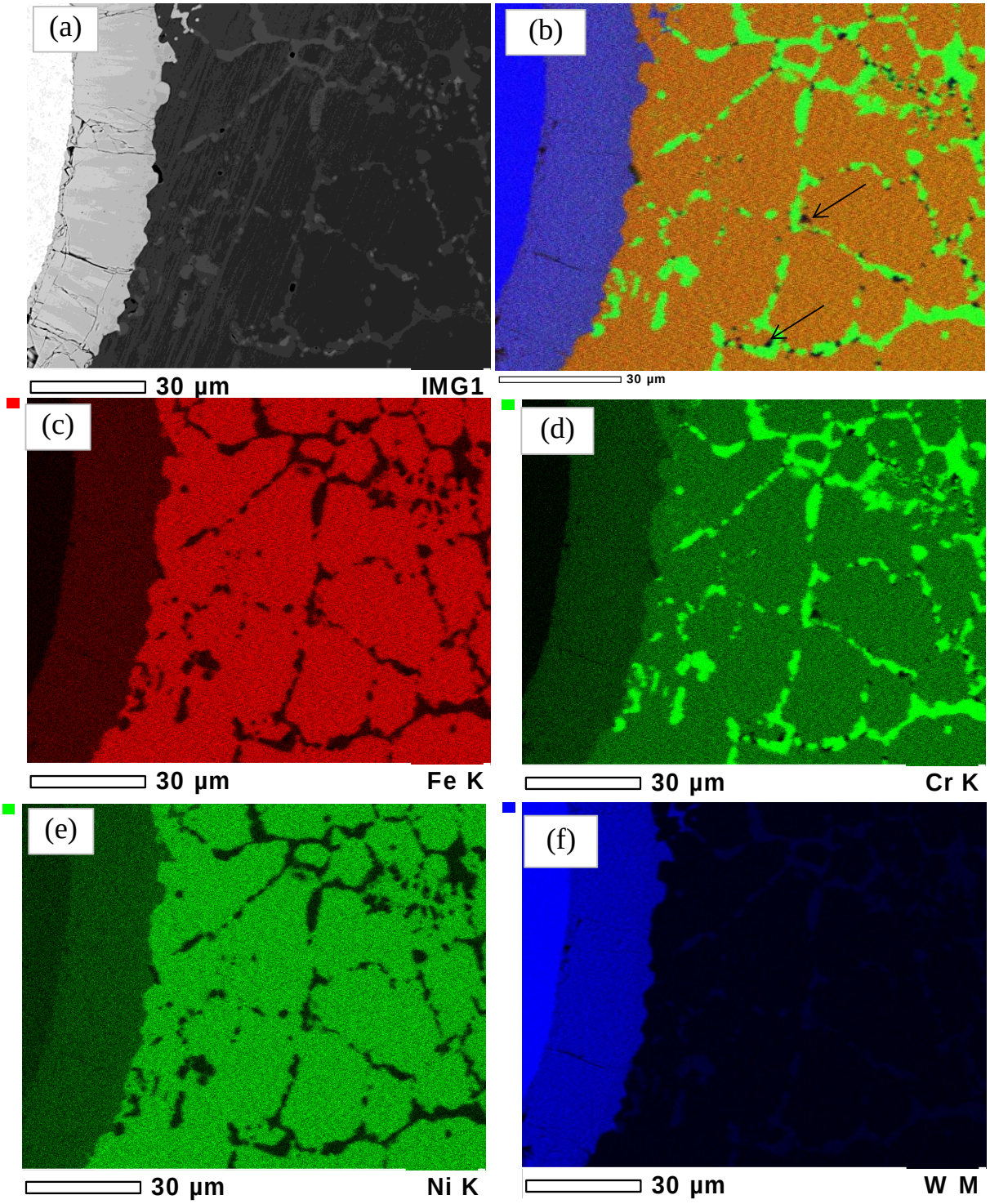

Figure 6.9: (a) BSE image and (b) colour composite image formed by combining X-ray maps of Cr, Fe and W. (c, d, e, f) are the X-ray maps of Fe, Cr, Ni and W in W/HP composite after 1100°C/500hours annealing. Black regions in the composite image (black arrows) are rich in Nb.

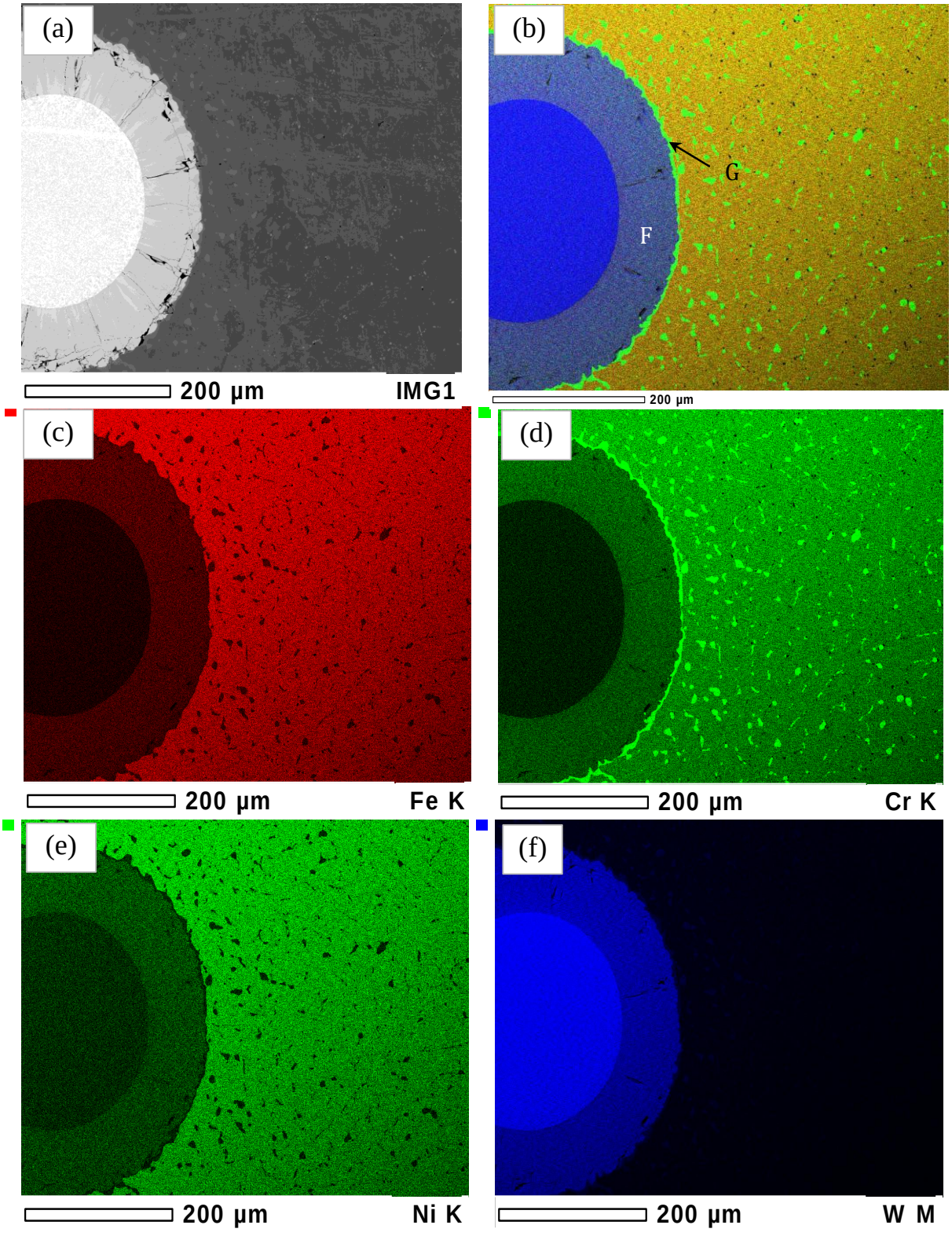

Figure 6.10: (a) BSE image and (b) colour composite image formed by overlaying Cr, Fe and W maps of W/HP composite annealed at 1200°C/500hours. (c), (d), (e) and (f) are the X-ray maps of Fe, Cr, Ni and W.

The chemical composition of the reaction layers formed around the W wire in the annealed composites is presented in Figure 6.11. There is no change in the crystal structures of the reaction layer phases upon diffusion annealing and EBSD analysis confirmed them to be isomorphous with η-phase at all the diffusion annealed temperatures.

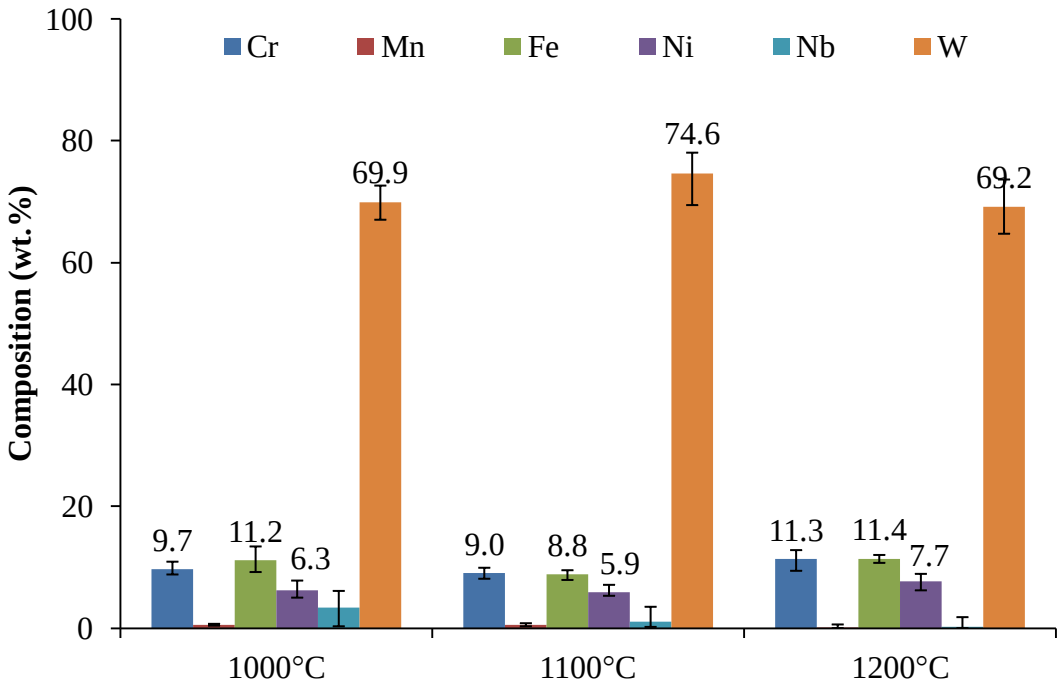

Figure 6.11: Chemistry of the reaction layers formed in W/HP composite after 500 hours annealing at different temperatures. Error bar is maximum and minimum composition.

The chemical composition of the Cr-rich layer at the η/matrix interface (G in Figure 6.10) was determined to be 54Cr, 11Fe, 1Mn, 4Ni and 24W. The crystal structure of this layer is consistent with $M_{23}C_6$ carbide, where M represents Fe, Cr, Ni and W.

6.2.1.3 Microstructure of η-phase Reaction Layer

The microstructure of the η-phase reaction layer in 1200°C/500hours annealed composite is shown in Figure 6.12. Based on the grain morphology, the layer can be divided into two regions as shown in the Figure. Region 1 is represented by columnar grains which are orientated parallel to the diffusion direction. The region 2, which is closer to the matrix, has equiaxed grains. There are randomly distributed spherical voids (<1µm diameter) in the reaction layer.

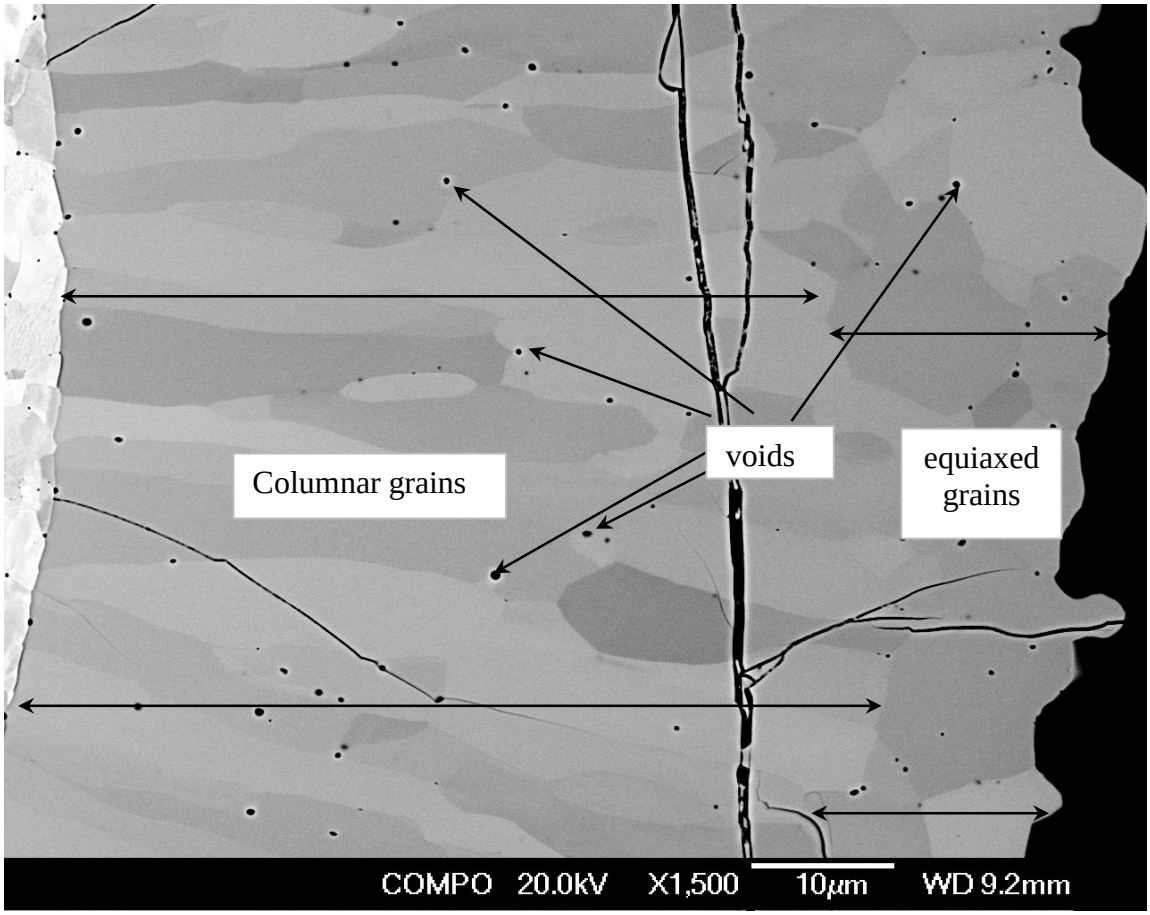

Figure 6.12: BSE image of the reaction layer microstructure developed in W/HP composite during annealing at 1200°C for 500 hours.

6.2.2 Growth Kinetics of the Reaction Layer

Measured thickness of the η-phase reaction layer in the samples annealed for different time intervals was plotted against square root of time according to Equation 5.1. The plots are shown in Figure 6.13. The data points were fitted to a line with R^2 close to 1, suggesting that the kinetics of the reaction layers is diffusion controlled in the temperature range 1000-1200°C. Growth constants of the reaction layers at different temperature were extracted from the slopes of the plots and are given in Table 6.1. Activation energy (Q_G) and pre-exponential factor (k_0) for the layer growth was calculated from the Arrhenius plot (Figure 6.14). The calculated value of Q_G and k_0 for η-phase reaction layer growth are 225 ±3kJ $mole^{-1}$and 3.88E+08μm√h, respectively

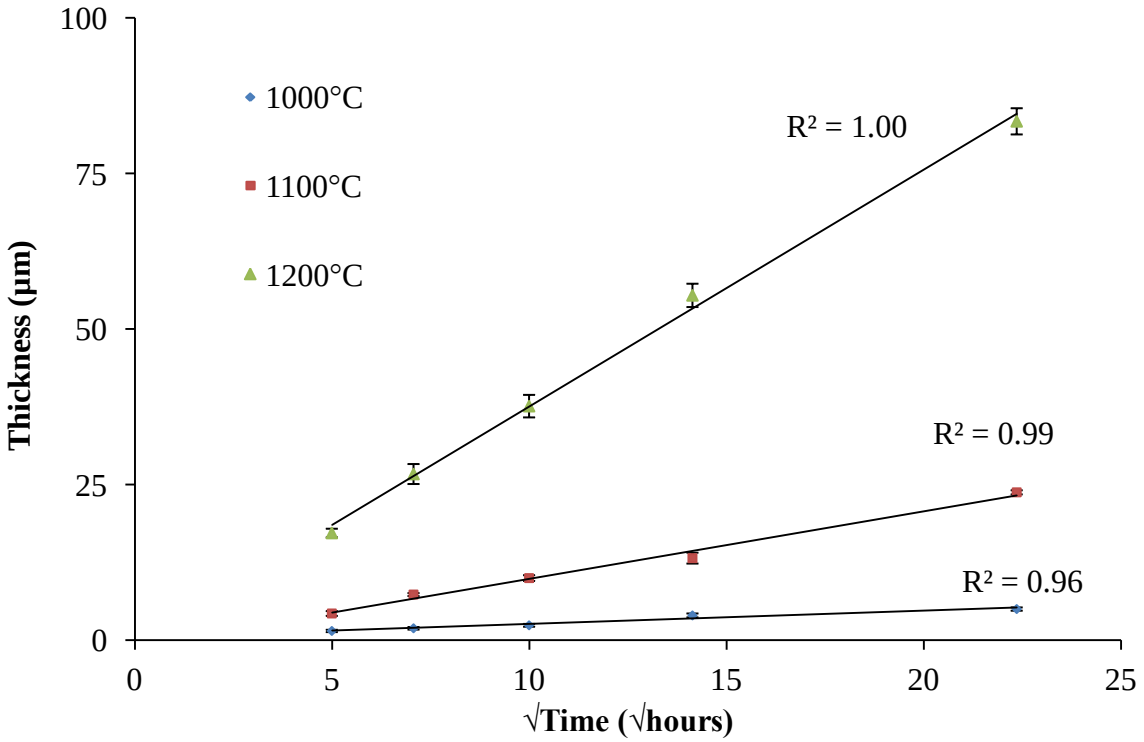

Figure 6.13: Reaction layer kinetics of η-phase at different diffusion annealing temperatures in W/HP composite. The slope of each line is the growth constant of the layer at that temperature. Error bars are the standard deviation on 10 thickness measurements.

Table 6.1: Growth constants of η-phase reaction layers in W/HP composite at 1000, 1100 and 1200°C.

Temperature (°C)	*k* (µm√h)
1000	0.21 ±0.02
1100	1.09 ±0.06
1200	3.80 ±0.12

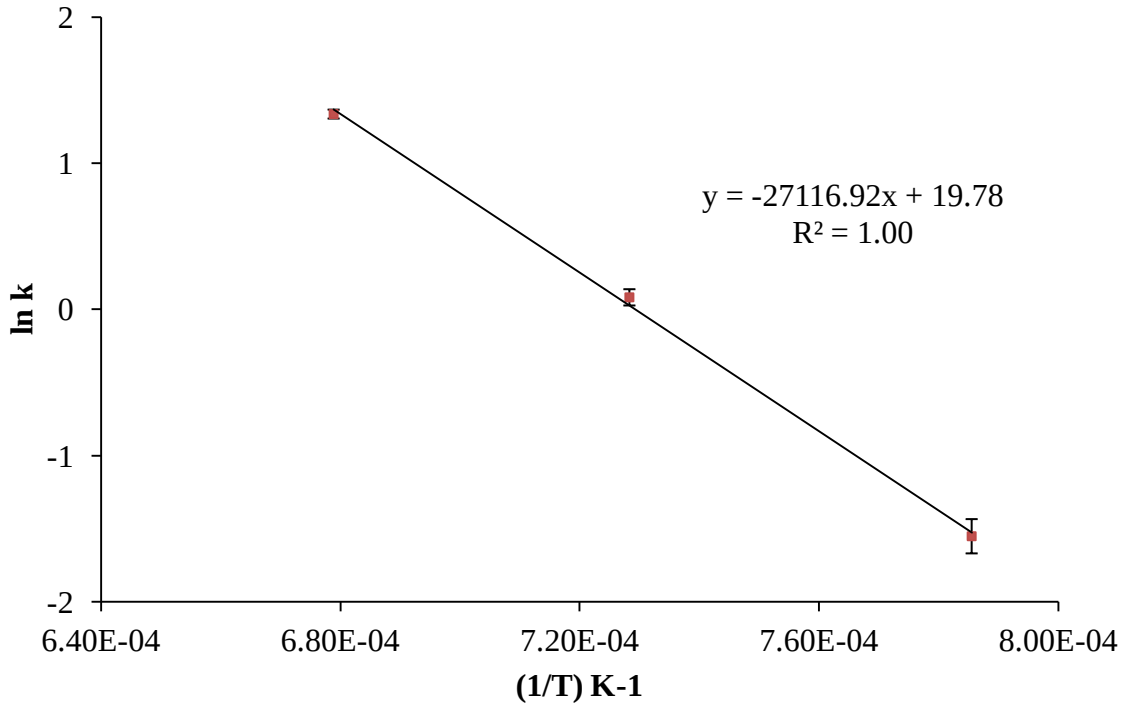

Figure 6.14: Arrhenius plot for the reaction layer growth constants in W/HP composite.

6.2.3 Interdiffusion Behaviour

6.2.3.1 Composition Profiles

Composition profiles of the reaction layers were acquired by EDS line scans on the polished samples of the composites annealed at 1000-1200°C for 500 hrs. The profiles are shown in Figures 6.15-6.17. Reinforcement, reaction layers and matrix phase are clearly distinguishable in the profiles based on sharp change in composition.

At 1100 and 1200°C, there is a positive composition gradient of W (towards the W wire) in the reaction layers suggesting W diffusion from wire to matrix. Due to the scatter of data points in the composition profiles, a clear visualization of the interdiffusion behaviour cannot be made in the case of other elements. At 1200°C, there is about 10 µm wide region between reaction layer and matrix where the Cr composition shoots up to ~75 at. %, but a sharp drop in the composition of Fe, Ni and W is observed in this region. This region belongs to $M_{23}C_6$ carbide layer which is present around the η-phase layer.

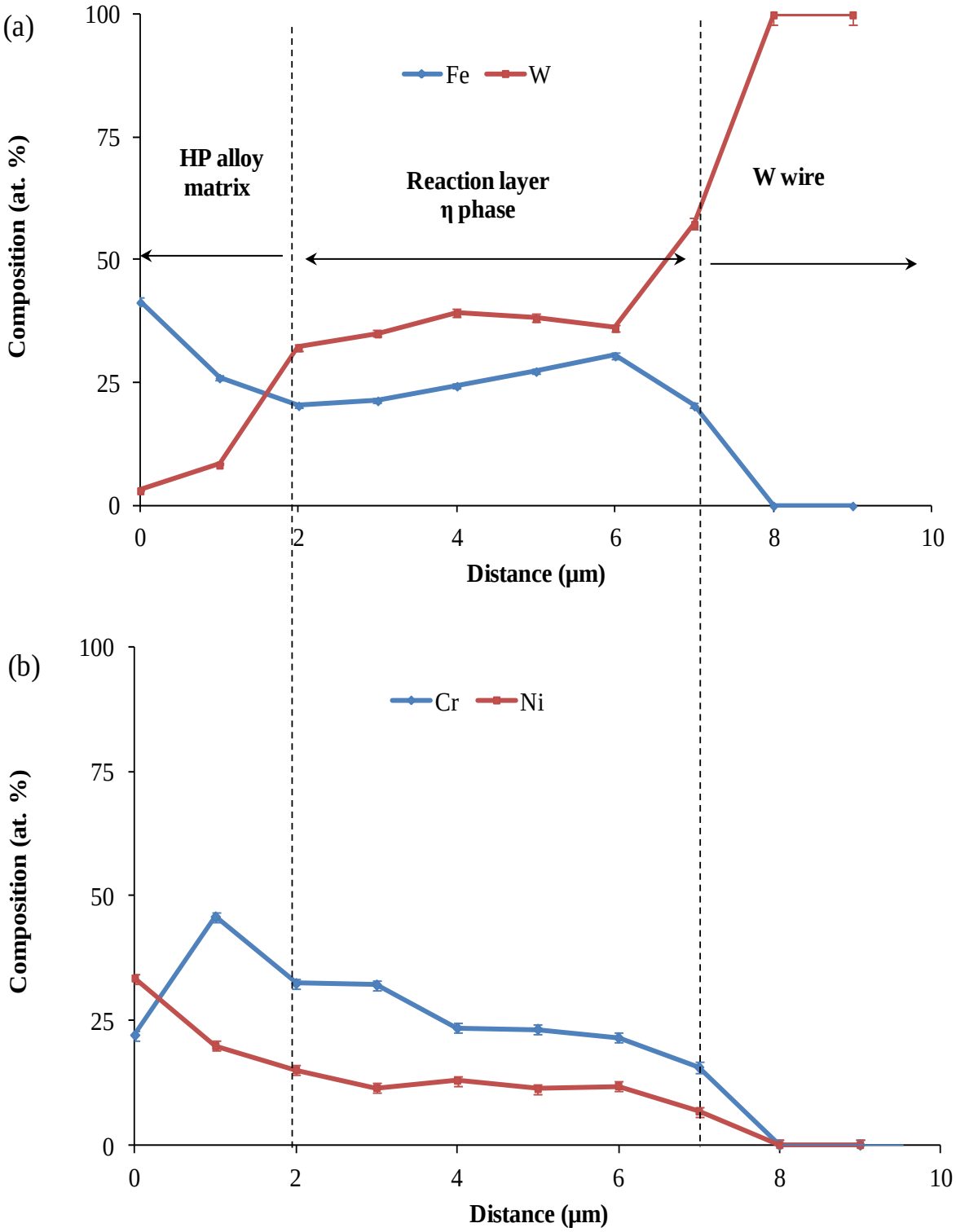

Figure 6.15: Composition profiles of (a) Fe, W and (b) Cr, Ni in W/HP composite diffusion annealed at 1000°C/500hours.

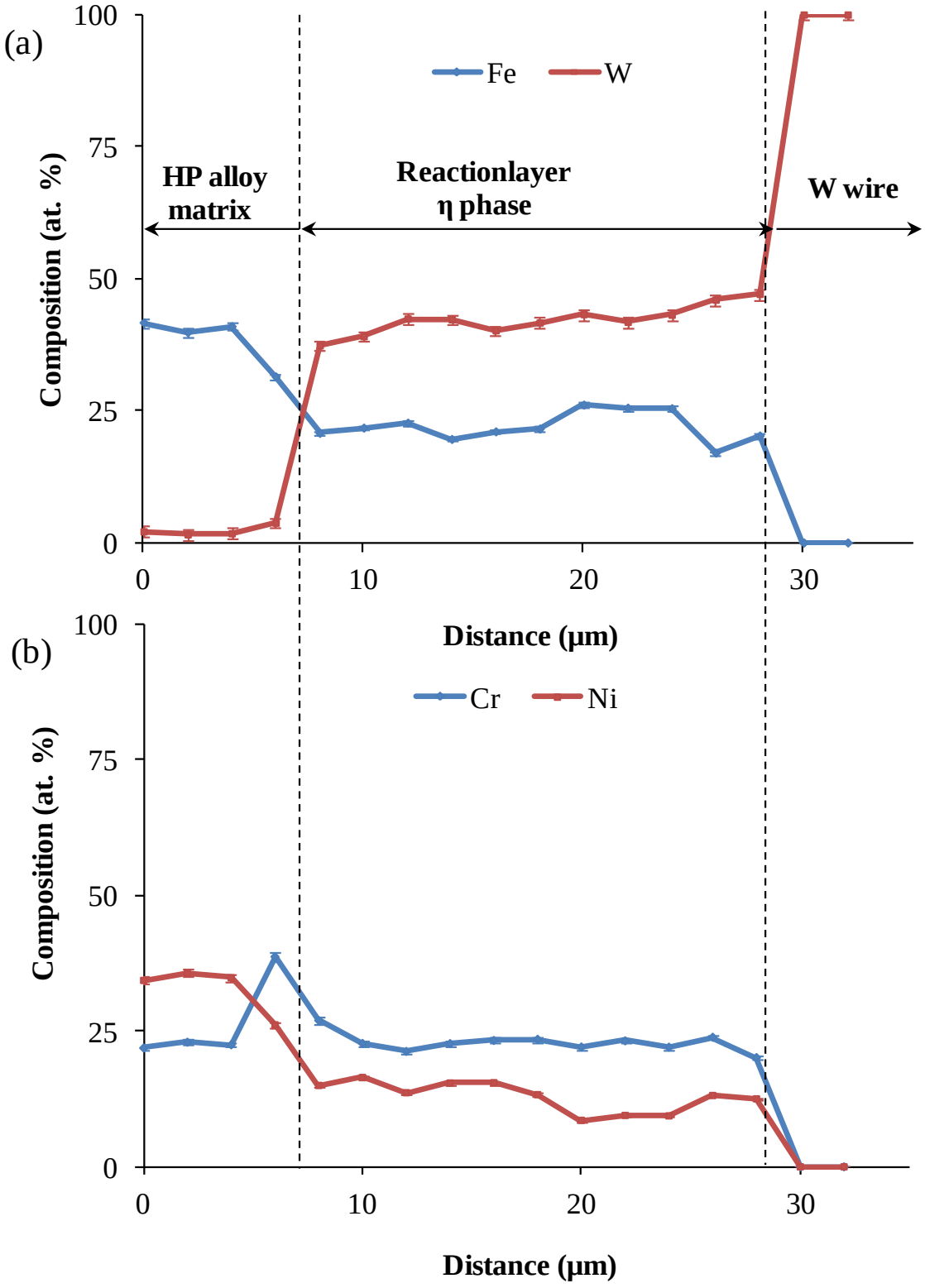

Figure 6.16: Composition profiles of (a) Fe, W and (b) Cr, Ni in W/HP composite diffusion annealed at 1100°C/500hours.

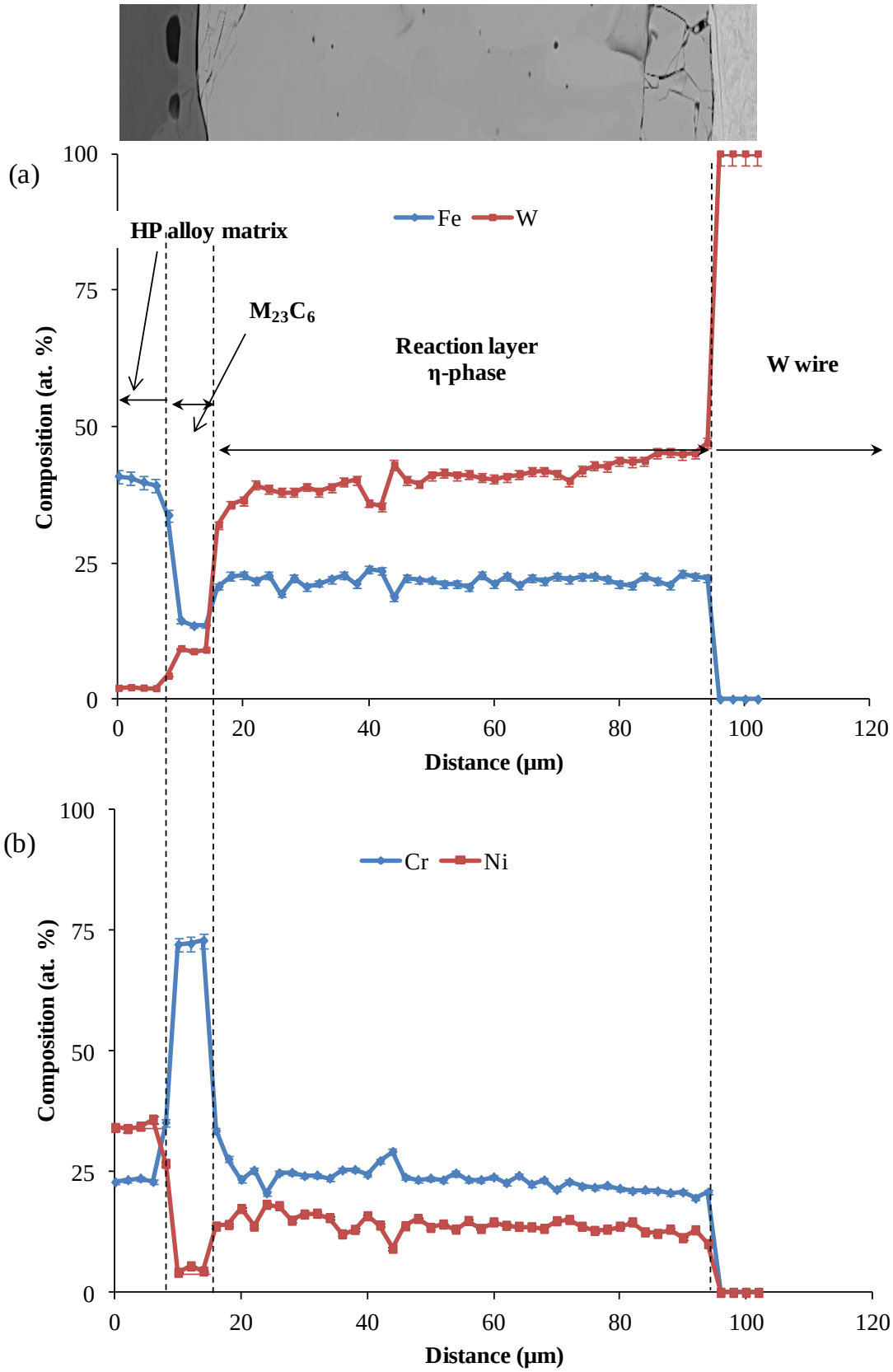

Figure 6.17: Composition profiles of (a) Fe, W and (b) Cr, Ni in W/HP composite diffusion annealed at 1200°C/500hours.

6.2.3.2 Diffusion Coefficients

For the calculation of average effective interdiffusion coefficients, $\overline{\widetilde{D}}^{i}_{eff}$ in the η-phase reaction layers, composition profiles acquired on the 1000-1200°C/500hours annealed samples were utilized. Multiple sets of composition profile were subject to linear fitting. The fitting resulted in poor R^2 value in most of the cases. The profiles were then filtered using F-statistics test as discussed in Appendix B. Those profiles which did not pass F-Test were excluded from further analysis. The data points of the selected composition profiles were converted to concentration according to Equation 5.2. Constant values of V_m - 9.78, 7.62 and 8.00 cm^3 $mole^{-1}$, respectively for W, η and γFe were used for the conversion of atomic percent to concentration.

Following this, $\overline{\widetilde{D}}^{i}_{eff\,(\eta)}$ in the reaction layers were calculated for Cr, Fe, Ni and W using the method described in Section 3.3.2. Calculated values of $\overline{\widetilde{D}}^{i}_{eff\,(\eta)}$ show little dependence on the composition within the reaction layers of the composites, which is apparent from the shallow composition gradients across the reaction layers in the profiles. Therefore, average values of $\overline{\widetilde{D}}^{i}_{eff\,(\eta)}$ are shown in Table 6.2. In most of the cases, these values are the average of $\overline{\widetilde{D}}^{i}_{eff\,(\eta)}$ calculated on two composition profiles for each diffusion condition.

Table 6.2: Average effective interdiffusion coefficients of various elements in the η-phase reaction layers of W/HP composite.

Temperature (°C)	$\overline{\widetilde{D}}^{i}_{eff\,(\eta)}$ (m^2/s)			
	Cr	Fe	Ni	W
1000	7.56E-19	1.64E-17	9.93E-18	7.99E-18
1100	1.77E-16	4.43E-16	2.67E-16	2.70E-16
1200	--	1.46E-14	4.80E-15	3.41E-15

$\overline{\widetilde{D}}^{i}_{eff\,(\eta)}$ for W and Ni are of the same order of magnitude at all the temperatures. $\overline{\widetilde{D}}^{i}_{eff\,(\eta)}$ of Fe is an order of magnitude higher than W and Ni at 1200 and 1000°C. Cr is the slowest diffusing element at 1000 and 1100°C.

The temperature dependence of $\overline{\widetilde{D}}^{i}_{eff\,(\eta)}$ was investigated by plotting ln $\overline{\widetilde{D}}^{i}_{eff\,(\eta)}$ versus 1/T. These plots for Cr, Ni and W are shown in Figure 6.18. Fitted straight lines in these plots are consistent with the Arrhenius relation (Equation 3.64) for diffusion. The activation energies of diffusion (Q_D) and pre-exponential factors (D_0) of different elements in the η-phase reaction layers were calculated from Arrhenius plots and are listed in Table 6.3.

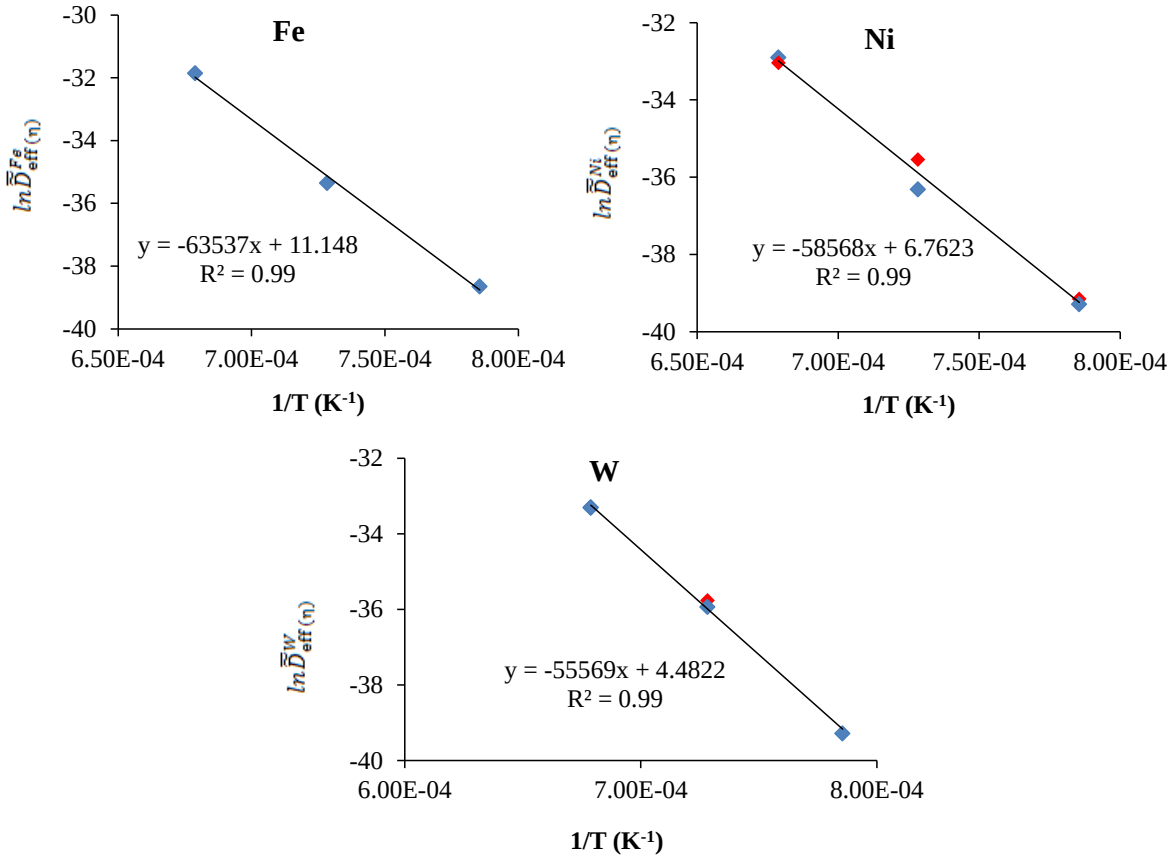

Figure 6.18: Arrhenius plots for Fe, Ni and W in the η-phase reaction layers of W/HP composite diffusion annealed for 500 hours at 1000-1200°C. Blue and red markers represent two data sets that are fitted to a line.

Table 6.3: Activation energies and pre-exponential factors for diffusion of various elements in the η-phase reaction layers of W/HP composites.

Elements	Q_D^i (kJ mole^{-1})	D_0 (m^2/s)
Fe	528	6.9E+04
Ni	487	8.6E+02
W	462	8.8E+01

6.3 Discussion

Microstructure investigation has shown that η-carbide forms in the as-cast W/HP composite. Since HP alloy contains high carbon ~0.45wt.%, its microstructure is greatly influenced by the presence of carbon. The solubility of carbon in γ decreases with decreasing temperature and also with increasing Ni content in γ. Therefore, high carbon and high Ni content (35 wt. %) in HP alloy ensure sufficient excess carbon to form carbides. Common carbides that are observed in the solidified microstructure of HP alloy are $M_{23}C_6$ and NbC. Formation of these carbides in the alloy occurs via eutectic solidification [87] and they generally form at the grain boundaries of γ. Interaction of W with high carbon containing steels leads to formation of carbides containing tungsten. As shown in the isothermal section of C-Fe-W phase diagram (Figure 6.19) [88], there are two η-carbide phases ($M_{12}C$ and M_6C) that appear when C is added to Fe-W. Formation of η-carbides have also been reported in C-Cr-Fe-W [89] and C-Fe-Ni-W [90] isothermal sections at 1250 and 1200°C, respectively. These carbides differ in the amount of carbon present in them. $M_{12}C$ is a carbon deficient version of M_6C with C absent from half of the interstitial sites. Regardless of stoichiometry, both $M_{12}C$ and M_6C are characterized by having $FD\bar{3}$m space group with variable lattice parameters [38]. Contrary to chromium carbide ($M_{23}C_6$), η-carbides have higher stability temperature. The highest temperature at which η-carbide ($M_{12}C$) can exist is 1400°C [91]

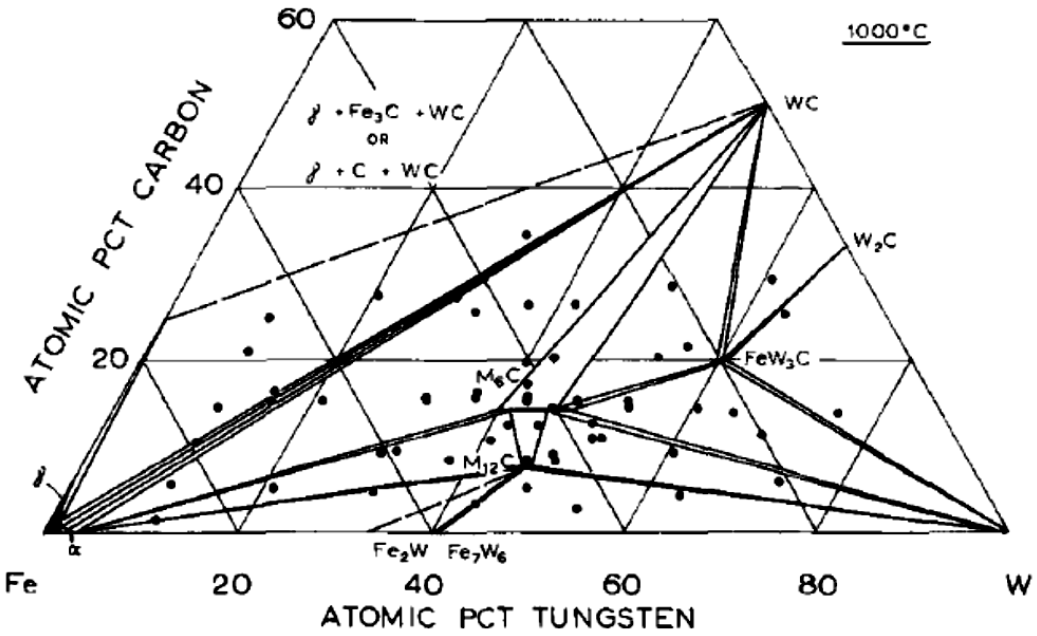

Figure 6.19: Isothermal section of C-Fe-W phase diagram at 1000°C [88].

In case of W/HP solidification, there is indication of W wire dissolution in molten alloy as seen in Figure 6.1. Therefore, the formation of η-phase in W/HP composite might also have occurred via eutectic solidification, L→η+γ in the reaction zone. This is also evident form the Chinese script morphology of η-carbides which is a characteristic feature of eutectic solidification. Past studies on W wire reinforced composites do not have much information on η-phase formation and there is only one study in which η-carbide was identified in the reaction zone of W/MAR-200 composite [26, 29].

Carbides based on Cr and Nb were identified in the matrix of W/HP composite which are common features of the HP alloy microstructure. These carbides transform to η-carbides and become part of reaction layer during diffusion annealing. There was an additional layer of $M_{23}C_6$ carbides observed adjacent to η-carbide layer in the W/HP samples annealed at 1200°C for 500 hours. The formation of this layer at 1200°C only can be related to the stability of $M_{23}C_6$ carbide. It has been reported that $M_{23}C_6$ carbides are not stable at high temperature and during heating above 1100°C they dissolve in austenite [92]. Rapid quenching from high temperature may result in a precipitation free austenite matrix, but if the sample is air cooled from high temperature, precipitation of $M_{23}C_6$ carbides can take place. Therefore, re-precipitation of $M_{23}C_6$ carbides might have occurred during cooling of the

W/HP composite after annealing treatment at 1200°C. Kirkendall voids near the η/γ interface provided sites for the nucleation of these carbides that resulted in their precipitation adjacent to η-phase.

A key application of HP alloy steel is in the reformer furnace operation for the production of methanol Typical service temperature of the alloy in this operation is 900°C [93]. This study has shown that η-carbide reaction layer starts forming even at 900°C and grows to significant thickness at higher temperatures. Therefore, there may not be any advantage of reinforcing HP alloy with W wires.

6.4 Comparison of W/316L and W/HP Composites

Results of microstructure analysis revealed the evolution of different reaction phases in as - cast W/316L and W/HP composites. High carbon content in HP alloy led to the formation of η reaction phase in W/HP composite, while μ reaction phase was formed in the W/316L composite. During diffusion annealing in the temperature range 1000-1200°C, these phases grew as continuous reaction layers around the W wires in the respective matrices. Cracks proliferation is ubiquitous on the reaction layers of W/316L and W/HP diffusion annealed composites. This type of brittle reaction layers can have negative implications on the composite strength as they cannot transfer stresses from matrix to the wire and thus lower the apparent strength of the composite.

Table 6.4 lists growth and diffusion parameters of the reaction layers in W/316L and W/HP composites. Q_G for η-phase layer in W/HP is about 34% higher compare to μ-phase layer in W/316L composite. Similarly Q_D values for Cr and W are higher in W/HP composite. Due to higher activation energy barriers for growth and diffusion, the growth of η-layers was slower in the temperature range 1000-1200°C.

Table 6.4: Growth and diffusion parameters in W/316L and W/HP composites.

Composite	Growth parameters		Diffusion parameters		
	k_0 (μm/√h)	Q_G (kJ mole^{-1})	Elements	Q_D (kJ mole^{-1})	D_0(m^2/s)
W/316L (μ-phase)	9.31E+05	149 ±1	Cr	436	1.3E+01
			Fe	337	1.2E-02
			W	347	2.0E-02
W/HP (η-phase)	3.88E+08	225 ±3	Cr	528	6.9E+04
			Ni	487	8.6E+02
			W	462	8.8E+01

Under similar diffusion annealing conditions, the difference in the reaction layer growth can be attributed to the composition of the reinforcement and matrix phases of the composites from which the layer grows. Since the composition of W wire is fixed in both the composites, the matrix composition can be thought of affecting the layer growth. Comparison of three major elements – Cr, Fe and Ni in 316L and HP alloy reveals that there is significant difference in Fe and Ni contents in these alloys. The Fe:Ni ratios in 316L and HP alloy are approximately 7 and 1. Therefore, slow diffusion and growth in W/HP alloy may be related to low Fe:Ni ratio in the composite matrix.

6.5 Summary

Microstructure evolution, growth kinetics of η-phase reaction layers and diffusivity of various elements in the reaction layers in W/HP composite were investigated in this chapter. Following are the key results of the study:

- Interaction of W wires with liquid HP alloy resulted in the formation of η-phase in the as-cast W/HP composite. During diffusion annealing, a transition in the η-phase morphology took place in the diffusion zone resulting in the formation of a brittle reaction layer around the W wire. Segregation of $M_{23}C_6$ was observed at the layer/matrix interface that constituted a thin layer of phase around the main reaction layer (η-phase) in 1200°C/500hrs diffusion annealed W/HP composite.

- Calculated growth constants of the η-phase reaction layers are 0.21, 1.09 and 3.80 µm/√h at 1000, 1100 and 1200°C. The activation energy associated with the layer growth is 225 ±3kJ mole^{-1} in the studied temperature range.

- $\widetilde{\overline{D}}^{i}_{\text{eff }(\eta)}$ values were calculated for Cr, Fe, Ni and W. The values of activation energy for diffusion of Fe, Ni and Cr are 528, 487 and 462 kJ mole^{-1} in the temperature range 1000-1200°C.

- A microstructure comparison of W/316L and W/HP composites show that brittle reaction layers evolved in both composites at diffusion annealing temperatures. A small increase in the service temperature of 316L due to W wire reinforcement can be achieved but it is not feasible in case of HP alloy.

- Slow growth kinetics of η-phase reaction layer was observed in W/HP composite which can be due to the low Fe:Ni ratio in the composite matrix.

Chapter 7. Preparation of Fe-Ni-Cr based Alloys with Different Fe:Ni Ratios

7.1 Introduction

A key finding of the studies on W/316L and W/HP composites reported in the previous chapters is that the growth kinetics of the intermetallic/carbide layers was slower in HP alloy matrix compared to 316L. Both these alloys contain Cr, Fe and Ni as major alloying elements. Additionally these alloys also contain other minor and trace elements like C, Mo, Si, Mn and Nb. Because of their multicomponent nature, it is difficult to assess the role of individual alloying elements on the growth behaviour of the reaction layers in the composites. Considering Fe:Ni ratio in 316L and HP alloy steel matrices, it can be hypothesised that the growth kinetics of reaction layer is sluggish in the W wire reinforced alloy matrices with low Fe:Ni ratio. In order to validate this hypothesis, new experimental alloys based on Cr, Fe and Ni only were prepared. This chapter describes the composition design and experimental procedures for the casting of experimental alloys. Chemical composition of the cast alloys was analysed using EDS and the discrepancies observed in the cast alloy composition are discussed with reference to the designed composition.

7.2 Composition Design

Five alloy compositions based on Fe-Ni-Cr system were selected for preparation by casting method. The criterion for selection was to narrow down the composition variables to three only. Out of these three variables one can be fixed and other two can be varied in order to have the alloys with different compositions. Therefore, in the designed Fe-Ni-Cr alloys, Cr content was fixed and Fe:Ni ratio was varied. Based on this, the selected alloy compositions can be divided in two groups. First group of alloys contain Cr content equivalent to the average Cr (17 wt.%) in 316 grade stainless steel. In the second group of alloys, the Cr content was fixed to Cr (25 wt.%) in HP alloy stainless steel. In both the alloy groups, the amount of Fe and Ni was varied in order to have Fe:Ni ratios of 0.5 and 2. Table 7.1 shows the designed compositions of the two groups of the experimental alloys. The alloy E-IV listed in the table has Fe:Ni ratio similar to that of standard HP alloy but without any minor and trace elements.

Table 7.1: Designed compositions of the experimental Fe-Ni-Cr alloys. The alloys E-I and E-II have equivalent Cr content as 316L grade stainless steel and alloys E-III, E-IV and E-V have equivalent Cr content as standard HP alloy steel.

Alloys	Composition (wt.%)			Fe:Ni
	Cr	Fe	Ni	
E-I	17	28	55	0.5
E-II	17	55	28	2
E-III	25	25	50	0.5
E-IV	25	37.5	37.5	1
E-V	25	50	25	2

Figure 7.1 shows experimental Fe-Ni-Cr and standard 316L and HP alloy compositions on an isothermal section of the Fe-Ni-Cr phase diagram. All these compositions lie in the γ phase field of the phase diagram.

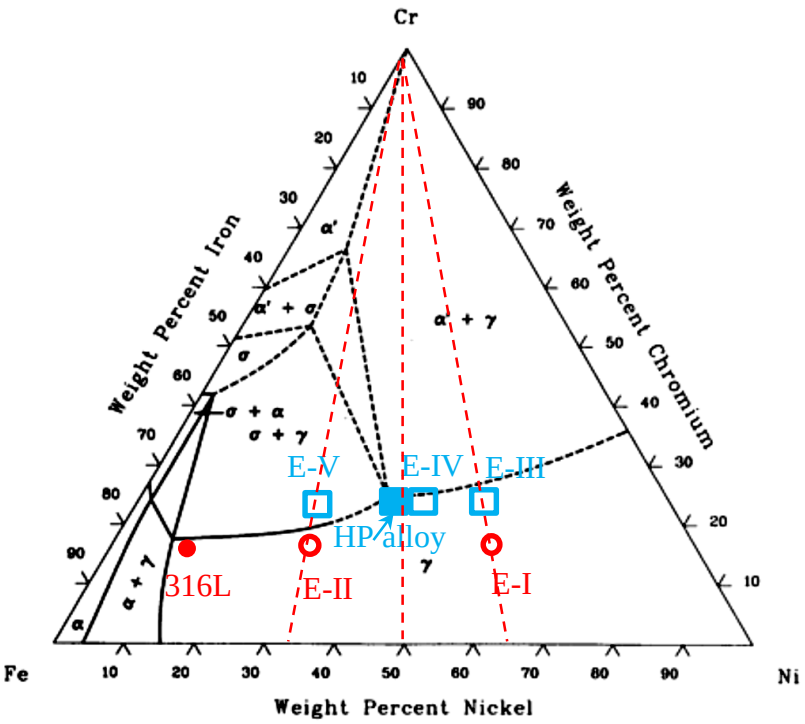

Figure 7.1: Experimental alloys E-I to E-V and standard 316L and HP alloy compositions shown on Fe-Ni-Cr isothermal section. The phase diagram represents phase equilibria at 650°C.The diagram is adopted from [75] .

7.3 Experimental Procedures

7.3.1 Materials and Alloy Preparation

High purity Fe (99.99%, flakes), Ni (99.99%, sheets) and Cr (99.999, flakes) metals procured from ESPI metals-Oregon, USA were used to prepare the experimental Fe-Ni-Cr alloys. For each alloy, a total 1 kg of Cr, Fe and Ni in the required proportion was weighed and placed in a high purity alumina crucible (Size: ID80mm x H93mm, procured from AdValue Technology Arizona, USA). A bench top resistance furnace (heating zone Size: 150mm x 150mm x180mm,. make: Ceramic Engineering-Sydney, Australia) capable of attaining 1700°C was employed for the melting. The crucible containing the metals was placed inside the furnace and heated to a temperature of 1600°C. The molten metal was held for 30 minutes at this temperature in order to ensure complete melting and mixing of constituents to form a uniform molten alloy. After the hold, the melt was cast in the form of rods of size ϕ20mm x L100mm in a steel split mold. Prior to casting, the inside cavity of the mold was coated with a refractory coating and the mold was preheated to 110°C to eliminate any moisture content. A sketch of a typical casting is shown in Figure 7.2.

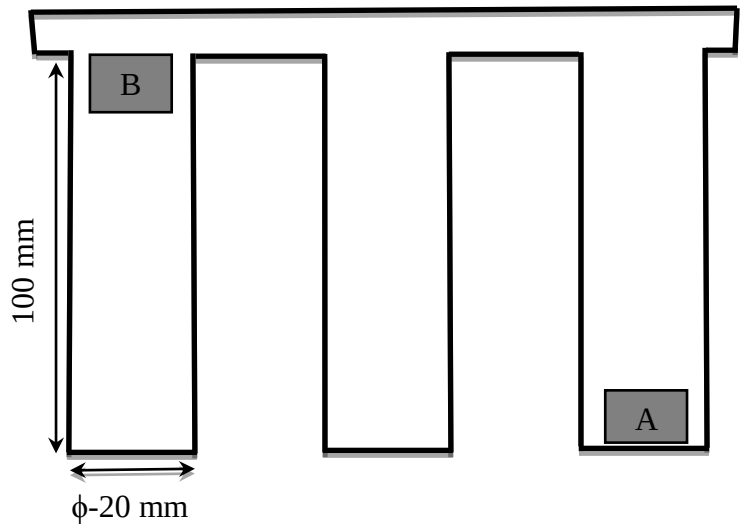

Figure 7.2: Sketch of an alloy casting in the form of three rods. A and B are the locations representing start and finish, respectively, of the liquid metal pouring and the locations of the samples sectioned for chemical analysis.

7.3.2 Sample Preparation and Characterization

For chemical analysis, samples from two locations representatives of first and last solidified liquid were sectioned (A and B in Figure 7.2) and prepared for examination using the standard metallography procedure described in Section 4.4. The chemical analyses on the cast alloy samples were performed using EDS system (JEOL EX-2300 BU) attached to a FEG-SEM (JEOL 7000F). EDS spectra were acquired from the five different locations on each sample to determine the average composition.

7.4 Results and Discussion

The results of EDS analyses on locations A and B are shown in Figure 7.3 for the five experimental alloys. The Figure shows average compositions of Cr, Fe and Ni in the cast alloys at these locations. There is composition inhomogeneity at A and B in all the cast alloys. For example in E-I, the location B has lower Cr and Fe compared to location A. In contrast, Ni content at location B is higher than location A.

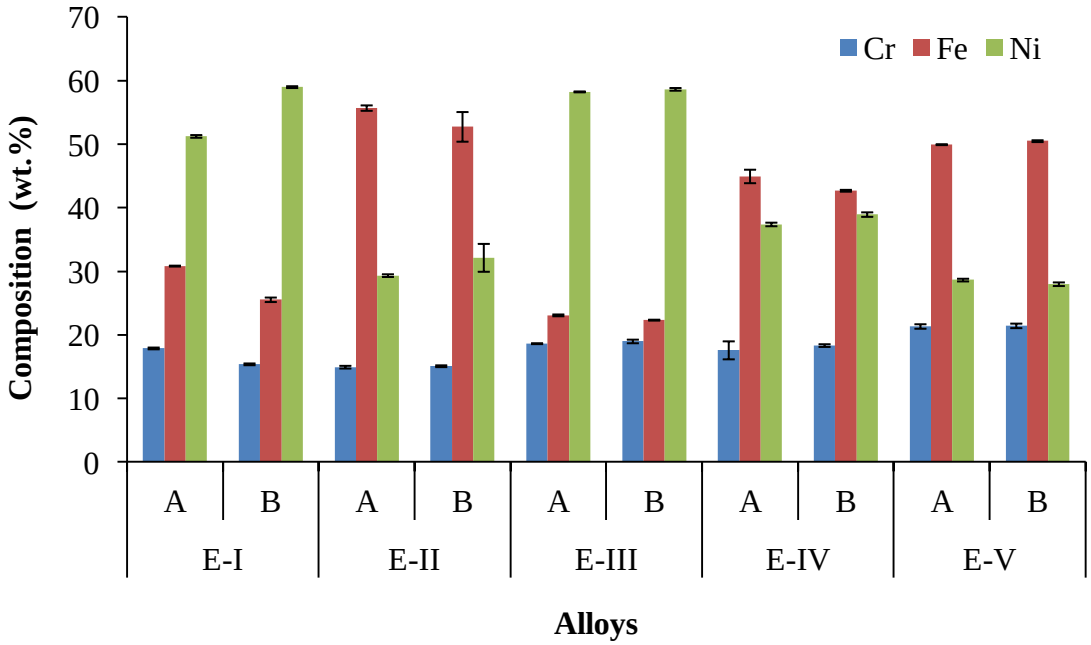

Figure 7.3: Chemical composition of the cast alloys determined by EDS. Error bars are standard deviation of five measurements. A and B are the first and last cast metal (in Figure 7.2).

The average alloy compositions were calculated from an average of composition at locations A and B and are listed in Table 7.2.

Table 7.2: Average chemical compositions and Fe:Ni ratios in the cast experimental alloys.

Alloys	Composition (wt.%)			Fe:Ni
	Cr	Fe	Ni	
E-I	16.7 ±1.4	28.2 ±3.1	55.1 ±4.5	0.5 ±0.1
E-II	15.0 ±0.2	54.2 ±2.2	30.8 ±2.1	1.8 ±0.1
E-III	18.8 ±0.3	25.7 ±0.4	55.5 ±0.3	0.5 ±0.0
E-IV	18.0 ±0.9	43.8 ±1.4	38.2 ±0.9	1.1 ±0.0
E-V	21.4 ±0.3	50.2 ±0.3	28.3 ±0.4	1.8 ±0.0

Cr composition in all the cast alloys is below the targeted composition. The difference is quite significant in the second set of alloys (E-III, E-IV and E-V) where a 16-28% negative deviation from the targeted Cr composition is observed. There are positive and negative deviations in Fe and Ni compositions in the cast alloys. For example in alloys E-I, E-III, E-IV and E-V, Fe and Ni contents exceed from the targets but in E-II Fe is less and Ni is more than the targeted composition. Irrespective of these deviations in Fe and Ni contents, Fe:Ni ratios close to the targets are achieved in all the alloys.

The determined compositions of the experimental alloys are plotted on the Gibbs triangle of the Fe-Ni-Cr phase diagram (Figure 7.4). All the compositions fall in the γ field, indicating that these alloys have solidified with austenitic microstructure.

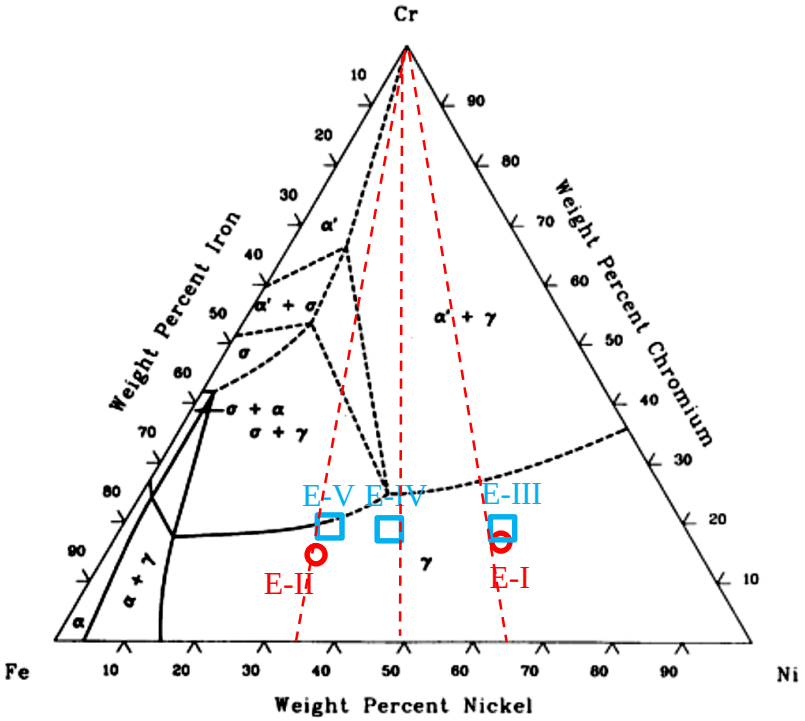

Figure 7.4: Actual composition of the experimental alloys shown on the isothermal section of the Fe-Ni-Cr ternary system at 650°C.

The inhomogenieties and the deviations in the cast alloy compositions from the designed compositions were expected because of the limitations in the melting practice used to cast the alloys. These can be due to (i) no stirring of the liquid alloy, (ii) oxidation of Fe and Cr due to slow heating and melting in open air and (iii) higher melting point of Cr which was difficult to achieve with the existing furnace.

In order to have a better mixing of alloying elements, fast heating of the charge and stirring of molten metal is required. Without any agitation, it is not possible to achieve complete mixing of the alloying constituents in the molten melt. Slow heating due to the use of alumina crucible and melting in open atmosphere resulted in significant loss of elemental Fe and Cr due to oxidation. Bridging of the metal charge was also observed during the alloy melting which was due to the presence of iron and chromium oxides and solid Cr. Bridging restricted the mixing of solid charge and liquid metal during melting. This resulted in the incomplete melting of the alloy constituents which was evident from visual inspection of the residue in the crucible after melting. Since these alloys were to be melted for composites fabrication, it was anticipated that the re-melting would reduce the composition inhomogenieties in the composites matrices.

7.5 Summary

Five Fe-Ni-Cr based alloy compositions with different Fe:Ni ratios were designed. The alloys were cast at 1600°C and their chemical compositions were determined using EDS. All the alloys showed chemical inhomogenieties in the first and last solidified liquid. There was also composition deviation in the cast alloys from the designed composition. In the cast alloys E-II and E-IV, a maximum 28% deviation in Cr from the targeted composition was observed. Overall, Fe:Ni ratios closer to the targeted values were achieved in all the cast experimental alloys.

Chapter 8. Effect of Matrix Composition on Reaction Layer Formation and Growth in Tungsten Wire Reinforced Fe-Ni-Cr Alloys

This chapter presents the studies on microstructure characterization, growth kinetics and diffusivity of the elements in the reaction layers of W wire reinforced Fe-Ni-Cr alloy composites. In the beginning, experimental procedures for the composite fabrication, diffusion annealing and specimens preparation are discussed. It is followed by results which are divided in three sections. In the first section microstructural evolution, chemistry and crystal structure identification of the phases in the reaction zones are presented. In the second section results on the growth kinetics of the reaction layers are described. The third section is on the composition profile analyses and the diffusivity measurements in the reaction layers of the composites. In the end a summary of the findings is presented.

8.1 Experimental Procedures

The cast experimental alloys discussed in Chapter 7 were reinforced with W wires for further investigations. The detailed procedures described in Sections 4.2 to 4.5 were followed for the fabrication, diffusion annealing and characterization of the W/experimental alloy composites. All experimental parameters were the same except the superheat temperature was 1550°C in the fabrication of composites with experimental alloy matrices.

As-cast and diffusion annealed composite specimens were investigated for microstructure evolution, chemistry and crystal structure of the phases formed in the reaction zones of the composites. Thickness measurements on the reaction layers were made to determine the growth kinetics of the layers. Composition profiles acquired across the reaction layers were used to calculate the diffusivities of various elements in the layers.

8.2 Results

8.2.1 Microstructure and Chemistry

8.2.1.1 As-cast Composites

Microstructures in the reaction zones of the composites were investigated at different locations on each cast composite plate. There were variations observed in the microstructures at different locations. The micrographs shown in the following sections are representative of the microstructure of W wires and the region covering reaction zones of the composites.

Microstructures of the as-cast composites with 0.5 Fe:Ni matrix ratio (E-I and E-III) are shown in Figure 8.1. In both cases, there are matrix regions around the wires with different Z contrast in the BSE images (Figure 8.1(a) and (d)). EDS on these matrix regions confirms that they are solid solutions of W in austenite containing 18-20 wt.%W (Table 8.1). This indicates that the W wires in the alloy matrices have experienced dissolution during the process of casting. High magnification images (Figure 8.1(b) and (e)) show no second phase formation around the wire/matrix interfaces in these composites. At some of the locations, penetration of liquid metal inside W wires has occurred (Figure 8.1(c) and (f)). This is visible as the dark regions present at W grain boundaries in the wire. Qualitative EDS analyses from these areas showed that they are composed of Cr, Fe and Ni confirming that liquid metal has penetrated inside some of the W wires during composite fabrication.

Microstructures of as-cast composites with 1 and 2 Fe:Ni matrix ratios (E-IV, E-II and E-V) are shown in Figures 8.2 and 8.3. These composites share some common microstructural features. Reaction zones form around the W wires containing W solid solution in austenite (Figure 8.2 (a) and 8.3 (a), (d)). The average W compositions in the austenite are 21, 22 and 19 wt.% , respectively in E-IV, E-II and E-V composites (Table 8.1). Additionally, a second phase has formed in the reaction zones of these composites that is visible as grey particles in the magnified images (Figure 8.2 (b) and 8.3 (b and e)). EDS analyses on these particles showed that they are rich in W with average W compositions 64, 60, and 60 wt.% in W/E-IV, W/E-II and W/E-V composites, respectively (Table 8.2). Microstructure investigations on different wires in W/E-V composite also revealed the formation of a compound layer around some wires (Figure 8.3 (e)). This type of layer is absent in some other wires, an example of which is shown in the inset image.

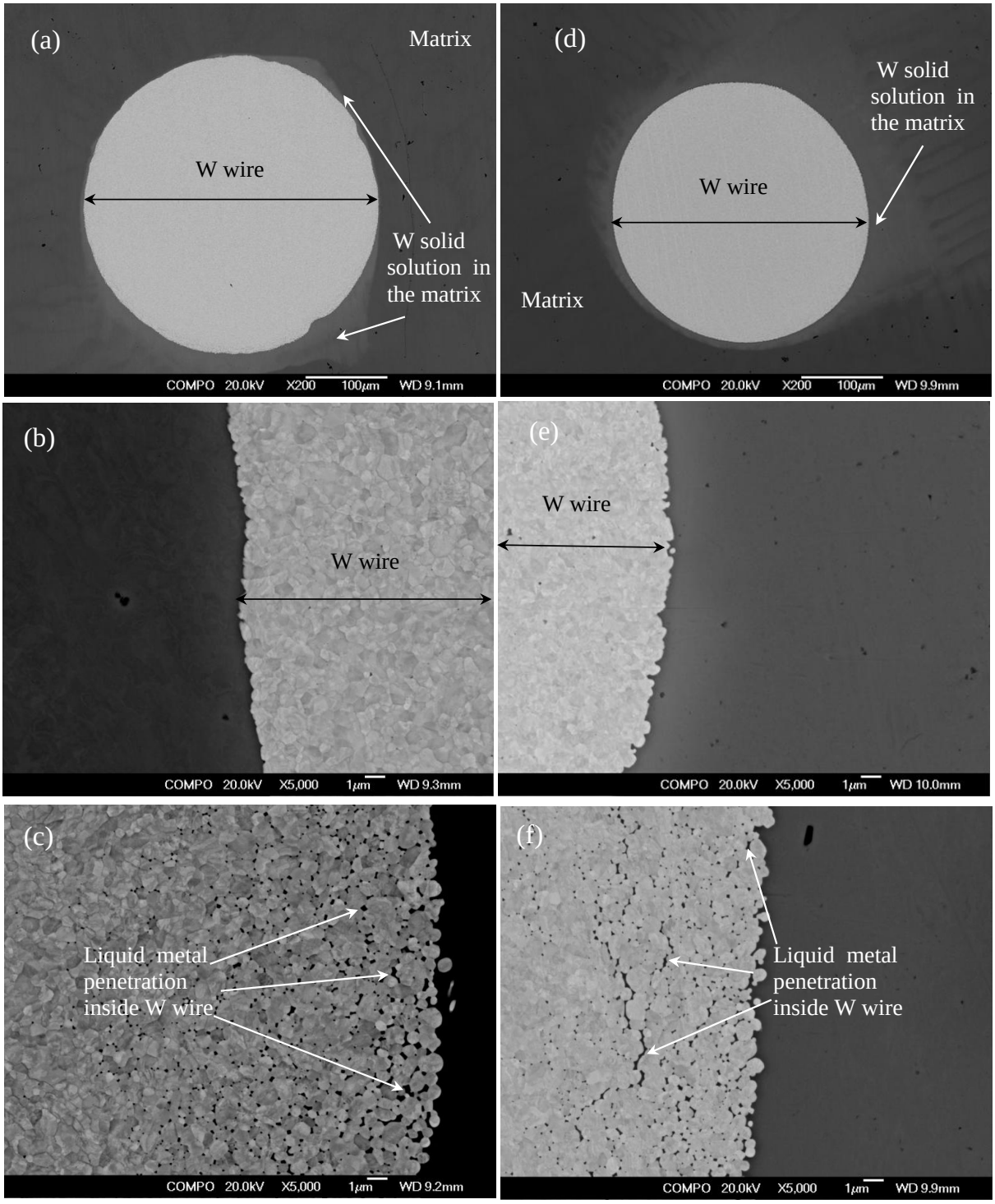

Figure 8.1: BSE images of transverse cross-sections of the W wires in the experimental alloy matrices. (a), (b) and (c) are full wire, reaction zone and liquid metal penetration, respectively for W/E-I composites. (d), (e) and (f) are the corresponding images for W/E-III composite.

The liquid metal penetration inside W grains is observed again in some of the W wires in these composites as shown in Figure 8.2(c) and 8.3(c) and (f).

The microstructures of all the composites discussed in the preceding paragraphs show irregular reaction zones around the wires. Also, there are inconsistencies in the liquid metal penetration inside the W wires. In some wires the penetration has occurred while in others it was not observed at all.

The inconsistencies seen in the microstructures can occur in the composites fabricated by casting method [94]. The presence of reinforcing wires can obstruct the diffusion of solute atoms in the liquid metal and it also affects heat transfer characteristics of the castings during solidification. Also, the W wires in the mold were not equally spaced. This could have caused different solidification conditions around different wires resulting in the observed microstructural inconsistencies in the composites.

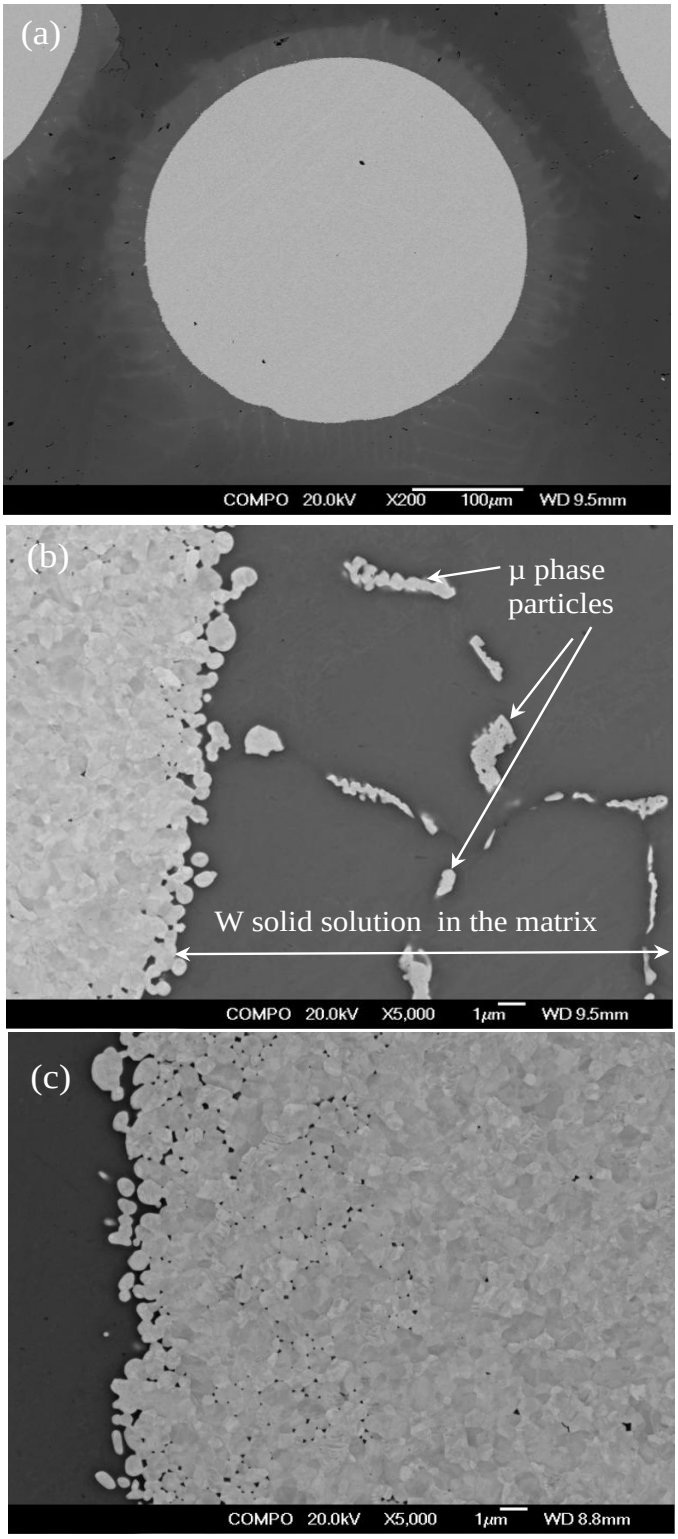

Figure 8.2: BSE images of transverse cross-sections of the W wire in E-IV matrix. Full wire view (a) and (b) the magnified image around the wire/matrix interface including the precipitation of μ-phase are shown. Image (c) shows a W wire inside which penetration of liquid alloy has taken place during the fabrication process.

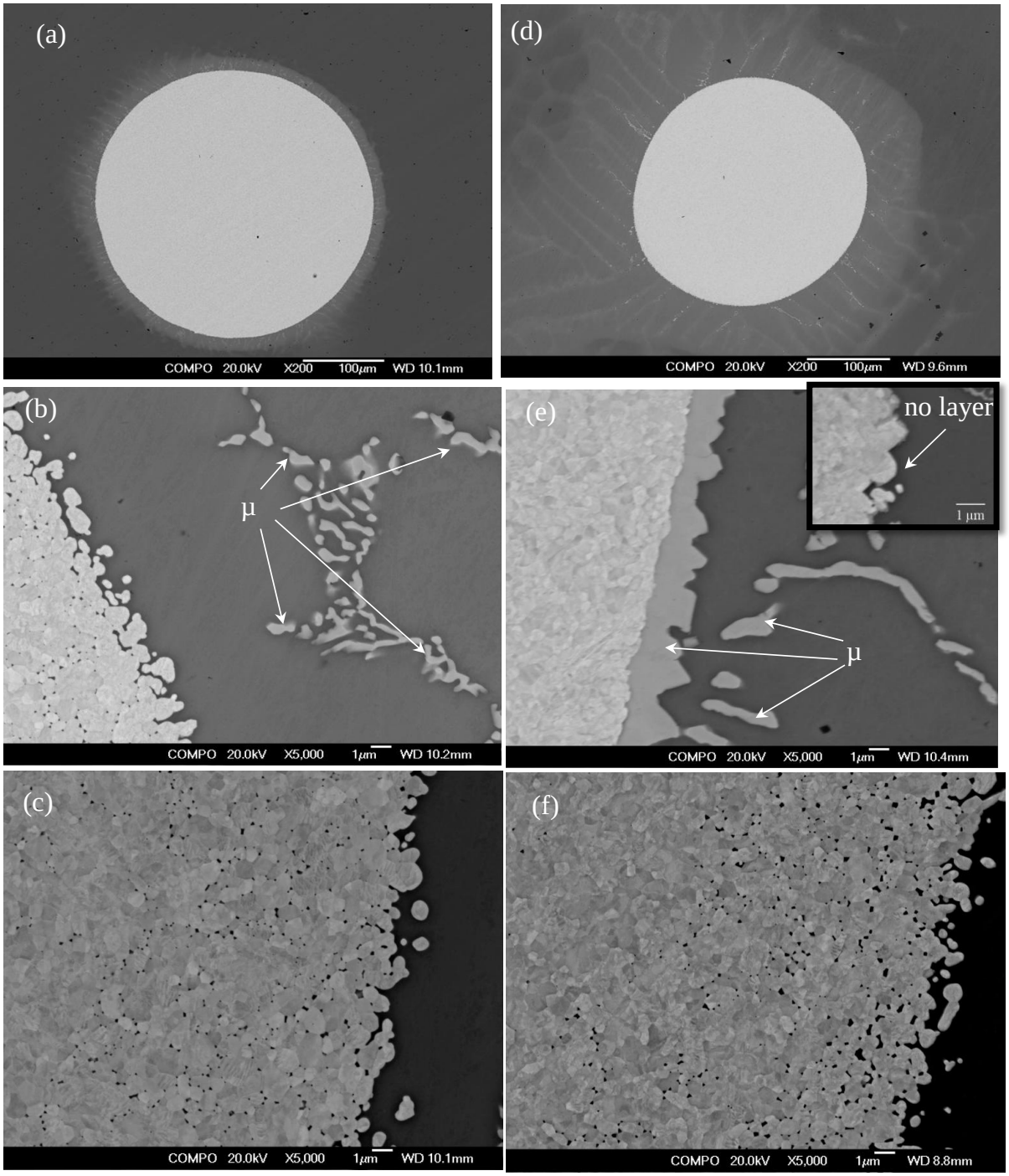

Figure 8.3: BSE images of transverse cross-sections of the W wires in the experimental alloy matrices. (a), (b) and (c) are full wire, reaction zone and liquid metal penetration for W/E-II composites. (d), (e) and (f) are the corresponding images for W/E-V composite. Inset image in (e) shows a wire with no reaction layer around it. Precipitation of μ-phase in the reaction zones is visible in both the composites.

The chemical compositions of the reaction zones and the second phase particles are compiled in Tables 8.1 and 8.2. The reaction zone chemistry in all the cases is quite similar in terms of W content, which ranges from 18-22 wt.%. Similarly, the second phase particles (including compound layer in W/E-V composite) has W composition ranging from 60-64 wt.%. Irrespective of the vast difference in the Ni composition in the composite matrices, the second phase particles have Ni composition ranging from 7-10 wt.% in all the cases. The crystal structures of the second phase particles observed in the matrices with 1 and 2 Fe:Ni ratios were identified by EBSD. The analyses showed that these phases have rhombohedral crystal structure which is consistent with μ-phase commonly found in Fe-W alloys.

Table 8.1: Chemical composition of reaction zones around the wires in the composites.

Composite matrix	Composition (wt.%)			
	Cr	Fe	Ni	W
E-I	10.8 ±1.0	22.4 ±0.8	47.1 ±1.3	19.8 ±3.0
E-III	14.3 ±0.5	20.6 ±1.1	46.9 ±1.1	18.3 ±2.6
E-IV	13.4 ±0.5	34.6 ±0.7	31.0 ±0.4	21.0 ±0.6
E-II	10.7 ±1.3	44.2 ±1.4	23.7 ±0.2	21.5 ±0.1
E-V	18.4 ±0.7	41.3 ±1.8	21.1 ±0.2	19.3 ±1.1

Table 8.2: Chemical composition of the μ-phase particles formed in the reaction zones of the composites with Fe:Ni ratios 1 and 2 in the matrices.

Composite matrix	Composition (wt.%)			
	Cr	Fe	Ni	W
E-IV	9.6 ±0.3	16.7 ±0.6	9.9 ±0.6	63.8 ±0.4
E-II	8.1 ±0.3	23.5 ±1.4	8.3 ±.1.1	60.1 ±2.5
E-V	11.9 ±2.1	21.0 ±2	7.4 ±1.5	59.7 ±5.6

8.2.1.2 Diffusion Annealed Composites

Diffusion annealing of the composites was done at 1000-1200°C for time intervals ranging from 25-500 hours. The microstructures of the composites after 500 hours diffusion annealing at different temperatures are presented and discussed below.

Particles with white contrast are formed in the composites with matrix 0.5 Fe:Ni ratio as a result of diffusion annealing (Figure 8.4).

These particles have two types of morphologies- blocky and plate like and they can be seen around the W wires at all the annealing temperatures. EDS analyses performed on these particles (Figure 8.5) showed that these are essentially rich in W, which is in the range 80-93 wt% in both the composites. They contain less than 5 wt.% Cr and Fe, while Ni ranges from 5-10 wt.%. It seems that there is an interrelation between W, Fe and Ni contents in these particles. These particles become richer in W at the expense of mainly Fe and Ni as the annealing proceeds. EBSD analyses on these phases showed that they have bcc crystal structure consistent with W metal.

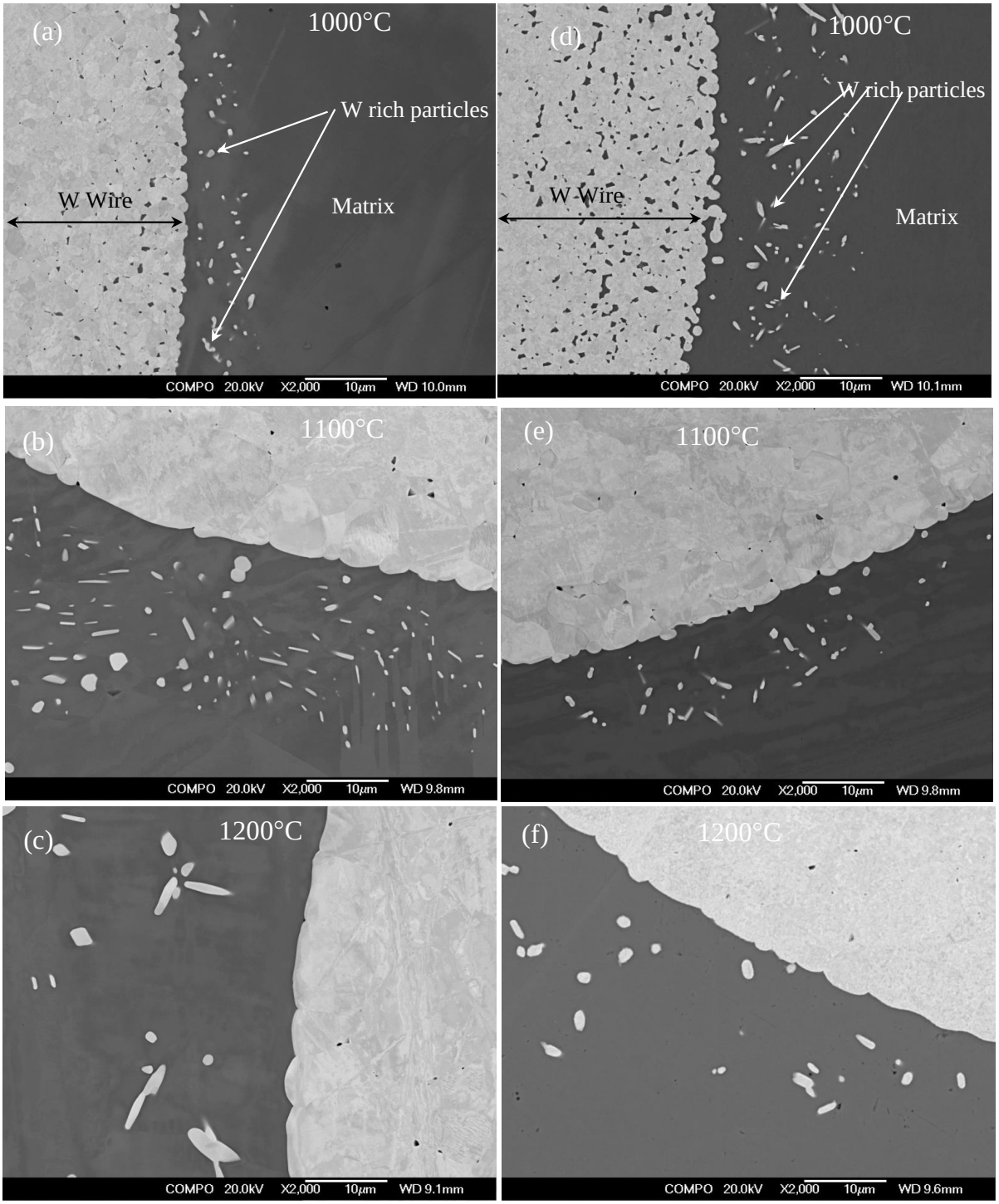

Figure 8.4: Microstructures of the composites after 500 hours diffusion annealing. (a), (b) and (c) are the micrographs for W/E-I composite after 1000, 1100 and 1200°C annealing, respectively. (d), (e), and (f) are the corresponding micrographs for W/E-III composite.

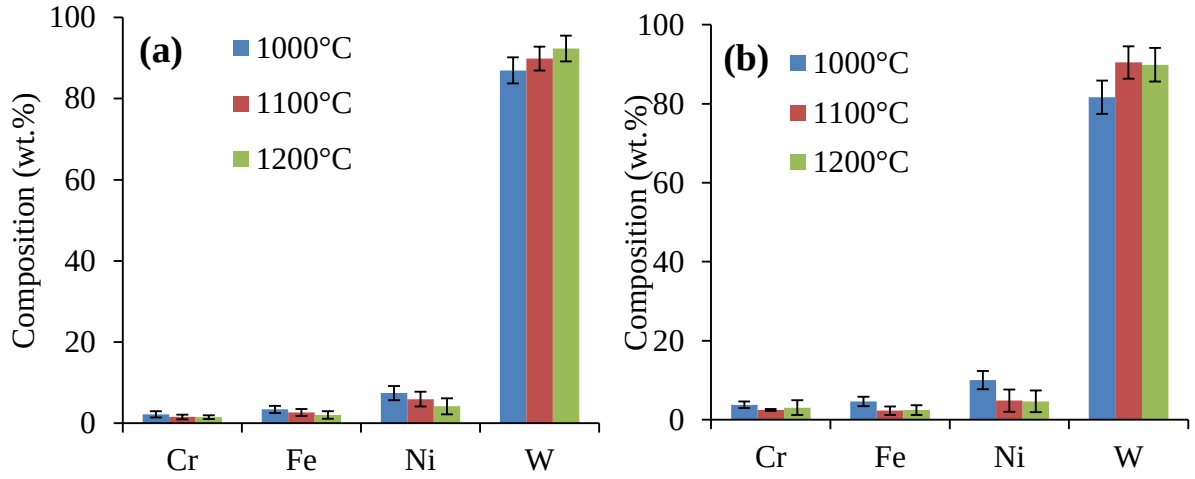

Figure 8.5: Chemical composition of the tungsten rich particles in (a) W/E-I and (b) W/E-III composites.

In the composites with 1 and 2 Fe:Ni matrix ratios, precipitation of second phase particles occurs in the reaction zones around the W wires (Figure 8.6, 8.7). There is also formation of continuous reaction layers around the wires in these composites. These layers grow with the increasing diffusion annealing temperature. The second phase particles in the reaction zones coalesce with increasing annealing temperature, and ultimately become part of the growing layer. It appears in the images that the layers also develop inside the W wires by the growth of the scattered regions in which liquid metal penetration was occurred during the composite fabrication. All the layers contain multiple cracks on them. A noteworthy feature in E-II and E-V is the presence of Kirkendall voids in the reaction zone. These voids are present at the layer/matrix interface at 1000°C and 1100°C (Figure 8.7 (a, b, d, e)), but become a part of the layers at 1200°C (Figure 8.7(c, f)).

Images show that the reaction layers and the particles formed in all these composites have similar Z contrast signifying their composition similarities. EDS results from the layers and particles are shown in Figure 8.8. Both are W-based compounds and the average composition in the particles is 63-65 wt.%, 65wt.% and 62-65 wt.% , respectively in E-IV, E-II and E-V matrices. In the reaction layers, W content is 66-69 wt.%, 67-69 wt.% and 62-65 wt.% in E-IV, E-II and E-V matrices.

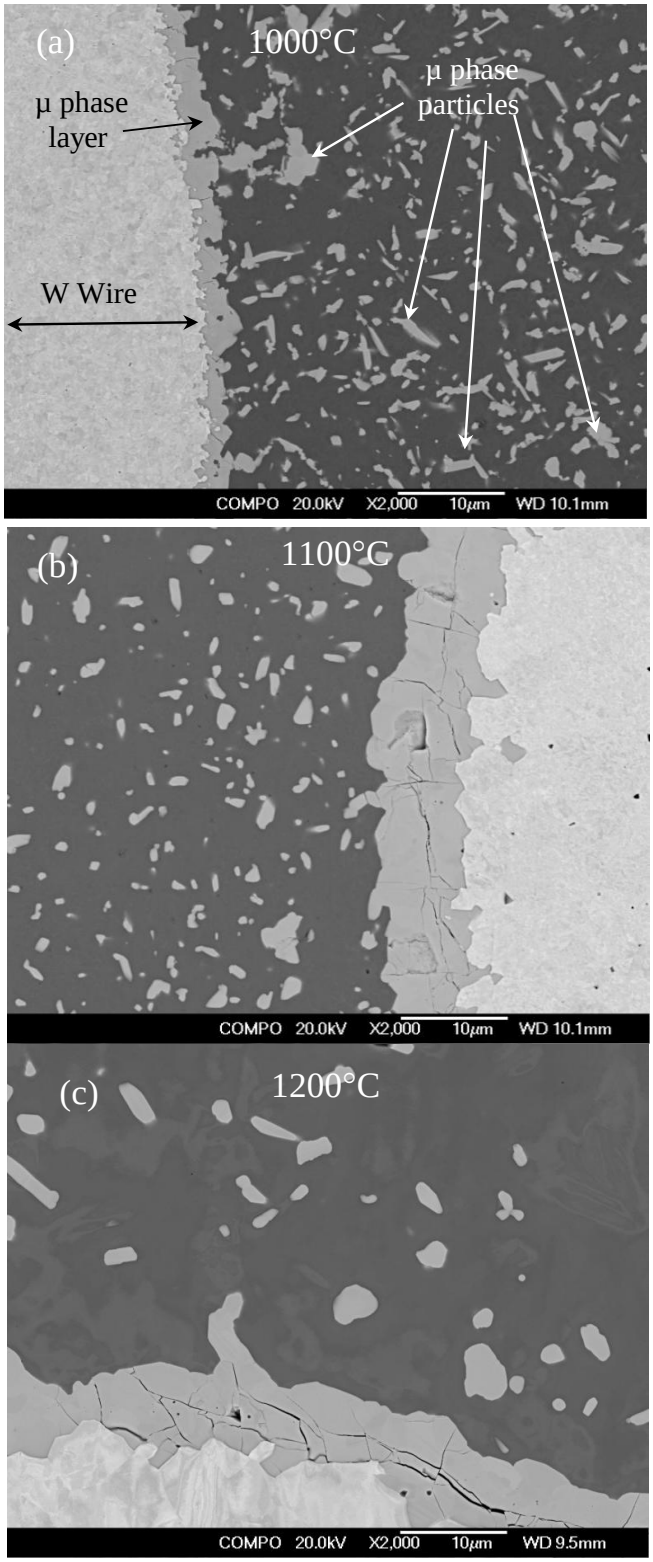

Figure 8.6: Microstructures of the W/E-IV composite after 500 hours diffusion annealing at (a) 1000, (b) 1100 and (c) 1200°C.

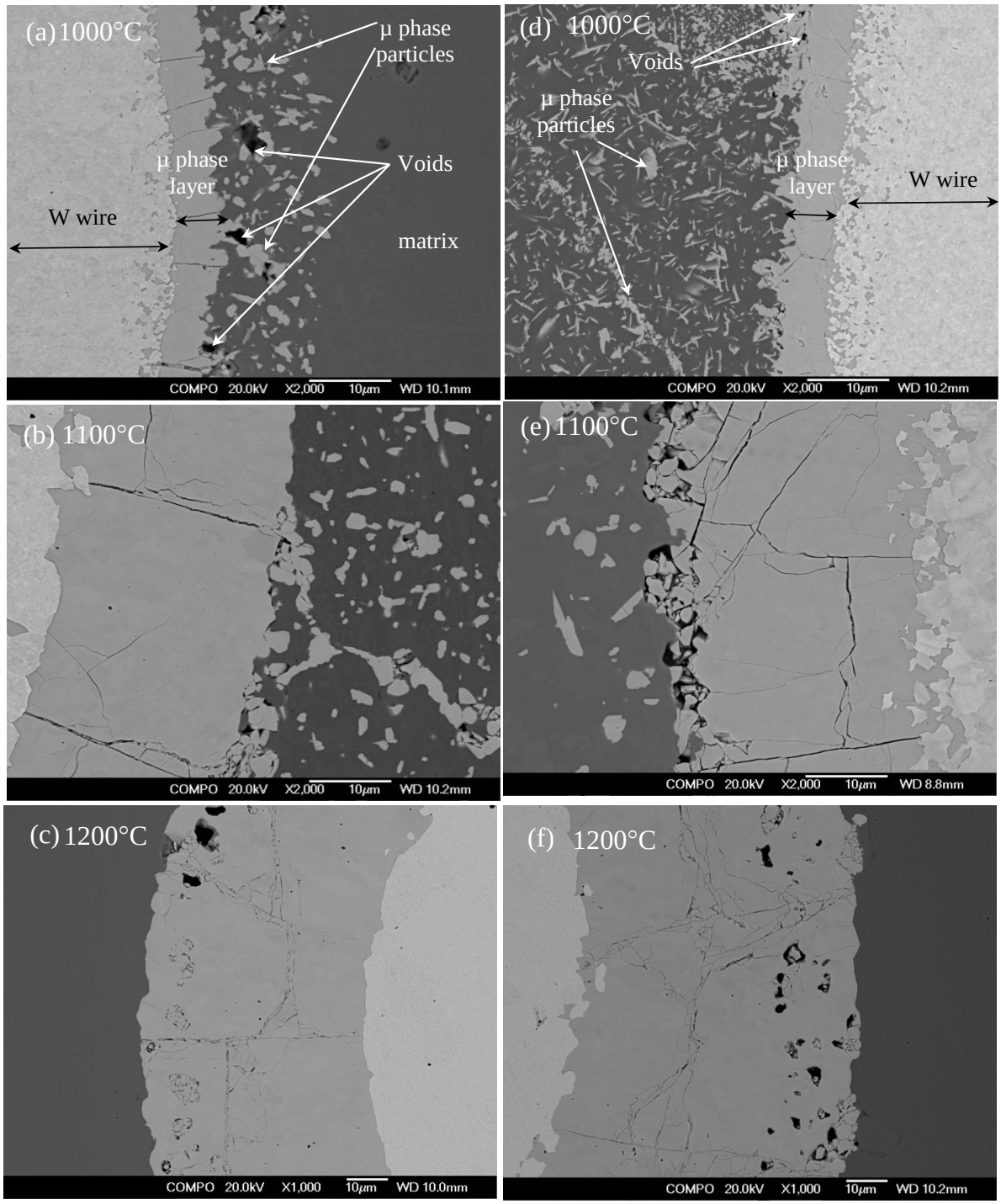

Figure 8.7: Microstructures of the composites diffusion annealed for 500 hours at 1000, 1100 and 1200°C (a, b, c) W/E-II and (d, e, f) W/E-V composite.

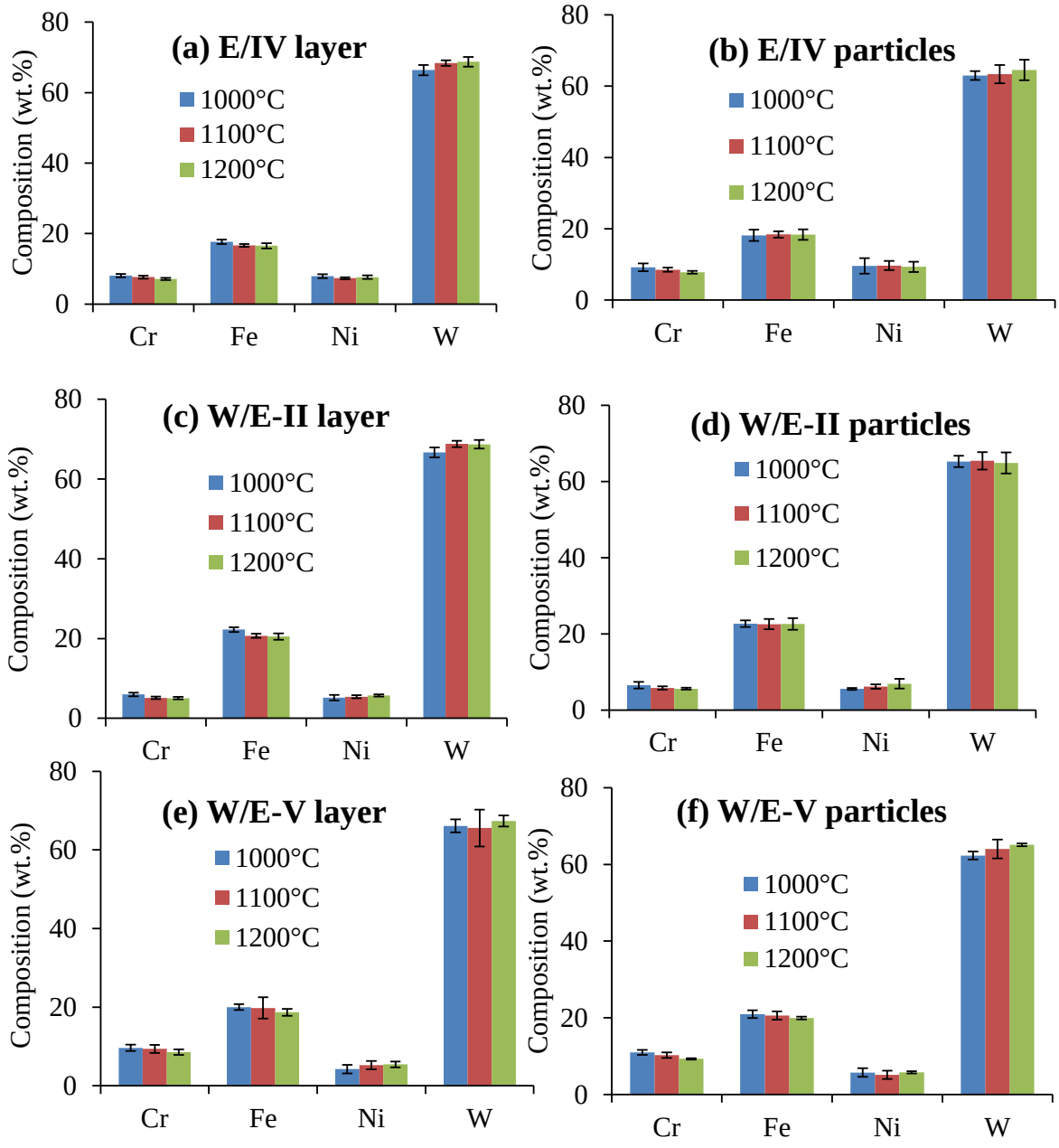

Figure 8.8: Composition of reaction layers and particles observed in the reaction zones of composites diffusion annealed at different temperatures for 500 hours. (a, b) W/IV (1Fe:Ni) (c, d) W/E-II (2Fe:Ni) and (e, f) W/E-V (2Fe:Ni) composite. Error bars are standard deviation of 10 measurements.

In order to determine the crystal structure, EBSP were acquired from the reaction layers and the particles. Matching of the acquired patterns with the probable phases confirmed that both the layers and the particles are isostructural with μ-phase.

The microstructure of the reaction layers in 1200°C/500hours in annealed E-IV, E-II and E-V composites is shown in Figure 8.9. The microstructure of all the layers consists of twins, which is consistent with observations of the μ-phase reaction layer formed in W/316L composite (Section 5.2).

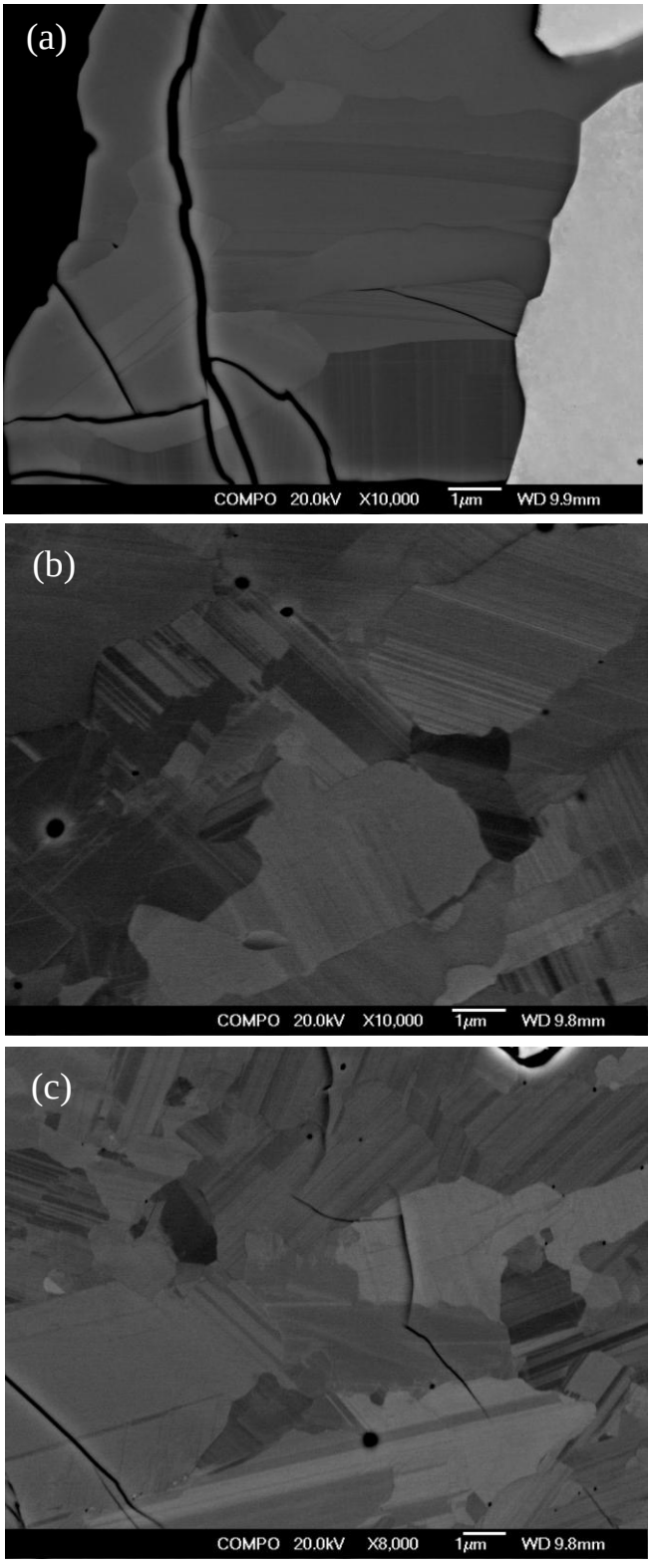

Figure 8.9: Microstructure of the intermetallic layers developed during 1200°C/500hours annealing in (a) W/E-IV (b) W/E-II and (c) W/E-V composites showing twinned grains and trans-granular cracking.

8.2.2 Growth Kinetics of the Intermetallic Layers

As discussed in the previous section, reaction layers consistent with μ intermetallic phase developed in the W reinforced alloys with Fe:Ni ratios 1 (E-IV) and 2 (E-II and E-V). Growth kinetics of these intermetallic layers were determined from the thickness measurements as a function of temperature and time. Figure 8.10 shows plots of intermetallic layer thickness and square root of time for various aging temperatures. The thickness of the intermetallic layers increases linearly with the square root of annealing time and the growth is faster at higher annealing temperatures. For the composite with 1 Fe:Ni matrix ratio (E-IV), the intermetallic layer growth is very sluggish and after 1200°C/500hours its average thickness is just 10 μm. There is significant error in thickness measurements in this case because of the irregular thickness of the layer. The growth of intermetallic layers in the composites with 2 Fe:Ni matrix ratios (E-II and E-V) is quite similar and both attain an average thickness 55 and 66 μm after 500 hours annealing at 1200°C (Figure 8.10 (b) and (c).

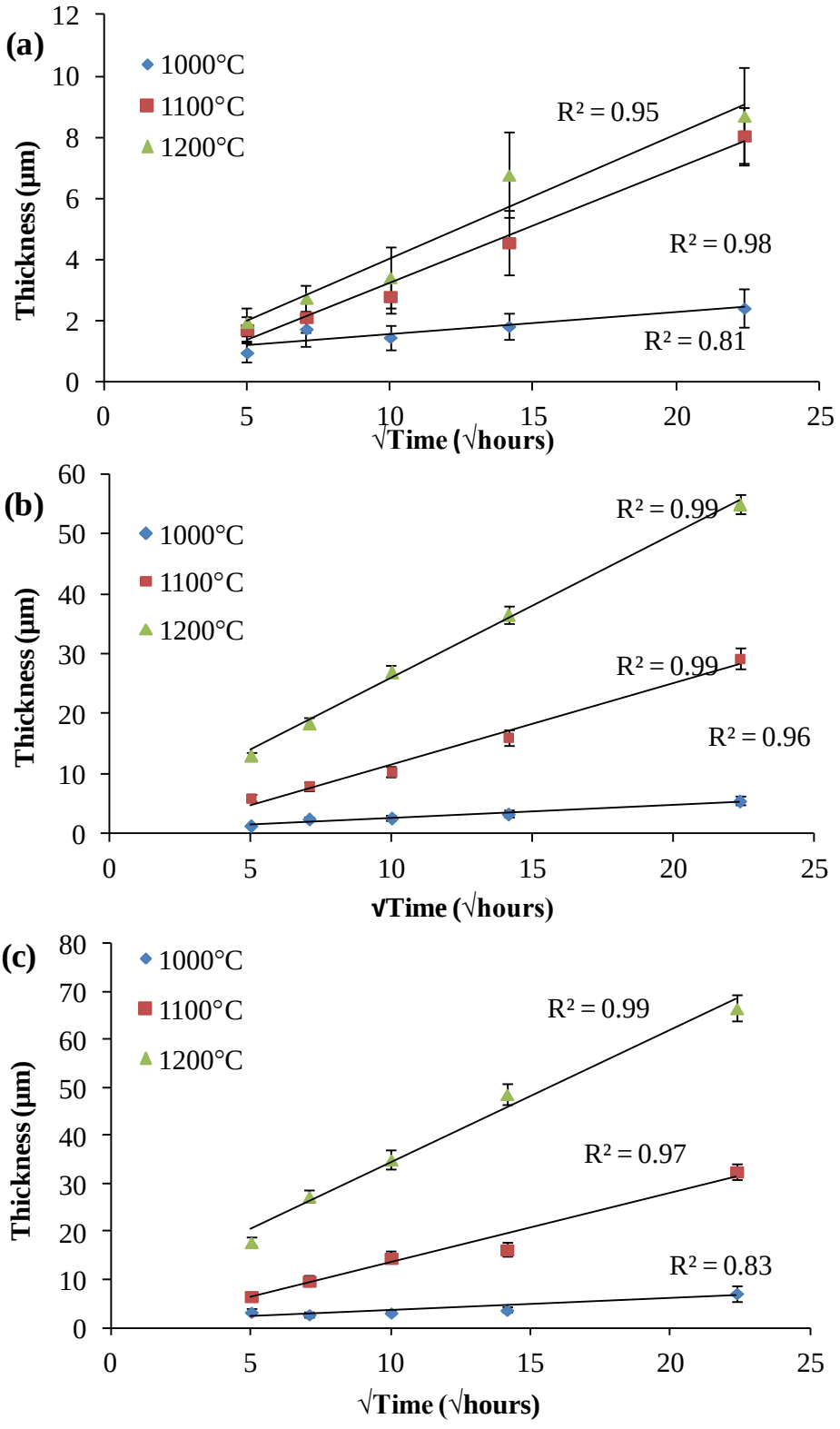

Figure 8.10: Thickness of intermetallic layer versus square root of time plots at different diffusion annealing temperatures in (a) W/E-IV, (b) W/E-II and (c) W/E-V composites. Error bars are standard deviation of 20 measurements. In some cases error bars are smaller than the data points.

Growth constants for intermetallic layers are the slopes of the thickness versus square root plots (Figure 8.10) and are shown in Table 8.3. The growth constants of the intermetallic layers in the composites with 2 Fe:Ni ratios in the matrix (W/E-II and W/E-V) are close to each other at all the temperatures. Comparison at 1200°C shows that growth constant of the reaction layer in the matrix with 1 Fe:Ni ratio (W/E-IV) is approximately 6-7 times slower than in the matrices with 2 Fe:Ni ratios (W/E-II and W/E-V).

Table 8.3: Growth constants for the μ-phase intermetallic layers in the composites with different Fe:Ni ratios in the matrices. Error bars are the standard errors in the slopes from Figure 8.10.

Temperature (°C)	k (μm√h)		
	W/E-IV	W/E-II	W/E-V
1000	0.07 ±0.02	0.22 ±0.02	0.24 ±0.06
1100	0.37 ±0.03	1.35 ±0.09	1.44 ±0.15
1200	0.41 ±0.05	2.41 ±0.07	2.75 ±0.19

We have discussed previously (Section 3.4) that the activation energy for the growth of reaction layers can be derived from the Arrhenius equation. Arrhenius plots for the composites W/E-IV, W/E-II and W/E-V are shown in Figure 8.11. The activation energies for layer growth (Q_G) and pre-exponential factors (k_0) calculated from the plots are listed in Table 8.4. The activation energy for intermetallic layer growth in matrix with 1 Fe:Ni ratio is the least, but there is large standard error (~ 47%) associated with it due to the inherent irregularities in the layer thickness. The activation energies for growth in the two matrices with 2 Fe:Ni ratio is almost similar and the standard error lies well within 25%.

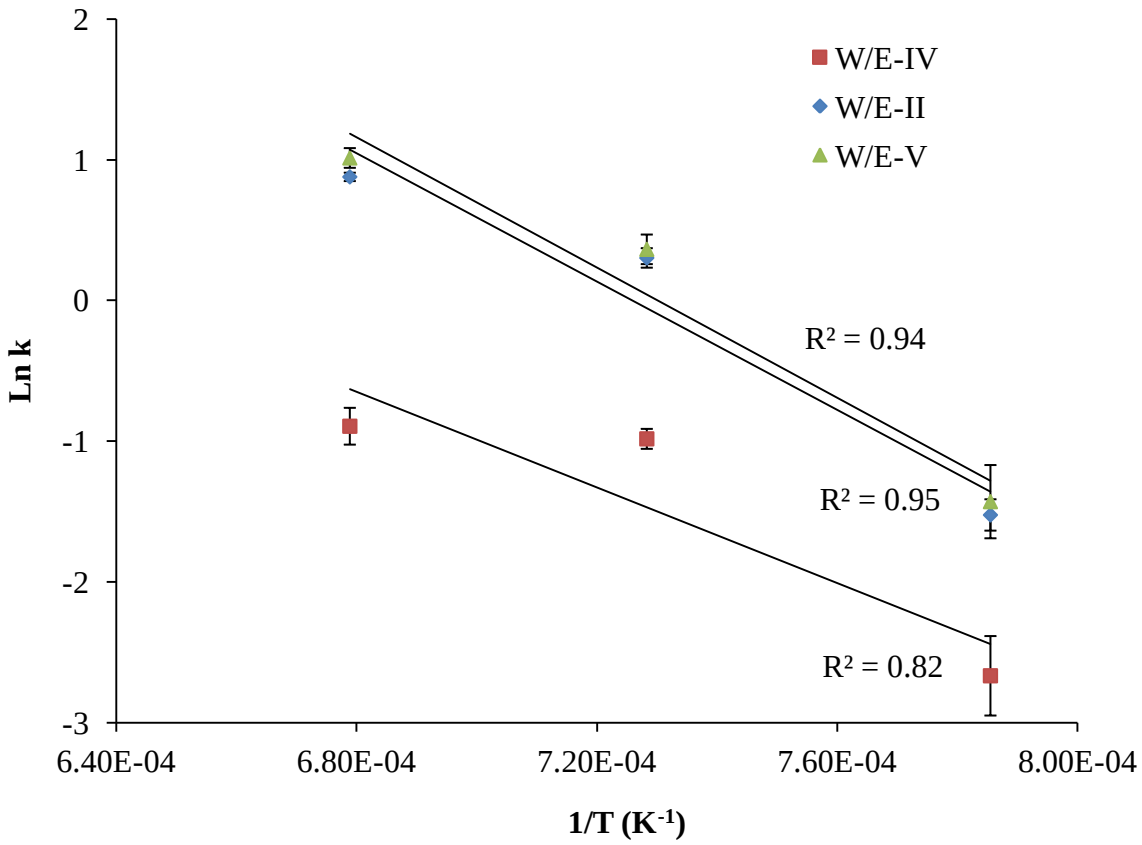

Figure 8.11: Arrhenius plots of the intermetallic growth constants in the composites with 1 (W/E-IV) and 2 Fe:Ni (W/E-II and W/E-V) matrix ratios.

Table 8.4: Activation energies and pre-exponential factors for µ-phase layer growth in W/E-IV, W/E-II and W/E-V composites in temperature range 1000-1200°C.

Composite	Q_G (kJ mole^{-1})	k_0 (µm/√h)
W/E-IV	141 ±47	5.42E+04
W/E-II	189 ±26	1.98E+07
W/E-V	192 ±23	1.51E+07

8.2.3 Interdiffusion Behaviour

In order to study the interdiffusion behaviour of Cr, Fe, Ni and W in the intermetallic layers, composition profiles across the layers were acquired by EDS according to the procedure detailed in Section 4.5.2. The acquisition was done on the samples annealed for 500 hours at temperatures 1000-1200°C. Typical composition profiles for 1200°C/500 hours diffusion annealed composites are discussed below.

8.2.3.1 Composites with 0.5 Fe:Ni Matrix Ratios

The composition profiles acquired from W/E-I and W/E-III are shown in Figures 8.12 and 8.13. There are sharp transitions in the composition of Cr, Fe, Ni and W at the wire/matrix interfaces. There is no observable intermediate phase between the wires and matrices in these composites. It appears that Ni composition in both matrices does not vary with distance indicating that no diffusion of Ni takes place in the matrices of these composites. W has a positive composition gradient in the matrix (towards the wire) showing that W diffusion down the concentration gradient takes place in the matrices of these composites. The Cr and Fe composition profiles have negative (towards the W wire), but very small gradients in the matrices of these composites.

There are no reaction layers formed in W/E-I and W/E-III composites. Therefore, no interdiffusion coefficients were determined.

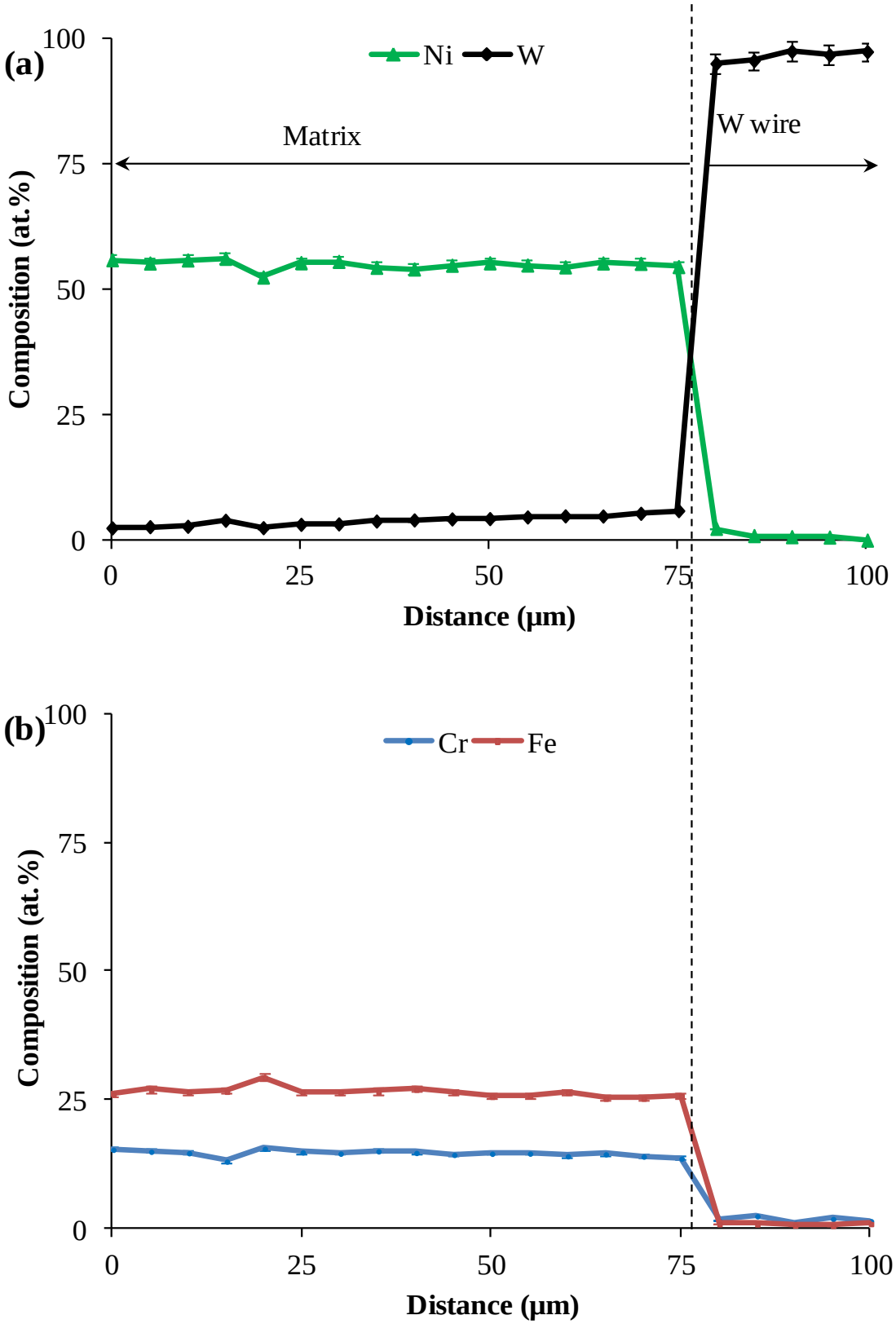

Figure 8.12: Composition profiles of (a) Ni, W and (b) Cr, Fe covering wire and matrix regions adjacent to W/matrix interface in 1200°C/500hours diffusion annealed composite with 0.5 Fe:Ni matrix ratio (W/E-I).

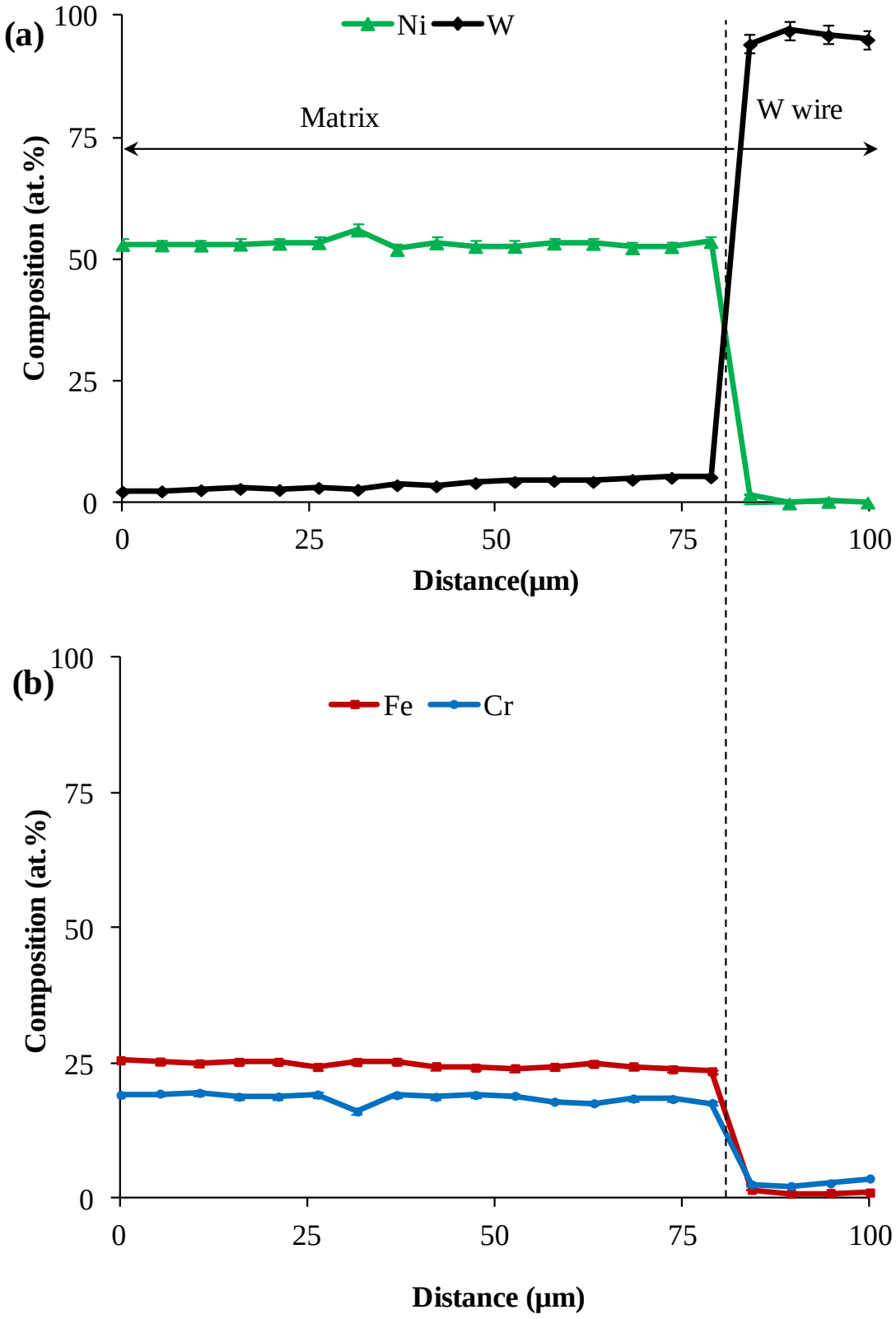

Figure 8.13: Composition profiles of (a) Ni, W and (b) Cr, Fe covering wire and matrix regions adjacent to W/matrix interface in 1200°C/500hours diffusion annealed composite with 0.5 Fe:Ni matrix ratio (W/E-III).

8.2.3.2 Composites with 1 and 2 Fe:Ni Matrix Ratios

Typical composition profiles across the intermetallic layers for composite matrices with 1 Fe:Ni ratio (W/E-IV) are shown in Figure 8.14. The profiles in these composites are divided into three distinct regions comprising matrix, intermetallic layer and W wires. In the intermetallic layer, Cr and Ni profiles do not show any composition gradient. There is a shallow positive gradient in W and negative gradient in Fe composition across the intermetallic layer.

The composition profiles of the composites with 2 Fe:Ni matrix ratios (W/E-II and W/E-V)) are shown in Figures 8.15 and 8.16. Cr, Fe, Ni and W profiles in both the cases seem to have no observable composition gradient in the intermetallic layers.

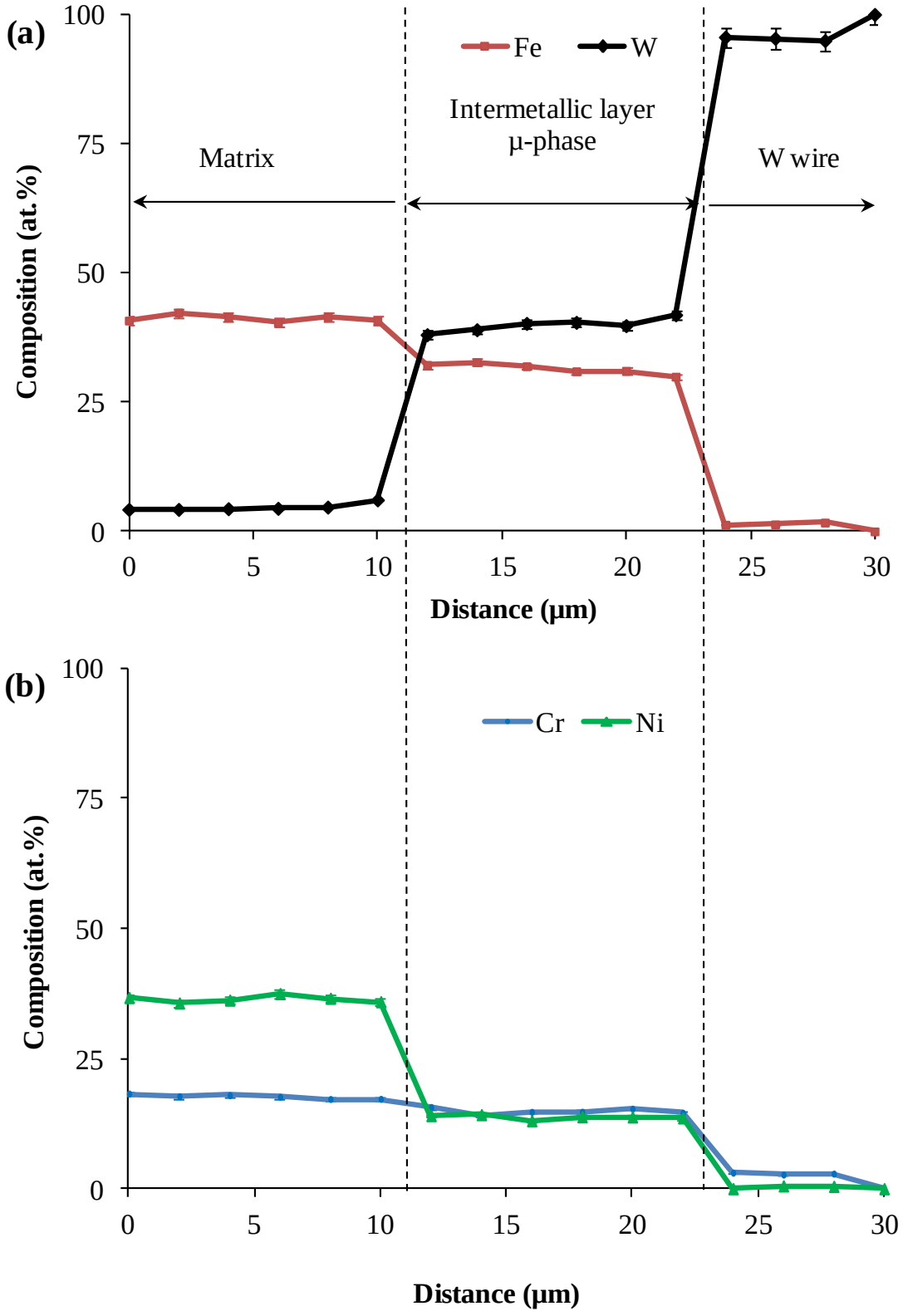

Figure 8.14: Composition profiles of (a) Fe, W and (b) Cr, Ni covering wire and matrix regions and the whole intermetallic layer in W/E-IV composite after 500 hours annealing at 1200°C.

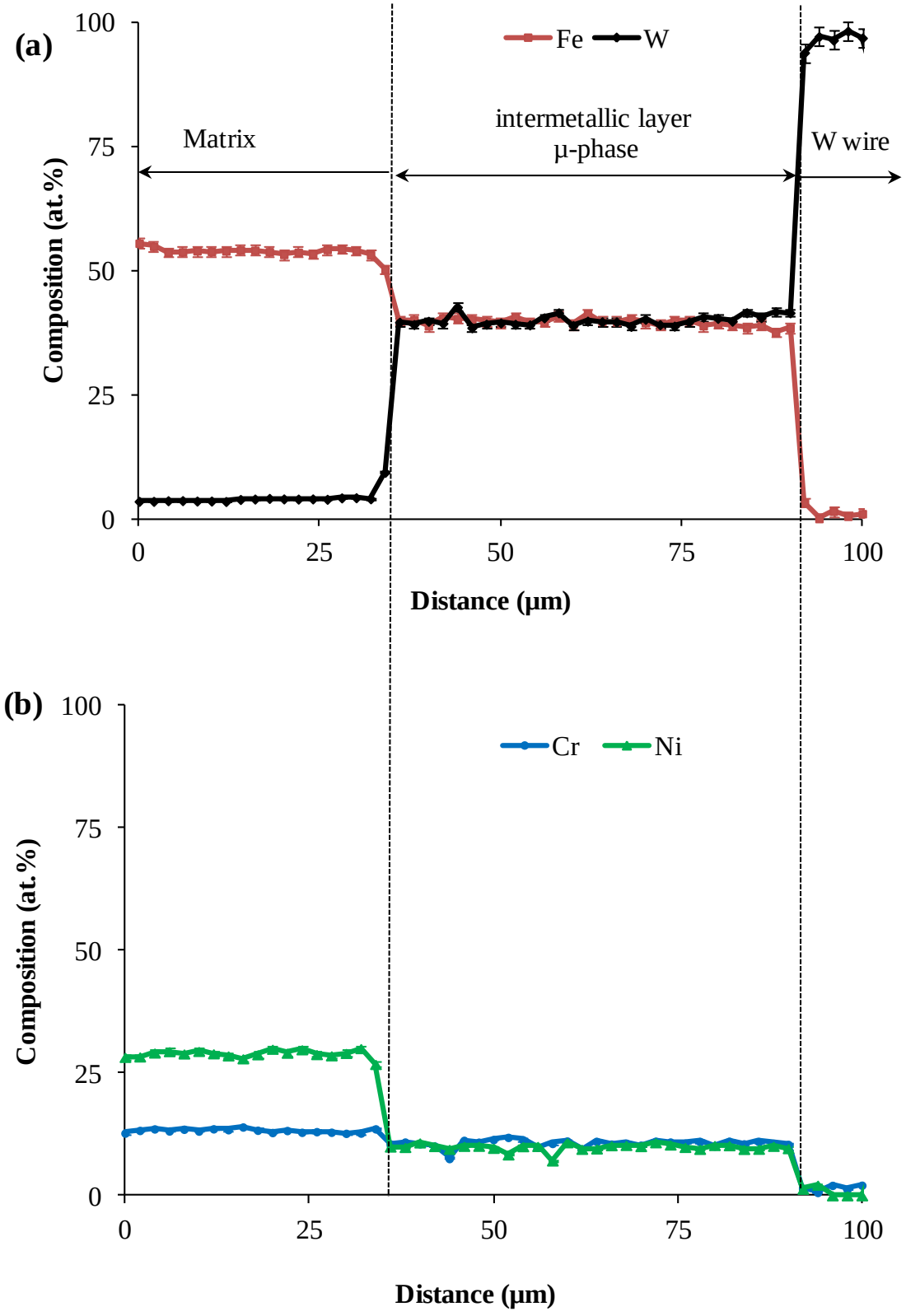

Figure 8.15: Composition profiles of (a) Fe, W and (b) Cr, Ni covering wire and matrix regions and the whole intermetallic layer in W /E-II composite after 500 hours annealing at 1200°C.

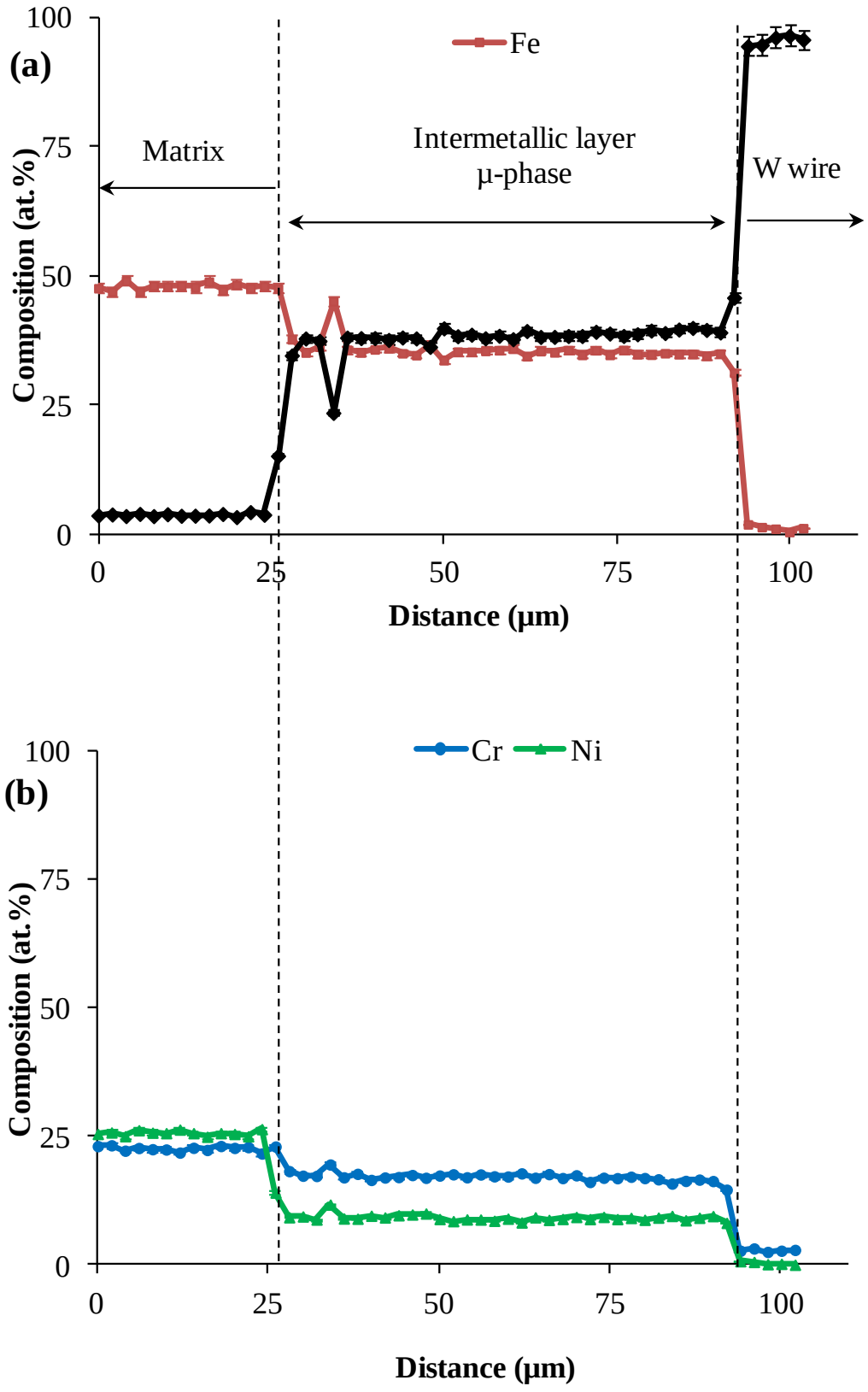

Figure 8.16: Composition profiles of (a) Fe, W and (b) Cr, Ni across the intermetallic layer in W /E-V composite after 500 hours annealing at 1200°C.

8.2.3.3 Diffusion Coefficients

The $\widetilde{\overline{D}}^{i}_{eff\,(\mu)}$ in the intermetallic layers were determined in the composites with matrix ratios 1 and 2. For the calculation of $\widetilde{\overline{D}}^{i}_{eff\,(\mu)}$, all the composition profiles were subjected to linear fitting. The fitting resulted in poor R^2 values and as described in Appendix.B, the composition profiles were filtered out using the F-test. $\widetilde{\overline{D}}^{i}_{eff\,(\mu)}$ for the composition profiles that passed the F-test were calculated using the procedure given in Section 3.3. The results are presented in Table 8.5.

Table 8.5: Calculated average effective interdiffusion coefficients of Cr, Fe, Ni and W in the intermetallic layers of W/Fe-Ni-Cr composites at different temperatures.

Composite	Temperature (°C)	$\widetilde{\overline{D}}^{i}_{eff\,(\mu)}$ (m^2/s)			
		Cr	Fe	Ni	W
W/E-IV	1000		3.0E-18	2.6E-18	4.6E-18
	1100			5.1E-17	5.9E-17
	1200		8.0E-17		2.1E-16
W/E-II	1000			3.7E-17	
	1100	2.5E-16	1.5E-15	1.3E-15	1.2E-15
	1200		5.9E-15		9.3E-15
W/E-V	1000	1.2E-17	2.3E-17		3.6E-17
	1100	4.7E-16	8.2E-16		1.2E-15
	1200	2.8E-15	2.4E-15		3.3E-15

Comparison of $\widetilde{\overline{D}}^{i}_{eff\,(\mu)}$ in W/E-IV and W/E-V at 1200°C shows that with an increase in the Fe:Ni ratio, $\widetilde{\overline{D}}^{Fe}_{eff\,(\mu)}$ increased by two orders of magnitude while for W, the interdiffusion coefficient increased by one order in magnitude.

The temperature dependence of $\widetilde{\overline{D}}^{i}_{eff\,(\mu)}$ was investigated for W/E-V composite by plotting ln $\widetilde{\overline{D}}^{i}_{eff\,(\mu)}$ versus *1/T*. These plots for Cr, Fe and W are shown in Figure 8.17. Fitted straight

lines in these plots are consistent with the Arrhenius relation (Equation 3.64) for diffusion. The activation energies (Q_D) of diffusion and pre-exponential factors (D_0) for different elements in the intermetallic layers were calculated from the Arrhenius plots and are listed in Table 8.6.

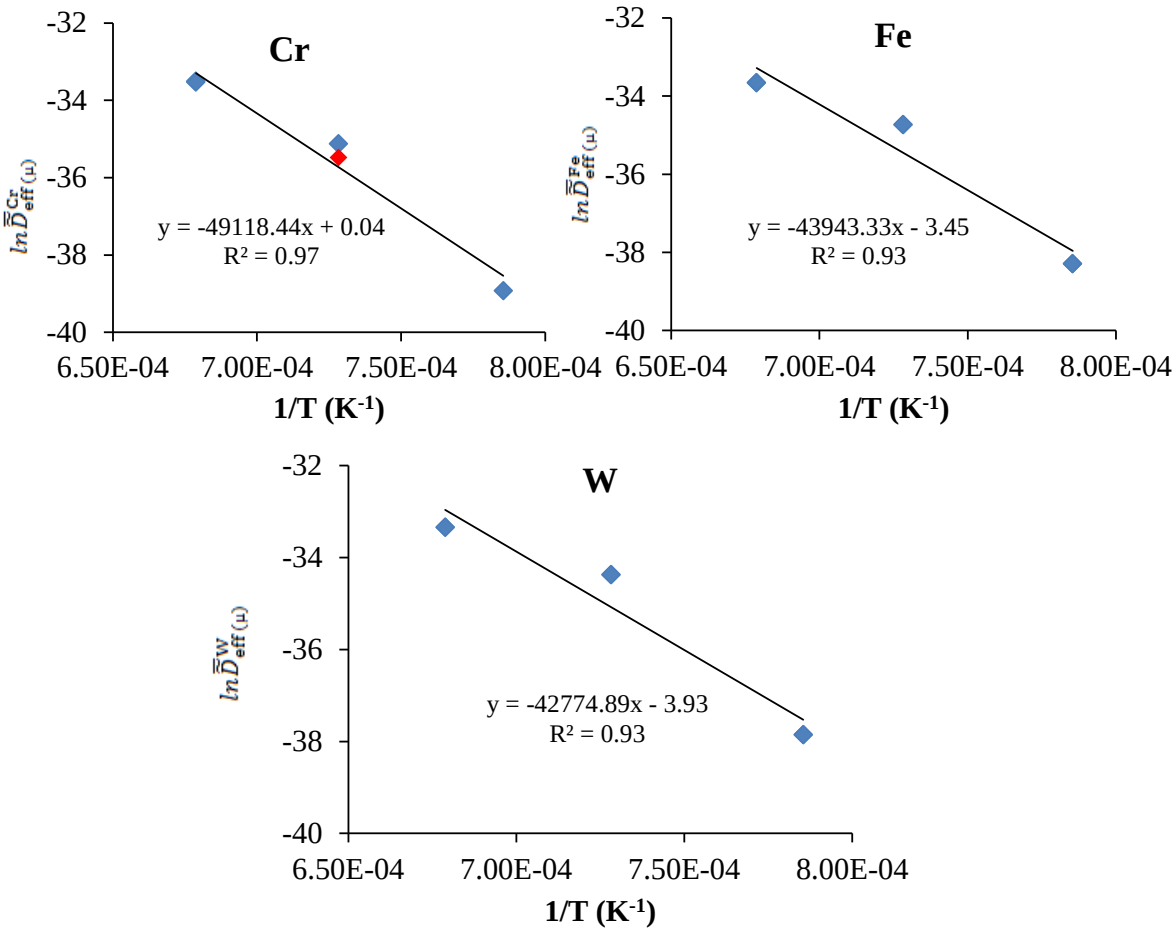

Figure 8.17: Arrhenius plots for Cr, Fe, and W in µ-phase layers of W/E-V composite annealed for 500 hours in the temperature range 1000-1200°C.

Table 8.6: Activation energies for diffusion and pre-exponential factors for various elements in the μ-phase reaction layers of W/E-V composite.

Element	Q_D^i (kJ mole^{-1})	D_0 (m^2/s)
Cr	408	1.3E+01
Fe	415	1.2E-02
W	356	2.0E-02

8.3 Discussion

Results of W/Fe-Ni-Cr studies clearly show the effect of matrix composition on intermetallic phase formation and growth in the composites. Low Fe:Ni matrix ratio (0.5:1) inhibits formation of intermetallic phases in the composites. However, when the ratio in the composite matrix was increased to 1 and 2, the μ-phase appeared in the reaction zone of the composites.

Furthermore, composites with 0.5Fe:Ni ratio in the matrix remained intermetallic free after diffusion annealing for as long as 500 hours at 1000-1200°C. Annealing of the composites with 1 and 2 Fe:Ni matrix ratio under similar conditions caused growth of μ-phase reaction layers between W wires and the matrices. The growth kinetics of these interphase layers during annealing is also found to be dependent on Fe:Ni ratio. Layers in composite matrix with 1 Fe:Ni ratio developed more slowly than the layer in the matrix with 2Fe:Ni ratio.

The absence or presence of μ-phase in the composites can be understood from the phase diagrams. Isothermal sections of Fe-Ni-W phase diagram given in Figure 8.18 show equillibria between γ and other phases at different temperatures. It appears from the diagrams that solubility of W in γ decreases with decreasing temperature and also γ+μ+(W)/γ+(W) phase boundary moves towards higher Ni contents in the diagrams. We have seen that the solidification of the composites resulted in the dissolution of about 20% W in γ matrix in the reaction zones of all the composites with different Fe:Ni matrix ratios (Table 8.1).

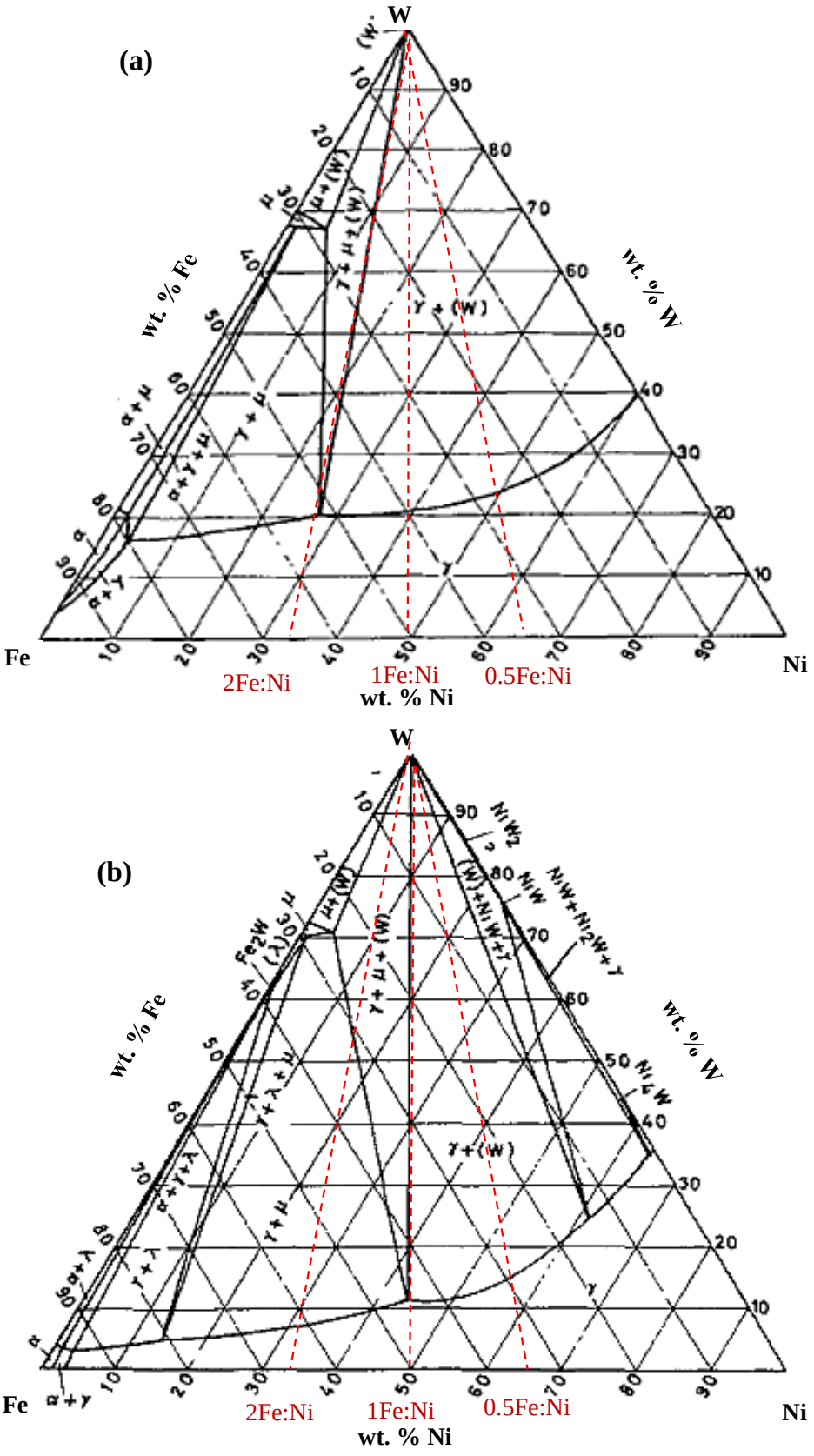

Figure 8.18: Isothermal sections of Fe-Ni-W phase diagram at (a) 1300 and (b) 800°C [81]. Red dotted lines represent three Fe:Ni ratios: 2, 1 and 0.5.

Since 0.5Fe:Ni ratio lies in the γ+(W) phase field on the isothermal sections (Figure 8.18), it appears that during diffusion annealing the composites with 0.5Fe:Ni matrix ratio will result in the precipitation of W in γ matrix containing dissolved W. Alloys with a 2:1 Fe:Ni ratio lie in the region where equilibrium between γ/γ+μ exists. Therefore, it can be anticipated that in the composites with this matrix ratio, precipitation of μ phase will occur during diffusion annealing. The Fe:Ni ratio 1 also lies in the γ+W phase field, but formation of μ-phase reaction layer was observed in these composites. It is important to mention that the justification made here does not take into account the effect of non-equilibrium solidification of the composites and also the presence of Cr in the composite matrix. Both these factor can alter the phase equillibria between various phases shown in the phase diagram.

Slow growth of μ-phase reaction layer was observed in the matrices with low Fe:Ni ratio (1 and 2). The observed parabolic growth of reaction layers suggested that the growth was controlled by diffusion of elements in the layer. All the μ-phase reaction layers developed in the composites under investigation have similar composition, irrespective of the matrix composition in which they grow. If the growth was purely due to the diffusion through the layer, it would not be significantly influenced by the matrix composition because excess matrix elements were rejected back into the matrix during diffusion annealing and they did not participate in the reaction. Therefore, the growth kinetics of the μ-phase reaction layers would be approximately equal for different matrices. However, in the present study, the layer growth was found to be a strong function of matrix composition. The observed differences of the growth in various matrices can be attributed to change in reactivity of the diffusing elements at the reaction layer/matrix interface due to matrix chemistry, which led to different growth rate of the reaction layers.

From the application point of view, the composites with 1 and 2 Fe:Ni ratios may not be suitable for use as creep resistant materials because the brittle intermetallic phase μ forms and grows during exposure to higher temperature. The weak interface between the wire and the matrix developed in these composites may not effectively transfer load from the matrix to stiffer W wire, which is a prerequisite for realizing better creep strength in the composites. On the other hand, there was no formation of intermetallic phases in the composites with 0.5 Fe:Ni matrix ratio after diffusion annealing. Commercial Fe-Ni-Cr alloys with more that 50% Ni are reported to have service temperatures >1000°C [95] indicating that alloys with 0.5 Fe:Ni can be used in service at least up to 1000°C. Also no cracking or voids were observed

at the wire/matrix interface of the composites with this matrix ratio that ensures strong bonding between W wire and alloy matrix. Note that the matrix of these composites does not contain any carbide forming element like Cr, Nb and Ti that provide creep strength in commercial stainless steels. However, the reinforced W wires in these alloys will bear the load at high temperature and prevent matrix deformation due to creep. For effective load transfer, the absence of brittle reaction layers is desirable. Therefore, the alloy with 0.5Fe:Ni ratio can be an ideal matrix alloy and should be further studied for any improvement in creep properties as a result of its reinforcement with W wires.

8.4 Summary

The effect of composition on the microstructure evolution and growth of intermetallic phases in W/Fe-Ni-Cr composites was studied in this chapter. The results are summarized below.

- The intermetallic phase formation and growth in the composites was found to dependent on Fe to Ni ratio in the matrix of the composites. In the composites with 0.5 Fe:Ni matrix ratio, intermetallic phase formation in the reaction zone was suppressed. An increase in Ni content in the matrix (Fe:Ni ratios 1 and 2) resulted in the formation of μ intermetallic phase in the reaction zones of the composites.

- The growth kinetics of the reaction layers in the composites was also a strong function of matrix composition. Increased Ni content at the expense of Fe in the composite matrices resulted in a decrease in the growth rate of the intermetallic layers. The calculated growth constants of the intermetallic layers are 0.41 and 2.41 to 2.75 μ/√hours in in 1200°C/500hours annealed composites with 1 and 2 Fe:Ni matrix ratios. The activation energies of the intermetallic layer growth are 141 ±47kJ/mole, and 192 ±23kJ mole^{-1} for W/E-IV and W/E-V composites in the temperature range 1000-1200°C.

- Calculated average interdiffusion coefficients have also shown dependence on the matrix compositions. $\overline{\widetilde{D}}^{i}_{\text{eff}\,(\mu)}$ of Fe, Ni and W are higher in the composites with high Fe/Ni ratio. At 1200°C, $\overline{\widetilde{D}}^{Fe}_{\text{eff}\,(\mu)}$ is two order of magnitude higher and $\overline{\widetilde{D}}^{W}_{\text{eff}\,(\mu)}$ is one order of magnitude higher in the composite with 2Fe:Ni ratio compare to the lower ratio.

- The calculated values of activation energy of diffusion are 408, 415 and 356 kJ/mole, respectively for Cr, Fe and W in composite with 2Fe:Ni matrix ratio (W/E-V).

- There is feasibility of improving creep properties of the Fe-Ni-Cr alloy with 0.5Fe:Ni ratio by its reinforcement with W wires.

Chapter 9. Conclusions and Future Outlook

9.1 Conclusions

W wire interaction with two commercial (316L and HP alloy) stainless steels and some experimental Fe-Ni-Cr alloys with different Fe:Ni ratios was investigated in this thesis. The aim was to study the phase evolution, growth kinetics and dependence of these on the matrix composition of the composites. Important outcomes of this work are summarized in Table 9.1.

Table 9.1: Summery of the reaction layer phases and growth parameters in the studied composites.

Composite	Fe/Ni ratio	Reaction layer phase	k (μm/√h)		
			1000°C	1100°C	1200°C
W/316L	7	μ	0.69	1.96	4.68
W/Fe-Ni-Cr	2	μ	0.23	1.39	2.58
W/Fe-Ni-Cr	1	μ	0.07	0.37	0.41
W/Fe-Ni-Cr	0.5	none	-	-	-
W/HP	1	η	0.21	1.09	3.80

There are two significant contributions of this research that have industrial importance. Firstly, it has been shown that undesirable brittle intermetallic/carbide phases evolve in W/316L and W/HP composites due to W wire interaction with the alloy matrices. Secondly, the research has identified an alloy composition that does not form any intermetallic phase when reinforced with W. The alloy composition looks promising for developing creep resistant composites as no intermetallic phase was formed even after diffusion annealing in the temperature range 1000-1200°C.

Through systematic microstructural study, this research has characterized various phases that evolved in the W reinforced stainless steels. Results showed that presence of carbon in the composite matrix influence the phase formation in the reaction zones of the composites. In

316L matix with <0.03 wt.%C and some carbon free experimental alloy matrices, intermetallic phase μ formed when these matrices were reinforced with W wires. In the HP alloy matrix with 0.45wt.%C, formation of η and $M_{23}C_6$ carbides occured in the as-cast composites.

Diffusion annealing of the composites caused growth of the phases in the reaction zones of the composites. The phases developed as continuous layers surrounding W wires in the composites. The reaction phase that constitute major reaction layers in W/HP composite was η-carbide. In W/316L and W/Fe-Ni-Cr (1 and 2 Fe:Ni matrix ratios) composites, reaction layers consistent with μ-phase were developed during diffusion annealing. A noteworthy but undesirable feature of η and μ reaction layers developed in the annealed composites was their brittleness, which was evident from the multiple cracks observed within.

These reaction layers in the studied composites developed according to parabolic growth law during diffusion annealing at 1000-1200°. On comparing the growth of μ-phase reaction layers in the composites, highest growth rate was observed in W/316L composites. From the growth kinetics studies, the decreasing order of the growth constants for μ-phase layers at all temperatures is $k_{316L}>k_{2Fe:Ni}>k_{1Fe:Ni}$. This order foreshadowed the dependence of μ layer growth on Fe:Ni ratios in the matrix. Growth rate of the reaction layer increases with increasing Fe:Ni ratio in the composite matrix.

Results of microstructure study on W reinforced experimental alloy composites further elucidated the effect of matrix composition on the phase formation in the reaction zones of the composites. No intermetallic phase was observed in as-cast and diffusion annealed W wire reinforced composite matrices containing 0.5:1 Fe to Ni ratio. Intermetallic phase μ was formed in as-cast composites with 1:1 and 2:1 Fe: Ni matrix ratios. These observations clearly show a link between intermetallic phase formation and matrix composition in W/Fe-Ni-Cr composites.

The overall conclusion drawn from this study is that the W wires interaction with 316L, HP and Fe-Ni-Cr alloy with 1 and 2 Fe:Ni ratios leads to the formation of brittle reaction phases which are likely to be undesirable in creep resistant composites due to their low toughness and ensuant crack like defects formed upon annealing. The studies on the W/Fe-Ni-Cr matrices have shown that intermetallic phase formation does not take place in the matrix with 0.5 Fe:Ni ratio. The W wire reinforced composites fabricated using this alloy should be studied for their creep properties.

9.2 Future Outlook

This research has addressed the objectives highlighted in the introductory chapter of the thesis. Following are the major directions in which further studies in this area may be useful:

- **Phase diagram calculation:** Phase diagrams are essential tool for studying phase evolution and transformation during solidification and annealing. For binary and ternary systems, these diagrams are usually available in literature. The composite systems studied in this research comprise at least four major elements - Cr, Fe, Ni and W. The phase diagram data on this quaternary system is not available in literature. Due to the lack of this information, it was not possible to fully understand the phase formation and their transformation during solidification and diffusion annealing of the composites. Phase diagrams required to understand this can be computed utilizing thermo dynamical database (e.g. thermo-Calc) which would provide a better theoretical base for understanding solidification and phase evolution in the composites.

- **Creep testing:** The impetus behind studying W wire stability in the stainless steels was the fact that wire and matrix interaction leads to the evolution of phases that directly influence the creep strength of the composites fabricated using these alloys. The formation of brittle phases was observed in W/316L, W/HP and some W/Fe-Ni-Cr composites with high Fe:Ni ratios. These phases are considered harmful and therefore, are not desirable in the composites designed for high temperature applications. A Fe-Ni-Cr based composition with 0.5Fe:Ni ratio was identified in this research that does not form brittle intermetallic phase when reinforced with W wires. The composite remains intermetallic free even after diffusion annealing in 1000-1200°C. This finding looks very promising and the high temperature properties of the composite should be studied further by carrying out creep tests. The challenge in this regard is to fabricate composites with a controlled wire architecture (volume fraction and inter-wire spacing in the composite), which seems to be difficult using the casting method employed in this study. A melt infiltration method where the liquid metal is forced into the mold will be suitable for fabrication the composites for creep testing.

- **Coating application on tungsten wires:** The present work has shown that commercial 316L and HP alloy steels are prone to intermetallic/carbides formation with tungsten. However, the application of a suitable coating on W wires may help eliminate the brittle phase formation in these alloy matrices. In present study, it was found that W wire interaction with the alloy containing about 20%Cr and 0.5Fe:Ni ratio does not result in intermetallic phase formation. A coating of this alloy can be applied on W wires before reinforcing them in 316L and HP alloy matrices. But, this makes casting method unsuitable for composite fabrication because there are chances that the coating applied on the wires may dissolve due to high fabrication temperature used in the method. However, a powder metallurgy method that utilizes relatively low temperature for composite consolidation can be successfully used for reinforcing coated W wires in the desired commercial stainless steel matrices.

References

1. Petrasek, D.W., R.A. Signorelli, and J.W. Weeton, *Refractory Metal Fiber-Nickel Based Alloy Composites for use at High Temperature.* National Aeronautics and Space Administration TN 4787, 1968.
2. Petrasek, D.W. and R.A. Signorelli, *Preliminary Evaluation of Tungsten Alloy Fiber-Nickel-Base Alloy Composites for Turbojet Engine Applications.* National Aeronautics and Space Administration TN D-5575, 1970.
3. Stephens, R., D.W. Petrasek, and R.H. Titran, *Refractory Metal Alloys and Composites for Space Power Systems.* International Journal of Refractory Metals and Hard Materials, 1990. 9(2): p. 96-103.
4. Petrasek, D.W. and R.A. Signorelli, *Tungsten Fiber Reinforced Superalloys-A Status Review.* Proceedings of the 5th Annual Conference on Composites and Advanced Ceramic Materials: Ceramic Engineering and Science Proceedings. 2008: John Wiley & Sons, Inc. 739-786.
5. Glenny, R.J.E., *Fibrous Composites with High Melting Point Matrices.* Proceedings of the Royal Society of London. Series A, Mathematical and Physical Sciences, 1970. 319(1536): p. 33-44.
6. Brentnall, W.D. and D.J. Moracz, *Tungsten Wire Nickel base Alloy Composite Development*, in *TRW ER-7849*. 1976, NASA Cleveland, Ohio.
7. Petrasek, D.W. and J.R. Stephens. *Fiber Reinforced Superalloys for Rocket Engines*. in *AGARD Conference Proceedings on Applications of Advanced Materials for Turbomachinary and Rocket Propulsion*. 1989. Bath, UK.
8. Morris, A.W.H. and A. Burwood-Smith, *Some Properties of a Fibre-Reinforced Nickel-Base Alloy.* Fibre Science and Technology, 1970. 3(1): p. 53-78.
9. Dean, A.V., *Reinforcement of Nickel-Base Alloys with High-Strength Tungsten Wires.* Institute of Metals Journal, 1967. 95(3): p. 79-86.

10. Žitňanský, M. and M. Martinkovič, *Infiltration of the Metal through a Bundle of Continual Fibers.* Journal of Materials Processing Technology, 2000. 106(1-3): p. 163-166.

11. Ahmad, I. and J.M. Barranco, *Reinforced Cobalt Alloy Composites for Turbine Blade Applications.* SAMPE Quarterly, 1977. 8(3): p. 38-49.

12. Severdenko, V.P., A.S. Matusevich, and A.E. Piskarev, *Production of Composite Sheet Materials Based on KhN77Tyur and VZh98 alloys.* Powder Metallurgy and Metal Ceramics, 1974. 13(6): p. 476-479.

13. Westfall, L.J., *Tungsten Fiber Reinforced Superalloy Composite Monolayer Fabrication by an Arc Spray Process*, in *National Aeronautics and Space Administration TM-86917*. 1985.

14. Warren, R., L.O. Larsson, and T. Garvare, *A Method for the Fabrication of Wire-Reinforced, Metal Matrix Composites.* Composites, 1979. 10(2): p. 126-127.

15. Ochiai, S., K. Shimomura, M. Mizuhara, and Y. Murakami, *Effects of Interfacial Reaction on Deformation and Fracture Behaviour of Tungsten Fibre-Nickel Matrix Composites.* Transactions of the Japan Institute of Metals, 1975. 16(8): p. 463-471.

16. Brentnall, W.D., D.J. Moracz, and I.J. Toth, *Metal Matrix Composites for High Temperature Turbine Blades*. 1975, TRW Inc.: Cleveland Ohio.

17. Larsson, L.O. and R. Warren, *Fiber Reinforced Metals in Turbine Blades.* Journal of Engineering for Power, 1980. 102(3): p. 573-578.

18. Banas, F.P., A.A. Baranov, and E.V. Yakovleva, *Deformation of Composite Material during Alternate Heating and Cooling. Report 1.* Strength of Materials, 1975. 7(6): p. 744-748.

19. Dudnik, G.I., F.P. Banas, and B.V. Aleksandrov, *Nature of failure of Reinforced Sheets Subjected to Thermal Cycling.* Strength of Materials, 1973. 5(1): p. 106-107.

20. Warren, R., L.O. Larsson, P. Ekstrom, and T. Jansson, *Thermal Cycling of W-Wire Reinforced Metal Matrix Composites*, in *Progress in Science and Engineering of Composites*. 1982, Japan Society for Composite Materials: Tokyo, Japan. p. 1419-1426.

21. Mirotvorskii, V.S. and A.A. Ol'shevskii, *Reactions of Thoriated Tungsten Fibers with Iron-Base Powder Matrices.* Powder Metallurgy and Metal Ceramics, 1976. 15(7): p. 534-540.

22. Mirotvorskii, V.S. and A.A. Ol'shevskii, *Reactions of Tungsten Fibers with Cobalt-Base Matrices.* Powder Metallurgy and Metal Ceramics, 1978. 17(7): p. 536-541.

23. Mirotvorskii, V.S. and A.A. Ol'shevskii, *Interaction of Thoriated Tungsten at 1200-1600°C with Matrices Based on Various Metals.* Metal Science and Heat Treatment, 1979. 21(11-12): p. 826-829.

24. Klypin, B.A., A.M. Maslov, and S.B. Maslenkov, *Reinforcement of Heat Resistant Alloys with Filaments.* Metal Science and Heat Treatment, 1971. 13(8): p. 621-625.

25. Gruenling, H. and G. Hofer, *Deferred Recrystallization of Tungsten Wire in Nickel and Nickel-Chromium Matrices.* Zeitschrift fuer Werkstofftechnik, 1974. 5: p. 69-72.

26. Warren, R., *The Mechanical Properties of Fibre Reinforced Superalloy Composites*, in *Sintered Metal-Ceramic Composites*, G.S. Updhayaya, Editor. 1984, Elsevier Science B.V.: New Delhi. p. 215-237.

27. Caulfield, T. and J. Tien, *High Temperature Reaction Zone Growth in Tungsten Fiber Reinforced Superalloy Composites: Part I. Application of the Moving Boundary Equations.* Metallurgical Transactions A, 1989. 20A(2): p. 255-266.

28. Caulfield, T., R. Bellows, and J. Tien, *Interdiffusional Effects between Tungsten Fibers and an Iron-Nickel-Base Alloy.* Metallurgical Transactions A, 1985. 16A(11): p. 1961-1968.

29. Mazzei, P.J., G. Vandrunen, and M.J. Hakim. *Powder Fabrication of Fibre-Reinforced Turbine Blades*. in *AGARD Conference Proceedings on Advananced Fabrication Techniques in Powder Metallurgy and Their Economic Implications*. 1976. Paris, France.

30. Donachie, M.J. and S.J. Donachie, *Superalloys: A Technical Guide*. Second ed. 2002, USA: ASM International.

31. Isaikin, A.S., et al., *Tendency of Precipitation-Hardening Tungsten Wire in Contact with Nickel Alloys to Recrystallize.* Metal Science and Heat Treatment, 1980. 22(11): p. 824-827.

32. Chen, P.S., B. Panda, J.A. Lee, and B.N. Bhat, *Chemical Compatibility of Cast Waspaloy Composites Reinforced with Tungsten Wires,* in *Proceedings of the Symposium on High Performance Metal and Ceramic Matrix Composites*, K. Upadhya, Editor. 1994, The Minerals, Metals and Materials Society. p. 175-181.

33. Signorelli, R.A. and J.W. Weeton, *Metal-Matrix Fiber Composites for High Temperatures,* in *National Aeronotics and Space Administration Special Publication* 1970: Washington, D.C. p. 187-205.

34. Savchuk, A.N., V.E. Ol'shanetskii, and G.A. Krasnova, *Strength Characteristics of ÉI435-Molybdenum (or Tungsten) Filament Composites with an Alloyed Contact Zone.* Strength of Materials, 1975. 7(8): p. 970-973.

35. Villars, P. and K. Cenzual, *Pearson's Crystal Data: Crystal Structure Database for Inorganic Compounds (on CD-ROM)*. 2010, ASM International: Materials Park, Ohio, USA.

36. Sinha, A.K. and W. Hume Rothery, *The Iron-Tungsten System.* Journal Iron Steel Institute (London), 1967. 205: p. 1145-1149.

37. Kostakis, G., *Intermetallic Phases of the System Fe-W.* Zeitschrift fuer Metallkunde/Materials Research and Advanced Techniques, 1985. 76(1): p. 34-36.

38. Posthill, J. and D. Edmonds, *Matrix and Interfacial Precipitation in the W-Ni-Fe System.* Metallurgical Transactions A, 1986. 17A(11): p. 1921-1934.

39. Gladyshevskiy, E.I., V.S. Telegus, T.F. Fedorov, and Y.B. Kuz'ma, *The Ternary W-Cr-C System.* Russian Metallurgy, translated from Izvestiya Akedemii Nauk SSSR, Metally, 1967(1): p. 190-193.

40. Yakel, H.L., *Atom Distributions in Tau-carbide Phases: Fe and Cr Distributions in* $(Cr_{23}\text{-}xFe_x)C_6$ *with x=0, 0.74, 1.70, 4.13 and 7.36.* Acta Crystallographica, Section B (Structural Science), 1987. 43(3): p. 230-238.

41. Rundqvis, S. and G. Runnsjo, *Crystal Structure Refinement of* Cr_3C_2. Acta Chemica Scandinavica, 1969. 23(4): p. 1191-1199.

42. Bojarski, Z. and J. Leciejewicz, *Neutron Diffraction Study of the Crystal Structure of Tungsten Iron Carbides.* Archiwum Hutnictwa, 1967. 12(3): p. 255-263.

43. Epremain, E. and D. Harker, *The Crystal Structure of Ni_4W.* Journal of Metals (AIME) 1949. 185: p. 267-273.

44. Lonnberg, B. and T. Lundstrom, *Crystal Growth of Solid Solutions of the Group IV-VI Transition Metal Monocarbides from Molten Aluminium.* Chemica Scripta, 1987. 28(1): p. 25-32.

45. Cratchley, D., *Experimental Aspects of Fiber Reinforced Metals.* International Materials Reviews, 1965. 10(1): p. 79-144.

46. Grube, G. and A. Jedele, *Die Diffusion der Metalle im festen Zustand. 5. Mitteilung. Diffusion und Korrosion von Kupfer-Nickel-Legierungen.* Zeitschrift für Elektrochemie und Angewandte Physikalische Chemie, 1932. 38(10): p. 799-807.

47. Peirce, B.O., *A Short Table of Integrals*. 1929, Boston: Ginn & Company.

48. Matano, C. and O. Chujiro, *On the Relation between the Diffusion-Coefficients and Concentrations of Solid Metals (The Nickel-Copper System).* Transactions of Japanese Journal of Physics 1933. 8(3): p. 109-113.

49. Sauer, F. and V. Freise, *Diffusion in binären Gemischen mit Volumenänderung.* Zeitschrift für Elektrochemie, Berichte der Bunsengesellschaft für physikalische Chemie, 1962. 66(4): p. 353-362.

50. Boltzmann, L., *Zur Integration der Diffusionsgleichung bei Variabeln Diffusions Coefficienten.* Annalen der Physik, 1894. 289(13): p. 959-964.

51. Onsager, L., *Reciprocal Relations in Irreversible Processes. I.* Physical Review, 1931. 37(4): p. 405-426.

52. Onsager, L., *Reciprocal Relations in Irreversible Processes. II.* Physical Review, 1931. 38(12): p. 2265-2279.

53. Dayananda, M. and Y. Sohn, *A New Analysis for the Determination of Ternary Interdiffusion Coefficients from a Single Diffusion Couple.* Metallurgical and Materials Transactions A, 1999. 30A(3): p. 535-543.

54. Dayananda, M. and C. Kim, *Zero-Flux Planes and Flux Reversals in Cu−Ni−Zn Diffusion Couples.* Metallurgical and Materials Transactions A, 1979. 10A(9): p. 1333-1339.

55. Dayananda, M., *An Analysis of Concentration Profiles for Fluxes, Diffusion Depths, and Zero-Flux Planes in Multicomponent Diffusion.* Metallurgical and Materials Transactions A, 1983. 14A(9): p. 1851-1858.

56. Roper, G.W. and D.P. Whittle, *Theoretical Diffusion Profiles in Single-Phase Ternary Systems.* Metal Science, 1980. 14(11): p. 541-549.

57. Wagner, C., *The Evaluation of Data Obtained with Diffusion Couples of Binary Single-Phase and Multiphase Systems.* Acta Metallurgica, 1969. 17(2): p. 99-107.

58. Divya, V.D., U. Ramamurty, and A. Paul, *Interdiffusion and Growth of the Phases in CoNi/Mo and CoNi/W Systems.* Metallurgical and Materials Transactions A, 2012. 43(5): p. 1564-1577.

59. Kidson, G.V., *Some Aspects of the Growth of Diffusion Layers in Binary Systems.* Journal of Nuclear Materials, 1961. 3(1): p. 21-29.

60. Zener, C., *Theory of Growth of Spherical Precipitates from Solid Solution.* Journal of Applied Physics, 1949. 20(10): p. 950-953.

61. Porter, D.A., K.E. Easterling, and M. Sherif, *Phase Transformations in Metals and Alloys*. Third ed. 2009, Boca Raton Florida: CRC Press.

62. Karpinos, D.M., L.I. Tuchinskii, and L.R. Vishnyakov, *Stability of Metal Base Composite Materials.* Powder Metallurgy and Metal Ceramics, 1973. 12(3): p. 229-233.

63. Karpinos, D.M., V.K. Fedorenko, A.L. Burykina, and V.V. Gorskii, *Interfacial Reactions in Composite Materials with 80% Ni - 20% Cr Alloy Matrices and Tungsten and Molybdenum Base Fibers.* Powder Metallurgy and Metal Ceramics, 1974. 13(2): p. 138-147.

64. Warren, R., C.H. Andersson, and L.O. Larsson, *Fibre/Matrix Interactions in a Tungsten Alloy Wire-Reinforced Stainless Steel Composite.* Composites, 1979. 10(2): p. 121-125.

65. Tien, J., T. Caulfield, and Y. Wu, *High Temperature Reaction Zone Growth in Tungsten Fiber Reinforced Superalloy Composites: Part II. Matrix Chemistry Effects.* Metallurgical Transactions A, 1989. 20A(2): p. 267-272.

66. Lassner, E. and W.D. Schubert, *Tungsten: Properties, Chemistry, Technology of the Element, Alloys, and Chemical Compounds*. 1999, New York: Kluwer Academic.

67. Osterman, V. and H. Antes, eds. *Critical Melting Points and Reference Data for Vacuum Heat Treating*. 2010, Solar Atmosphere: Pennsylvania.

68. Rasband, W.S., *ImageJ*. 1997–2011, National Institutes of Health: Maryland, USA.

69. Goldstein, J., et al., *Scanning Electron Microscopy and X-ray Microanalysis*. Third ed. 2003, New York: Springer.

70. Randle, V., *Microtexture Determination and its Applications*. Second ed. 2003, London: Maney for the Institute of Materials, Minerals and Mining.

71. Randle, V., *Electron Backscatter Diffraction: Strategies for Reliable Data Acquisition and Processing*. Materials Characterization, 2009. 60(9): p. 913-922.

72. Friel, J.J., *X-Ray and Image Analysis in Electron Microscopy*. 2004, Princeton, New Jersey: Princeton Gamma-Tech.

73. Leng, Y., *Materials Characterization: Introduction to Microscopic and Spectroscopic Methods*. 2009, Singapore: John Wiley & Sons (Asia).

74. Day, A.P., *Channel 5 User Manual*. 2001, HKL Technology A/S: Hobro,Denmark.

75. Baker, H. and H. Okamoto, *Alloy Phase Diagrams*. ASM Handbook. Vol. 3. 1992, Materials Park, Ohio, USA: ASM International.

76. Zhu, J. and H.Q. Ye, *On the Microstructure and its Diffraction Anomaly of the μ Phase in Superalloys.* Scripta Metallurgica et Materialia, 1990. 24(10): p. 1861-1866.

77. Hiraga, K., T. Yamamoto, and M. Hirabayashi, *Intermetallic Compounds of the μ and P Phases of Co_7Mo_6 Studied by 1 MV Electron Microscopy.* Transactions of the Japan Institute of Metals, 1983. 24(6): p. 421-428.

78. Carvalho, P.A., et al., *HRTEM study of Co_7W_6 and its Typical Defect Structure.* Acta Materialia, 2000. 48(10): p. 2703-2712.

79. Antoni-Zdziobek, A., T. Commeau, and J.-M. Joubert, *Partial Redetermination of the Fe-W Phase Diagram.* Metallurgical and Materials Transactions A, 2013. 44(7): p. 2996-3003.

80. Predel, B. and M. O., *Landolt-Bornstein, Group IV Physical Chemistry - Phase Equilibria, Crystallographic and Thermodynamic Data of Binary Alloys, Volume 5.*

81. Guillermet, A. and L. Östlund, *Experimental and Theoretical Study of the Phase Equilibria in the Fe-Ni-W System.* Metallurgical and Materials Transactions A, 1986. 17(10): p. 1809-1823.

82. Bahadur, A. and O.N. Mohanty, *Aluminium Diffusion Coatings on Medium Carbon Steel.* Materials Transactions-Japan Institute of Metals, 1995. 36(9): p. 1170-1175.

83. Shackelford, J.F., W. Alexander, and J.S. Park, *Handbook of Materials Science & Engineering*. 2001, Boca Raton, Florida: CRC Press.

84. Rothman, S.J., L.J. Nowicki, and G.E. Murch, *Self-Diffusion in Austenitic Fe-Cr-Ni Alloys.* Journal of Physics F: Metal Physics, 1980. 10(3): p. 383-398.

85. Mehrer, H., *Diffusion in Intermetallics.* Materials Transactions, JIM, 1996. 37(6): p. 1259-1280.

86. Tillack, D.J. and J.E. Guthrie, *Wrought and Cast Heat Resistant Stainless Steels and Nickel Alloys for the Refining and Petrochemical Industries.* NiDI Technical Series, 1998. 10071: p. 265.

87. Wu, X.Q., et al., *The Eutectic Carbides and Creep Rupture Strength of 25Cr20Ni Heat-Resistant Steel Tubes Centrifugally Cast with different Solidification Conditions.* Materials Science and Engineering: A, 2000. 293(1–2): p. 252-260.

88. Pollock, C.B. and H.H. Stadelmaier, *The eta carbides in the Fe−W−C and Co−W−C systems.* Metallurgical Transactions, 1970. 1(4): p. 767-770.

89. Bergström, M., *The Eta-Carbides in the Quaternary System Fe-W-C-Cr at 1250°C.* Materials Science and Engineering, 1977. 27(3): p. 271-286.

90. Stadelmaier, H.H. and C. Suchjakul, *Overview of the Quaternary System Iron-Nickel-Tungsten-Carbon.* Zeitschrift Fur Metallkunde, 1985. 76(3): p. 157-161.

91. Bergström, M., *The Eta-Carbides in the Ternary System Fe-W-C at 1250°C.* Materials Science and Engineering, 1977. 27(3): p. 257-269.

92. Bhadeshia, H. and R. Honeycombe, *Steels: Microstructure and Properties*. 2011, Oxford, UK: Elsevier Ltd.

93. Swaminathan, J., et al., *Failure Analysis and Remaining Life Assessment of Service Exposed Primary Reformer Heater Tubes.* Engineering Failure Analysis, 2008. 15(4): p. 311-331.

94. Asthana, R., *Reinforced cast metals: Part I Solidification microstructure.* Journal of Materials Science, 1998. 33(7): p. 1679-1698.

95. Davis, J.R., *Nickel, Cobalt, and their Alloys*. ASM Specialty Handbook. 2000, Materials Park, Ohio, USA: ASM International.

96. Kanaya, K. and S. Okayama, *Penetration and Energy-Loss Theory of Electrons in Solid Targets.* Journal of Physics D: Applied Physics, 1972. 5(1): p. 43.

97. Castaing, R., *Application des Sondes Électroniques à une Méthode d' Analyse Ponctuelle Chimique et Cristallographique*. 1951, University of Paris: Paris.

98. ASTM, *Standard Guide for Quantitative Analysis by Energy Dispersive Spectroscopy*. 1998, ASTM: Philadelphia.

Appendix A. Chemical Analysis and Crystal Structure Identification by Energy Dispersive Spectroscopy and Electron Backscattered Diffraction Techniques

The studies presented in this thesis utilised energy dispersive spectroscopy (EDS) and electron backscattered diffraction (EBSD) techniques for the chemical analysis and crystal structure identification of various phases in the W wire reinforced alloys. This appendix highlights the working principles of these techniques and major factors affecting the analyses.

A.1. Beam Specimen Interaction in SEM

When an electron beam strikes a specimen in a scanning electron microscope, various signals are generated as shown in Figure A.1.

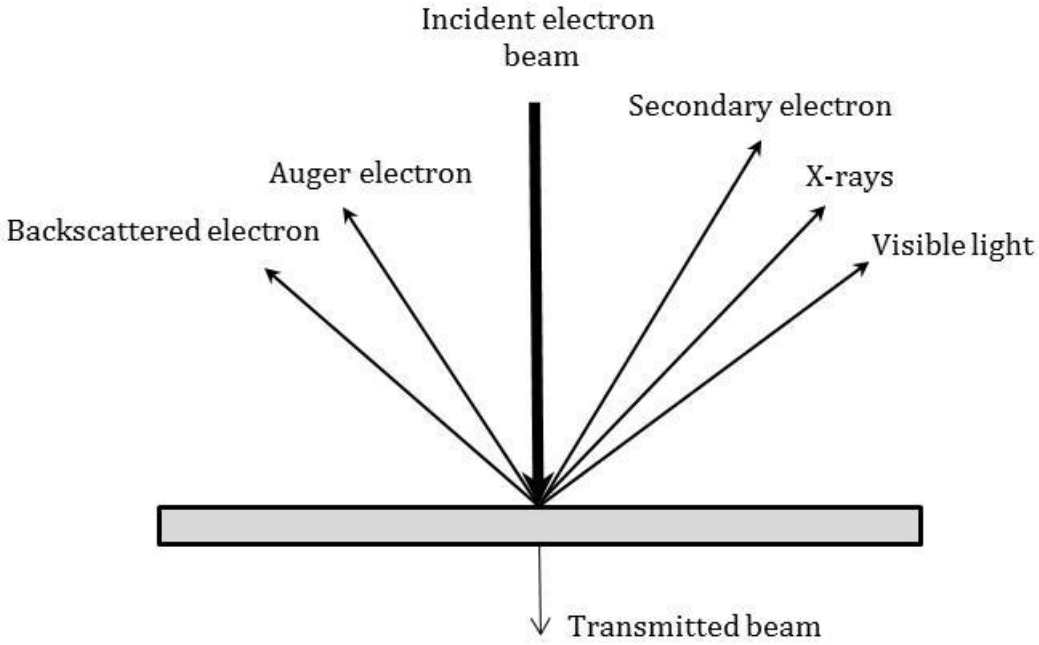

Figure A.1: Signals generated during electron beam-specimen interaction in SEM.

Secondary electrons (SE) are generated from close to the specimen's surface (~5-50 nm), electrons are backscattered (BSE) from a somewhat greater depth (~300nm) and characteristic X-rays are generated throughout the interaction volume of the specimen.

The interaction volume through which electron beam penetrates strongly depends on the atomic number of the material being examined, accelerating voltage of the microscope and the angle of specimen tilt. A higher voltage penetrates deeper into the sample and generates a larger interaction volume. Heavy elements can absorb more electrons and produce a smaller interaction volume. The interaction volume is generally described by a single parameter called electron range. The electron range represents the penetration depth of incident electrons. For a perfectly flat and electron opaque sample, the penetration depth can be calculated from the Kanaya-Okayama Formula [96] as:

$$R = \frac{0.276A}{Z^{0.89}\rho} E_0^{1.67} \qquad \text{A.1}$$

Where R is the penetration depth (µm), A is the atomic weight (g/mole), Z is the atomic number, ρ is the density (g/cc), and E_0 is the electron beam energy (keV). For example, in case of Fe, when an incident electron beam at an accelerating voltage of 20 keV strikes the specimen, the electron penetration depth will be approximately 1.6µm.

A large tilt angle θ (tilted off normal) produces a smaller interaction volume. The reduction in the electron range as a function of θ is described as:

$$R(\theta) = R(0)cos\,\theta \qquad \text{A.2}$$

where R(0) is the penetration depth at normal beam incidence.

With an increasing tilt angle, the interaction volume becomes longer in the direction downhill from where the beam strikes. With a tilt angle >60°, a large proportion of beam electrons escape and the electron volume dimension parallel to the tilt axis decreases.

Since X-rays are generated from very deep in the interaction volume, it dictates the spatial resolution in the EDS analysis. Larger interaction volume can results in excitation of X-rays from the bulk of the sample and may lead to inaccurate results while analysing small/thin features. Also, while doing spot analysis on the sample, if the distance between two spots is less than the width of the interaction volume, X-ray intensities from the adjacent spots may overlap.

There are two ways to reduce interaction volume, (i) analysing very thin specimens, which is possible only in transmission electron microscope (TEM) and (ii) reducing the accelerating voltage of the electron beam. Roughly, there is a threshold value for accelerating voltage in EDS analysis. It should be at least twice the energy of the highest energy lines that can be generated from elements in the specimen. Therefore, in the current study an accelerating voltage between 15-20keV was needed to accurately record all the X-ray peaks from the specimen. Lower accelerating voltages can result in reduced interaction volumes but because of the limited energy resolution of current EDS detectors, it is difficult to resolve the low energy X-ray lines of different elements.

A.2. Energy Dispersive Spectroscopy

EDS is a powerful technique to extract qualitative as well as quantitative information about the chemistry of materials. The technique makes use of the detection and discrimination of X-rays produced from the sample when it is bombarded with a high energy electron beam in SEM.

A.2.1. Generation of X-Rays

Two types of X-rays are produced as a result of inelastic interaction between the electron beam and the specimen. These are:

Characteristic X-rays: The individual shells in an atom are represented by letters K, L, M, N and so on. Characteristic X-rays are produced when the electron beam knocks off electrons from the inner shell of the atom in the specimen. When the hole created by the electron beam in the innermost K shell is filled by dropping of electron from the higher order shells, a K X-ray peak is emitted. Similarly, emission of L X-ray peak takes place when L-shell electrons are knocked off by the beam electron and are replaced by electron from the higher order shells (Figure A.2). Characteristic X-rays appear as sharp peaks in the spectrum and are called so because their specific energies are characteristic of the particular element from which they are excited.

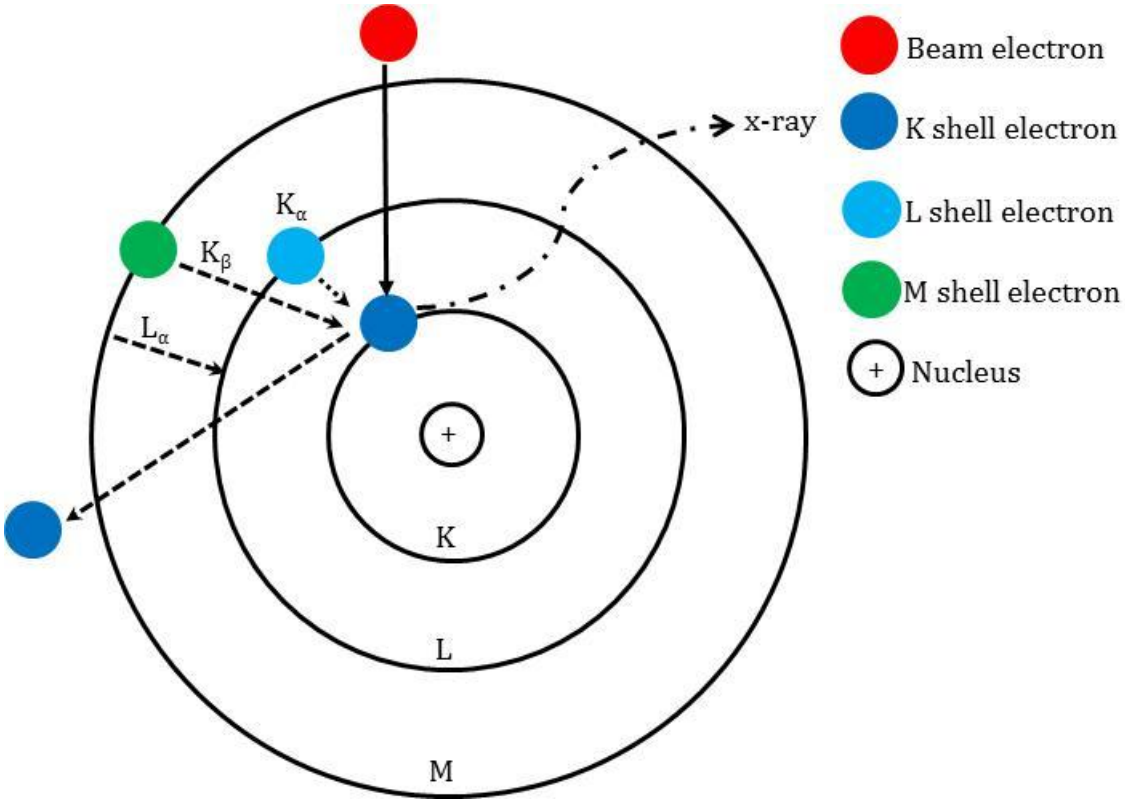

Figure A.2: Schematic diagram showing emission of characteristic X-rays from an atom

Continuum X-rays: These X-rays are produced as a result of the interaction between electron beam and electrical field of the nucleus of the specimen atoms. These X-rays do not constitute sharp peaks and appear as a continuous background in X-ray spectrum on which characteristics X-rays are superimposed. These X-rays are considered as nuisance and need to be differentiated from the characteristic X-rays for accurate elemental identification. Figure A.3 shows an X-ray spectrum containing both continuum and characteristic X-rays.

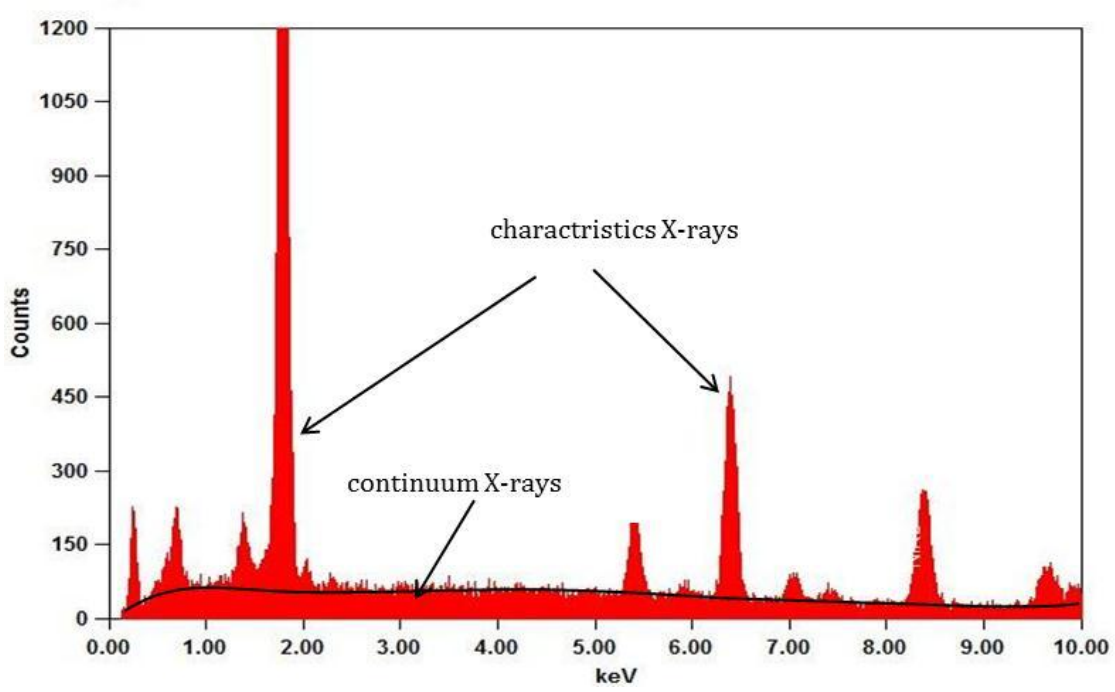

Figure A.3: A typical EDS spectrum showing characteristic and continuum X-rays

A.2.2. Detection and Processing of X-rays

Typically, a lithium drifted silicon detector is employed for the detection of X-rays in modern EDS systems. The X-rays hitting the detector produce electron-hole pairs in silicon. The electron-hole pairs created by the incoming X-rays are swept away by bias voltage of several hundred volts and converted to a charge pulse. The charge pulse is converted into a voltage pulse by means of a pre-amplifier. The processed signal is then displayed as a histogram of X-ray intensity versus voltage.

A.2.3. Critical Parameters in EDS analysis

Accelerating voltage: In order to ensure that all the energy lines from the samples are excited, an accelerating voltage greater than the energy of the most probable highest energy line is chosen in EDS analysis. Typical accelerating voltages are 2 times the highest energy line and 10 to 20 times the lowest energy line of interest.

Dead time and count rate: The voltage pulse entering the detector is shaped and filtered to remove the noise associated with it before displaying it as an energy peak on the spectrum. The time taken for this is known as process time. Longer process times ensure better peak

resolution, but fewer X-rays will be measured by the detector which results in a low output count rate. This causes pulse pileup at the detector and its counting efficiency decreases. To minimize pulse pileup, a certain time is allowed during which the incoming pulses are not measured by the detector. This time is called as dead time and is represented by:

$$\text{dead time } (\%) = \left(1 - \frac{R_{out}}{R_{in}}\right) \times 100 \qquad \text{A.3}$$

where R_{in} and R_{out} are input and output count rates, respectively. A dead time of 20-40% gives maximized R_{out}. This range of dead time can be achieved by controlling probe current that ultimately controls R_{in}.

Take-off angle: The angle between X-ray trajectory and sample surface under observation is called take-off angle. This is a combination of detector angle, working distance and sample tilt. Typical angle in EDS ranges from 25-40°.

A.2.4. Qualitative Analysis

The energy of characteristic radiations is specific to the atomic number and the energy difference between shells, that changes in a regular step when the atomic number changes by one unit. This is the well-known Moseley's law which is the basis of qualitative elemental analysis with EDS and can be written as:

$$E = A(Z - C)^2 \qquad \text{A.4}$$

where E is the energy of X-ray line and Z is the atomic number of emitter element. A and C are constants which differ for each X-ray series. Equation A.4 can be used to measure the energy of X-ray lines and from it, the atomic number producing that line can be identified. The detailed description for manual qualitative identification of peaks is given in [69]. Almost all the modern SEM-EDS systems are equipped with software to perform automatic identification of peaks within constraints set by the user.

A.2.5. Quantitative Analysis

Standard Quantitative Analysis: Identification of X-ray peaks in the acquired spectrum is the prerequisite for standard-based quantification of the elements in sample under observation. For standard-based quantitative analysis, X-ray spectra of the specimen and

standard are acquired under identical instrumental conditions. For accurate results, it is necessary that the composition of the standard must be similar to that of the specimen. The X-ray spectra from the specimen and the standard are compared. If the contribution from artefacts to the X-ray generation is negligible, the measured X-ray intensity ratios between specimen and standard will be roughly equal to the ratios of the weight fraction of standard and the emitting element. This relation was first observed by Castaing [97] and is known as Castaing's first approximation to quantitative analysis:

$$\frac{C_i}{C_{(i)}} = \frac{I_i}{I_{(i)}} = k_i \qquad \text{A.5}$$

where C_i and $C_{(i)}$ are the weight percent of the element i in the unknown and in the standard and I_i and $I_{(i)}$ are the X-ray intensities in the unknown and standard, respectively.

In practice, standards with composition close to that of specimen are seldom available. When the standard differs in composition from the specimen, there can be significant deviations between the ratio of X-ray intensities and ratio of concentration. This happens because of matrix effects that occur due to the elastic and inelastic scattering processes and propagation of X-rays from the specimen to the detector. In such cases, certain mathematical corrections are applied to the measured intensities from the standard and sample to determine the accurate specimen composition. One such correction procedure is called ZAF correction. For conceptual understanding and ease of calculations, matrix effects can be broken into three factors:

- **Atomic number factor (Z_i):** The atomic number factor corrects for the difference between the X-rays that are generated in the specimen compared with those generated in the standard. It arises because of differences in the backscatter coefficient and the electron stopping power between sample and standard.

- **X-ray absorption (A_i):** This factor is related to the decrease in intensity of X-rays because of absorption and is usually the most important one. It corrects for those X-rays that are generated in the specimen but absorbed before they are able to escape and be detected.

- **X-ray fluorescence (F_i)**: The characteristic fluorescence factor is usually the least significant. It corrects for those X-rays that are caused by fluorescence mechanism.

These X-rays are the result of secondary fluorescence caused by X-rays that were generated but absorbed by the other atom that later on emitted as its own characteristic X-rays.

Using these matrix effect factors, the general formula for standard based quantitative analysis can be written as:

$$\frac{C_i}{C_{(i)}} = [ZAF]_i \frac{I_i}{I_{(i)}} = [ZAF]_i k_i \qquad \text{A.6}$$

The equation is applied separately for each element present in the specimen to correct the matrix effects and is the basis for X-ray microanalysis in SEM.

A.2.6. Standardless Quantitative Analysis

For standardless analysis, only the X-ray spectrum from the unknown specimen is used. The standard X-ray intensities in the denominator of the Equation A.6 are calculated rather than measured. This type of analysis falls into two categories depending on how the required standard intensities are calculated.

- **True-Standardless analysis** in which the required standard intensities are calculated from first principles, considering all aspects of X-ray generation, propagation and detection.

- **Fitted-Standard standardless analysis** in which the standard intensities are derived from a suite of experimental standards measurements performed on the instrument at the software manufacturer laboratory. These remotely measured standard intensities are then adjusted for the characteristics of the local instrument actually being used to measure the unknowns.

With either method used to calculate standard intensities, the resulting Standardless k ratios (unknown/calculated standard) are subjected to matrix correction with one of the usual approach like ZAF correction described in previous section.

In general, fitted-standards standardless analysis works well for specimens consisting of transition elements of which the K lines span the range 5-10 keV, such as stainless steels. Though standard-based quantitative analysis always gives more accurate results (with

homogeneous standard having similar composition to sample), it has been observed that standardless analysis also works well and gives similar results as that of standards based analysis in case of analysis of major elements (>10wt.%)[98].

A.2.7. Light Element Analysis by EDS

Elements with atomic number <11 are considered light for the purposes of X-ray microanalysis in conventional EDS detectors with a beryllium (Be) window. Quantitative analysis of light elements is difficult and often inaccurate, because these elements produce soft X-rays which are hard to detect, easily absorbed and subjected to chemical shifts. Low count rates generated from the light elements and uncertainties in the matrix correction reduce the accuracy of the analysis. Carbon contamination deposited on the specimen also leads to inaccuracies for the light elements. The contamination comes from interaction of the electron beam with residual pump oil in the chamber of the microscope. Lower peak to background ratios for soft X-rays also degrade the minimum delectability limit for light metals. It is recommended [98] that if the stoichiometry of the compound containing light elements is known, then calculation by stoichiometry is the most accurate method to quantify those light elements.

A.3. Alternative Technique

There is another technique called wavelength dispersive spectroscopy (WDS) that can be used instead of EDS for elemental analyses. A common instrument that uses this technique is electron microprobe analysis (EPMA). WDS gives better resolution as compared to EDS (5 eV vs. 130eV), which means it can resolve X-ray peaks that are difficult to resolve by EDS. It can detect trace elements down to 100 ppm and also light elements with atomic numbers >4. Although WDS is a better technique in terms of accuracy, there are disadvantages associated with it that makes it less attractive than EDS in practical situations. In EDS, X-rays of all energies are detected simultaneously by the detector and entire spectrum of interest can be acquired in a short time (10-100s). This allows rapid analysis of major and minor constituents present in a specimen. WDS makes use of multiple crystal detectors to separate X-ray wavelengths and only one wavelength is detected at any time. Therefore, a longer time and better skills are needed to collect a full WDS spectrum.

A.4. Electron Backscattered Diffraction (EBSD)

EBSD integrated with SEM is a relatively new technique that is finding widespread application in orientation measurement and discrimination/identification of phases in crystalline materials. Comprehensive phase identification in materials requires simultaneous composition and diffraction data collection from the phase of interest and it can easily be accomplished by technique such as EDS with which majority of modern SEMs are equipped with. Some of the main advantages of using SEM-EBSD for phase identification are easy sample preparation requirements and reasonably good spatial resolution. In a tungsten filament SEM, the spatial resolution is ~50 nm and angular resolution is in the range 0.5° to 1°. Diffraction techniques based on X-rays and transmission electron microscopy are alternatives to SEM-EBSD and Table A.1 compares these techniques.

Table A.1: Comparison of various diffraction techniques used to study crystal structure of materials

Attribute	X-ray Diffraction	SEM-EBSD	TEM
Sample preparation	Easy	Easy/moderate	Difficult
Ease of use	Moderate	Easy	Difficult
Speed	Minutes	Minutes	Hours
Spatial resolution	0.1mm	0.1µm	~1 nm

A.4.1. Principle of Operation

Phase identification by EBSD is based on the acquisition and indexing of electron back-scattered patterns (EBSP), also known as Kikuchi patterns generated from the phase under investigation in a specimen. The backscattered diffracted electrons which interfere constructively according to Bragg's law produce Kikuchi patterns. To increase the collection efficiency of these patterns, the specimen stage of the microscope is tilted, usually at 70° from horizontal so that the specimen surface makes an angle, typically 20° with the incoming electron beam. A special detector unit attached to the SEM is used to detect the Kikuchi

patterns. The unit consists of a phosphor screen and a low light camera (10^{-4} lux). The camera is connected to a computer with a frame grabber that captures and display EBSP image on screen. Since diffraction occurs at very small angle (1-2°), the bands appear as straight lines on the screen.

A.4.2. EBSP Indexing

The acquired diffraction pattern contains vast amount of crystallographic information that can be used to identify probable phases in the specimen. A typical electron backscattered pattern is shown in Figure A.4. The pattern consists of number of lines in the form of bands that intersect with each other. Each band represents a lattice plane and width of the band is inversely proportional to the inter planer spacing in the lattice. Intersections of the Kikuchi bands are the projections of zone axis of the crystal.

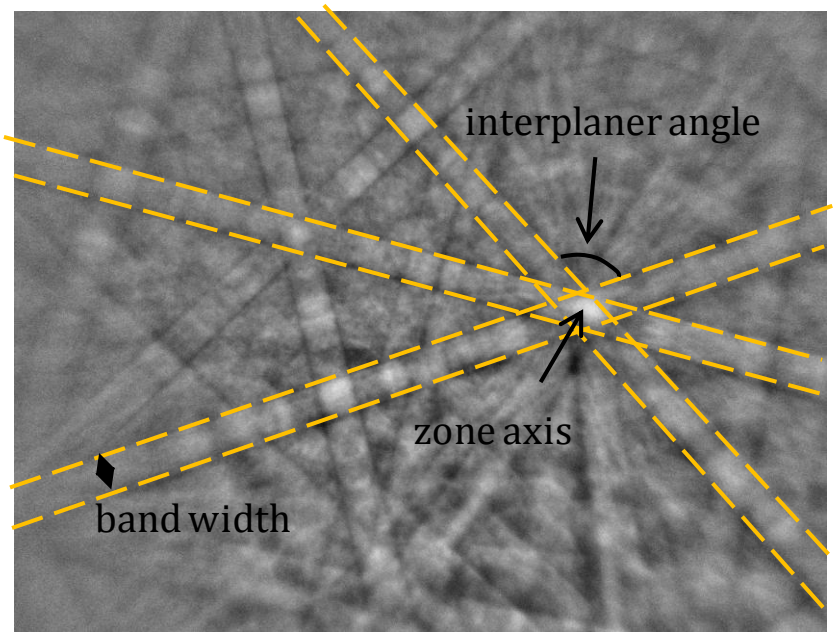

Figure A.4: Example of an EBSD pattern showing crystallographic informations.

Indexing an EBSP involves assigning indices to the visible Kikuchi bands or the intersections of Kikuchi bands. The following procedure is generally followed for phase identifications:

- Collect several high quality EBSP and also chemical information by EDS from the phase of interest.
- Based on the chemistry of the phase, search the crystallographic database to compile a list of probable candidate phases.

- Index the acquired diffraction patterns using all the candidate matches until a consistent set of indices for the Kikuchi bands are found.

- Simulate the diffraction pattern using the chosen parameters from the crystallographic database and check the fit with experimental pattern. Matching is considered successful if mean angular deviation which is the average misfit between detected and simulated Kikuchi bands is <1°.

A.4.3. Pattern Quality and Indexing Problems

A well calibrated EBSD system is capable of indexing the majority of the good quality Kikuchi patterns. However, the following are the issues that may affect pattern solving:

- **Indistinct patterns:** Since EBSP are generated from the top few nm of the specimen surface, the pattern quality is very sensitive to the imperfections present in this surface layer. Sometimes inadequately prepared specimens contain damage and deformation from the polishing abrasive (diamond particles in most cases) that degrade the patterns quality. The damage can be minimized by using either electropolishing or etching and polishing with colloidal silica as a final polishing step. Commercially available colloidal silica solution consists of negatively charged particles of silicon dioxide (SiO_2) with a pH value between 8 and 11. The solution polishes and slightly etches the specimen, removing most of the surface deformation layer

- **Simultaneous multi pattern sampling:** This situation arises when analysing a specimen with fine microstructure when the EBSP is formed from two or more phases. Ideally fine microstructures require a fine probe size which usually means using a FEG-SEM.

- **Complex crystal structures and multiphases:** These can cause problems in pattern indexing. Usually pattern indexing is more difficult for low symmetry systems than for phases with high symmetry.

- **Null indexing:** Null indexing occurs when the acquired pattern cannot be indexed or no pattern with threshold quality is sampled. This can happen if the surface under observation contains cracks, inclusions or interfaces. Sampling points which are located on the interface generally return null solution because of grooving effects

and/or sampling of two patterns on either side of the interface. If the number of null solutions is high, one should look for the overlooked phases or inappropriate solve parameters.

Appendix B. F-Test for the Selection of Composition Profiles for Diffusion Analyses

An example of the regression analysis and filtering of reliable data for diffusion analyses is presented here.

Table B.1 shows experimental composition versus distance data determined by EDS on η-phase reaction layer in W/HP composite annealed at 1200°C for 500 hours.

EXCEL inbuilt function LINEST was used to calculate the parameters of straight line that fit best to the data. The equation for the line is:

$$y = mx + C \qquad \text{B.1}$$

where m is the slope of the line and C is the intercept that the line makes at y. In addition to the slope and intercept, the LINEST function also returns additional regression statistics which are useful to further analyse the fits. The statistical parameters generated in the present case are presented in Table B.2. Table also shows R^2 value, which is considered as a measure of goodness of fit of the data and is calculated as:

$$R^2 = \frac{SS_{reg}}{SS_{tot}} = \frac{\sum(\hat{y}_i - y_{av})^2}{\sum(y_i - y_{av})^2} \qquad \text{B.2}$$

where SS stands for sum of squares. $\hat{y}_i$ and y_i represent the fitted and the experimental y values and y_{av} is the average value.

The value of R^2 close to one is good but it does not always mean that there is a linear relationship among the data points. The quality of a fit can better be judged by uncertainty in the slope of the fitted line and its intercept at y axis. Even for R^2 close to one, there can be large uncertainties in the slope and the intercept. A better statistical test to judge the goodness of fit is the F-statistics that determines whether the observed relationship between the dependent and independent variables occurs by chance only or indeed there is a linear relationship between them. The F-statistics is the ratio of the explained and unexplained variances and is expressed as:

$$F_{stat} = \frac{varience\ explained}{varience\ unexplained} = \frac{\sum_i^n (\hat{y}_i - y_{av})^2 / V_1}{\sum_i^n (y_i - y_{av})^2 / V_2} \qquad \text{B.3}$$

where V_2 is the degree of freedom and V_1 is a parameter which is calculated from number of data points (N) and V_2 as:

$$V_1 = N - (V_2 + 1) \qquad \text{B.4}$$

The value of F_{stat} returned by LINEST function is used in F-test. Using V_1 and V_2, the critical (F_{crit}) values for various levels of significance can be found from the standard Table. In the present case V_1 and V_2 are 1 and 38, respectively. For these values, the corresponding F_{crit} value for 95% confidence interval is 4.1. Confidence level tells us how sure we can be about the linear relationship between the data points. 95% confidence level means we are 95% certain that there is a linear relationship between the data points. $F_{stat} > F_{crit}$ means that there exists a linear relationship between the data points, otherwise data is just a random scatter of points. For example, comparing F_{stat} given in Table B.2 with the F_{crit} value noted from the statistical Table, we find that for Fe $F_{stat} < F_{crit}$. Therefore, the composition profile of Fe is just a random scatter of data points without any linear relationship. Similar comparison was performed on multiple sets of composition profiles and the profiles that did not satisfy the criteria were excluded from the diffusion analyses.

Table B.1: Experimentally determined composition profiles in η-phase reaction layer of W/HP composite diffusion annealed at 1200°C for 500 hours.

Distance (μm)	Composition (at.%)			
	Cr	Fe	Ni	W
16	30	20.74	13.72	32.03
18	27.64	22.63	14.05	35.69
20	23.42	22.81	17.36	36.4
22	25.31	21.68	13.72	39.29
24	20.61	22.66	18.23	38.5
26	24.74	19.32	17.95	37.99

28	24.85	22.23	14.94	37.98
30	24.16	20.65	16.22	38.97
32	24.3	21.28	16.39	38.03
34	23.67	22.04	15.47	38.83
36	25.35	22.73	12.11	39.81
38	25.45	21.23	13.04	40.28
40	24.4	23.83	15.86	35.9
42	27.25	23.49	13.94	35.33
44	29.2	18.69	9.14	42.96
46	23.84	22.2	13.78	40.18
48	23.37	21.84	15.31	39.48
50	23.67	21.81	13.45	41.07
52	23.29	21.09	14.14	41.48
54	24.71	21.11	13.09	41.08
56	23.41	20.54	14.87	41.18
58	23.34	22.78	13.23	40.64
60	23.89	21.15	14.59	40.38
62	22.71	22.62	13.88	40.79
64	24.21	20.91	13.68	41.2
66	22.44	22.22	13.57	41.77
68	23.28	21.65	13.25	41.83
70	21.31	22.55	14.82	41.33
72	22.9	22.01	15.1	39.99
74	21.96	22.42	13.69	41.93
76	21.75	22.59	12.82	42.84
78	22.18	22.02	13.09	42.71
80	21.55	21.06	13.7	43.69
82	21.03	20.83	14.59	43.56
84	21.27	22.51	12.52	43.71

86	21.03	21.67	12.2	45.09
88	20.66	20.95	13.09	45.29
90	20.76	22.99	11.32	44.93
92	19.5	22.51	12.94	45.06
94	20.78	22.17	10.08	46.97

Table B.2: Statistical parameters generated by linear fitting of the data given in Table B.1

Elements	y=mx+C		R^2	F_{stat}
	m	C		
Cr	-0.07	27.44	0.53	43.61
Fe	0.00	21.56	0.01	0.39
Ni	-0.04	16.25	0.28	14.73
W	0.12	34.32	0.76	122.25